

Investigating spatial and temporal patterns of deformation and erosion in orogens

Insights from
Himalaya-Tibet Orogen & European Alps

Dissertation

der Mathematisch-Naturwissenschaftlichen Fakultät
der Eberhard Karls Universität Tübingen
zur Erlangung des Grades eines
Doktors der Naturwissenschaften
(Dr. rer. nat.)

vorgelegt von

Solmaz Mohadjer

aus Teheran

Tübingen

2019

Gedruckt mit Genehmigung der Mathematisch-Naturwissenschaftlichen Fakultät der
Eberhard Karls Universität Tübingen.

Tag der mündlichen Qualifikation:

18.11.2019

Dekan:

Prof. Dr. Wolfgang Rosenstiel

1. Berichterstatter:

Prof. Todd Ehlers, Ph.D.

2. Berichterstatterin:

Prof. Rebecca Bendick, Ph.D.

Abstract

Recent advances in high resolution topography, geochronology and satellite geodesy techniques have provided datasets and tools that can be used to investigate the spatio-temporal patterns of deformation and erosion in mountain landscapes. These datasets are critical ingredients for constraining and mitigating geologic hazards which are also spatial and/or temporal in nature. By compiling and displaying datasets related to Quaternary faulting in a relational database and results from statistical analysis of fault slip rate data, this dissertation aims at refining the tectonic evolution of the Himalaya-Tibet orogen and the surrounding regions, with an emphasis on resolving spatial and temporal variations in deformation rates. Similarly, this dissertation investigates temporal variations in post-glacial erosion and the role of rockfalls in the evolution of a deglaciated valley in the European Alps. This is achieved using frequency-magnitude statistics.

The relational database displays >1,000 Quaternary fault traces, with fault parameters for 123 Quaternary faults, and >34,000 earthquakes within the India-Asia collision zone. Nearly all regions of high seismicity overlap with where Quaternary faults have been mapped. However, not all faulted areas within these regions show high levels of seismicity. Displaying faults with paleoseismic records and/or slip rate data highlights regions that are capable of producing large earthquakes. The analysis of 57 Quaternary/Global Positioning System (GPS) slip rate pairs for 19 Quaternary faults from the database suggest that a moderate percentage (71%) of the total variation in the Quaternary slip rates can be statistically explained by a linear relationship between the GPS and Quaternary rates. The remaining 29% may be due to other factors such as temporal variations in slip rates over timescales individual methods are sensitive to and/or methodological shortcomings. In the deglaciated Lauterbrunnen valley, there appears to be large temporal variations in rockfall activity since deglaciation. Long timescale (~11 ka) rockfall inventories indicate higher rates of rockfall activity than intermediate (1 ka) and short (5.2 years) timescales as predicted by power-law and terrestrial laser scans (TLS) observations, respectively. This is likely due to debuttressing and stress relaxation effects after glacial retreat, and/or the influence of frost-shattering due to climatic oscillations in the past 11 ka.

Taken together, results from this study shed light into the kinematics of deformation and postglacial erosion rates in mountainous settings. Over large spatial scales, there appears to be little temporal variation in deformation rates. Over smaller scales, there are large temporal variations in erosion rates. The datasets and methods used in this dissertation provide a platform for further investigation of spatio-temporal patterns of deformation and erosion in mountain environments, and guide future research by identifying where data gaps exist.

Zusammenfassung

Neueste Fortschritte in Techniken der hochauflösenden Topographie, Geochronologie und Satellitengeodäsie haben Datensätze und Instrumente hervorgebracht, mit denen die räumlich-zeitlichen Verformungs- und Erosionsmuster in Gebirgslandschaften untersucht werden können. Diese Datensätze sind wichtige Bestandteile zur Begrenzung und Minderung geologischer Gefahren, die auch räumlicher und/oder zeitlicher Natur sind. Diese Arbeit zielt darauf ab, Kenntnisse der tektonischen Entwicklung des Himalaya-Tibet-Orogens und der umliegenden Regionen zu verfeinern, insbesondere in Bezug auf räumliche und zeitliche Schwankungen in Deformationsraten. Dies gelingt durch die Zusammenstellung und Darstellung von Datensätzen zu quartären Störungen in einer relationalen Datenbank und durch Ergebnisse aus der statistischen Analyse von Daten zu Relativbewegungsraten an Störungen. Gleichmaßen untersucht diese Arbeit zeitliche Schwankungen der postglazialen Erosion und den Einfluss von Steinschlägen auf die Entwicklung eines kürzlich eisfrei gewordenen Tals in den europäischen Alpen. Dies wird mit Magnituden-Häufigkeits-Statistik erreicht.

Die relationale Datenbank zeigt >1.000 quartäre Störungsspuren mit Störungsparametern für 123 quartäre Störungen und >34.000 Erdbeben innerhalb der Kollisionszone von Indien mit Asien. Nahezu alle Regionen mit hoher Seismizität überschneiden sich mit Gebieten, in denen quartäre Störungen kartiert wurden. Es weisen jedoch nicht alle Störungsgebiete auch eine hohe Seismizität auf. Bei der Darstellung von Störungen mit vorhandenen paläoseismischen Daten und/oder Relativbewegungsraten werden Regionen hervorgehoben, in denen große Erdbeben auftreten könnten. Die Analyse von 19 Störungen, an denen es insgesamt 57 Paare von quartären und GPS-bestimmten Relativbewegungsraten gibt, hat ergeben, dass ein mäßiger Prozentsatz (71%) der gesamten Schwankung in den quartären Relativbewegungsraten statistisch durch eine lineare Beziehung zwischen den GPS-bestimmten und den quartären Raten erklärt werden kann. Die restlichen 29% können auf andere Faktoren zurückzuführen sein, wie zeitliche Schwankungen in den Relativbewegungsraten über Zeiträume, die den Empfindlichkeiten der einzelnen Messmethoden entsprechen, oder aber methodische Schwächen. Im geologisch kürzlich eisfrei gewordenen Lauterbrunnental scheint es seit dem Gletscherückzug große zeitliche Schwankungen der Steinschlagaktivität zu geben. So deuten langfristige Steinschlaginventare (über die eisfreie Zeit von ~11 ka) auf höhere Raten der Steinschlagaktivität hin als solche, die mittlere (1 ka) und kurze (5,2 Jahre) Zeiträume betrachten. Letztere wurden jeweils durch das Potenzgesetz und Beobachtungen mittels terrestrischem Laserscanning (TLS) bestimmt. Die Schwankungen in der Steinschlagaktivität sind vermutlich auf die fehlende Stützwirkung des zurückweichenden Gletschers und Entspannungseffekte nach dem Abschmelzen des Gletschers und/oder

den Einfluss von Frostsprengung durch Klimaschwankungen in den letzten 11 ka zurückzuführen.

Zusammenfassend geben die Ergebnisse dieser Studie einen Einblick in Verformungskinetik und postglaziale Erosionsraten in Gebirgslagen. Über große räumliche Skalen hinweg scheint es wenig zeitliche Schwankungen in Verformungsraten zu geben. Im Gegensatz dazu gibt es über kleinere Skalen große zeitliche Schwankungen in Erosionsraten. Die Datensätze und Methoden, die in dieser Arbeit verwendet werden, stellen eine Basis für die weitere Untersuchung von räumlich-zeitlichen Mustern der Verformung und Erosion in Gebirgslandschaften dar und steuern zukünftige Forschung, indem sie bestehende Datenlücken aufzeigen.

To Peter and to all my friends in Tübingen for their enduring support and encouragement and to Eric Godfrey for making the impossible possible.

Contents

| | | |
|----------|--|-----------|
| 1 | Introduction | 1 |
| 1.1 | Geohazards in orogens and mountainous regions..... | 2 |
| 1.2 | Study Regions | 4 |
| 1.2.1 | The India-Asia Collision Orogen | 4 |
| 1.2.2 | The Bernese Oberland (Switzerland)..... | 7 |
| 2 | Aims & Hypotheses | 11 |
| 2.1 | Combing datasets to constrain the spatial distribution of seismic hazards..... | 12 |
| 2.2 | Comparing GPS and Quaternary fault slip rates at the orogen-scale | 14 |
| 2.3 | Sensitivity of rockfall frequency-magnitude to observation duration..... | 16 |
| 2.4 | Sensitivity of rockwall retreat rates to observation duration | 18 |
| 3 | Methods | 19 |
| 3.1 | Database design and programming..... | 19 |
| 3.2 | Statistical analysis (Linear regression and Pearson's Correlation)..... | 21 |
| 3.3 | Terrestrial light detection and ranging | 24 |
| 3.4 | Frequency-Magnitude calculations | 32 |
| 4 | Results | 34 |
| 4.1 | Online database of fault locations, fault attributes and seismicity..... | 34 |
| 4.1.1 | Author contributions..... | 34 |
| 4.1.2 | Paper: "A Quaternary fault database for Central Asia" | 36 |
| 4.1.3 | Supplements for "A Quaternary fault database for Central Asia" | 50 |
| 4.2 | Exploring the relationship between Quaternary and GPS fault slip rates | 51 |
| 4.2.1 | Author contributions..... | 51 |
| 4.2.2 | Paper: "Review of GPS and Quaternary fault slip rates in the Himalaya-Tibet orogen"..... | 52 |
| 4.2.3 | Supplements for "Review of GPS and Quaternary fault slip rates in the Himalaya-Tibet orogen"..... | 66 |
| 4.3 | Quantifying rockfall frequency-magnitude relationship and wall retreat rates..... | 71 |
| 4.3.1 | Author contributions..... | 71 |
| 4.3.2 | Manuscript (<i>in Revision</i>): "Temporal variations in rockfall and rockwall retreat rates in a deglaciated valley over the last 11 ka"..... | 72 |

| | | |
|----------|--|------------|
| 4.3.3 | Supplements for “Temporal variations in rockfall and rockwall retreat rates in a deglaciaded valley over the last 11 ka” | 84 |
| 4.4 | Determining temporal, spatial and geometric details of rockfalls using TLS and environmental seismology | 96 |
| 4.4.1 | Author contributions | 96 |
| 4.4.2 | Paper (co-authorship): “Seismic monitoring of small alpine rockfalls - validity, precision and limitations” | 97 |
| 4.4.3 | Supplements for “Seismic monitoring of small alpine rockfalls - validity, precision and limitations” | 113 |
| 5 | Conclusions..... | 123 |
| 5.1 | A summary – The hypotheses revisited | 123 |
| 5.2 | Outlook and future work..... | 125 |
| | References for Sections 1-3 and 5..... | 129 |
| | Appendix A: Location of data files | 139 |
| A.1 | Manuscripts | 139 |
| A.2 | Datasets & Source Codes..... | 139 |
| A.3 | Dissertation Files | 140 |

Figures

| | | |
|-------------|---|----|
| Figure 1.1 | Patterns in global geoscience datasets | 3 |
| Figure 1.2 | The India-Asia collision orogen | 5 |
| Figure 1.3 | The Lauterbrunnen Valley | 9 |
| Figure 1.4 | Historical rockfalls in Lauterbrunnen Valley | 10 |
| Figure 2.1 | USGS seismic hazard map for Asia | 13 |
| Figure 2.2 | GEM's Global Seismic Hazard Map | 13 |
| Figure 2.3 | Locations of fault slip rate measurements | 16 |
| Figure 3.1 | Flowchart of database development | 20 |
| Figure 3.2 | Example of database interface | 21 |
| Figure 3.3 | Visual representation of coefficient of determination | 22 |
| Figure 3.4 | Sketch of TLS device operation and data acquisition | 24 |
| Figure 3.5 | Setup of Optech ILRIS-LR for TLS measurements | 26 |
| Figure 3.6 | Locations of scan positions and look directions | 27 |
| Figure 3.7 | Defining scan setting using ILRIS PC Controller | 28 |
| Figure 3.8 | Step stare scanning pattern | 28 |
| Figure 3.9 | Workflow of TLS data processing for rockfall volume | 29 |
| Figure 3.10 | Pre-registration of TLS data in JRC software | 30 |
| Figure 3.11 | Rockfall detection in JRC software | 31 |
| Figure 3.12 | Photographs of rockwalls with rockfalls | 31 |

Tables

| | | |
|-----------|--------------------------------------|----|
| Table 4.1 | Contributions of authors for paper 1 | 35 |
| Table 4.2 | Contributions of authors for paper 2 | 51 |
| Table 4.3 | Contributions of authors for paper 3 | 71 |
| Table 4.4 | Contributions of authors for paper 4 | 96 |

Equations

| | | |
|------------|--------------------------------------|----|
| Equation 1 | Coefficient of determination | 22 |
| Equation 2 | Pearson's Correlation Coefficient | 23 |
| Equation 3 | Time of flight | 24 |
| Equation 4 | Power law | 32 |
| Equation 5 | Rockfall return time | 32 |
| Equation 6 | Total volumetric erosion of rockwall | 33 |

Abbreviations

| | |
|-----------|---------------------------------------|
| 2D | Two-dimensional |
| 3D | Three-dimensional |
| GPS | Global positioning system |
| ICP | Iterative closest point |
| IXF | Integration exchange format |
| JRC | Joint research center |
| KS | Kolmogorov-Smirnov |
| LiDAR | Light detection and ranging |
| PCC | Pearson's correlation coefficient |
| PHP | Hypertext preprocessor |
| PSHA | Probabilistic seismic hazard analysis |
| ROI | Region of interest |
| SQL/MySQL | Structured query language |
| TLS | Terrestrial laser scans/scanning |
| ToF | Time of flight |

Publications

a) Accepted papers

Mohadjer, S., Ehlers, T.A., Bendick, R. and Mutz, S.G., 2017. Review of GPS and Quaternary fault slip rates in the Himalaya-Tibet orogen. *Earth-Science Reviews*, 174, pp.39-52.

Mohadjer, S., Ehlers, T.A., Bendick, R., Stübner, K. and Strube, T., 2016. A Quaternary fault database for central Asia. *Natural Hazards and Earth System Sciences*, 16(2), pp.529-542.

Dietze, M., **Mohadjer, S.**, Turowski, J. M., Ehlers, T. A., and Hovius, N., 2017a. Seismic monitoring of small alpine rockfalls - validity, precision and limitations, *Earth Surface Dynamics*. 5(4), pp.653-668.

b) Manuscript in revision

Mohadjer, S., Ehlers, T.A., Nettesheim, M., Ott, M.B., Glotzbach, C., and Drews, R. (in revision). Temporal variations in rockfall and rockwall retreat rates in a deglaciated valley over the last 11 ka. *Geology*.

1 Introduction

Finding and explaining patterns are something we humans are good at, especially in large datasets. Consider the following four global datasets: earthquake locations and depths, recent volcanic activity, topography and bathymetry, and seafloor age (Figure 1.1). Observe each dataset separately, and then together. The eyes are drawn to distinct shapes and patterns. Earthquake locations and volcanic activity look like narrow bands winding through the continents and oceans. In the oceans, these bands are associated with young seafloor age, and often mark the location of young, growing mountains and deep ocean trenches. When superimposed on the tectonic plate boundaries map, these data relationships become more noticeable. In general, plate boundaries are the scene of geologic actions, and what happens at each boundary defines the boundary type and the driving processes. When combined, these datasets and other observations reveal and explain what we know today as the plate tectonic theory.

When it comes to geologic hazards, looking for patterns and relationships in data is not just a catalyst that leads to new discoveries, but has social implications. For example, to understand earthquakes and to address earthquake hazards, looking for patterns in different datasets not only enhances our understanding of regional- and continental-scale tectonics but also can address seismic hazards. Datasets containing Quaternary fault locations and large earthquakes can reveal fault systems responsible for major earthquakes. Overlaying these datasets with GPS data can help identify structures that show ongoing strain accumulation. This information can then be used to assist with regional hazard identification and risk assessment. Similarly, rockfall inventories can be used to investigate rockfall hazards as well as erosion rates and underlying process controls deriving landscape evolution. For example, datasets containing rockfalls of known dates and magnitudes can be used to calculate rockfall frequency-magnitude relationship and rockwall erosion rates. Together with seismic signal data emitted from rockfalls, dynamics of individual events can be further characterized. Ultimately, these observations can contribute to rockfall forecasting and risk analysis.

The overarching goal of this dissertation is to contribute to a better understanding of how mountain hazards are linked to mountain building processes, continental deformation rates and erosion. To achieve this, previously published and new datasets are compiled to investigate the spatio-temporal relationships between Quaternary faulting, seismicity, and fault slip rates, as well as patterns in rockfall activity over different timescales. Two regions are chosen for these investigations: the India-Asia collision orogen and the European Alps where mountain hazards such as earthquakes and rockfalls present a major issue, particularly in areas of high population density (e.g., alpine valleys).

The structure of the dissertation is as follows: section 1 provides background information on mountain hazards and previous work related to geohazards in the study areas. Section 2 states the hypotheses that are addressed. Section 3 provides background information on the methods applied in this dissertation (i.e. relational database, correlation analysis, terrestrial laser scanning (TLS), and rockfall frequency magnitude calculations). Section 4 includes the results in the form of 3 published papers and 1 manuscript in revision. Finally, section 5 summarizes the outcomes, revisits the hypotheses and provides suggestions for future work.

1.1 Geohazards in orogens and mountainous regions

A glance at any topographic map of the world shows that most orogens and mountainous regions are located along the margins of continents and closely follow the distributions of volcanoes, earthquakes, as well as current and former areas of tectonic plate collisions (Figure 1.1). Mountain regions occupy approximately one fifth of the Earth's land surface, and are home to 12% of the world's population (~720 million people) (Schild, 2008). While mountains are beneficial to their habitants, providing rainfall and water storage, they are characterized by a wide range of geological and geomorphic processes that make their population vulnerable to the impacts of geohazards and climate change. Geohazards in mountain regions range from floods, debris flows, landslides and rockfalls to earthquakes and volcanic eruptions. Avalanches, permafrost-related hazards and glacial lake outburst floods are more unique to high mountain environments.

Mountain hazards are mainly products of steep topographic relief, intense precipitation and human activity. For example, the 2015 Nepal earthquake (also known as the Gorkha earthquake) with rupture nucleated on the well-studied Main Himalayan Thrust took the lives of nearly 9,000 people and triggered at least 25,000 landslides throughout the steep Himalayan mountains (Gallen et al., 2017). Villages such as Langtang were completely destroyed by avalanches and landslides (Lacroix, 2016). In the aftermath of the earthquake, more slope failures occurred as the heavy monsoon rainstorms destabilized the already quake-weakened slopes. In addition, other factors such as deforestation, road construction, rapid population growth and poorly designed structures significantly contributed to the loss of life and assets.

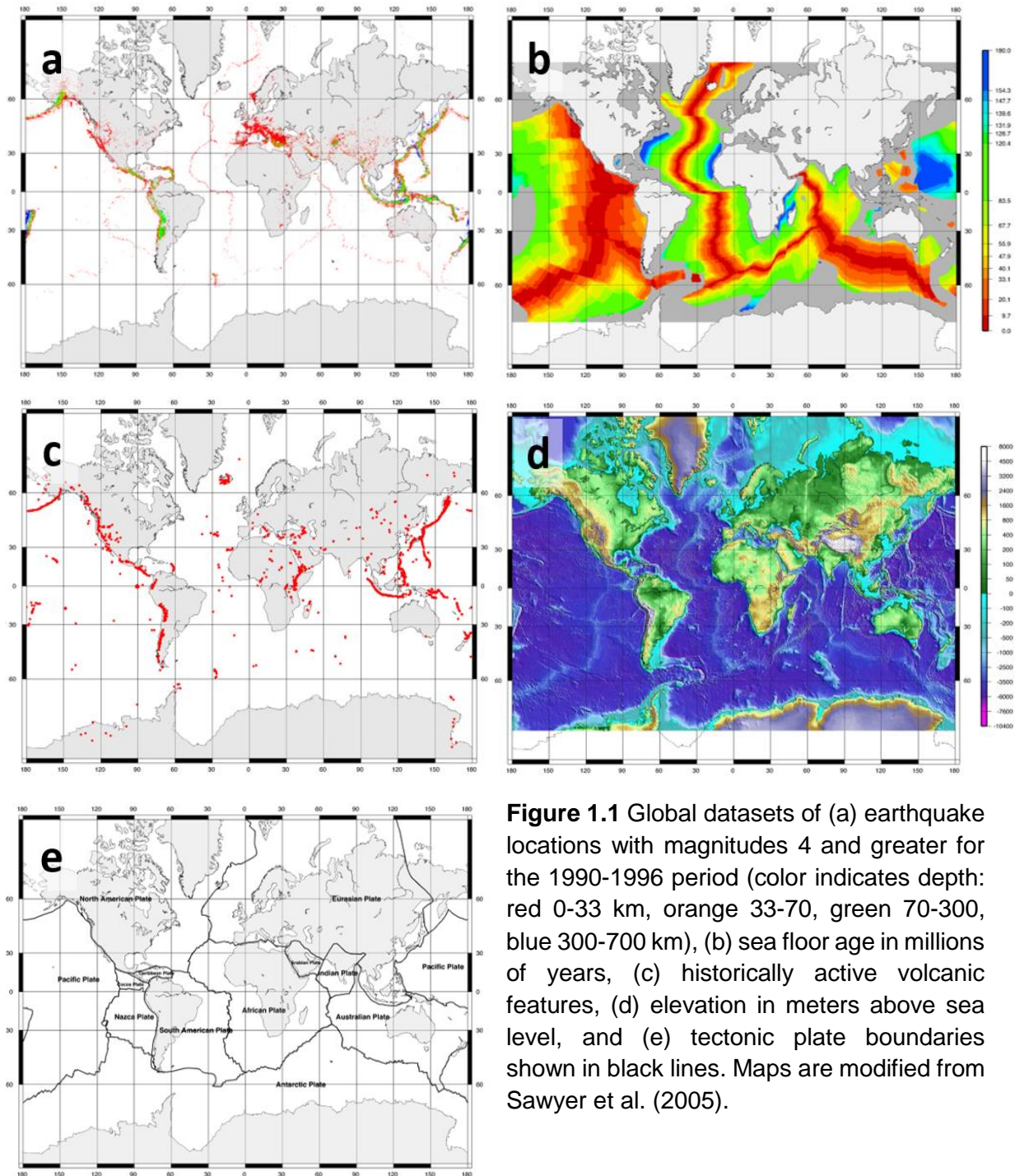


Figure 1.1 Global datasets of (a) earthquake locations with magnitudes 4 and greater for the 1990-1996 period (color indicates depth: red 0-33 km, orange 33-70, green 70-300, blue 300-700 km), (b) sea floor age in millions of years, (c) historically active volcanic features, (d) elevation in meters above sea level, and (e) tectonic plate boundaries shown in black lines. Maps are modified from Sawyer et al. (2005).

Intimately connected to their environment, mountain communities have historically developed cultural and environmental adaptations to geohazards risk (Hewitt and Mehta, 2012). For example, knowledge about geohazards and approaches for coping with earthquakes is evident in indigenous building practices and vernacular architectural styles throughout the Himalayan region (Gautam et al., 2016; Kumar and Pushplata, 2013; Ortega et al., 2017). However, modernization, urbanization, and shifts in housing preference have diminished levels of indigenous hazard knowledge in many communities, making them highly vulnerable to geohazards (Gautam et al., 2015; Halvorson and Hamilton, 2007).

The overall risk from geohazards is determined by the combined understanding of three factors: hazard, exposure, and vulnerability (Cardona, 2005). To develop effective risk models, comprehensive datasets embracing these three factors are required. While it is difficult to measure vulnerability (i.e., population's ability to cope with hazard), the intensity and frequency of a natural phenomenon at a given magnitude (hazard) and the elements at risk (exposure) can be determined using physical parameters and demographic datasets. By compiling datasets of physical parameters related to earthquakes and rockfalls, this dissertation investigates the spatial and temporal distributions of these hazards within the India-Asia collision orogen and a deglaciated alpine valley in the European Alps. This section provides a brief overview of previous work related to geohazards in the aforementioned study areas.

1.2 Study Regions

1.2.1 The India-Asia Collision Orogen

The ongoing collision of India with Eurasia since ~50 Ma has created an active deformation field that is not only localized near and around plate margins but is also observed thousands of kilometers away from the suture zones. This zone of active deformation hosts wide orogenic belts and is characterized by complex fault systems, folds and intense seismicity (Figure 1.2). GPS measurements of surface displacements indicate that the Himalayan arc accommodates nearly half of the total 40-50 mm/yr of convergence between India and Eurasia (Bilham et al., 1997; Jouanne et al., 2004). The rest of this motion is distributed further north by slips on faults in and around the Tibetan Plateau, those located in the Pamir-Hindu Kush and the Tien Shan, as well as active structures in the western boundary of the India-Eurasia plate. This widespread deformation is evident in the seismic hazard map of Asia, where much of the collision zone is subject to high ground shaking levels (Pagani et al., 2018; and Figure 2.2).

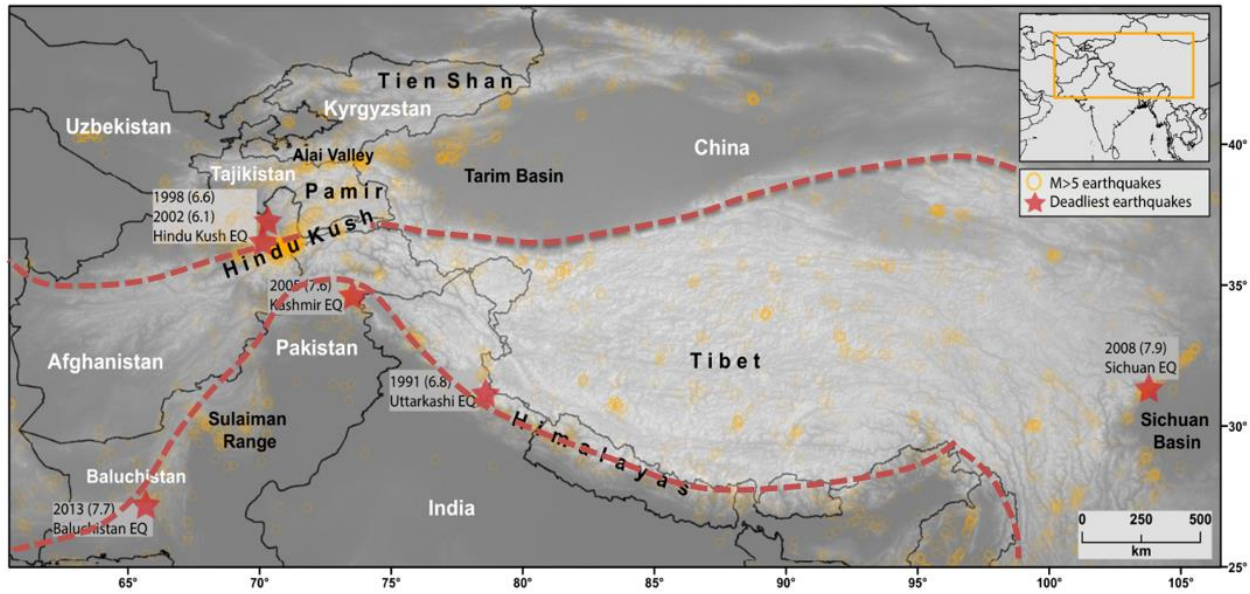


Figure 1.2 The Himalaya-Tibet orogen and the surrounding region. Earthquakes with $M \geq 5$ (orange circles) shown for the 1900–2014 period are from ANSS Comcat (2014). Red stars mark the location of the deadliest earthquakes for the 1900–2014 period (USGS, 2014). The Alpine-Himalayan earthquake belt is shown in dashed lines. Figure modified from Mohadjer et al. (2016).

The Alpine-Himalayan earthquake belt (Figure 1.2), the second-most seismically active region in the world, is responsible for ~20% of the world's largest earthquakes. Since 1800, the cumulative earthquake fatality in the Himalayan region is about 138,000, half of which can be attributed to the 2005 Kashmir earthquake (Bilham, 2019). A more recent example is the 2015 Mw 7.8 Gorkha earthquake that resulted in considerable damage throughout Kathmandu and central Nepal, leaving ~9,000 dead, 22,000 injured and 3.5 million people homeless. In the past 200 years, the regional population has increased by a factor of 10, accompanied by an increase in the seismic vulnerability of building stock (Bilham, 2019). Therefore, more fatalities are expected in future earthquakes in this region.

Previous studies of the India-Asia collision orogen have produced a large amount of data that enhance our understanding of regional- and continental-scale tectonics as well as seismic hazards in the region. The availability of precise geodetic measurements (e.g., Bendick et al., 2015; Ischuk et al., 2013; Mohadjer et al., 2010; Zubovich et al., 2010; Bendick et al., 2007; Reigber et al., 2001; Abdrakhmatov et al., 1996), high-resolution imagery (e.g., Klinger et al., 2005), and sophisticated seismic analysis methods have provided more detailed patterns and rates of deformation associated with individual faults and other major structures throughout the region. Previously recognized faults are more accurately mapped (e.g., Chevalier et al., 2012; Robinson, 2009; Taylor and Yin, 2009; Strecker et al., 2003) and those previously unknown but potentially active, are detected

and investigated (e.g., Ruleman et al., 2007). In addition, paleoseismic studies (e.g., Schiffman et al., 2013; Korjenkon et al., 2012; Ran et al., 2010; He et al., 2007; Kumar et al., 2006; Washburn et al., 2003), though limited in their coverage, have provided constraints on the magnitude and recurrence time of past earthquakes for some faults. These datasets provide baseline observations for understanding patterns and rates of Quaternary faulting within the orogen and the surrounding regions.

Despite advances in the scientific understanding of earthquakes, there are several shortcomings that impede adequate assessment of earthquake hazard in the region. These issues are related mainly to information sharing and methods used for seismic hazard assessment. As explained in the above paragraph, previous studies have generated a large amount of data related to seismic hazards within the India-Asia collision orogeny. These data, however, are documented in a wide range of formats that are often published in non-open access journals. Despite initiatives that provide a centralized platform for data storage, maintenance and display of data specific to other regions of the world, few attempts have been made for data from the India-Asia collision orogen.

There are also methodological problems that hinder the application of earthquake risk reduction in the region. These problems arise from the assumptions that are embedded in the probabilistic seismic hazard analysis (PSHA) method. This method determines the probability of future shaking intensity, and is the most widely taken approach for making regional and national hazard maps in countries located within the India-Asia collision zone. Recent studies using this method (e.g., Abdrakhmatov et al., 2003; Bindi et al., 2012; Ullah et al., 2015) use earthquake data with little information on active fault locations and parameters to calculate seismic hazard in the region. These studies attribute this to the lack of accurate fault information. The PSHA also rests on a number of assumptions known to conflict with earthquake physics (Mulargia et al., 2017; Stein et al., 2012; Bilham 2009) including the assumption that the instrumental, historical, and paleoseismic records of earthquakes are complete and accurate enough to sample the seismic cycle for individual faults. These assumptions are particularly problematic for the India-Asia region where earthquake return intervals can be long (>100,000 years), and the instrumental, historical and paleoseismic records are short and sometimes inaccurate (Bilham, 2009). An online database containing fault locations and important parameters such as slip rates, can help with addressing these issues by centralizing and enhancing public access to information that can be used to constrain seismic hazards in the region.

1.2.2 The Bernese Oberland (Switzerland)

Rockfalls constitute a major hazard in populated mountainous regions where rock slopes are often steep and pronounced environmental changes such as permafrost melting and repeat glacial cycles can alter mechanical stress within underlying bedrock and result in progressive slope failure (Grämiger et al., 2018; Krautblatter et al., 2013). Rockfalls range in size from a few dm^3 to 10^4 m^3 events, and can travel at high velocities across long distances, posing a high risk to people, property and infrastructure. Rockfall location, size, and time can be used for evaluating rockfall dynamics and hazard assessment (e.g., Dussauge et al., 2003; Biagi et al., 2017; Lari et al., 2014). However, very few natural slopes or rockwalls are continuously monitored for exact time of rockfall occurrence, location and volume. Therefore, rockfall inventories are often incomplete and contain biases due to this irregularity in sampling time, space and size domains (Dussauge et al., 2002; Malamud et al., 2004). This dissertation focuses on generating a high resolution rockfall inventory based on TLS measurements collected over >5 years of monitoring rockwalls. The study setting is an alpine, deglaciaded valley with rockwall surfaces that have minimal vegetation and snow cover throughout the year, making it an ideal site for rockfall detection using TLS.

The Lauterbrunnen Valley is located in the Bernese Oberland, Switzerland (Figure 1.3). The U-Shaped valley is about 6 km long and 400-700 m wide, with nearly vertical limestone walls (88.5°). The rockwalls are incised by hanging valleys that host more than 70 waterfalls. The landscape topography is a product of repeated glacial advances, incision and carving. Following the last glacial maximum (~10,000 years ago), the Aar Glacier system retreated to higher elevations, exposing and leaving behind steepened cliffs that are prone to rockfalls.

Rockfalls represent a significant natural hazard in the Lauterbrunnen Valley for more than one hundred thousand yearly visitors and residents of the valley. Evidence for past rockfall activity includes large individual fallen blocks and talus slopes that are covered with fresh debris in many locations (Figure 1.4). Data on historic events show several damaging large-scale slope failures since 1750 including the 1889 landslide which released $>10^4 \text{ m}^3$ of debris material into the valley, covering agricultural lands and destroying infrastructure (Michel, 1979). Currently, the large, deep-seated Gryfenbach landslide endangers part of the Lauterbrunnen village as well as the main entrance to the entire valley (Tobler and Keusen, 2013). It creeps on average at a rate of ~10-20 mm/yr, with two landslides recorded in 1966 and 1983 in the steep frontal part of the sliding mass. More recently, in November 2018, a rockfall with a volume of ~3,600 m^3 occurred near the village, causing minimal damage.

Previous rockfall datasets for the Lauterbrunnen valley include 122 rockfalls totaling a volume of 523.72 m³ over an 18-month period (Strunden et al. 2015) and 49 rockfalls detected using seismic signals over a 6-month period (Dietze et al., 2017b). In the former dataset, the largest detected rockfall is about 120 m³, with those less than 1 m³ being most common. Rockfall events from this dataset are compared with several environmental factors. A high correlation factor ($r = 0.6$) is observed for freeze-thaw cycles and rockfall events smaller than 1 m³ with a 2-month delay between temperature extremes and rockfalls. Similarly, 10% of the rockfalls detected in the dataset of Dietze et al. (2017b) were found to be influenced by freeze-thaw transitions. Furthermore, the authors inferred a systematic downward shift of a rock mass release zone, driven by a continuously lowering water table inside the limestone wall. This dissertation presents an additional four years of new TLS data and analysis techniques, the results of which are shown in sections 4.3. and 4.4.

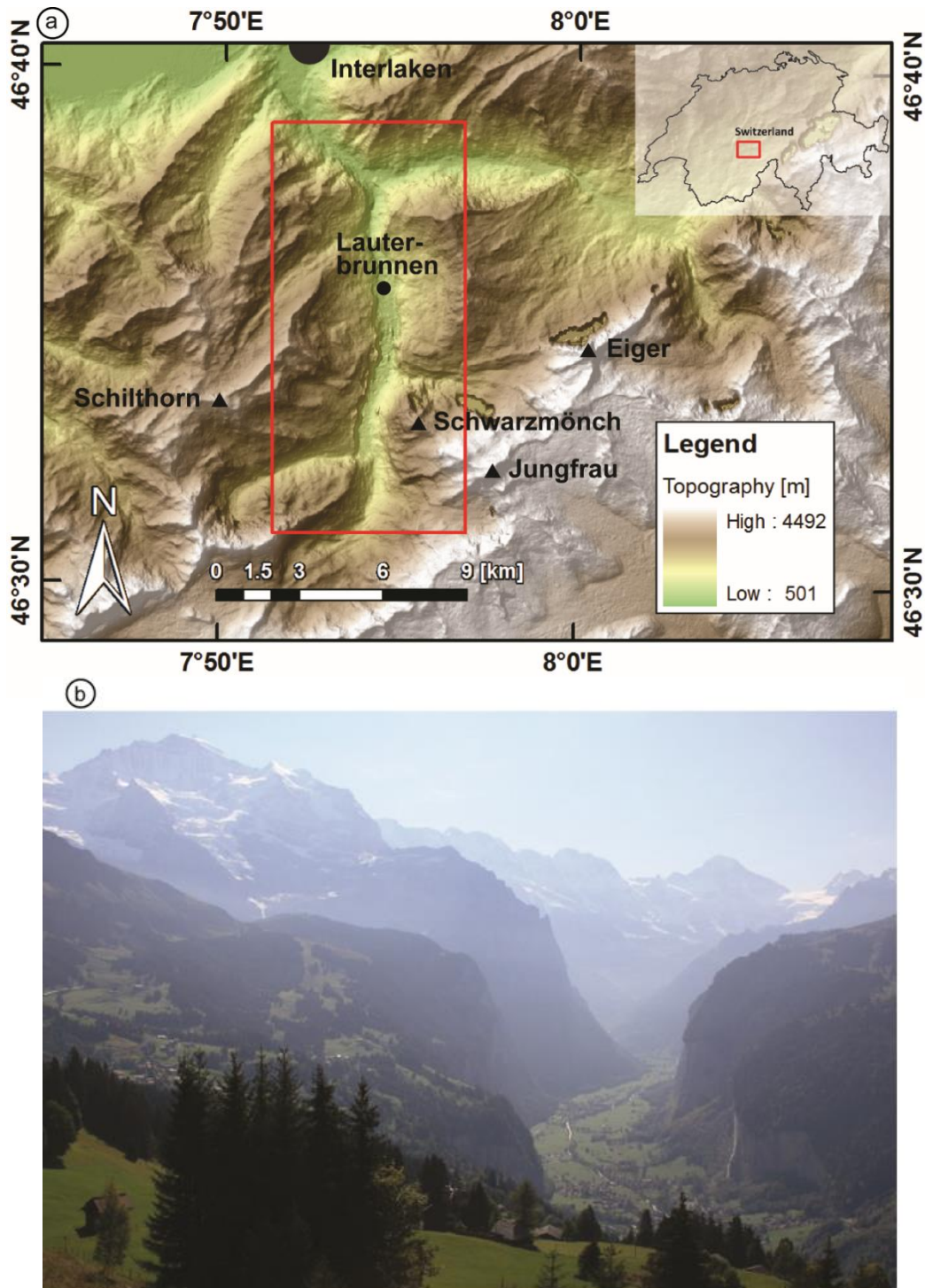


Figure 1.3 Shaded relief digital elevation model showing the location of the Lauterbrunnen Valley with study area in red box (a), and the U-shaped deglaciated Lauterbrunnen Valley with steep limestone walls (looking toward the south from Wengen) (b). Figure from Strunden et al. (2015).



Figure 1.4 Examples of previous rockfalls in the Lauterbrunnen Valley. The May 1889 landslide covered by vegetation (a), and an example of a large rockfall (b). Photos by M. Kloos (a) and D. Brehm (b).

2 Aims & Hypotheses

The main objective of this dissertation is to contribute to a better understanding of mountain building processes, continental deformation and erosion over different timescales, and ultimately how these processes are linked to mountain hazards. This overarching objective is framed around the following four hypotheses:

- 1) Quaternary fault locations, fault attributes and seismicity provide similar information on the spatial distribution of earthquake hazard as do conventional hazard maps. (Paper A in section 4.1.2, published)
- 2) Fault slip rates from GPS and geologic techniques provide consistent spatial and temporal slip rate information at the orogen scale, suggesting that over the Quaternary, there is minimal transience in slip rates. (Paper B in section 4.2.2, published)
- 3) Rockfall frequency-magnitude calculations from laser scanning measurements are not sensitive to observation duration of 1.5 vs. >5 years. (Paper C in section 4.3.2, in revision)
- 4) Over different timescales (10^0 - 10^4 years), rockwall retreat rates can vary by an order of magnitude in a deglaciated alpine landscape. (Paper C in section 4.3.2, in revision)

The main aim of all four hypotheses is to evaluate existing and new datasets in order to investigate the temporal and spatial relationships between different datasets, to identify and explain factors influencing these relationships, and ultimately to quantify mountain hazards. Additionally, these investigations guide future research by identifying research areas where further investigations are needed.

The first two hypotheses are investigated using previously published datasets related to Quaternary faulting in the India-Asia collision zone. To address the last two hypotheses, new rockfall datasets are generated and analyzed for a deglaciated valley located in the Bernese Alps, Switzerland. All hypotheses are elaborated in more detail in the following sections. The actual results are presented in section 4.

2.1 Combing datasets to constrain the spatial distribution of seismic hazards

Earthquakes occur on active faults. Therefore, a large number of previous and current investigations have focused on accurately mapping the location of active faults. Quaternary fault databases have been developed for many parts of the world including the United States (Haller et al., 2004), New Zealand (Langridge et al., 2016), Japan (AIST, 2016), Italy (Michetti et al., 2000), Iberia (Garcia-Mayordomo et al., 2012), and France (Jomard et al., 2017). These datasets are widely used for fault characterization and seismic hazard calculations at national level. Other databases such as the HimaTibetMap of Taylor and Yin (2009) for the India-Asian collision zone have focused on documenting Quaternary faults and other active structures at an orogen scale. There are also global initiatives such as the Global Earthquake Model's Faulted Earth of Christophersen et al. (2015) which aimed at developing a uniform fault database, providing access to consistently derived fault sources.

Though the location of active faults can help with determining the regions in which earthquakes are most likely to occur, without seismologic, geodetic and geologic data, a coherent pattern of earthquake hazards cannot emerge. Fault maps are often incomplete, missing faults that are potentially active (e.g., blind faults). For example, a previously unmapped fault was responsible for the 2010 Mw 7.0 earthquake that devastated the Port-au-Prince region of Haiti (Calais et al., 2010). This earthquake, however, was forecasted and expected based on the historical seismicity and geodetic data. At the same time, historical records and instrumental seismic catalogs (started in 1900) can provide an incomplete or sometimes inaccurate earthquake history for many parts of the world. For example, the 2008 M 7.9 Wenchuan earthquake occurred on a mapped fault that was classified as low hazard (solid black box in Figure 2.1) based on lack of evidence for large earthquakes in the past thousand years. However, geologic and geodetic data available prior to the earthquake showed that the accumulated moment on the fault was enough to produce a M8 earthquake (Wang et al., 2011).

Similarly, conventional hazard maps for many of the countries within the India-Asia collision orogen (e.g., Abdrakhmatov et al., 2003; Bindi et al., 2012; Ullah et al., 2015) are often defined by patterns of seismicity rather than by fault position and characterization (exception: Ischuk et al., 2018), and yield different results depending on map makers' assumptions and limitations in parameters used in map making (Stein et al., 2012). For example, the global seismic hazard maps of Zhang et al. (1999) and Pagani et al. (2018) (Figure 2.1 and 2.2, respectively) show different distributions of seismic hazards for the India-Asia collision zone. While the latter incorporates tectonic and geologic information in addition to seismicity, the former is mainly based on seismic data.

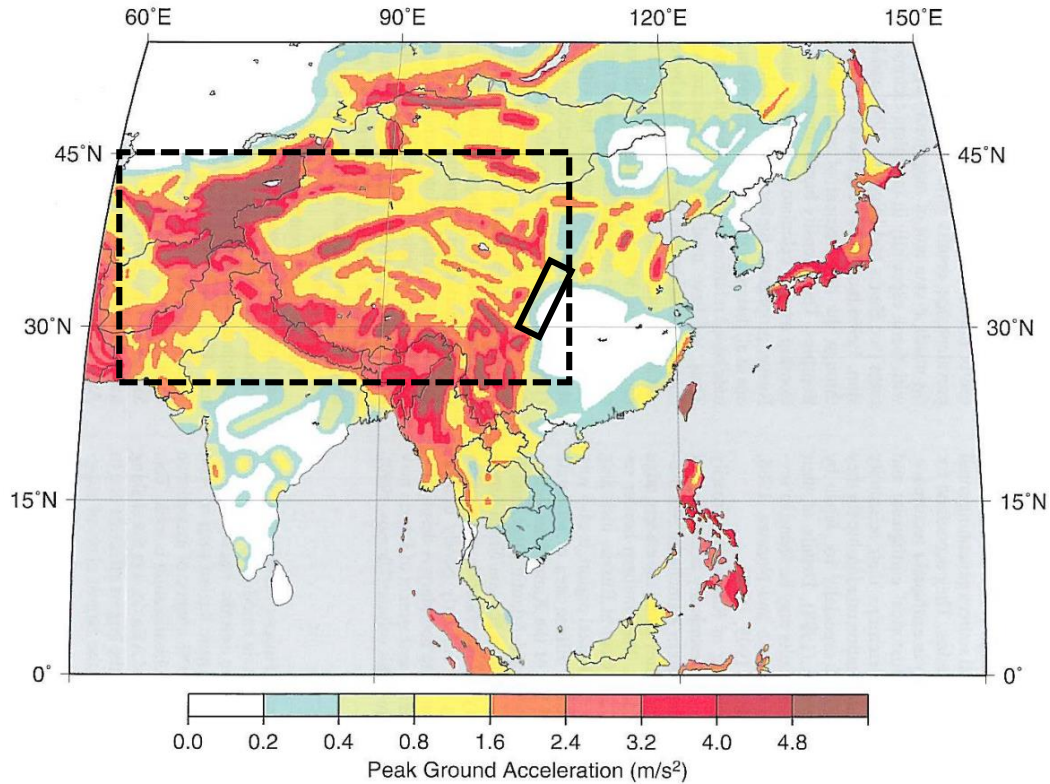


Figure 2.1 The outdated seismic hazard map of Asia, showing Peak Ground Acceleration (PGA) in units of m/s^2 with a 10% probability of exceedance in 50 years. The dashed box shows the map extent displayed in Figure 2.2. The solid black box marks the location of the Longmenshan fault, responsible for the 2008 Wenchuan earthquake. Figure modified from Zhang et al. (1999).

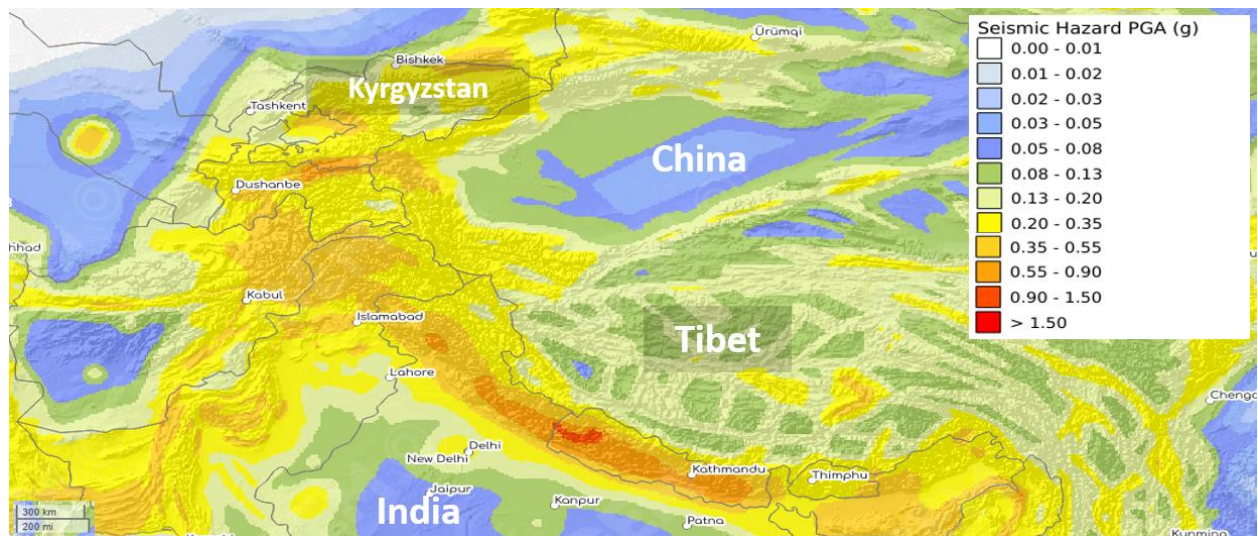


Figure 2.2 The seismic hazard maps of Asia, showing Peak Ground Acceleration (PGA) in units of g with a 10% probability of exceedance in 50 years. Figure modified from Pagani et al. (2018).

As these examples demonstrate, no dataset alone can constrain the spatial location of seismic hazard. To address gaps in data, a combined database approach has the potential to provide a more complete overview of earthquake hazards at regional/orogen scale. Furthermore, data maps that show fault location and parameters combined with instrumental and historical earthquakes, may provide similar (if not more realistic) information on the spatial distribution of earthquake hazard as do conventional maps.

We explored these approaches by focusing on the India-Asia collision zone where the deformation zone is characterized by active faulting and seismicity, and where abundant data on Quaternary faulting are available. Therefore, the India-Asia collision zone is an ideal place for testing the first hypothesis:

Quaternary fault locations, fault attributes and seismicity provide similar information on the spatial distribution of earthquake hazard as do conventional hazard maps.

To test this hypothesis, we created a database that displays previously published datasets separately and together in order to reveal a more complete pattern of regional seismic hazards. Two features that enable this are a web-based interactive map and a search tool that are linked to an online database. Both allow users to search, sort, and display data by data layers or fields. The database contains the location of >1,000 Quaternary fault traces, >30,000 earthquake, and fault attributes (e.g., earthquake history and slip rates) for >100 faults.

2.2 Comparing GPS and Quaternary fault slip rates at the orogen-scale

Earthquakes occur when energy stored in elastically strained rocks is suddenly released. The rates at which strain energy accumulates on faults are a measure of slip rates (Wang et al., 2011). Therefore, slip rate data are a key indicator of potential seismic hazard. Fault slip rates are calculated by dividing measurements of the offset of geologic, geomorphic or manmade features by the time over which that offset accumulated. These rates can be obtained using different methods (e.g., geodesy, geo-thermo-chronology and tectonic geomorphology) over different timescales (10^{-9} to 10^7 years). While slip rates obtained from geologic methods can provide average, long-term rates that span multiple seismic cycles, those derived from geodetic techniques give access to short term rates (ranging from 1 to 20 years), covering only a small fraction of the seismic cycle.

Within the India-Asia collision zone, there appears to be a large variability in geodetic and geologic slip rate for many large faults (>1,000 km long), and some studies have challenged the assumption that geodetic slip rates are representative of geologic slip

rates (Chevalier et al., 2005; Ul-Hadi et al., 2013). Differences in rates are often attributed to secular rate changes, differences in measurement sensitivity between methods, or methodological oversights. Furthermore, the disagreements over rates for major faults lie at the heart of the ongoing debate over the long-term behavior of the Tibetan plateau. Fast Quaternary rates have been used to argue for the plate-behavior of Tibet while slow GPS rates have been used to support a fluid-like behavior.

Previous studies mainly focus on comparing slip rates for individual faults or fault systems, some of which compare rates from GPS and geologic methods measured at different sections of the fault and/or compare GPS rates with geologic rates that are averaged over timescales larger than the Quaternary. If such temporal and spatial differences are reduced, the existing discrepancies between fault slip rates from GPS and geologic techniques may be resolved. Additionally, factors influencing the relationship between different rates may be identified. Therefore, we focus on the India-Asia collision zone where abundant previous data exist for continental deformation over the last ~2 Myr (Figure 2.3), to investigate the second hypothesis:

Fault slip rates from GPS and geologic techniques provide consistent spatial and temporal slip rate information at the orogen scale, suggesting that over the Quaternary, there is minimal transience in slip rates.

To test this hypothesis, a dataset of 57 Quaternary/GPS slip rate pairs, representing 19 faults is compiled from previous studies. A least squares and Pearson correlation analysis are applied to investigate the overall relationship between GPS and Quaternary slip rates. The slip rates are then systematically re-sampled to evaluate the sensitivity of the slip rate relationship to the presence/absence of individual faults and different Quaternary dating methods.

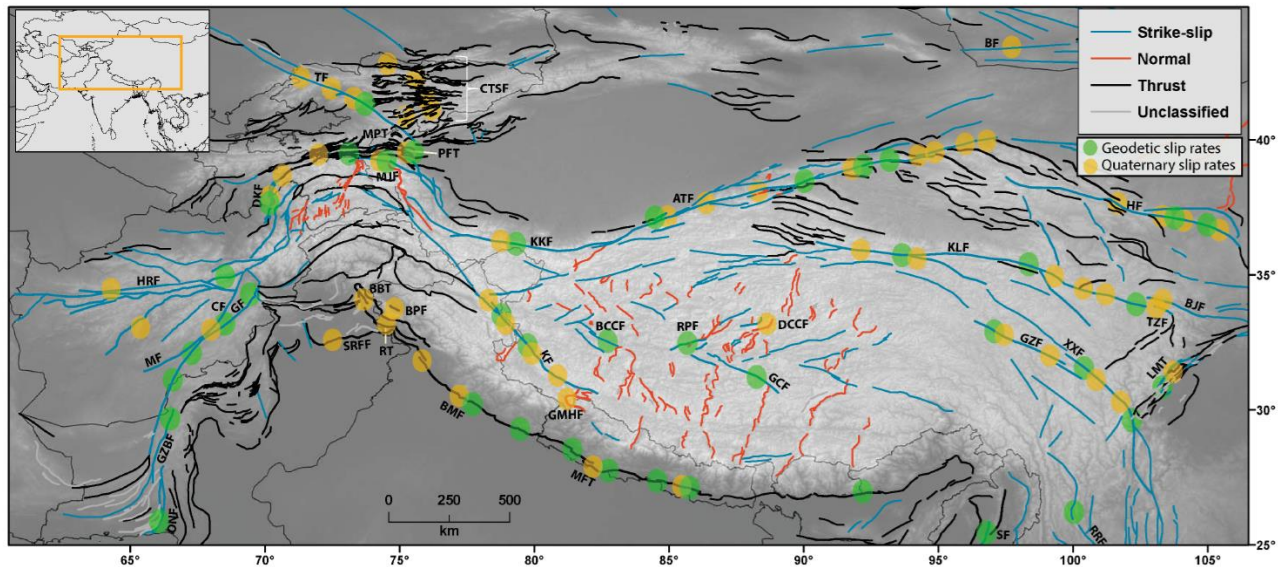


Figure 2.3 Map showing the locations of reported slip rates in colored circles (green: GPS; orange: Quaternary). Quaternary fault traces are color coded based on their sense of movement. For abbreviations of fault names, see Table 1 in section 4.2.2. Figure from Mohadjer et al. (2016).

2.3 Sensitivity of rockfall frequency-magnitude to observation duration

Some natural hazards such as earthquakes, floods, mass movements including rockfalls, and forest fire have been shown to exhibit scale-invariant statistics (i.e., their statistical properties will not change with the scale of investigations). Scale invariance has been documented in the rockfall frequency-magnitude distributions (Barlow et al., 2012; Dussauge et al., 2003; Guzzetti et al., 2003; Hergarten, 2012; Malamud et al., 2004; and Rosser et al., 2007) where the frequency of rockfall occurrence as a function of its magnitude has been shown to obey a negative power law function. This relationship has been used to estimate the frequency of unrecorded, and potentially dangerous rockfall events, by extrapolating the power law obtained for the smaller, more frequent events (e.g., Dussauge et al., 2002; Guzzetti et al., 2002, 2003; Picarelli 2005). Therefore, this relationship is an important component of hazard and risk assessment.

Small rockfalls (if detected at all) are seldom reported in historical rockfall inventories, making accurate quantification of rockfall frequency-magnitude distributions a challenging task. With recent advancements in remote sensing, TLS applications have enabled accurate measurement and analysis of a wide range of geomorphic processes including rockfalls. Using TLS, small rockfalls (such as those with volumes less than 0.1 m^3) and those occurring on steep, inaccessible slopes can be accurately detected and characterized.

Many recent studies have generated and used TLS-detected rockfall inventories for establishing the rockfall frequency-magnitude relation for a wide range of environments and purposes. While the effects of sampling interval (duration between scans) on rockfall detection and the corresponding frequency-magnitude relationship have been the topic of several studies (e.g., Tonini and Abellán, 2014; Carrea et al., 2015; Janeras et al., 2015; and van Veen et al., 2017), little attention has been given to the effects of the total observation duration on the frequency-magnitude relationship of rockfalls. For instance, it is not clear if (and how) observation duration of one versus five years can affect the rockfall frequency-magnitude relationship. Answering this question is not only useful for optimizing the scheduling of scans, but it can increase our understanding of how long (as oppose to how often) TLS data should be collected in order to create a substantially complete rockfall inventory and a robust frequency-magnitude distribution.

Located in the Bernese Oberland, the Lauterbrunnen Valley has experienced several damaging rockfalls as evident from large fallen blocks and talus slopes in the valley. The 5.2 km² vertical valley walls are devoid of vegetation, making this valley an ideal location for documenting rockfall activity, particularly with TLS. These walls have been the focus of several recent studies ranging from TLS and seismic monitoring of rockfalls (Strunden et al., 2015 and Dietze et al., 2017a,b, respectively) to measuring rockfall activity using Structure-from-Motion (Schwarz, 2019) or from talus volumes (Ott, 2017). Therefore, the Lauterbrunnen valley where existing rockfall data exist is chosen for investigating the third hypothesis:

Rockfall frequency-magnitude calculations from TLS measurements are not sensitive to observation duration of 1.5 versus >5 years. (Paper C, in revision)

This hypothesis is addressed by comparing the TLS rockfall inventory of Strunden et al. (2015) covering a period of 1.5 years with the new TLS rockfall inventory collected over a period of ~5 years (this dissertation). The sensitivity of rockfall frequency-magnitude to these different observation durations is then evaluated.

2.4 Sensitivity of rockwall retreat rates to observation duration

Rockwall retreat rates have been investigated over a variety of spatial and temporal scales using different methods. Assessment of retreat rates over a specific timescale depends on quantification of rockfall activity over that time scale. While short-term rockfall activity can be efficiently quantified with remote sensing techniques such as terrestrial laser scanning or from substantially complete historical records, retreat rates over longer timescales can be obtained using the magnitude-frequency relationship of rockfalls or inferred from volume calculation of rockfall debris (e.g., talus deposits) accumulated at the foot of rockwalls. Rockwall retreat rates are not constant, and are shown to be influenced by climate or tectonics among other factors (Herman et al., 2013). The variability in rates is evident in deglaciated alpine landscape where retreat rates and accumulation of talus deposits are enhanced following deglaciation. In these settings, previous studies suggest that the removal of the supporting buttress of glacial ice from oversteepened valley walls destabilizes the rockwalls, resulting in rock slope failures. Comparison of rockwall retreat rates from different timescales can provide insights into post-glacial erosion and the role of rockfalls in the evolution of alpine landscapes.

Due to the availability of high resolution rockfall datasets, the Lauterbrunnen Valley is well suited for investigating rockwall retreat rates in a deglaciated landscape over three different timescales: short (~5 years), intermediate (1 ka) and long (~11 ka) timescales. We expect the short-term retreat rates to be lower than those measured over longer timescales. Hence, the following hypothesis:

Over different timescales (10^0 - 10^4 years), rockwall retreat rates can vary by an order of magnitude in a deglaciated alpine landscape. (Paper C, in revision)

To investigate this hypothesis, TLS-derived rockfall inventories are used to constrain the wall retreat rates over both short and intermediate (power law) timescales. These rates are then compared with those inferred from the calculation of talus volume.

3 Methods

Relational databases and statistical methods are used to reveal patterns and relationships between different datasets. This dissertation investigates the spatial and temporal relationships between different sets of data such as fault slip rates obtained from different methods, or rockfall inventories to identify and explain potential factors that influence these relationships. This is achieved by developing a relational Quaternary fault database and performing statistical assessment of data using the least squares, Pearson's correlation, and frequency-magnitude statistics. The results of this work have bearing on mountain hazard and risk assessment studies, both at orogen and local scales. The background behind these methods is provided in the following sections.

3.1 Database design and programming

Earth sciences data have significantly increased in volume and complexity, resulting in a greater need for open-access and user-friendly databases (Overpeck et al., 2011; Düsterhus et al., 2016). Relational databases are commonly used to organize a wide range of geoscience data, including Quaternary fault data (Lunina et al., 2014), hydrogeologic data (Horsburgh et al., 2009), paleomagnetic data (Veikkolainen et al., 2017); earthquake data (Migliaccio et al., 2019), and geochronologic data (Puetz, 2018). Relational databases store data in tables (rows and columns) that are linked together. This is done by assigning a unique identification number (also known as the *key*) to each row, and a value to each data attribute stored in each column. This allows users to identify and access data in relation to another type of data in the database. In a relational database, the tables are typically populated and managed in an open source SQL (structured query language) database that is commonly used for web application development and often accessed using PHP (hypertext preprocessor), an open source scripting language.

A large number of relational databases focus on centralizing data relevant to geohazards, and are used for geologic investigations, hazard modelling as well as education and infrastructure planning. Some of the most common features of geohazards databases are interactive maps that are linked to online databases where users can obtain more information on selected features (e.g., a fault system or an earthquake). These features (e.g., lines, points, polygons) are spatial data, originally documented in a wide range of formats (e.g., digital, texts, maps, and images) that cannot be immediately integrated into the database. For example, scanned maps, unlike most satellite images, usually do not contain spatial reference information and must be georeferenced using existing spatial data. One of the most commonly used software for data digitization, geo-

referencing, editing and publishing is ArcMap. In this dissertation, a relational database is developed by (1) compiling, (2) preparing and (3) managing geoscience data related to Quaternary faulting for (4) online display. These four steps are shown in Figure 3.1 and briefly described below.

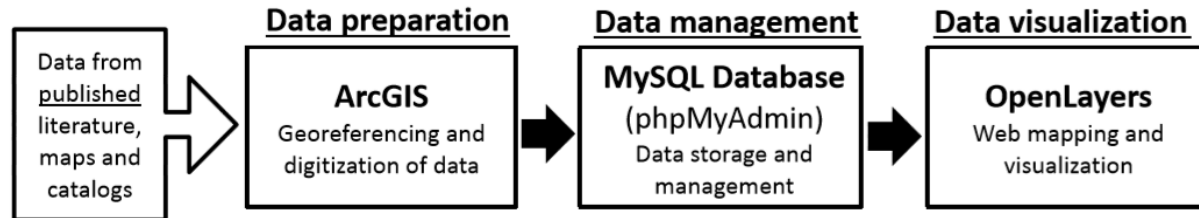


Figure 3.1 Flowchart of the process for the database development. Figure from Mohadjer et al. (2016).

Data compilation - Previously published literature (>250 papers) and databases related to Quaternary faulting in Central Asia were compiled, reviewed, and used to create the main datasets used in the database including fault locations, fault attributes and seismicity. The fault location dataset includes locations of the 1,196 fault traces, 569 of which are from the digital database of Quaternary faults located in the India-Asia collision zone (Taylor and Yin, 2009). Fault attributes describe fault behavior, and its geographic characteristics (e.g., name, location, level of exposure), seismic characteristics (e.g., slip rate, earthquake history, paleoseismic data) and structural characteristics (sense of movement, geometry) characteristics. The seismicity dataset includes global and regional earthquake catalogs, containing 34,000 earthquakes. These events are displayed based on their size and depth.

Data preparation - Using ArcMap, fault traces were georeferenced, digitized, and attributed. Since fault traces were digitized from their original sources, their location accuracy depends on the scale of observation used in original studies. When digitizing a fault, a map is aligned with available datasets (e.g., country boundaries, river network) and georeferenced using more accurate data layers such as Advanced Spaceborne Thermal Emission and Reflection Radiometer (ASTER) Global Digital Elevation Model (GDEM2) (30 m resolution). When there are discrepancies in fault locations, position of previously mapped faults is adjusted to coincide with surface features visible on ASTER GDEM2 data that are indicative of their trace.

Data management - Fault trace data (i.e., geographic coordinates of points that made up a fault trace) were stored in a fault location table created in a MySQL database, using an open source, web-based application called phpMyAdmin (<https://www.phpmyadmin.net/>). Similar tables were created to store and organize fault attribute information and earthquake data including location coordinates, depth,

magnitude and source values. The reference table containing citation appearance and manuscript title, was used to generate an automated query in Google Scholar by clicking on a citation listed for a fault.

Data visualization – The fault location, attribute, and earthquake data were extracted from the tables in the MySQL database using PHP scripting for display in an open source web-mapping application called OpenLayers (Figure 3.2).

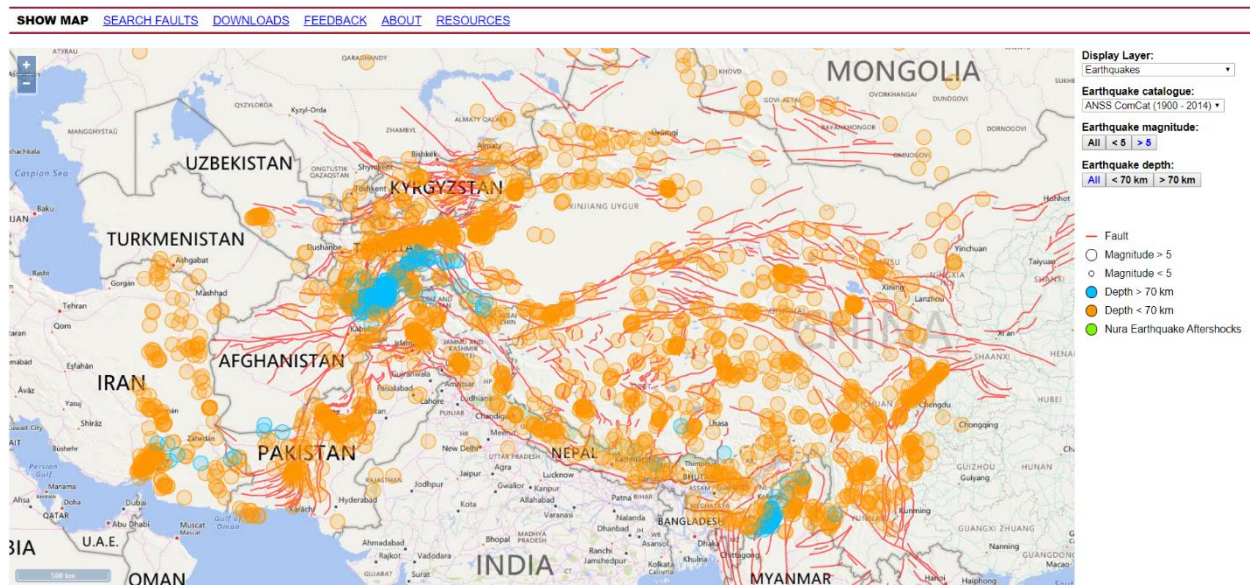


Figure 3.2 Display of Quaternary fault trace and earthquake data in OpenLayers. Figure from the Quaternary fault database of Mohadjer et al. (2016): <https://esdynamics.geo.uni-tuebingen.de/faults/>

3.2 Statistical analysis (Linear regression and Pearson's correlation)

Linear regression is an efficient method for statistical analysis, and has been widely used to quantify the linear relationship between a dependent variable (Y) and one or more independent variables (X). Since performing linear regression makes sense only if the relationship is linear, using a scatter plot to assist with the initial judgement of a possible relationship between variables in question is recommended (Schneider et al., 2010). Simple linear regression has a form $Y = mX + c$ where m is the slope of the line and c is the y intercept. The parameters m and c are estimated from the values of the dependent variable Y and the independent variable X. The slope m of the regression line is the regression coefficient, and a measure of the contribution of the independent variable X toward explaining the dependent variable Y. The coefficient of determination (r^2) is a measure of how well the regression model describes the observed data.

The least square error is a popular approach for the linear regression model. It consists of finding the best fitting straight line (i.e. the regression line) through a set of data points by minimizing the sum of squared errors. In other words, the least squares regression line is the line that makes the vertical distance from the data points to the regression line as small as possible. For statistical measure of how close the data points are to the fitted regression line, the coefficient of determination (r^2) is calculated using the following formula:

$$r^2 = 1 - \frac{SS_{error}}{SS_{total}} = 1 - \frac{\sum_i^n (y_i - \hat{y}_i)^2}{\sum_i^n (y_i - \bar{y}_i)^2} \quad (1)$$

where SS_{error} is the error sum of squares, SS_{total} is the total sum of squares, y_i is the actual value of the dependent variable, \hat{y}_i is predicted or fitted value of y_i , and \bar{y}_i is the mean of dependent variables. Taken together, SS_{error} is the “unexplained” variation in the dependent variable while SS_{total} is the total variation of the dependent variable around its mean value. Figure 3.3 provides a visual presentation of this formula.

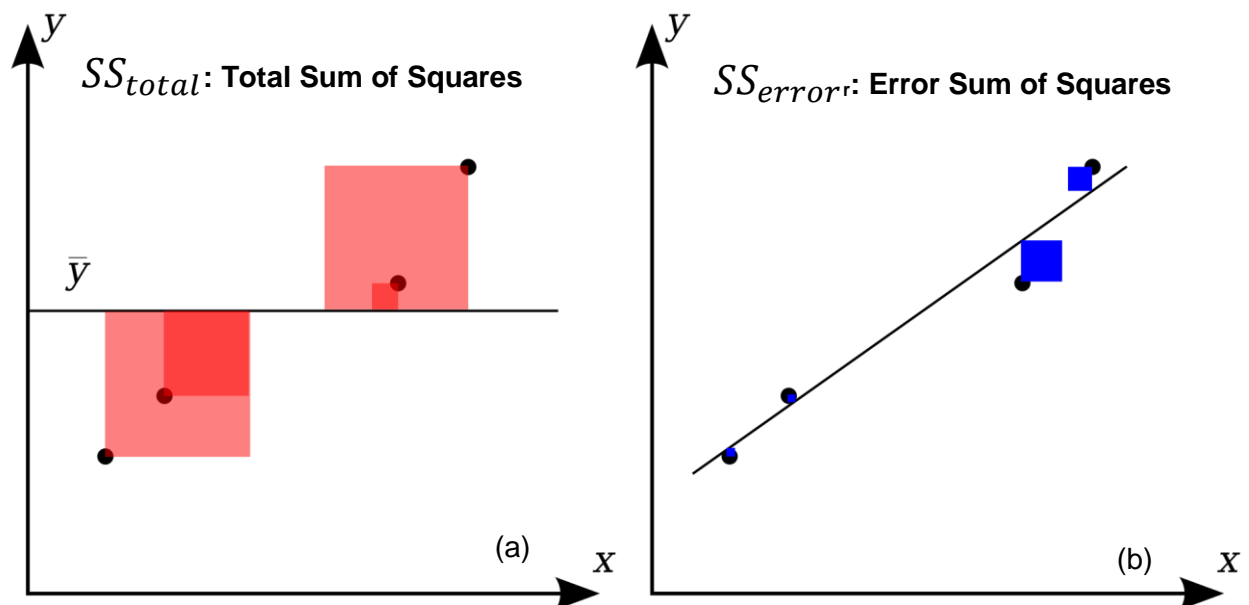


Figure 3.3 Visual representation of the coefficient of determination (r^2). (a) The areas of red squares represent the squared residuals with respect to the average value of data points (mean of y), (b) the areas of blue squares represent the squared residuals with respect to the linear regression. The coefficient of determination is one minus the ratio of the area of the blue squares vs. the area of the red squares. Figure modified from Orzetto (2010).

Statistical dependence of GPS and Quaternary rates was further evaluated by calculating the Pearson's Correlation Coefficient (PCC). The PCC measures the strength and the direction of the linear relationships between pairs of variables, and is a dimensionless quantity in the range of -1 to +1. A correlation coefficient of +1 or -1 indicates total positive or negative linear relationship between variables, while correlation coefficient of 0 is indicative of no linear relationship. The stronger the correlation, the closer the correlation coefficient to ± 1 . For a correlation between variables x and y (i.e. GPS slip rates and Quaternary slip rates, respectively), the formula for calculating the sample PCC is given by

$$r_{xy} = \frac{\sum_{i=1}^n (x_i - \bar{x})(y_i - \bar{y})/n}{\sqrt{\sum_{i=1}^n (x_i - \bar{x})^2} * \sqrt{\sum_{i=1}^n (y_i - \bar{y})^2}} \quad (2)$$

In equation 2, the numerator is sample covariance and is defined in terms of sample means (\bar{x} is mean of x variable, \bar{y} is mean of y variable and n is total number of observation). The denominator is the product of sample standard deviations. The sample standard deviations are the square root of their variance. The variance is a numerical measure of how the data values are dispersed around the mean.

The above statistical methods were applied to investigate the overall relationship between Quaternary and GPS slip rates for 19 faults in the India-Asia collision zone. A total of 57 data points (i.e., Quaternary/GPS slip rate pairs) were visualized in a scatter plot. These points represented slip rates for 19 Quaternary faults. To identify the extent to which these rates relate to each other, a least squares regression line was computed. The regression line was calculated by forcing it through the origin and to calculate an r^2 value as a measure of the statistical dependence between GPS (independent variable) and Quaternary (dependent variable) slip rates. Statistical dependence of GPS and geologic rates were further assessed by calculating the PCC using equation (2). The sensitivity of the PCC value to slip rates associated with each fault was then evaluated for 19 sample subsets (one for each fault investigated). In each subset, all data points (i.e., GPS/Quaternary rate pairs) associated with an individual fault were excluded from calculation of the PCC. This process was repeated for each of the 19 faults investigated. The uncertainties associated with each data point were taken into consideration by means of Monte Carlo style experiments. The same procedure was applied to data points associated with individual Quaternary dating methods to evaluate if individual dating techniques have biases that strongly influence the sensitivity of the PCC. These statistical approaches are further explained in section 4.2.2.

3.3 Terrestrial light detection and ranging

Over the last few decades, advancements in remote sensing technologies have enabled researchers to capture high resolution terrain information and three-dimensional (3D) spatial data, allowing for rapid and accurate mapping of geomorphic factors. Light detection and ranging (LiDAR) is an effective remote sensing method, capable of producing high resolution Digital Terrain Model in 3D point clouds.

A TLS has three main components including a transmitter, rotating mirrors and a receiver. The transmitter produces pulsed laser signals (laser beams), which are emitted and oriented through rotating mirrors, in the direction of the object of interest (e.g., rock surface) (Figure 3.4a). The backscattered laser pulses and the corresponding reflection intensity are then detected by the receiver (Figure 3.4b) The TLS calculates the distance to the object of interest (e.g., rock surface) using the time-of-flight technique (Abellán et al., 2014) according to the following equation:

$$R = c \times \frac{\text{ToF}}{2} \quad (3)$$

where R is the distance between the scanner and the object of interest (also known as range), c is the speed of light and ToF is the time-of-flight. In addition to ToF, the reflectance intensity and values for x-, y-, and z-coordinates for each measured point are recorded. The reflectance intensity is defined as the ratio of the amount of emitted and reflected signals, and its value depends on the range, angle of incidence, moisture, surface geometry and object material (Abellán et al., 2011).

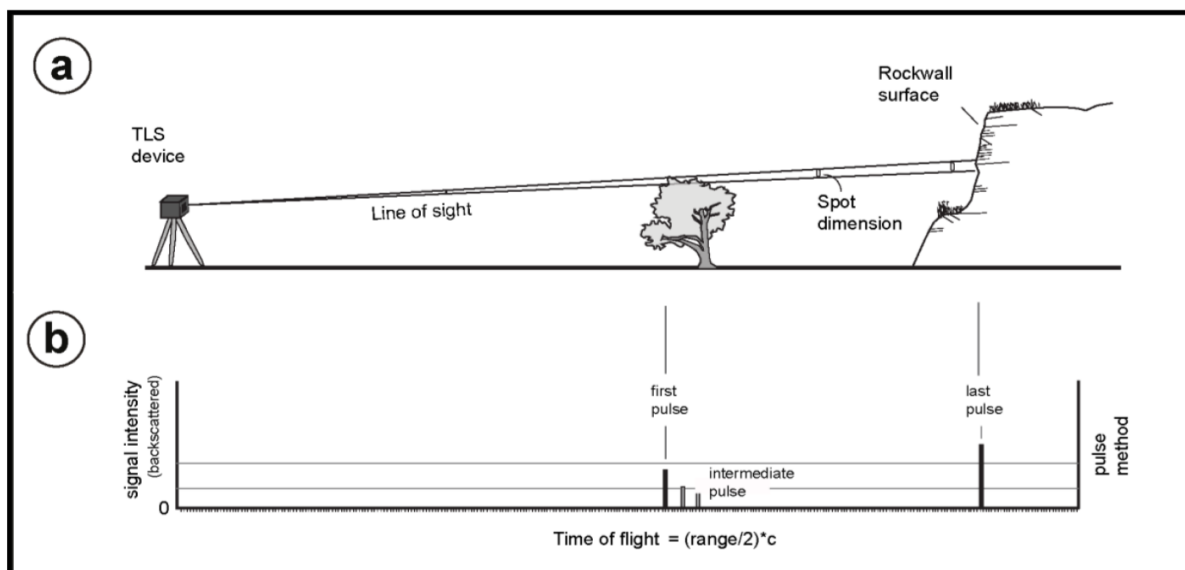


Figure 3.4 Sketch illustrating basic operation of a TLS device (a), and TLS data acquisition using the pulse method (b). Figure modified from Abellán et al. (2014).

In this dissertation, an Optech ILRIS-LR terrestrial light detection and ranging scanner was used to acquire high density 3D point clouds of rockwalls (Figure 3.5 and 3.6). The scanner has scan frequencies of 10 kHz, a beam wavelength of 1,064 nm, and reflectivity of 80% at 3 km distance. The field of view is 40° in both vertical and horizontal directions. It uses a dual-mirror system, where the mirrors are controlled by different scanning methods selected by the user. The controller program allows the user to define and control a scan and set various scan settings including spot spacing, scan pattern, and pulse mode (Figure 3.7). The spacing at which points are collected is set to ~7 mm. This corresponds with angle distance of ~0.008° between laser pulses. The lower point spacing values produce higher resolution scans. The scan pattern is set to *step stare* in which one moving mirror produces the horizontal or x-axis while a second moving mirror produces the vertical or y-axis (Figure 3.8). The scan pulse mode is set to “last”, in which the range (distance between scanner and the object of interest) is determined by measuring the last pulse returning to the scanner, filtering the earlier returns. This is ideal for scanning in poor conditions such as scanning in fog, rain, or dust.

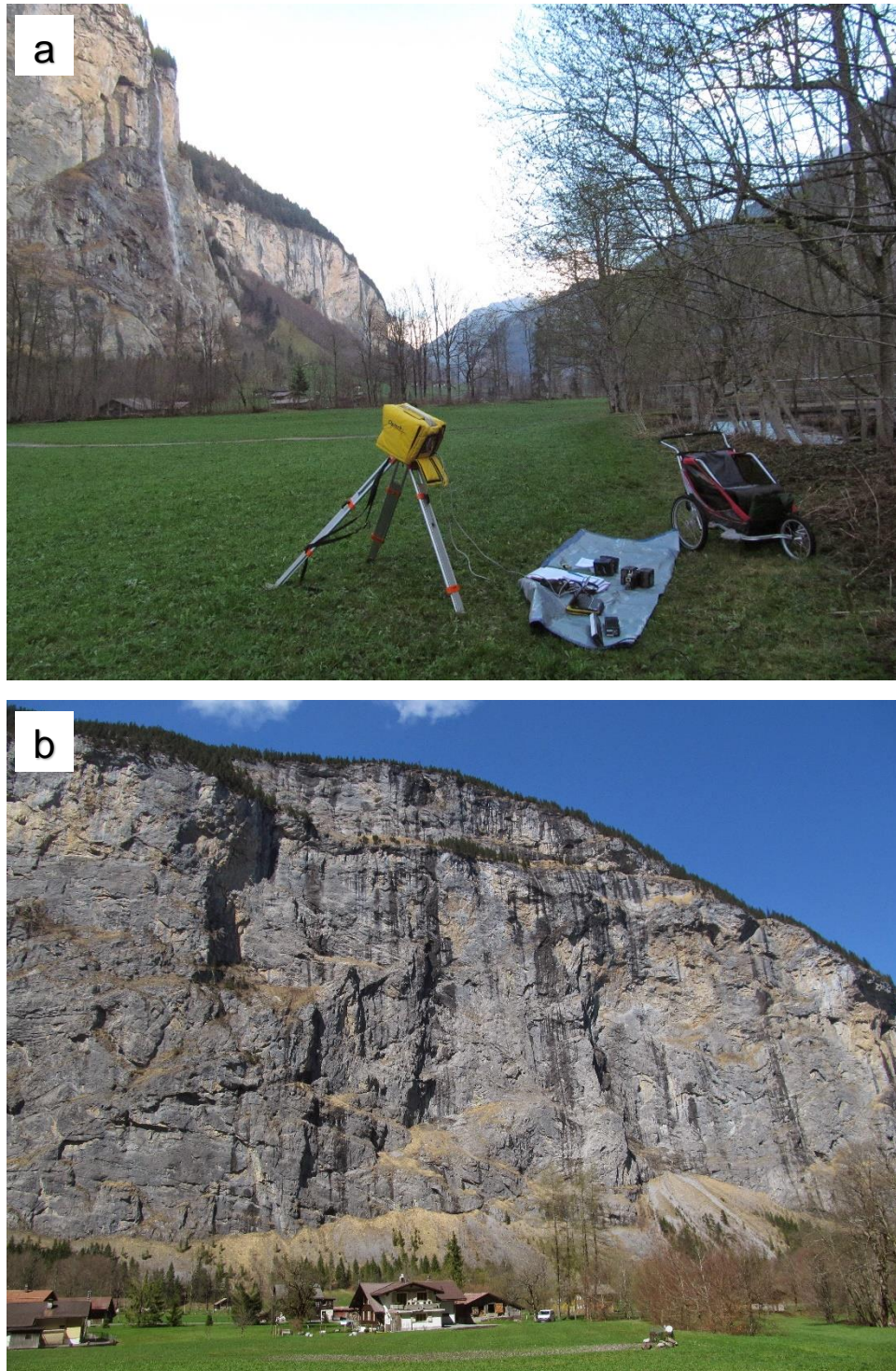


Figure 3.5 Setup of the Optech ILRIS-LR terrestrial laser scanner in the Lauterbrunnen Valley (a). An ideal scan position provides a clear view and nearly orthogonal perspective to rockwalls, a secure zone of 114 m in front of the scanner, allowing for sufficient overlap between scans and minimizing occluded areas by scanning from different angles. An example of a near-vertical rockwall chosen for scanning (b).

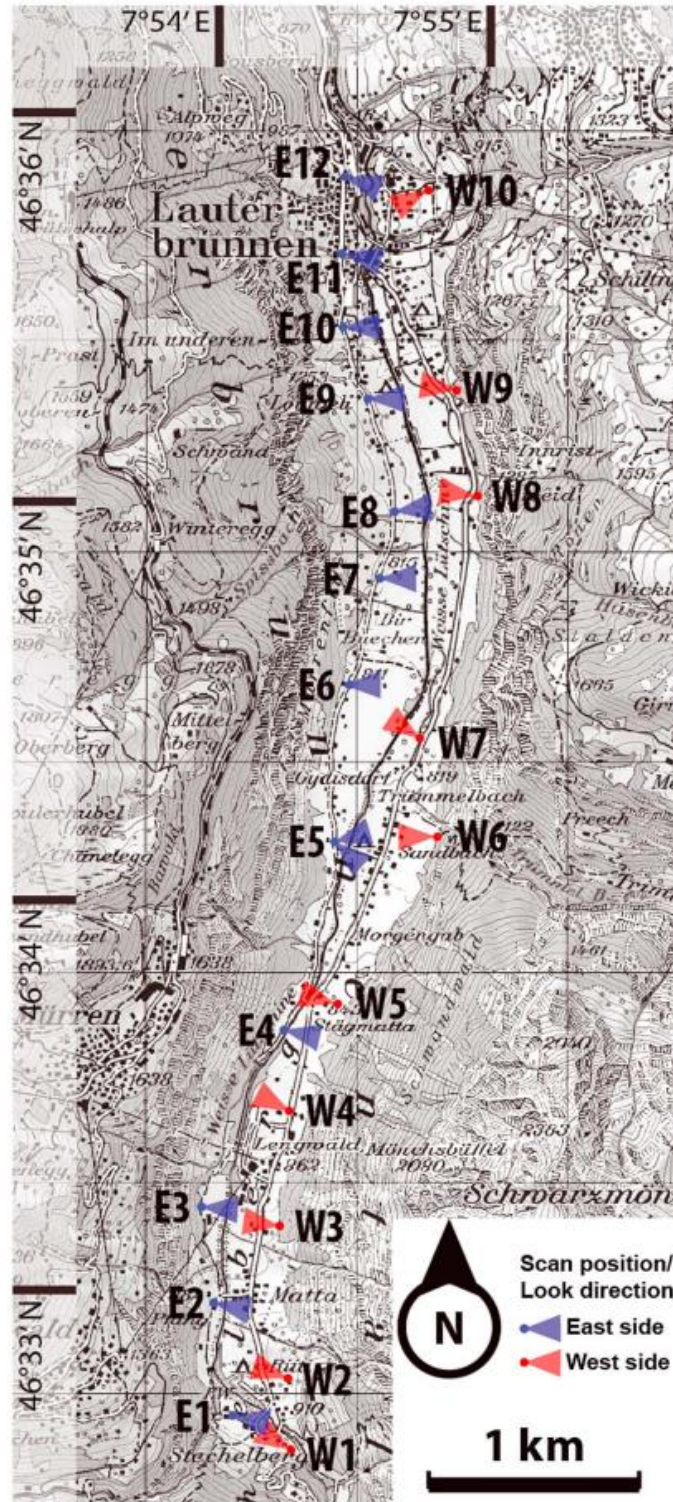


Figure 3.6 Topographic map of the Lauterbrunnen Valley including the scan positions and look direction. Two scans with different look directions were collected from each location. Labels “E” and “W” indicate on which side of the valley the LiDAR scanner was positioned to collect point cloud data from the opposite side of the valley. Figure from Strunden et al. (2015).

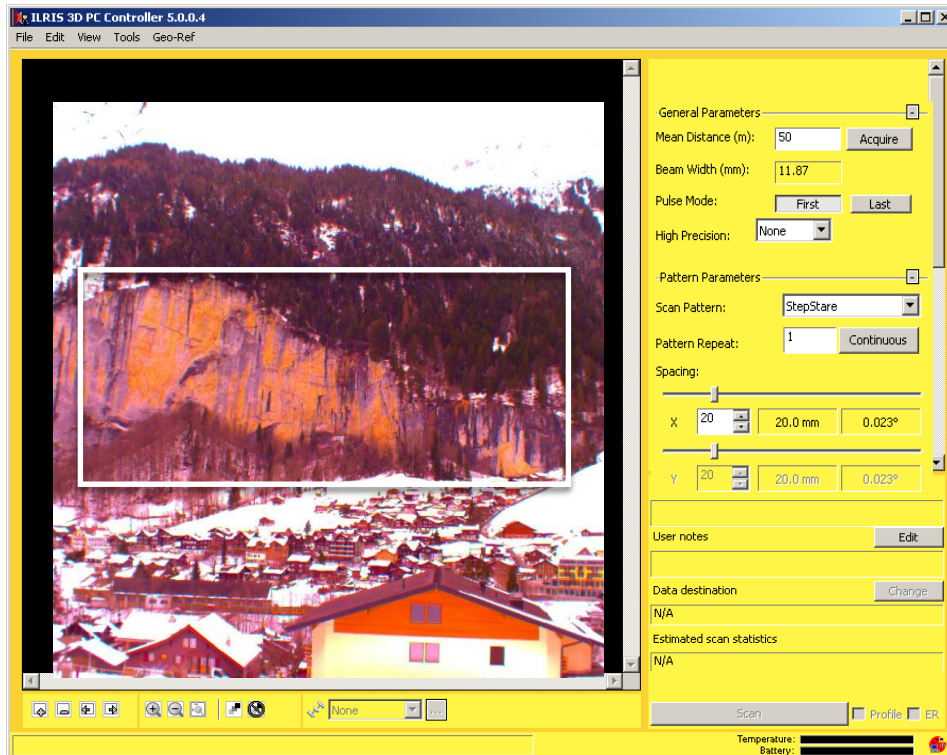


Figure 3.7 Defining scan settings. The ILRIS PC Controller provides a graphical real-time display of ILRIS-LR scan settings and operation. The white box marks the region of interest selected for scanning.

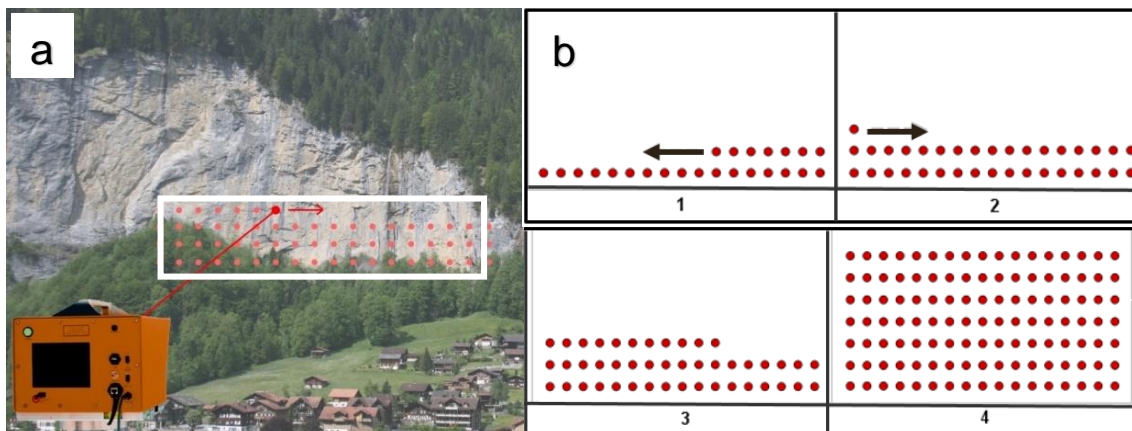


Figure 3.8 Step stare scanning pattern. The white rectangular area in (a) represents a region of interest (ROI) selected for scanning by the user, and the red dots represent laser pulses emitted from the scanner window, starting from the lower left corner of the ROI (panel 1 in b) and continuing until the entire ROI is scanned (panel 4 in b).

The software package (Joint Research Center (JRC) Reconstructor 2) and specific methods of processing used in this study had been established for use at this field site by Strunden et al. (2015) for rockfall detection and volume estimation. An overview of the TLS data processing workflow is shown in Figure 3.9 and described in more detail below.

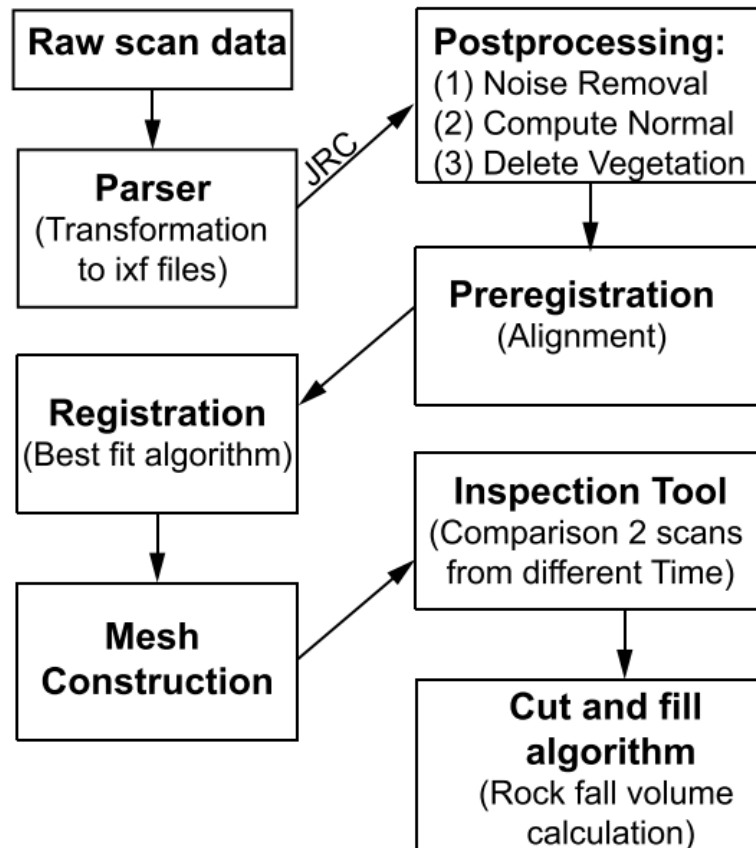


Figure 3.9 TLS data processing workflow for quantifying rockfall volumes. Figure from Strunden et al. (2015)

Post-processing - The raw scan data are converted to the IXF (Integration Exchange Format) format using the Parser software from Optech. In the JRC software, a set of algorithms are applied to remove noise in data. Vegetation and artefacts are removed manually in a two dimensional (2D) image.

Pre-registration and Registration - To compare scans from the same scan position collected at subsequent times, the point cloud of the first scan (reference scan) is first manually aligned with the later scan (moving scan) by identifying a set of corresponding points among the two scans during pre-registration (Figure 3.10). During registration, this alignment is refined automatically using the Iterative Closest Point (ICP) algorithm. The

algorithm finds points (i.e., control points) on the moving cloud that are close to the reference cloud. The algorithm then iteratively moves the moving cloud to reduce the distance of the control points to the reference models.

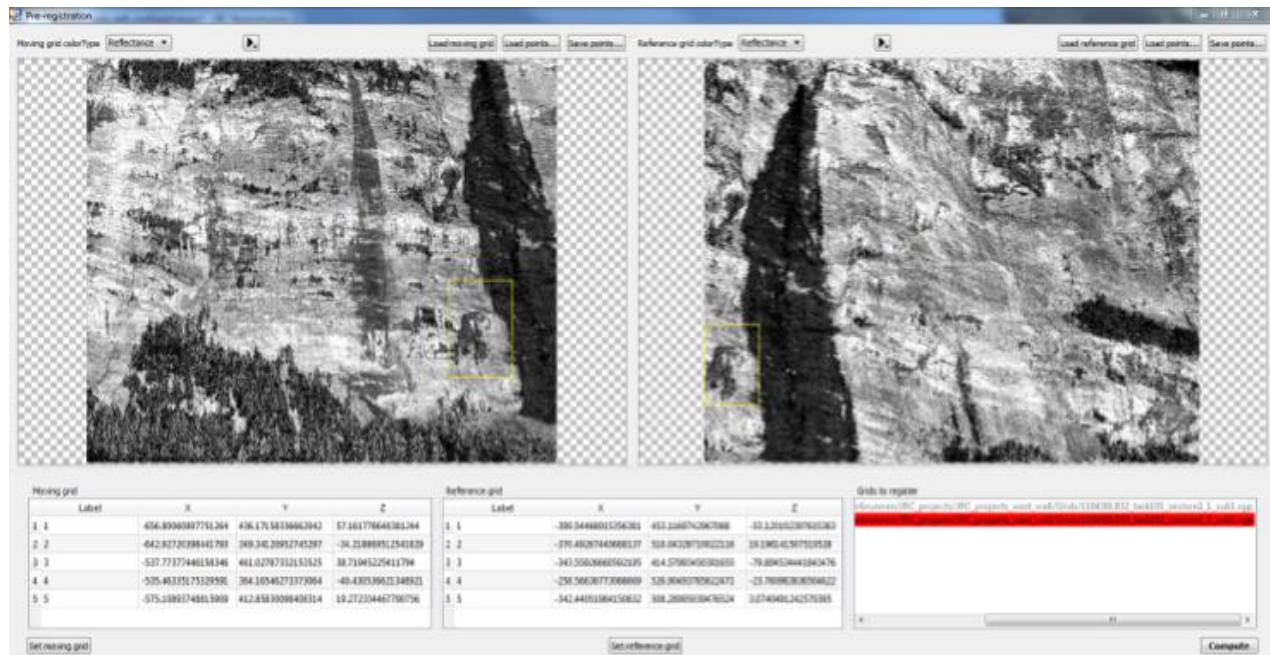


Figure 3.10 Pre-registration dialog in the JRC software. This technique allows user to manually compute a rough alignment between two point clouds. The image on the right is the reference grid, and the image on the left is the moving grid. Selected control points are shown below the grids. The alignment can be later refined automatically using the ICP registration.

Meshing and Inspection: A triangulated mesh of the reference scan is computed from a predefined view/projection. To create a mesh, the algorithm projects all the points on a 2D surface (the near plane of the selected projection). These points are then meshed with a standard 2D meshing algorithm named Delaunay, and the resulting mesh is projected back into the 3D space. Using the inspection tool, the distance between each point in the moving scan and the reference mesh is computed along a specific axis, and changes are visualized in pseudo colors (Figure 3.11a). Rockfalls regions of interest (ROI) are identified by visual identification of changes between scans (Figure 3.11b), and comparison to photographs taken during each scan (Figure 3.12).

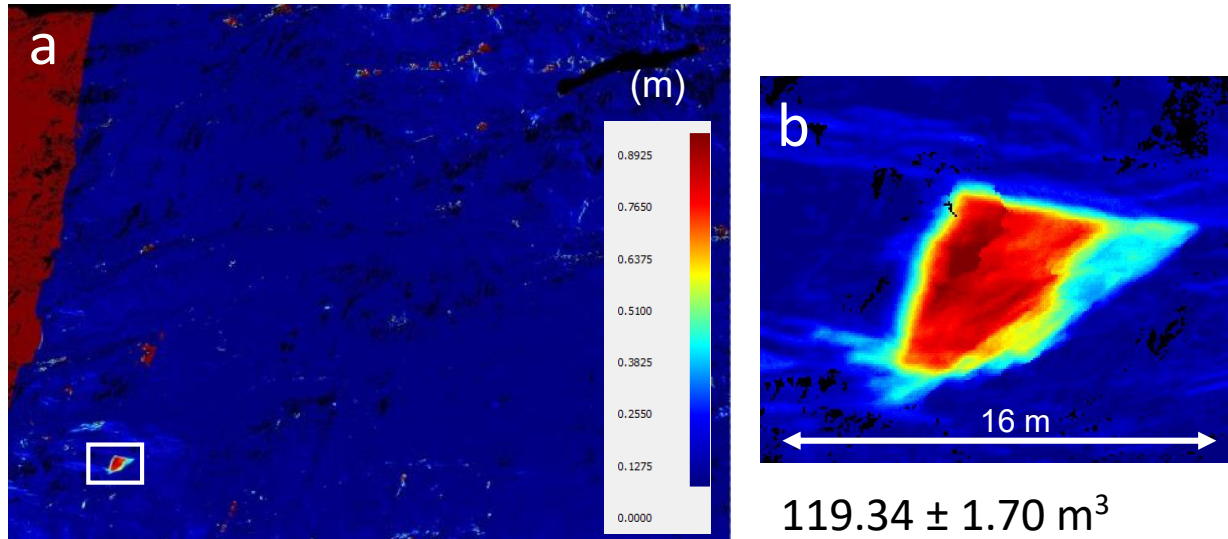


Figure 3.11 An example of the difference image where the results are shown as a new color layer that carries for each point its measure distance from the reference model (a). Example of an individual rockfall (b); color code is blue: no volume change; red: cut distance in meters. The exact rockfall volume including the uncertainty is shown below box (b). The white box in (a) shows the extent of the image displayed in (b).

Rockfall volume calculation: The ROI extent is digitized and a cut-and-fill volume calculation is carried out by creating a mesh of the ROI and comparison with the reference mesh. Cut values represent material loss due to rockfall, loss of snow cover, or vegetation loss. Fill values show added volumes such as from snow cover, or vegetation growth. Photographs taken during each scan assist with distinguishing rockfall events from other features.

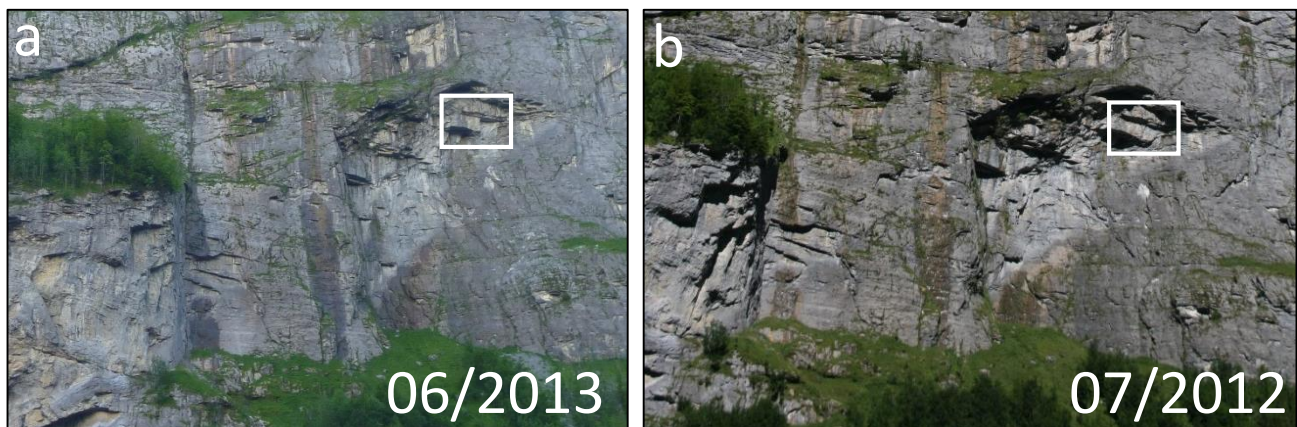


Figure 3.12 Photographs taken one year apart are used for distinguishing rockfall events from other features. The white box shows the location of the rockfall event detected in Figure 3.11.

3.4 Frequency-Magnitude calculations

The frequency-magnitude relationship of rockfalls is an important component of rockfall hazard and risk assessment and has been used to estimate the repeat time of larger rockfall events (Guzzetti et al., 2003; Hergarten, 2012; Strunden et al., 2015). Previous studies have shown that there is a relationship between rockfall volume and cumulative rockfall frequency, defined by a power law:

$$N(V) = a V^{-b} \quad (4)$$

where $N(V)$ is the cumulative number of rockfalls, V is the rockfall volume and prefactor a and scaling exponent b are empirically-determined constants. This relationship can be evaluated through the use of a rockfall inventory. Previous work using TLS-derived rockfall inventories have shown that above a certain magnitude, the frequency of rockfalls appears to decay as a power-law (Barlow et al., 2012; Guerin et al., 2014; Santana et al., 2012; van Veen et al., 2017). Below this magnitude (also known as rollover), there is no clear trend. The rollover volume as to be determined, and events smaller than the rollover volume should be excluded, before estimating a power-law distribution.

To estimate the rollover volume, two approaches are used in this study. First, nonlinear fits to the data are computed for all possible rollover volumes, and the best fit, as determined by the highest R^2 value, is selected. The use of a least-square linear fit on log-transformed data is avoided as this procedure yields a biased estimate for the scaling exponent b by distributing the error in the tail of the power law distributed data unevenly (Barlow et al., 2012; Clauset et al., 2007; Goldstein et al., 2004). Second, the choice of the rollover volume and its corresponding maximum-likelihood estimate for the scaling component b are tested using the Kolmogorov-Smirnov (KS) goodness-of-fit test, in which the lowest KS value describes the best fit.

The calculated power law relationship is then used to extrapolate to the time between larges events, following the method described by previous studies (e.g., Bennett et al., 2012; Malamud et al., 2004; Strunden et al., 2015), using this relationship:

$$N(V) = \left(\frac{N_o}{T}\right) * \left(\frac{V}{V_o}\right)^{-b} \quad (5)$$

where $\frac{N_o}{T}$ is the number of events larger than the volume V in the observation time T .

The long-term averaged total eroded volume V_T is calculated by integrating the frequency density of rockfall magnitudes multiplied by the event volume following the method described in Barlow et al. (2012):

$$V_T = \int_{V_{min}}^{V_{max}} a V^{-b} V dV \quad (6)$$

where V_{min} is the minimum rollover volume and V_{max} is the maximum expected rockfall volume based on historic records. From the total eroded volume, a corresponding rockwall retreat rate can be calculated.

4 Results

The main scientific results that address the hypotheses outlined in section 2 of this dissertation are shown in the following sections (i.e., 4.1-4.4). These results are presented as published or manuscripts in revision. Supplement files associated with each manuscript is shown at the end of each section.

4.1 Online database of fault locations, fault attributes and seismicity

4.1.1 Author contributions

The following section of the dissertation has been published and is available online: <https://doi.org/10.5194/nhess-16-529-2016>. The full citation is:

Mohadjer, S., Ehlers, T.A., Bendick, R., Stübner, K. and Strube, T., 2016. A Quaternary fault database for central Asia. *Natural Hazards and Earth System Sciences*, 16(2), pp.529-542.

The original manuscript is provided in section 4.1.2 and the original supplement file is given in section 4.1.3. The online database and associated data files are available at: <https://esdynamics.geo.uni-tuebingen.de/faults/>

Five authors contributed to the work presented in this paper: Solmaz Mohadjer (SM), Todd Ehlers (TAE), Rebecca Bendick (RB), Konstanze Stübner (KS), and Timo Strube (TS). A summary of the contributions is provided in Table 4.1. The detailed contributions are as follows: RB sparked the overall idea about the need for an open-access fault database for Central Asia. The idea was further developed by SM and TAE. All data files were compiled, prepared in ArcGIS, and furthered managed in phpMyAdmin by SM. Programming work for data web mapping and online visualization was done by TS with input from SM. Analysis and interpretation of results were done by SM with contributions from TAE, RB and KS. SM drafted the first version of the manuscript along with all Figures and tables. The manuscript was further reviewed and edited by TAE, RB, KS, and TS, as well as three external reviewers during the peer review process.

Table 4.1: Summary of contributions to joint work for the paper “A Quaternary fault database for Central Asia”, indicating the average fraction of work of the respective author in percentage.

| Author | Position | Scientific Ideas (in %) | Data generation (in %) | Analysis and Interpretation (in %) | Paper writing (in%) |
|---------------|-----------------|--------------------------------|-------------------------------|---|----------------------------|
| SM | [1] | 60 | 60 | 70 | 70 |
| TAE | [2] | 30 | 0 | 10 | 10 |
| RB | [3] | 10 | 0 | 10 | 10 |
| KS | [4] | 0 | 0 | 10 | 5 |
| TS | [5] | 0 | 40 | 0 | 5 |

4.1.2 Paper: “A Quaternary fault database for Central Asia”

Nat. Hazards Earth Syst. Sci., 16, 529–542, 2016
 www.nat-hazards-earth-syst-sci.net/16/529/2016/
 doi:10.5194/nhess-16-529-2016
 © Author(s) 2016. CC Attribution 3.0 License.



Natural Hazards
 and Earth System
 Sciences  Open Access

A Quaternary fault database for central Asia

Solmaz M ohadjer¹, Todd Alan Ehlers¹, Rebecca Bendick², Konstanze Stübner¹, and Timo Strube¹

¹Department of Geosciences, University of Tübingen, Tübingen, Germany

²Department of Geosciences, University of Montana, Missoula, Montana, USA

Correspondence to: Solmaz M ohadjer (solmaz.mohadjer@gmail.com)

Received: 27 July 2015 – Published in Nat. Hazards Earth Syst. Sci. Discuss.: 23 September 2015

Revised: 14 January 2016 – Accepted: 26 January 2016 – Published: 24 February 2016

Abstract. Earthquakes represent the highest risk in terms of potential loss of lives and economic damage for central Asian countries. Knowledge of fault location and behavior is essential in calculating and mapping seismic hazard. Previous efforts in compiling fault information for central Asia have generated a large amount of data that are published in limited-access journals with no digital maps publicly available, or are limited in their description of important fault parameters such as slip rates. This study builds on previous work by improving access to fault information through a web-based interactive map and an online database with search capabilities that allow users to organize data by different fields. The data presented in this compilation include fault location, its geographic, seismic, and structural characteristics, short descriptions, narrative comments, and references to peer-reviewed publications. The interactive map displays 1196 fault traces and 34 000 earthquake locations on a shaded-relief map. The online database contains attributes for 123 faults mentioned in the literature, with Quaternary and geodetic slip rates reported for 38 and 26 faults respectively, and earthquake history reported for 39 faults. All data are accessible for viewing and download via <http://www.geo.uni-tuebingen.de/faults/>. This work has implications for seismic hazard studies in central Asia as it summarizes important fault parameters, and can reduce earthquake risk by enhancing public access to information. It also allows scientists and hazard assessment teams to identify structures and regions where data gaps exist and future investigations are needed.

1 Introduction

The ongoing collision of the Indian subcontinent with Asia results in active deformation and seismicity in the Indo-Asian collision zone (Fig. 1). Continental collision initiated in the early Cenozoic (ca. 55 Ma) and is marked by large spatial and temporal variations in deformation across the Himalaya and surrounding areas (e.g., Hodges, 2000; Avouac, 2007; Thiede and Ehlers, 2013). India–Eurasia collision has created a complex zone of deformation that is characterized by an intricate network of faults, some of which have historically caused devastating earthquakes and continue to pose threats to the population at risk. Seven of the 28 deadliest earthquakes reported for 1990–2014 (USGS, 2014) are located in this zone with magnitudes ranging from 6.1 to 7.9 (Fig. 1). According to the United States Geological Survey, these events caused at least 195 796 fatalities in total, corresponding to 23 % of total death toll reported for all deadly earthquakes in the world for the above period. Earthquakes in this region do not have to be particularly large to cause heavy damage. Only one of the 28 largest earthquakes reported for the above period is located within the India–Eurasia collision zone (i.e., the 2008 M 7.9 Sichuan earthquake). Smaller events of magnitudes 6.1 and 6.6 that occurred in the Hindu Kush region in 2002 and 1998 respectively, caused over 5000 fatalities, and left about 10 000 injured and tens of thousands homeless. To understand earthquakes and to address earthquake hazards, it is crucial to locate and characterize Quaternary faults accurately. In particular, fault location, earthquake history and cycle, as well as slip rate, are important input parameters that are used in calculations of earthquake hazards and probabilities. This information can serve as the basis for understanding faulting and earthquake behavior in the region (Trifonov and Kozhurin, 2010; Field et al., 2013; Wills et al.,

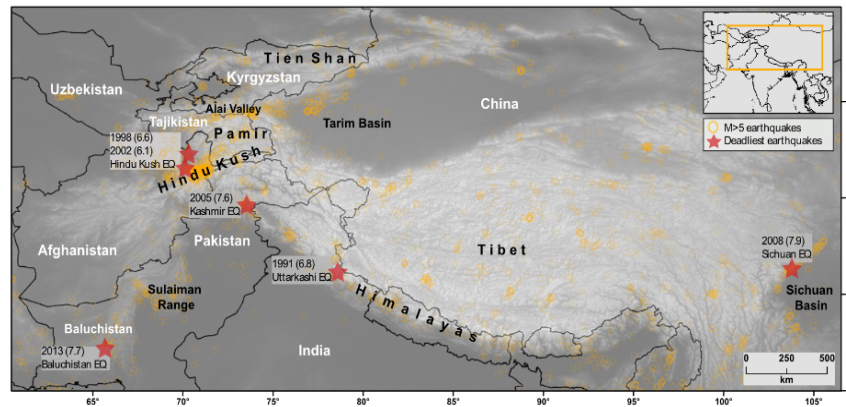


Figure 1. Map of the study area showing $M \geq 5$ earthquakes (orange circles) for the 1900–2014 period from ANSS Comcat (2014). Red stars mark the location of the deadliest earthquakes for the 1900–2014 period that are discussed in the text. The only exception is the 2001 $M 7.7$ Bhuj earthquake which is located outside the study area, but it is still considered to be within the India–Eurasia collision zone.

2008; Plesch et al., 2007; Ruleman et al., 2007; Tapponnier et al., 2001).

Previous studies in central Asia have produced a large amount of data that enhance our understanding of regional and continental-scale tectonics as well as seismic hazards in the region. Geodetic measurements using the Global Positioning System (e.g., Bendick et al., 2015; Ischuk et al., 2013; Mohadjer et al., 2010; Zubovich et al., 2010; Bendick et al., 2007; Reigber et al., 2001; Abdrahmatov et al., 1996) and regional seismic investigations and catalogs (e.g., Feld et al., 2015; Schneider et al., 2013; Sippl et al., 2013; Mechie et al., 2012; Haberland et al., 2011; Mellors et al., 1995) continue to provide a more detailed pattern and rates of deformation associated with individual faults and other major structures. High-resolution imagery allows for more accurate mapping of previously recognized faults and their geomorphic expressions (e.g., Chevalier et al., 2012; Robinson, 2009; Taylor and Yin, 2009; Strecker et al., 2003), and a significant number of previously unknown, but potentially active structures have been detected and interpreted based on satellite images and digital topographic data (e.g., Ruleman et al., 2007). Despite being limited in their coverage, recent paleoseismologic studies (e.g., Schiffman et al., 2013; Korjenkov et al., 2012; Ran et al., 2010; He et al., 2007; Kumar et al., 2006; Washburn et al., 2003) provide improved constraints on the magnitude and recurrence time of past earthquakes for some faults. The paleoseismic history of many faults, however, remains poorly understood. Previous investigations have often been limited to the Himalayan main frontal thrusts (Kumar et al., 2001, 2006; Lavé et al., 2005) and other major structures such as the Kunlun and Altyn Tagh faults (He et al., 2007; Washburn et al., 2001, 2003, respectively), or were only conducted in the aftermath of large events such as the 2005 Kashmir and the 2008 Sichuan earthquakes (Kaneda et

al., 2008 and Ran et al., 2010, respectively). A more complete paleoseismic record can enhance our understanding of fault behavior and earthquake hazard in the region. All data from previous work provide baseline observations for understanding patterns and rates of Quaternary faulting in central Asia.

Despite considerable advancements provided by previous work, there are several shortcomings that impede information sharing and adequate assessment of fault activity and hazards in the region. Previous investigations have generated data that are documented in a wide range of formats (e.g., digital, texts, maps, and images) that are often published in non-open access journals. This can make access, usage, and dissemination of fault data a time-consuming and resource-intensive task, particularly for non-academic users and the general public. Despite initiatives that aim to provide a centralized platform for storage, maintenance, and the display of fault data specific to other regions of the world such as the online Quaternary Fault and Fold Database of the United States Geological Survey (<http://earthquake.usgs.gov/hazards/qfaults/>), few attempts have been made for central Asian faults (e.g., Ioffe and Kozhurin, 1996; Ioffe et al., 1993; Trifonov, 2000). The HimaTibetMap of Taylor and Yin (2009) is currently the only publicly available digital database of active structures located in central Asia. Users can download and view fault location data on a semi-interactive map. The fault data, however, are unsearchable and limited to only a few parameters. The Global Earthquake Model Global Active Faults Database (<http://www.globalquakemodel.org/>) is currently being tested with no fault data from central Asia. Therefore, there is a clear need for an open-access database with fault information that focuses on central Asia.

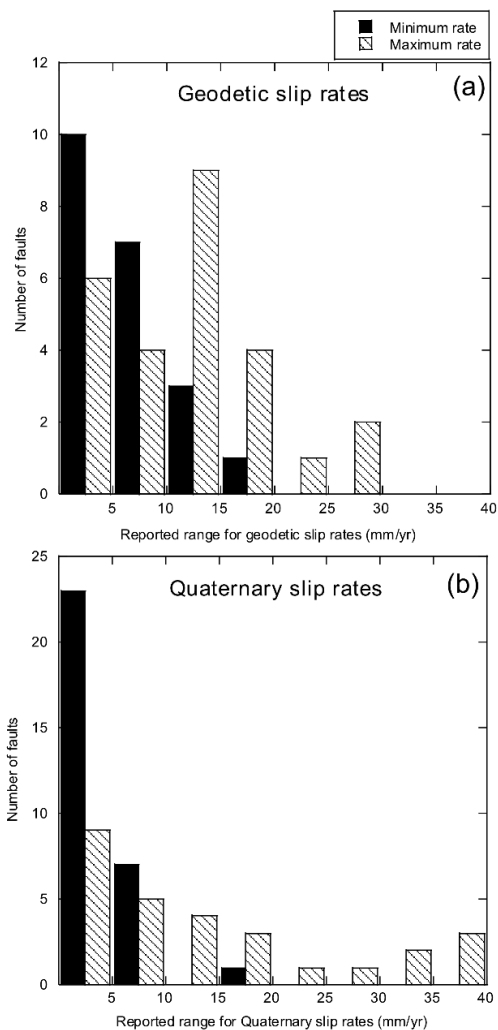


Figure 2. Distribution of geodetic (a) and geologic (b) slip rates as reported in the CAFD.

Our work complements previous efforts by providing an open-access and searchable database that includes an interactive map that is linked to an online database. Database users can generate simple and complex queries to access and view not only fault locations, but also important fault parameters such as slip rates and earthquake history. All data on this website are the product of work in progress and subject to change based on community's feedback and future refinement as more studies become available. An objective of this work is to make fault information available to not only the scientific community, but also to the general public, and to encourage local and international organizations to consider fault location and parameters in their project analysis.

2 Data sets

The central Asia Fault Database (CAFD) contains three data sets including fault locations, fault attributes, and seismicity (Table 1). Published maps of faults in the study region identify the location of 1196 Quaternary (<2.6 Ma) traces that define the location of 123 faults that have attributes. Fault attributes (Table 2) are divided into six categories (i.e., identifiers, geographic characteristics, seismic characteristics, structural characteristics, description, and references). Each category contains fields that show relevant fault information. The database fields range from fault name, exposure, and country to Quaternary and geodetic slip rates, earthquake history, geomorphic markers of activity, paleoseismic data, and fault length and sense of motion. Additionally, a brief description and a list of references are provided for each fault. Table 3 provides a more detailed description for each field. Seismicity data include location, magnitude, and depth of over 34 000 earthquakes that were recorded throughout the region using global (ANSS ComCat, 2014) and regional (Sippl et al., 2013) seismic networks. All data sets are based on our review of over 250 published papers. The forthcoming sections provide a more detailed description of each data set, and the criteria used for data set selection and evaluation.

2.1 Fault locations

Detailed and accurate mapping of fault systems and subsidiary features are essential to understanding of fault characteristics and activity. Precise fault locations can also aid with identification of promising sites for paleoseismic and geomorphic investigations (Zachariassen and Prentice, 2008). Locations of the 1196 fault traces in the current version of CAFD are based on maps and figures that come from 84 published studies. These studies include both those that have broadly defined the location and behavior of Quaternary faults (e.g., northern extension of the Chaman Fault in Afghanistan) and those that more accurately have mapped and described individual strands of fault systems (e.g., Karakoram Fault strands). The latter was chosen for the database when available. The database contains 569 fault traces from the HimaTibetMap of Taylor and Yin (2009), which is an open-source digital database of Quaternary faults located in the Indo-Asian collision zone. The faults taken from the HimaTibetMap are based on field observations and interpretations of satellite images and digital topographic data (Styron et al., 2010; Taylor and Yin, 2009; Taylor et al., 2003) as well as other previously published work.

When digitized data are not available, individual fault traces were digitized from their original sources and at the original publication map scale using the ArcMap software. To digitize a fault, a map is first aligned to available data sets (e.g., country boundaries) and georeferenced using more accurate data layers such as ASTER GDEM 2 (30 m resolution digital topography). The faults are digitized and attributed in

Table 1. Overview of the data sets used in the CAFD.

| Data | # of entries | Source | Remarks |
|------------------|--------------------|-----------------------------|--|
| Fault locations | 1196 fault traces | Published literature | Faults with Quaternary traces (< 2.6 Ma) |
| Fault attributes | 123 faults | | |
| Earthquakes | 9000 earthquakes | TIPAGE; Sippl et al. (2013) | 08/2008–06/2010 |
| | 25 000 earthquakes | ANSS ComCat; ANSS (2014) | 1900–2014 |

Table 2. Structure of the CAFD and queryable search fields.

| | Database fields | Queryable | |
|--------------|----------------------------|------------------------------------|-----|
| Fault system | Identifiers | Fault ID | – |
| | | Name | Yes |
| | Geographic characteristics | Country | Yes |
| | | Physiographic province | Yes |
| | | Exposure | – |
| | Seismic characteristics | Slip rates (geologic and geodetic) | Yes |
| | | Historic earthquake | Yes |
| | | Geomorphic expression | Yes |
| | | Paleoseismic studies | Yes |
| | Structural characteristics | Primary sense of motion | Yes |
| | | Strike and dip direction | – |
| | | Length | – |
| | Description | Brief summary and remarks | – |
| | References | Citations | – |

ArcMap. The attribute table contains information about each fault including its name, sense of movement (if known), references, and other important remarks such as variations in the fault name or location. Fault location accuracy depends on the scale of observation used in previous investigations. Since investigations were conducted at a variety of different scales and methods, some structures are located more precisely than others. For example, Ruleman et al. (2007) mapped features mostly from 90 m resolution Landsat ETM (Enhanced Thematic Mapper) data at a maximum scale of about 1:50 000 (□ 25 m raster resolution) while Schurr et al. (2014) relied on 1:200 000 maps (□ 100 m raster resolution) for their interpretation of Cenozoic faults. To increase location accuracy, Schurr et al. (2014) also used satellite imagery and fieldwork. These examples demonstrate that uncertainties in the positions of each fault in this database are variable, and therefore users are encouraged to consult the original source provided in the comments field within the database for a detailed understanding of the location uncertainties associated with each fault.

In general, the position accuracy for each fault is suitable for visualizing and plotting faults at a regional scale and most likely not suited for site-specific studies without consulting the original study provided in the references. When there are discrepancies in fault locations, we adjusted the position of previously mapped faults to coincide with surface

features visible in ASTER GDEM2 data that are indicative of their trace. This is noted in the comment fields of the database. Faults with an undetermined level of Quaternary activity (e.g., Herat Fault in Afghanistan) are included in the database to avoid creating false impressions about seismic hazard and risk in some localities. Finally, Quaternary faults not documented in this study exist and may be active, but are unfortunately not yet documented sufficiently for inclusion in this study.

2.2 Fault attributes

All fault parameters used in the database fields (Table 3) are documented from original sources. More specific information about each parameter is reported in the comments field within the database, especially where discrepancies exist. The most common database fields with comments include fault name, exposure level, geodetic and geologic slip rates, and sense of motion. The comments field for fault name explains different names used to refer to the same fault including variations in spelling (e.g., North Pamir Thrust is also referred to as Main Pamir Thrust, Main Alai Thrust, and Pamir Thrust System). Similarly, the fault exposure comments are used for faults with varying levels of surface exposure (e.g., Himalayan Main Frontal Thrust being concealed within the mapping area of Raiverman et al. (1993) but displaying mor-

Table 3. Description of parameters and fields used in the CAFD.

| Database fields | Description |
|---|---|
| Name | The most commonly used fault name in the published literature. Name variations and spelling are included in the comment section. |
| Country | Name of countries where the fault trace is located. |
| Physiographical province | Name of regions with similar terrain and geologic history (e.g., Pamir, Tarim Basin, Alai Valley). |
| Exposure | Fault exposure level (exposed or concealed). |
| Geodetic slip rate (mm yr ⁻¹) | The reported geodetic slip rate as documented in the original studies. It is shown in mm yr ⁻¹ and as a minimum–maximum range. Comments specific to the geodetic slip rate including all reported rates, types, uncertainties, references, as well as methods are included in the comment section. |
| Geologic slip rate (mm yr ⁻¹) | The reported Quaternary slip rate as documented in the original studies. It is shown in mm yr ⁻¹ and as a minimum–maximum range. Comments specific to the geologic slip rate including all reported rates, types, uncertainties, dating methods, and references are included in the comment section. |
| Historic earthquake | Documented past earthquakes including location, magnitude, timing, related surface features (offsets, scarps, etc.), and references. |
| Geomorphic expression | Location and description of fault-related geomorphic markers (e.g., offset or deflected stream channels, sag ponds, scarps in young alluvium) as well as published analysis, interpretation, and references. |
| Paleoseismic studies | Location and description of paleoseismic studies and references including trench site location and observations. |
| Primary sense of motion | The dominant style of faulting as reported in published literature. Comments specific to fault motion including changes in style of faulting along the strike as well as other documented components of movements and references are included in the comment section. |
| Dip direction | Dip direction of the main fault trace or fault zone. Comments specific to dip direction including reported direction for specific fault traces. |
| Strike | Strike of the main fault trace or fault zone. Comments specific to the strike of the fault including reported strikes for specific fault traces. |
| Length (km) | Length of the fault trace in kilometers. Comments specific to fault length including length of studied traces, total fault length, and references are included in the comment section. |
| Description | A brief description of the fault and its geologic and tectonic settings. |
| References | References for fault parameters and trace(s) on the interactive map. |

phology indicative of surface faulting near Chapri Rao and west of the Tamuna River as shown in Wesnousky et al., 1999). Additional data for slip rates such as type, uncertainties and locations are included in the relevant comments fields. Where different types of fault movements are reported for the same structure (e.g., thrust with component of left-lateral shear reported for Oinak-Djar Fault) or when a fault's style of movement changes along its length (e.g., Konar Fault showing a progressively greater component of thrust faulting northeastward), the comments field reflects this information. Comments fields can also include references used for an entry in a database field. Important fault attributes such as Qua-

ternary and geodetic slip rates are discussed in more detail below.

2.3 Slip rates

Slip rate data are important in constraining seismic hazard as they are used to estimate the rate of earthquakes on known faults. The CAFD documents both Quaternary and geodetic slip rates for faults. Quaternary slip rates are often used in seismic hazard models as these values are thought to better represent deformation rates appropriate for hazard models (Dawson and Weldon, 2013). Where these rates are lacking or inaccurate, particularly in locations with no evidence for

Table 4. Summary of Quaternary and geodetic fault slip rates. All rates are estimates and demonstrate the ranges of reported slip rate values for each fault. Fault labels are as in Fig. 8.

| Fault label | Fault name | Geologic slip rate (mm yr ⁻¹) | Geodetic slip rate (mm yr ⁻¹) |
|-------------|-----------------------------------|--|--|
| ATF | Altyn Tagh fault | 2–> 20 | 6–11 |
| BMF | Black Mango fault | 10 | 14 |
| CF | Chaman fault | 25–35 | 8–17 |
| DKF | Darvaz-Karakul fault | 10–15 | 10 |
| HRF | Herat fault | 2–3 | < 2 |
| HF | Haiyuan fault | 3–19 | 4–8 |
| KF | Karakorum fault | 4–32 | 1–11 |
| KKF | Karakax fault | 20 | 5–7 |
| KLF | Kunlun fault | 2–13 | 1–12 |
| LMT | Longman Shan thrust belt | < 1 | < 1–4 |
| MFT | Main Frontal thrust | 6.3–21 | 13–20 |
| MJF | Muji fault | 4.5 | 4–5 |
| MPT | Main Pamir thrust | 2–6 | 10–15 |
| PFT | Pamir Frontal thrust | 6–7 | 6–9 |
| RRF | Red River fault | 2–3 | 1–2 |
| SF | Sagaing fault | 10–23 | 18 |
| TF | Talas-Fergana fault | 5–19 | < 1–3 |
| XXF | Xianshuihe-Xiaojiang fault system | 5–18 | 10–11 |

old or recent earthquakes, geodetic rates from GPS or InSAR are used to determine present-day deformation rates for faults. These rates include interseismic, coseismic, and post-seismic motions, yielding information that can help with identification of locked fault traces or creeping faults.

In the database, Quaternary and geodetic slip rates are reported in millimeters per year, showing minimum and maximum reported values from published literature. These values are reported as slip rates in referenced study and include slip components that reflect the predominant sense of slip for faults. Slip rate data are reported in a variety of ways in published literature (e.g., horizontal, vertical, or dip-slip). The database reports what was originally documented in the published study. This as well as other supporting data such as site location, offset feature, dating method, time interval over which the rate was calculated, and reported uncertainties are shown in the comments section of the database.

Figure 2 shows the distribution of geodetic and Quaternary slip rates for faults included in the database. Geodetic slip rates are reported for 26 faults, with values ranging from < 5 mm yr⁻¹ to < 30 mm yr⁻¹, with most rates reported as maximums with values between 10 and 15 mm yr⁻¹, and as minimums with values < 5 mm yr⁻¹ (Fig. 2a). Quaternary slip rates reported for 38 faults show values ranging from < 5 to 40 mm yr⁻¹, with most rates reported as minimum with values < 5 mm yr⁻¹ (Fig. 2b). There are only 18 faults that have both Quaternary and geodetic slip rates (Table 4). Corresponding uncertainties in fault slip rates as well as other supporting data such as site location, offset geomorphic feature, and dating method for offset features are reported from

the original studies and are included in the comments fields of the database.

2.4 Seismicity

The earthquakes in the current version of CAFD include over 25 000 events from the Advance National Seismic System Comprehensive Catalog (ANSS ComCat). These events were recorded by over 150 seismic stations distributed globally over 80 countries as part of the Global Seismographic Network (Gee and Leith, 2011). The events cover a period from 1900 to 2014. The magnitude for each event is calculated using several different methods, depending upon the type of earthquake, the amount of energy released, and the policies of the authoritative seismic network. The position uncertainty of a hypocenter location of an event in the ANSS ComCat is defined by its epicenter and focal depth, and is estimated to be tens of kilometers. Since the accuracy in determining the epicenter location, depth, and size of an earthquake is a function of the geometry and density of seismograph networks and available seismic data (Husen and Hardbeck, 2010), smaller-sized events ($M < 5$) in the database must be treated with caution as they are unlikely to have been accurately located. The ANSS ComCat is particularly useful for areas with no local network, and is commonly used in studies concerning active tectonics and seismicity in the India–Eurasia collision zone. However, users should be aware that the ANSS ComCat is a composite catalog, based on earthquake catalogs contributed by its member networks, and is not uniform in its coverage and magnitude completeness.

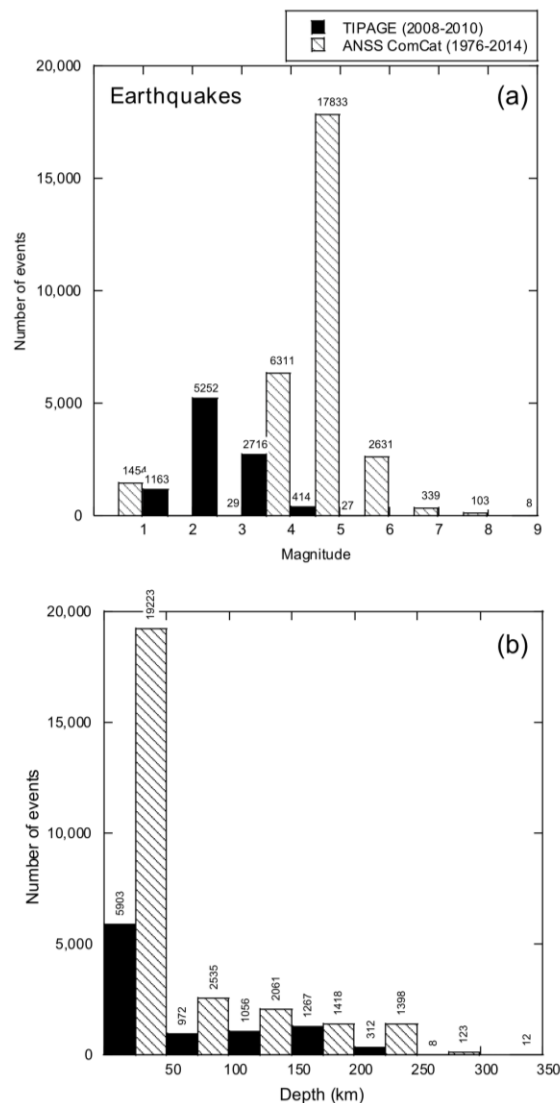


Figure 3. Earthquake distribution based on magnitudes (a) and depths (b) from global (ANSS ComCat) and regional (TIPAGE) catalogs.

The ANSS global catalog is complemented by events from local networks and other temporary station deployments in the Pamir, Hindu Kush, and South Tien Shan. The database displays over 9000 events from the local TIPAGE (Tien Shan PA mir GEodynamic Program) catalog. These events were detected by a network of 40 seismic stations in southern Kyrgyzstan and eastern Tajikistan over a period of 2 years from August 2008 to June 2010. Sippl et al. (2013) used a probabilistic earthquake relocation method (Lomax et al., 2000)

to measure absolute location errors. They estimated mean location uncertainties in longitudinal, latitudinal, and vertical directions, calculated for bins in different depth layers. Their results show vertical errors being larger than horizontal errors for all events, with horizontal errors lower than 7.5 km and vertical errors lower than 15 km throughout the Pamir.

In the database, all earthquakes are displayed based on their size (i.e., below or above magnitude 5) and depth (i.e., below or above 70 km depth). Events below magnitude 5 are considered to have intensity values of I–V on the Modified Mercalli Intensity Scale used by the United States Geological Survey, indicating micro to light shaking effects. Events over magnitude 5 are given intensity values of VI–VIII or above indicating moderate to great shaking effects that are felt over large areas and causing damage to structures. Events between 0 and 70 km are considered to be shallow while those above 70 km are intermediate or deep events. The earthquake locations are indicated by circles, each representing an earthquake's epicenter. Figure 3 shows the distribution of earthquakes from both catalogs based on magnitude and depth. Most events in both catalogs have magnitudes below 5 (Fig. 3a). Events with magnitudes between 1 and 3 are captured by the TIPAGE regional network and events with magnitudes above 5 are captured mostly by the ANSS global catalog. By combining these data sets, the database provides an improved catalog of past event magnitudes. Most events in both catalogs show depths of up to 50 km below the surface (Fig. 3b) with deeper events (> 250 km) represented by the ANSS global catalog only which might be due to larger uncertainties in the calculated depth for events from the ANSS catalog. In the east of Alai valley and within the Pamir thrust system, the 2008 Nura earthquake and its aftershock series (□ 3000 events) are captured by the TIPAGE catalog, and are included in the database in different colors (Fig. 5b) to allow users to differentiate them from background seismicity in the Alai valley.

3 Database construction

The CAFD construction follows four steps (Fig. 4). First, previously published literature and databases related to Quaternary faulting in central Asia were compiled and reviewed. Fault trace data were prepared in the ArcMap software, and used to populate tables created in a MySQL database using an open source, web-based application called phpMyAdmin (<https://www.phpmyadmin.net/>). The MySQL database is composed of data tables that can be queried. The fault location table was created to store geographic coordinates (i.e., latitude, longitude) of points that made up a fault trace. The fault attribute table was created to organize attribute information shown in Tables 2 and 3. To link the fault location table to the fault attribute table, a unique identification number was assigned to each fault and used in both tables. Using PHP scripting (<http://www.php.net/>), the fault loca-

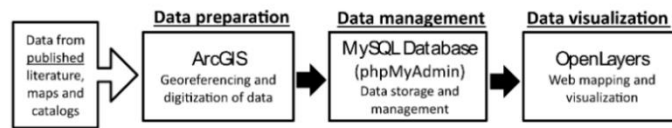


Figure 4. Flowchart of the process for the CAFD development.

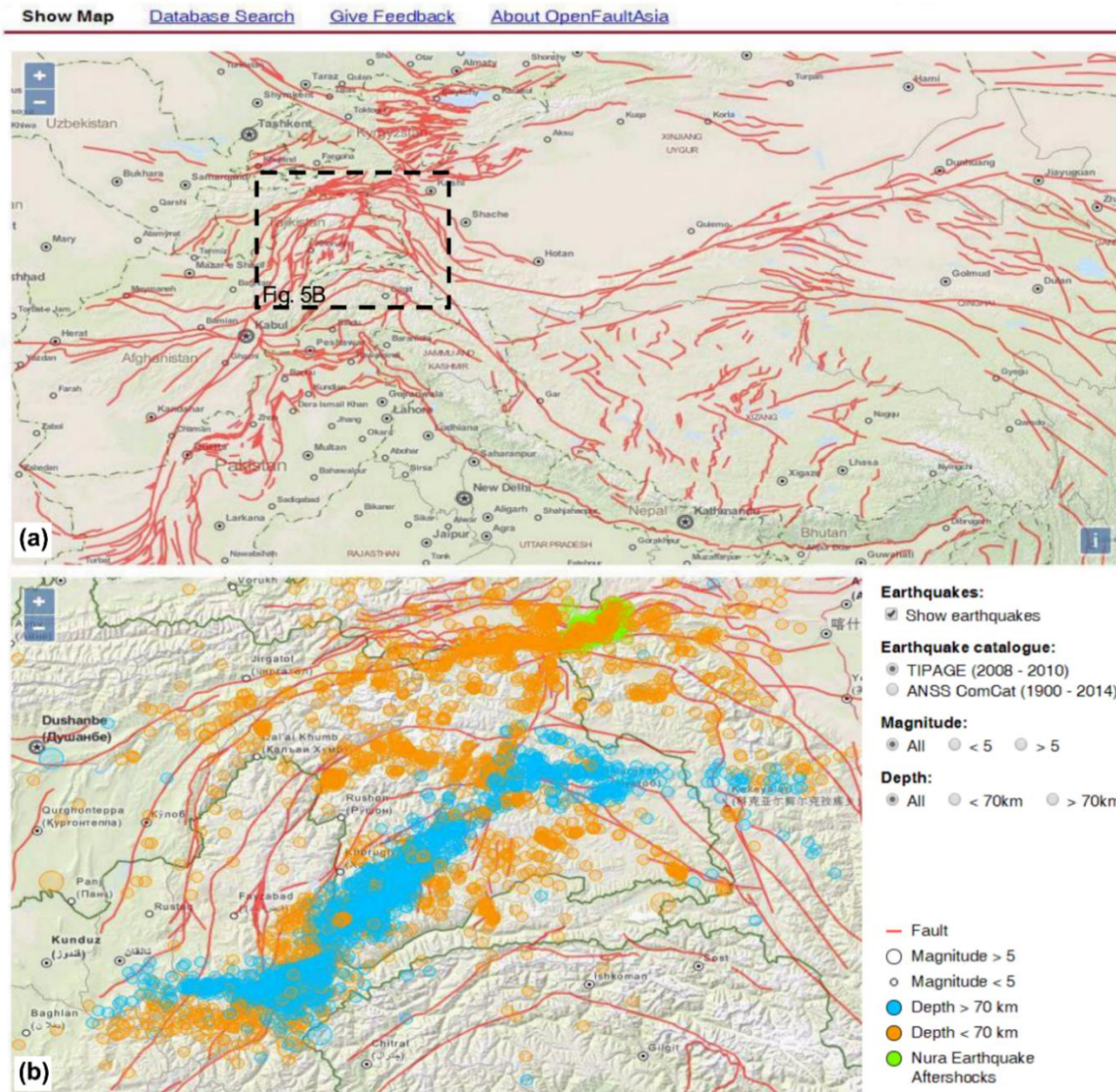


Figure 5. The database interface includes an interactive fault map with faults shown in red (a). Example of a map display with earthquake data set from Sippl et al. (2013) is shown for the Pamir and the Hindu Kush regions (b). Black dashed box in (a) shows the map extent displayed in (b).

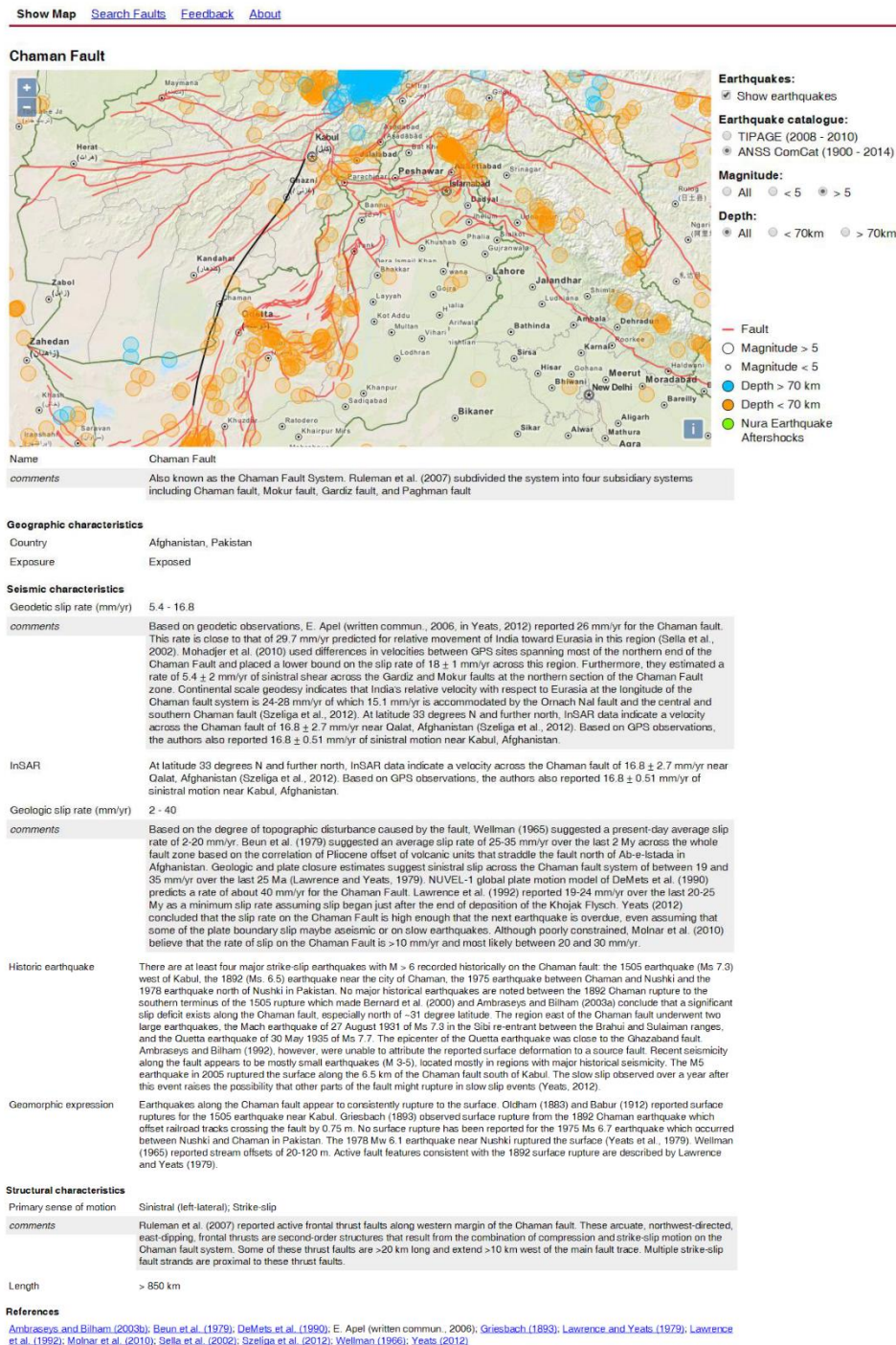


Figure 6. An example of a fault information page. The location map on top shows the selected fault in black (i.e., Chaman Fault). The fault description appears below the map. The description is organized into three distinct sections (i.e., geographic, seismic, and structural characteristics) with references linked to Google Scholar. Users can display earthquake data to visualize recorded seismicity in relation to the selected structure.

[Show Map](#) [Search Faults](#) [Feedback](#) [About](#)

Fill in one or more fields and start search. The search tool permits searches on fault name and location. Users can also limit their search results by making queries on seismic and structural characteristics of faults.

Fault Name

Geographic Characteristics

Country

Physiographic province

Seismic Characteristics

Geodetic Slip Rate (mm/yr) min: max:

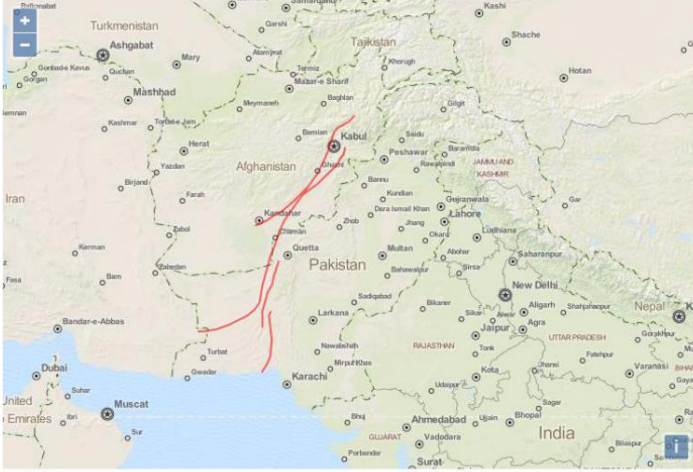
Quaternary Slip Rate (mm/yr) min: max:

Historical Earthquakes

Geomorphic expressions

Structural Characteristics

Sense of movement



Bella-Chaman-Kurram Fault Zone
Chaman Fault
Gardiz Fault
Ghazaband Fault
Mokur Fault
Ornach-Nai Fault
Paghman Fault
Panjshir Fault
Siahhan Fault

Figure 7. The database search tool allows users to search and sort fault information on a variety of fields. The above example shows search results for the Chaman Fault. The search yields results relevant to the Chaman fault including faults that are considered to be part of its extensions. These results are shown as a list and can be visualized on the map. Fault names and locations are linked to relevant fault information page.

tion and attribute data were then extracted from these tables for display in an open source web-mapping application called OpenLayers (<http://openlayers.org/>). To display earthquake data, a table was created in the database to store location coordinates, depth, magnitude, and source values. These data were similarly extracted from the database for display in OpenLayers. The reference table was created and displayed similarly, containing fields such as fault identification number, citation appearance, and manuscript title. This table was used to generate an automated query in Google Scholar by clicking on a citation listed for a fault. All raw data in the CAFD are accessible for viewing and download via <http://www.geo.uni-tuebingen.de/faults/> and the supplementary information accompanying this article. Users who download the data are encouraged to regularly check for new entries or subscribe to the email list server for this database.

4 User interface

The CAFD online interface includes an interactive fault map and a search tool. The fault map displays the locations of Quaternary faults (Fig. 5a) and includes a user-controlled earthquake data layer (Fig. 5b) that organizes data by magnitude, depth, and source. Clicking on a fault trace brings up an information page (Fig. 6) that is linked to the fault attribute and reference tables in the database, displaying relevant information organized by database fields (Table 3). The information page also contains a location map that highlights the fault location.

The search tool (Fig. 7) allows users to query the database using specific fields. Table 2 shows fields that are queryable. The queries can be simple (e.g., fault name or country location) or more complex (e.g., sorted by slip rate, sense of motion, earthquake history, etc.). A query can generate results (i.e., fault names shown in a list and on a map) that are linked to fault information and location pages described above.

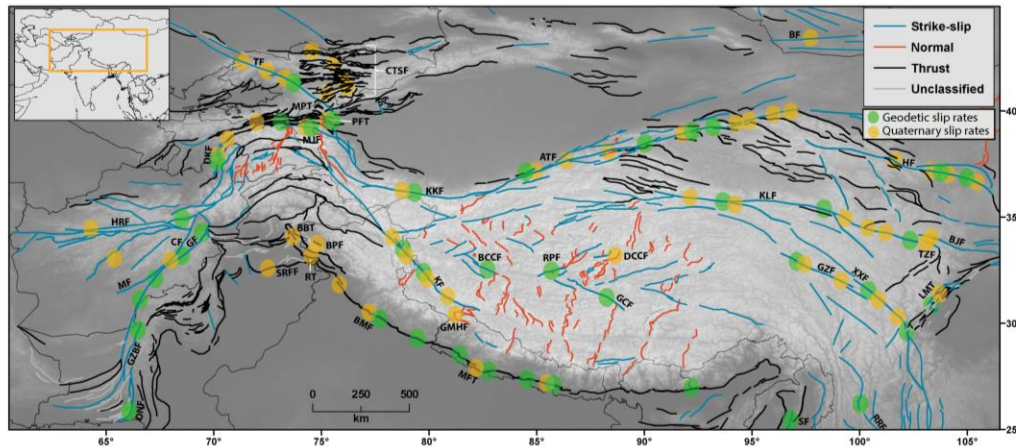


Figure 8. Map showing the locations of major Quaternary faults. Fault lines are color-coded based on their sense of movement. Locations of reported slip rates are marked with colored circles. Abbreviations of fault names: ATF: Altyn Tagh fault; BBT: Balakot-Bagh Thrust; BCCF: Bue Co Conjugate Fault system; BF: Bogd Fault; BPF: Balapora Fault; BJF: Bailong Jiang Fault system; BMF: Black Mango Fault; CF: Chaman Fault; CTSF: central Tien Shan faults (including Issyk-Ata, Akchop Hills, South Kochkor, Kadjerty, central Naryn, Oinak-Djar, North and South Kyrkungey faults); DCCF: Dong Co Conjugate Fault system; DKF: Darvaz-Karakul Fault; GCF: Gyaring Co Fault; GF: Gardiz Fault; GMHF: Gurla Mandhata-Humla Fault system; GZBF: Ghazaband Fault; GZF: Ganzi Fault; HF: Haiyuan Fault; HRF: Herat Fault; KF: Karakorum Fault; KKF: Karakax Fault; KLF: Kunlun Fault; LMT: Longmen Shan Thrust belt; MF: Mokur Fault; MFT: Main Frontal Thrust; MJF: Muji Fault; MPT: Pamir Main Thrust; ONF: Ornach-Nal Fault; PFT: Pamir Frontal Thrust; RPF: Riganpei Co Fault; RRF: Red River Fault; RT: Riassi Thrust; SF: Sagaing Fault; SRFF: Salt Range Front Fault; TF: Talas-Fergana Fault; TZF: Tazang Fault; XXF: Xianshuihe-Xiaojiang Fault system. The coordinate system for the map is Geographic (WGS84), with topography from ASTER GDEM 2.

5 Database completeness

The main objective of the CAFD is to provide a publicly accessible central source of information related to Quaternary faults in central Asia and to set a framework for future data additions and research. Similar to the HimaTibetMap of Taylor and Yin (2009), the data in the CAFD are drawn from published manuscripts that are based on limited studies, and require continual evaluation as newer data become available. For example, a large number of faults lack geodetic or Quaternary slip rates, and most faults contain no paleoseismic information.

Although the database has implications for seismic hazard studies in central Asia, it is impractical to construct a hazard map based solely on the information provided here. The database contains Quaternary faults with surface traces, providing only a two-dimensional representation of faults and potentially leaving out active nonplanar faults and those that are concealed beneath the Earth's surface. The accuracy of fault position data for faults with surface traces also depends on mapping methods and scales of observations, which vary significantly between individual studies. Similarly, the accuracy of fault attributes can vary between individual studies. For example, fault slip rate measurements are based on estimates of displacements along faults and age measurements of offset landforms, both of which contain uncertainties that

are obtained and reported differently across referenced studies. Database users, therefore, are encouraged to refer to comments fields in the database for more information about reported values, and to references cited for original work. These limitations combined with short seismological records and insufficient information about earthquake shaking intensities are a great challenge to mapping hazards in the region. A more complete hazard assessment process should consider long-term earthquake history of faults (available from paleoseismic data), GPS velocity data showing present-day strain accumulation across active structures, and more accurate mapping of Quaternary faults, especially those with no clear surface expression (e.g., blind faults).

5.1 Data gaps

At its current stage, the database guides future research by identifying areas where further investigations are needed. Figure 8 shows the locations of Quaternary faults as documented in the database, color-coded based on their sense of motion. Although the sense of motion for most active structures is well-characterized, slip rates for most remain unknown. Slip rates are reported for a total of 64 faults in the current version of the CAFD. This includes 26 geodetic and 38 Quaternary rates. Only 18 faults, however, have both types of slip rates. These faults are often > 1000 km long and bound

major topographic features (e.g., the \approx 1200 km-long Altyn-Tagh Fault at the northern margin of the Tibetan Plateau, the $>$ 1500 km-long Main Frontal Thrust system along the Himalaya, and the \approx 1000 km-long Chaman Fault system that bounds the western edge of the Indian Plate). Some faults such as the Altyn Tagh, Kunlun, and Karakoram faults have Quaternary slip rates that are constrained by several studies in different localities along the fault trace. Other fault zones such as those in northwest Tibet and the central Pamir, require further investigation. Quaternary slip rates in this region are often qualitative, associated with large uncertainty (e.g., the Darvaz-Karakul Fault) or disagree with GPS measurements (e.g., the Talas Fergana and Karakorum faults).

The northern and western margins of the Pamir have geodetic relative velocities of 13–15 and 10 mm yr⁻¹ respectively. Quaternary slip rates for these areas are only available for the central segment of the Pamir thrust system. Therefore, where and how these motions are accommodated remains poorly understood. Unlike central Tibet where Quaternary and geodetic slip rates are known for several fault systems (e.g., Bue Co and Dong Co conjugate fault systems), the faults located in the interior of the Pamir lack Quaternary rates despite accommodating 5–10 mm yr⁻¹ of east–west extension measured by GPS geodesy (Ischuk et al., 2013).

Further south, few geologic and geodetic constraints exist on slip rates for faults in Afghanistan and the Baluchistan province of Pakistan. The only available geodetic rates are for the Chaman Fault system and its northern (e.g., Gardiz and Mokur faults) and southern (e.g., Ornach-Nal and Ghazaband faults) extensions. Despite constraints placed by deformation models on the present-day kinematics of regions south and west of the western Himalayan Syntaxis (e.g., the Sulaiman Lobe and Range), it remains unclear exactly how and where this deformation is accommodated. The database highlights regions and fault systems that have well-constrained slip rate data and those that lack such data, and hence, can guide future research by identifying where data gaps exist.

6 Database maintenance

All domain and web hosting services are provided and maintained by the University of Tübingen, Germany. The content update is a collaborative process which includes content identification, content review, and database update. Content identification is done by a group of experts who are selected and contacted semiannually for published research results. A larger number of potential experts and users are also contacted using selected list servers. Users can submit new content directly via the website email (cafd@geo.uni-tuebingen.de) or by completing the feedback form on the website. Once content is submitted, it is checked for accuracy and consistency by the CAFD review team before being posted on the website.

7 Conclusion

The central Asia fault database contains 1196 fault traces that can be viewed, searched, and downloaded for plotting in ArcGIS and other programs. Fault parameters and descriptions for over 123 Quaternary faults are extracted and documented in the database and can be searched and viewed by users. Over 34 000 earthquakes from global and local catalogs are included in data layers to explore the relationship between seismicity and Quaternary faulting. This database is the first publicly available digital repository for Quaternary faults of central Asia and the surrounding region with search capabilities that allow users sort and view critical fault information on a variety of fields (e.g., geographic, seismic, geomorphic, structural). This information is critical for current and future analysis of earthquake hazard studies in the region. The database is designed to fulfill the needs of a wide range of users ranging from the science community to the general public and non-academic users. The database will be continuously updated as new information becomes available and as users identify data that have been overlooked using a web-based discussion forum or contacting the authors directly.

The Supplement related to this article is available online at doi:10.5194/nhess-16-529-2016-supplement.

Acknowledgements. We thank Steve Thompson, Ray Weldon, Mike Taylor, Richard Styron, Cal Ruleman, Bernd Schurr, and Richard Gloaguen for generously sharing their data. We also thank Peter Molnar, Roger Bilham, Kathy Haller, and Walter Mooney for their helpful discussions. Saeid Mohadjer, Faheem Merchant, Stéphane Henroid, Cassidy Jay, and Najibullah Kakar provided thoughtful feedback on website design, usability and content. Roland Schraven assisted with preparing earthquake and topography data used in this manuscript. In its early stage, this project benefited immensely from fruitful discussions with Michael Märker, Jason Barnes, and Lothar Ratschbacher. James Daniell, Kathy Haller, and Bernd Schurr are thanked for reviewing our paper and their constructive comments. This project was supported by the CAME project bundle TIPTIMON of the German Federal Ministry of Education and Research grant BMBF 03G0809 (to T. A. Ehlers) and the German Science Foundation grant STU 525/1-1 (to K. Stübner).

Edited by: O. Katz

Reviewed by: K. Haller, J. E. Daniell, and B. Schurr

References

- Abdrahmatov, K. Y., Aldazhanov, S. A., Hager, B. H., Hamburger, M. W., Herring, T. A., Kalabaev, K. B., Makarov, V. I., Molnar, P., Panasyuk, S. V., Prilepin, M. T., Reilinger, R. E., Sadybakasov, I. S., Souter, B. J., Trapeznikov, Y. A., Tsurkov, V. Y.,

- and Zubovich, A. V.: Relatively recent construction of the Tien Shan inferred from GPS, *Nature*, 384, 450–453, 1996.
- Advance National Seismic System Comprehensive Catalog (ANSS ComCat): available at <http://earthquake.usgs.gov/earthquakes/search/>, last access: December 2014.
- Avouac, J. P.: Dynamic processes in extensional and compressional settings – Mountain building from earthquakes to geological deformation, in: *Treatise on Geophysics*, edited by: Schubert, G., Elsevier, Amsterdam, 377–439, 2007.
- Bendick, R., Bilham, R., Khan, M. A., and Khan, S. F.: Slip on active wedge thrust from geodetic observations of the 8 October 2005 Kashmir earthquake, *Geology*, 35, 267–270, 2007.
- Bendick, R., Khan, S. F., Burgmann, R., Jouanne, F., Banerjee, P., Khan, M. A., and Bilham, R.: Postseismic relaxation in Kashmir shows lateral variations in crustal architecture and materials, *Geophys. Res. Lett.*, 42, 4375–4383, 2015.
- Chevalier, M. L., Tapponnier, P., Van der Woerd, J., Ryerson, F. J., Finkel, R. C., and Li, H.: Spatially constant slip rate along the southern segment of the Karakorum fault since 200 ka, *Tectonophysics*, 530–531, 152–179, 2012.
- Dawson, T. E. and Weldon II, R. J.: Appendix B: Geologic slip-rate data and geologic deformation model, U.S. Geol. Surv. Open-File Rept. 2013-1165-B, and California Geol. Surv. Special Rept. 228-B, 2013.
- Feld, C., Haberland, C., Schurr, Bernd, Sippl, C., Wetzels, H., Roessner, S., Ickrath, M., Abdybachaev, U., and Orunbaev, S.: Seismotectonic study of the Fergana Region (Southern Kyrgyzstan): distribution and kinematics of local seismicity, *Earth Plan. Space*, 67, 1–13, 2015.
- Field, E. H., Biasi, G. P., Dawson, T. E., Felzer, K. R., Jackson, D. D., Johnson, K. M., Jordan, T. H., Madden, C., Michael, A. J., Milner, K. R., Page, M. T., Parsons, T., Powers, P. M., Shaw, B. E., Thatcher, W. R., Weldon II, R. J., and Zeng, Y.: Uniform California earthquake rupture forecast, version 3 (UCERF3) – The Time-independent model: U.S. Geological Survey Open-File Report 2013-1165, 97 pp., California Geological Survey Special Report 228, and Southern California Earthquake Center Publication 1792, available at: <http://pubs.usgs.gov/of/2013/1165/>, last access: June 2015, 2013.
- Gee, L. S. and Leith, W. S.: The Global Seismographic Network: United States Geological Survey, Fact Sheet 2011-3021, available at <http://pubs.usgs.gov/fs/2011/3021/>, last access: May 2015, 2011.
- Haberland, C., Abdybachaev, U., Schurr, B., Wetzels, H.-U., Roessner, S., Sarnagoev, A., Orunbaev, S., and Janssen, C.: Landslides in southern Kyrgyzstan: understanding tectonic controls, *Eos T. Am. Geophys. Un.*, 92, 169–170, 2011.
- He, W., Xiong, Z., Yuan, D. Y., Ge, W. P., and Liu, X. W.: Paleo-earthquake study on the Maqu fault of East Kunlun Active Fault, *Earthquake Res. China*, 22, 126–133, 2007.
- Hodges, K.: Tectonics of the Himalaya and southern Tibet from two perspectives, *Geol. Soc. Am. Bull.*, 112, 324–350, 2000.
- Husen, S. and Hardebeck, J. L.: Earthquake location accuracy, Community Online Resources for Statistical Seismicity Analysis (CORSSA), version 1, doi:10.5078/corssa-55815573, available at <http://www.corssa.org/articles/themeiv/husenhardebeck>, last access: June 2015, 2010.
- Ioffe, A., Govorova, N., Volchkova, G., and Trifonov, R.: Database of active faults for the USSR area, *Geoinformatics*, 4, 289–290, 1993.
- Ioffe, A. I. and Kozhurin, A. I.: Database of active faults of Eurasia, *J. Earthquake Pred. Res.*, 5, 431–435, 1996.
- Ischuk, A., Bendick, R., Rybin, R., Molnar, P., Khan, S. F., Kuzikov, S., Mohadjer, S., Saydullaev, U., Ilyasova, Z., Schelochkov, G., and Zubovich, A. V.: Kinematics of the Pamir and Hindu Kush regions from GPS geodesy, *J. Geophys. Res.-Sol. Ea.*, 118, 1–9, 2013.
- Kaneda, H., Nakata, T., Tsutsumi, H., Kondo, H., Sugito, N., Awata, Y., Akhtar, S. S., Majid, A., Khattak, W., Awan, A. A., Yeats, R. S., Hussain, A., Ashraf, M., Wesnousky, S. G., and Kausar, A. B.: Surface Rupture of the 2005 Kashmir, Pakistan, Earthquake and Its Active Tectonic Implications, *B. Seismol. Soc. Am.*, 98, 521–557, doi:10.1785/0120070073, 2008.
- Korjenkov, A. M., Rust, D., Tibaldi, A., and Abdieva, S. V.: Parameters of the Strong Paleoearthquakes Along the Talas-Fergana Fault, the Kyrgyz Tien Shan, *Earthquake Research and Analysis – Seismology, Seismotectonic and Earthquake Geology*, edited by: D'Amico, S., InTech, Croatia, 2012.
- Kumar, S., Wesnousky, S. G., Rockwell, T. K., Ragona, D., Thakur, V. C., and Seitz, G. G.: Earthquake recurrence and rupture dynamics of Himalayan Frontal Thrust, India, *Science*, 294, 2328–2332, 2001.
- Kumar, S., Wesnousky, S. G., Rockwell, T. K., Briggs, R. W., Thakur, V. C., and Jayangondaperumal, R.: Paleoseismic evidence of great surface rupture earthquakes along the Indian Himalaya, *J. Geophys. Res.-Sol. Ea.*, 111, B03304, doi:10.1029/2004JB003309, 2006.
- Lavé, J., Yule, D., Sapkota, S., Basant, K., Madden, C., Attal, M., and Pandey, R.: Evidence for a Great Medieval Earthquake (□ 1100 A.D.) in the Central Himalayas, Nepal, *Science*, 307, 1302–1305, doi:10.1126/science.1104804, 2005.
- Lomax, A., Virieux, J., Volant, P., and Berge, C.: Probabilistic earthquake location in 3D and layered models: Introduction of a Metropolis-Gibbs method and comparison with linear locations, in: *Advances in Seismic Event Location*, edited by: Thurber, C. and Rabinowitz, N., Kluwer, Amsterdam, 101–134, 2000.
- Mechie, J., Yuan, X., Schurr, B., Schneider, F., Sippl, C., Ratschbacher, L., Minaev, V., Gadoev, M., Oimahmadov, I., Abdybachaev, U., Moldobekov, B., Orunbaev, S., and Negmatullaev, S.: Crustal and uppermost mantle velocity structure along a profile across the Pamir and southern Tien Shan as derived from project TIPAGE wide-angle seismic data, *Geophys. J. Int.*, 188, 385–407, 2012.
- Mellors, R. J., Pavlis, G. L., Hamburger, M. W., Al-shukri, H. J., and Lukk, A. A.: Evidence for a high velocity slab associated with the Hindu Kush seismic zone, *J. Geophys. Res.-Sol. Ea.*, 100, 4067–4078, 1995.
- Mohadjer, S., Bendick, R., Ischuk, A., Kuzikov, S., Kostuk, A., Saydullaev, U., Lodi, S., Kakar, D. M., Wasy, A., Khan, M. A., Molnar, P., Bilham, R., and Zubovich, A. V.: Partitioning of India-Eurasia convergence in the Pamir-Hindu Kush from GPS measurements, *Geophys. Res. Lett.*, 37, L04305, doi:10.1029/2009GL041737, 2010.
- Plesch, A., Shaw, J. H., Benson, C., Bryant, W. A., Carena, S., Cooke, M., Dolan, J., Fuis, G., Gath, E., Grant, L., Hauksson, E., Jordan, T., Kamberling, M., Legg, M., Lindvall, S., Magis-

- trale, H., Nicholson, C., Niemi, N., Oskin, M., Perry, S., Planansky, G., Rockwell, T., Shearer, P., Sorlien, C., Süß, M. P., Suppe, J., Treiman, J., and Yeats, R.: Community Fault Model (CFM) for Southern California, *B. Seismol. Soc. Am.*, 97, 1793–1802, 2007.
- Raiverman, V., Srivastava, A. K., and Prasad, D. N.: On the Foothill Thrust of northwestern Himalaya, *J. Himal. Geol.*, 4, 237–256, 1993.
- Ran, Y., Chen, L., Chen, J., Wang, H., Chen, G., Yin, J., Shi, X., Li, C., and Xu, X.: Paleoseismic evidence and repeat time of large earthquakes at three sites along the Longmenshan fault zone, *Tectonophysics*, 491, 141–153, 2010.
- Reigber, C., Michel, G. W., Galas, R., Angermann, D., Klotz, J., Chen, J. Y., Papschev, A., Arslanov, R., Tzurkov, V. E., and Ischanov, M. C.: New space geodetic constraints on the distribution of deformation in Central Asia, *Earth Planet. Sci. Lett.*, 191, 157–165, 2001.
- Robinson, A. C.: Geologic offsets across the northern Karakorum fault: Implications for its role and terrane correlations in the western Himalayan-Tibetan orogen, *Earth Planet. Sci. Lett.*, 279, 123–130, 2009.
- Ruleman, C. A., Crone, A. J., Machette, M. N., Haller, K. M., and Rukstales, K. S.: Map and Database of Probable and Possible Quaternary Faults in Afghanistan, United States Geological Survey Open-File Report, 2007-1103, available at: <http://pubs.usgs.gov/of/2007/1103/> (last access: July 2015), 2007.
- Schiffman, C., Bali, B. S., Szeliga, W., and Bilham, R.: Seismic slip deficit in the Kashmir Himalaya from GPS observations, *Geophys. Res. Lett.*, 40, 5642–5645, 2013.
- Schneider, F. M., Yuan, X., Schurr, B., Mechie, J., Sippl, C., Haberland, C., Minaev, V., Oimahmadov, I., Gadoev, M., Radjabov, N., Abdybachaev, U., Orunbaev, S., and Negmatullaev, S.: Seismic imaging of subducting continental lower crust beneath the Pamir, *Earth Planet. Sci. Lett.*, 375, 101–112, 2013.
- Schurr, B., Ratschbacher, L., Sippl, C., Gloaguen, R., Yuan, X., and Mechie, J.: Seismotectonics of the Pamir, *Tectonics*, 33, 1501–1518, 2014.
- Sippl, C., Schurr, B., Yuan, X., Mechie, J., Schneider, F. M., Gadoev, M., Orunbaev, S., Oimahmadov, I., Haberland, C., Abdybachaev, U., Minaev, V., Negmatullaev, S., and Radjabov, N.: Geometry of the Pamir-Hindu Kush intermediate-depth earthquake zone from local seismic data, *J. Geophys. Res.-Sol. Ea.*, 118, 1438–1457, 2013.
- Strecker, M. R., Hilley, G. E., Arrowsmith, J. R., and Coutand, I.: Differential structural and geomorphic mountain-front evolution in an active continental collision zone: the northwest Pamir, southern Kyrgyzstan, *Geol. Soc. Am. Bull.*, 115, 166–181, 2003.
- Styron, R., Taylor, M., and Okoronkwo, K.: Database of Active Structures From the Indo-Asian Collision, *Eos T. Am. Geophys. Un.*, 91, 181–182, 2010.
- Tapponnier, P., Ryerson, F. J., Van der Woerda, J., Mériaux, A. S., and Lasserre, C.: Long-term slip rates and characteristic slip: keys to active fault behavior and earthquake hazard, *Earth Planet. Sci. Lett.*, 333, 483–494, 2001.
- Taylor, M. and Yin, A.: Active structures of the Himalayan-Tibetan orogen and their relationships to earthquake distribution, contemporary strain field, and Cenozoic volcanism, *Geosphere*, 5, 199–214, 2009.
- Taylor, M., Yin, A., Ryerson, F., Kapp, P., and Ding, L.: Conjugate strike slip fault accommodates coeval north-south shortening and east-west extension along the Bangong-Nujiang suture zone in central Tibet, *Tectonics*, 22, 1044, doi:10.1029/2002TC001361, 2003.
- Thiede, R. C. and Ehlers, T. A.: Large spatial and temporal variations in Himalayan denudation, *Earth Planet. Sci. Lett.*, 371–372, 278–293, 2013.
- Trifonov, V. G.: Using active faults for estimating seismic hazard, *J. Earthquake Pred. Res.*, 8, 170–182, 2000.
- Trifonov, V. G. and Kozhurin, A. I.: Study of active faults: theoretical and applied implications, *Geotectonics*, 44, 510–528, 2010.
- United States Geological Survey (USGS): Largest and Deadliest Earthquakes by Year: 1990–2014, available at: <http://earthquake.usgs.gov/earthquakes/eqarchives/year/byyear.php> (last access: 24 July 2015), 2014.
- Washburn, Z., Arrowsmith, J. R., Forman, S., Cowgill, E., Wang, X. F., Zhang, Y., and Zhengle, C.: Late Holocene earthquake history of the Central Altyn Tagh Fault, China, *Geology*, 29, 1051–1054, 2001.
- Washburn, Z., Arrowsmith, J. R., Dupont-Nivet, G., Feng, W. X., Qiao, Z. Y., and Zhengle, C.: Paleoseismology of the Xorxol Segment of the Central Altyn Tagh Fault, Xinjiang, China, *Ann. Geophys.-Italy*, 46, 1015–1034, 2003.
- Wesnousky, S. G., Kumar, S., Mohindra, R., and Thakur, V. C.: Uplift and convergence along the Himalayan Frontal Thrust of India, *Tectonics*, 18, 967–976, 1999.
- Wills, C. J., Weldon II, R. J., and Bryant, W. A.: California fault parameters for the National Seismic Hazard Maps and Working Group on California Earthquake Probabilities, Appendix A in The Uniform California Earthquake Rupture Forecast, version 2 (UCERF 2): U.S. Geological Survey Open-File Report 2007-1437A, and California Geological Survey Special Report 203A, 48, available at: <http://pubs.usgs.gov/of/2007/1437/a/> (last access: June 2015), 2008.
- Zachariassen, J. and Prentice, C. S.: Detail mapping of the northern San Andreas Fault using LiDAR imagery, United States Geological Survey Final Technical Report 05HQGR0069, 1–47, available at <http://earthquake.usgs.gov/research/external/reports/05HQGR0069.pdf> (last access: July 2015), 2008.
- Zubovich, A. V., Wang, X., Scherba, Y. G., Schelochkov, G. G., Reilinger, R., Reigber, C., Mosienko, O. I., Molnar, P., Michajljow, W., Makarov, V. I., Li, J., Kuzikov, S. I., Herring, T. A., Hamburger, M. W., Hager, B. H., Dang, Y., Bragin, V. D., and Beisenbaev, R. T.: GPS velocity field for the Tien Shan and surrounding regions, *Tectonics*, 29, TC6014, doi:10.1029/2010TC002772, 2010.

4.1.3 Supplements for “A Quaternary fault database for Central Asia”

Electronic supplement to:

A Quaternary fault database for Central Asia by Mohadjer et al. (2016)

Central Asia Fault Database GIS Files

The attribute table in the ArcGIS file includes the following information:

- FID (Field ID)
- Shape (Polyline)
- X and Y coordinates of line centroid
- Shape_Length (length for line features)
- Name (fault name)
- Fault ID (unique fault identification number)
- Type (sense of movement for fault, if known)
- Source (references for line features)
- Remarks (e.g., variations in the fault name or location)

A unique identification number (Fault ID) is assigned to each fault trace in order to link the attribute table in ArcGIS to the fault location and attribute tables in the MySQL database. Some fields (e.g., Field ID, Shape, X and Y coordinates, and shape length) are automatically added, populated and maintained by ArcGIS. Faults with no assigned names are labeled “Unnamed Fault” in the Name field. Faults with unknown sense of movement are labeled “Unclassified” in the Type field. The Source field includes references to studies that define the location of each fault trace. The Remark field includes information on variations in the fault name or location.

The ArcGIS files were updated on January 26, 2016 and are updated periodically with no set update time. Users are encouraged to regularly check the website (<http://www.geo.unituebingen.de/faults/>) for the most updated version of the files.

4.2 Exploring the relationship between Quaternary and GPS fault slip rates

4.2.1 Author contributions

The following section of the dissertation has been published and is available online: <https://doi.org/10.1016/j.earscirev.2017.09.005>. The full citation is:

Mohadjer, S., Ehlers, T.A., Bendick, R. and Mutz, S.G., 2017. Review of GPS and Quaternary fault slip rates in the Himalaya-Tibet orogen. *Earth-Science Reviews*, 174, pp.39-52.

The original manuscript is provided in section 4.2.2 and the original electronic supplement file is provided in section 4.2.3.

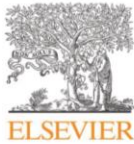
Four authors contributed to the work presented in this paper: Solmaz Mohadjer (SM), Todd A. Ehlers (TAE), Rebecca Bendick (RB), Sebastian G. Mutz (SGM). A summary of the respective contributions is provided in Table 4.2. The detailed contributions are as follow: SM, RB and TAE developed the idea of investigating the overall relationship between Quaternary and GPS slip rates and evaluating the sensitivity of this relationship to different factors. SM compiled and evaluated the slip rate dataset (Table 1 in section 4.2.2). Statistical analysis of the dataset was performed by SGM and SM with input from TAE. All authors took part in the interpretation of results. SM drafted the first version of the manuscript along with all Figures and tables (except Figures 4-5 which were made by SGM and modified by SM). The manuscript was further reviewed and edited by TAE, RB, and SGM, and one external reviewer during the peer review process.

Table 4.2: Summary of contributions to joint work for the paper “Review of GPS and Quaternary fault slip rates in the Himalaya-Tibet orogen”, indicating the average fraction of work of the respective author in percentage.

| Author | Position | Scientific Ideas (in %) | Data generation (in %) | Analysis and Interpretation (in %) | Paper writing (in %) |
|--------|----------|-------------------------|------------------------|------------------------------------|----------------------|
| SM | [1] | 60 | 100 | 30 | 70 |
| TAE | [2] | 30 | 0 | 10 | 15 |
| RB | [3] | 10 | 0 | 10 | 10 |
| SGM | [4] | 0 | 0 | 50 | 5 |

4.2.2 Paper: “Review of GPS and Quaternary fault slip rates in the Himalaya-Tibet orogen, Earth-Science Reviews”

Earth-Science Reviews 174 (2017) 39–52



Contents lists available at ScienceDirect

Earth-Science Reviews

journal homepage: www.elsevier.com/locate/earsci



Review of GPS and Quaternary fault slip rates in the Himalaya-Tibet orogen



Solmaz Mohadjer^{a,*}, Todd A. Ehlers^a, Rebecca Bendick^b, Sebastian G. Mutz^a

^a Department of Geosciences, University of Tübingen, Wilhelmstrasse 56, 72074 Tübingen, Germany

^b Department of Geosciences, University of Montana, 32 Campus Drive, Missoula, MT 59812, USA

ARTICLE INFO

Keywords:
GPS
Quaternary slip rate
Active faulting
India-Asia collision
Central Asia
Geochronology

ABSTRACT

Previous studies related to the active deformation within the India-Asia collision zone have relied on slip rate data from major faults to test kinematic models for the region. However, estimated geodetic and Quaternary slip rates demonstrate large variability for many of the major faults in the region (e.g., Altyn Tagh and Karakorum faults). As a result, several studies have challenged the assumption that geodetic slip rates are representative of Quaternary slip rates. In this review, slip rate data from the Quaternary fault database for Central Asia are used to determine the overall relationship between Quaternary and Global Positioning System (GPS) slip rates for 19 faults. A least squares and Pearson correlation analysis are applied to investigate this relationship. To evaluate the sensitivity of the slip rate relationship to the presence/absence of individual faults and different Quaternary dating methods, the slip rates were systematically re-sampled. To account for the range of published uncertainties for slip rates, the Monte Carlo method was applied. Regression through 57 Quaternary/GPS slip rate pairs yields an r^2 value of 0.71. Results from the re-sampling analysis show that the inclusion or exclusion of slip rate data from specific faults (e.g., the Ganzi fault, Karakorum fault, Himalayan Main Frontal thrust and Main Pamir thrust) have the highest influence on the strength of the correlation (changing the Pearson correlation coefficient by + 0.08, + 0.05, – 0.06, and + 0.06, respectively). Furthermore, there appears to be a systematic bias in the agreement between rates such that Quaternary rates tend to be higher than GPS rates. This bias is likely due to assumptions embedded in the geomorphic reconstructions of off set landforms used for estimating Quaternary slip rates in the dataset. Taken together, these results suggest that GPS slip rates are more likely to represent Quaternary slip rates when strict fault selection and geomorphic dating criteria are applied. Cases of inconsistencies in slip rates over different time scales may point to differences in the sensitivity of various fault slip measurement methods more often than secular rate changes.

1. Introduction

Mountain building and continental deformation are commonly studied using observations that span timescales ranging from 10^{-9} to 10^7 yr using techniques such as geodesy, geo- and thermo-chronology, and tectonic geomorphology. These timescales investigate mountain building processes that range from co-seismic and interseismic displacement on faults to the millions of years over which topography is produced (e.g., Glotzbach, 2015; Hetland et al., 2012; Stock et al., 2009; Thiede and Ehlers, 2013). Comparison of deformation rates between different techniques is appealing because of the potential to understand transients in, and pertinent timescales of, mountain building and erosional processes.

Within the India-Asia collision zone (Fig. 1), slip rates on active faults derived from geodetic methods are not always in agreement with those derived from geologic methods. Contrasting rates have been

reported for several large (> 1000 km long) faults in the region. For example, InSAR observations provide a slip rate of 1 ± 3 mm/yr for the Karakorum fault (Wright et al., 2004) while GPS studies yield rates ranging from 3 to 5 mm/yr (Chen et al., 2004; Jade et al., 2004; Kundu et al., 2014) to 11 mm/yr (Banerjee and Bürgmann, 2002). However, slip rates estimated by geologic methods range from > 2 mm/yr (Brown et al., 2002; Bohon, 2014; Chevalier et al., 2015) to > 7 mm/yr (Chevalier et al., 2005, 2012). Similar scatter in rates exists for faults in the Pamir and the Tien Shan (e.g., Pamir Main thrust and Talas-Fergana fault, respectively) and those located at the western boundary of India-Asia plates (e.g., Chaman fault system). Differences in estimated rates have been previously attributed to secular rate changes (e.g., Bennett et al., 2004; Chevalier et al., 2005; Oskin et al., 2008), differences in measurement sensitivity between methods (e.g., Brown et al., 2002, 2005; Cowgill, 2007), or even methodological oversights. Despite many individual studies that compare slip rates for individual faults, there

* Corresponding author.

E-mail addresses: solmaz.mohadjer@uni-tuebingen.de (S. Mohadjer), todd.ehlers@uni-tuebingen.de (T.A. Ehlers), bendick@mso.umt.edu (R. Bendick), sebastian.mutz@uni-tuebingen.de (S.G. Mutz).

<http://dx.doi.org/10.1016/j.earsci.2017.09.005>

Received 10 November 2016; Received in revised form 5 September 2017; Accepted 7 September 2017

Available online 09 September 2017

0012-8252/ © 2017 Elsevier B.V. All rights reserved.

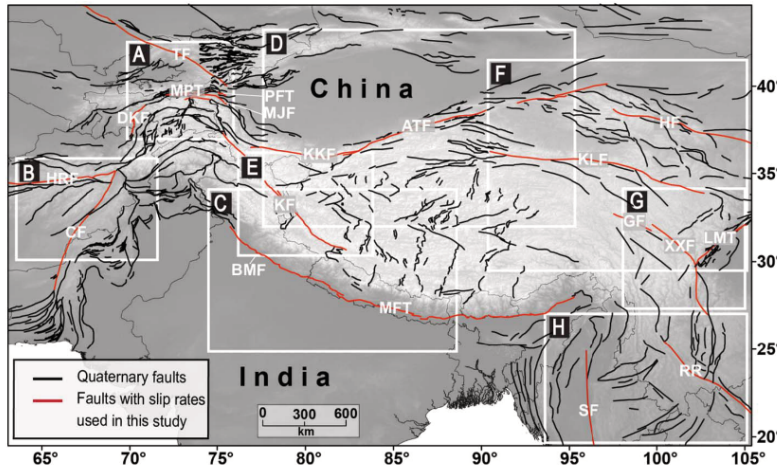


Fig. 1. Location of the study area. Black lines are Quaternary faults. Lines colored in red are faults with slip rates used in this study. The white boxes indicate outlines of detailed maps shown in Fig. 2. Abbreviations of fault names: ATF: Altyn Tagh fault, BMF: Black Mango fault, CF: Chaman fault, DKF: Darvaz-Karakul fault, GF: Ganzhi fault, HRF: Herat fault, HF: Haiyuan fault, KF: Karakorum fault, KKF: Karakax fault, KLF: Kunlun fault, LMT: Longmen Shan thrust, MFT: Main Frontal thrust, MJF: Muji fault, MPT: Main Pamir thrust, PFT: Pamir Frontal thrust, RR: Red River fault, SF: Sagaing fault, XXF: Xianshuihe-Xiaojiang fault. (For interpretation of the references to color in this figure legend, the reader is referred to the web version of this article.) (Modified from Taylor and Yin (2009) and, Styron et al. (2010).)

have been few attempts (e.g., Oskin et al., 2008; Thatcher, 2009; Tong et al., 2014) at comparing these rates systematically over large spatial scales. In this review study, we compile and use fault slip rate data to investigate whether deformation rates determined from GPS (corrected for seismic cycle variations) and geologic techniques provide consistent slip rate information at the orogen scale. Our emphasis is on the India-Asia collision zone where abundant previous data are available for continental deformation over the last ~ 2 Myr.

Previous studies that compare GPS and geologic rates for faults in the India-Asia collision zone rely on data from a small number of faults, often focusing on individual faults or fault systems. In the global comparison of slip rates of Thatcher (2009), only five of the 40 slip rate pairs belong to the India-Asia collision zone. These pairs represent four faults, and are among the largest mismatches observed globally for slip rate estimates. Studies that compare rates regionally are few in number (e.g., Taylor and Yin, 2009) and often use slip rate data limited to large strike-slip faults (e.g., Molnar and Dayem, 2010) or are limited by specific criteria for slip rate pair selection (e.g., Cowgill, 2007).

This review complements previous work by comparing GPS and geologic slip rates for 19 Quaternary faults in the India-Asia collision zone. The dataset includes 57 geologic/GPS rate pairs that come from over 63 published studies. The faults represented by these rates include the major faults (> 1000 km in length) of the Tibetan Plateau (e.g., Altyn Tagh, Kunlun, Haiyuan and Karakorum faults), the active deforming terrain of Pakistan and Afghanistan (e.g., Chaman fault), and the Pamir and Tien Shan regions (e.g., Pamir Main thrust, Darvaz-Karakul and Talas-Fergana faults). An objective of this work is to determine the overall relationship between Quaternary and GPS slip rates within the Indian-Asian collision. We use a linear regression, Pearson correlation coefficient (PCC), and systematic re-sampling with Monte Carlo analysis for propagation of slip rate uncertainties to examine the sensitivity of this relationship to different attributes such as the importance of individual faults used in the regression and biases in different techniques used for estimating Quaternary rates.

2. Methods

In this study, 57 Quaternary/GPS slip rate pairs, representing 19 faults, are selected for comparison (Figs. 1 and 2, and Table 1). Both slip rates and associated uncertainties are reported from the original publications. Since slip rates are often reported in a variety of ways (e.g., horizontal, vertical, or dip-slip), values used in this study are reported as slip rates in the original study and often reflect the predominant sense of slip for faults. These rates and other information such as

reported uncertainties, measurement methods, location coordinates, and references to original studies are shown in Table 1. To reduce spatial and temporal discrepancies between the GPS and Quaternary rates, we based our selection and pairing of the GPS and Quaternary rates on a set of criteria explained below.

2.1. Slip rate selection and pairing

Some discrepancies between GPS and Quaternary rates can be attributed to differences in the location of the two measurements. Given this, the rates from GPS and geologic methods that are measured approximately along the same section of the fault are paired together (see Fig. 2). For example, the GPS slip rate of 9 ± 5 mm/yr measured at 89–91°E along the Altyn Tagh fault (Bendick et al., 2000) is paired with the nearest Quaternary slip rate of 11.55 ± 3.04 mm/yr measured at 88.5°E (Cowgill et al., 2009) and of 13.9 ± 1.1 mm/yr measured at 90.6°E (Mériaux et al., 2012). Quaternary rates from Gold et al. (2011, 2017) are not considered because they are from sites located outside the longitude measurement range of the GPS rate (89–91°E). Similarly, the GPS slip rate of 4.3 ± 1.5 mm/yr (Li et al., 2009) is paired with the closest Quaternary rates of 4.5 ± 0.7 and 5 ± 2.5 from Li et al. (2009). Quaternary rates from other studies (e.g., Lasserre et al., 1999, 2002) are not considered because they are measured along different fault segments and are 136–300 km away from the nearest GPS rate. The average distance between Quaternary and GPS measurement locations that are paired in this study is approximately 55 km. Only five Quaternary/GPS pairs are located > 100 km from each other. These pairs belong to Altyn Tagh fault (ATF1, ATF4), Chaman fault (CF1, CF2) and Herat fault (HRF) as shown in Fig. 2b and d and Table 1. The locations for both rates are provided from the published study. When location coordinates are unavailable, they were estimated using figures from the published study and Google Earth Pro. If the Quaternary slip rate is calculated based on the sum of more than one measurement from multiple sites (e.g., Pamir Frontal thrust (PFT1) in Table 1), the reported coordinates represent the mean values of the locations. The location coordinates for the GPS slip rates represent either the midpoint between the reported latitude/longitude ranges or the midpoint between the GPS sites used for calculation of slip rates.

Different slip rate measurement methods are sensitive to different timescales. GPS measurements provide estimates of slip rates over years and decades while geologic rates are long-term average rates representing 10^2 to $> 10^3$ yrs. All geologic slip rates used in this study represent displacement of Quaternary-age (< 2.6 Ma) markers, most of which are Holocene in age (0–10 ka). Only one geologic rate

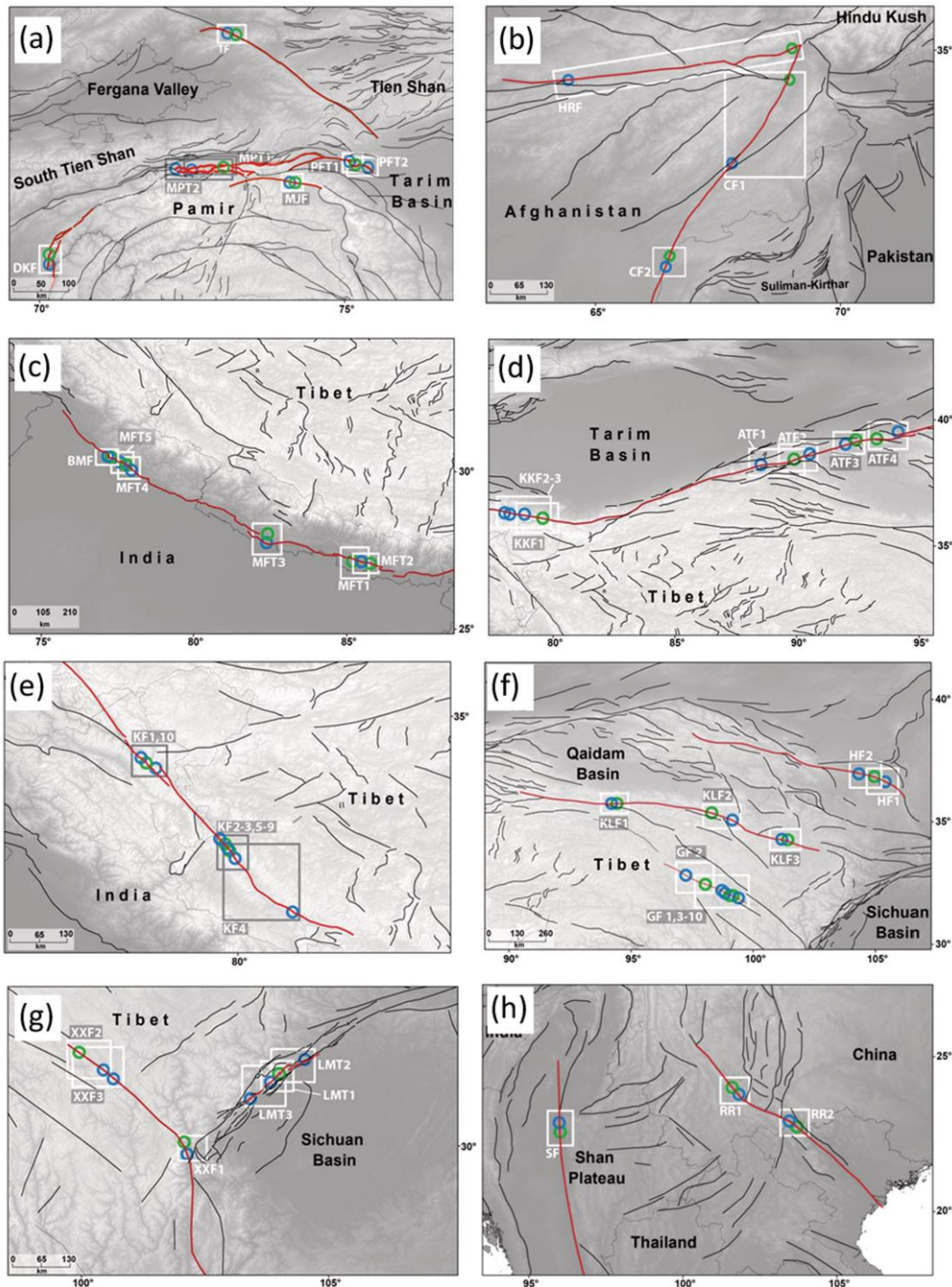


Fig. 2. Slip rate selection and pairing. Locations of slip rates used in this study are marked with open circles and color coded based on slip rate type (blue: Quaternary, green: GPS). Abbreviations of fault names are the same as those in Fig. 1, with numbers added to those with more than one slip rate measurement. Boxes are drawn around slip rates that are paired for analysis in this study. See Table 1 for more information about each measurement. (For interpretation of the references to color in this figure legend, the reader is referred to the web version of this article.)

Table 1

GPS and Quaternary fault slip rates used in this study. Abbreviations for Quaternary dating methods: LUM: luminescence, MST: magnetostratigraphy, OS: optically stimulated luminescence, RLT: relative dating, TL: thermally stimulated luminescence.

| Fault label | Fault name | Quaternary slip (mm/yr) | References for Quaternary rates | GPS slip (mm/yr) | References for GPS rates |
|-------------|----------------------|-------------------------|---|------------------|--|
| ATF(1) | Altyn Tagh | 11.55 ± 3.04 | Cowgill et al. (2009) | 9 ± 5 | Bendick et al. (2000), and Wallace et al. (2004) |
| ATF(2) | Altyn Tagh | 13.9 ± 1.1 | Mériaux et al. (2012) | 9 ± 5 | Bendick et al. (2000), and Wallace et al. (2004) |
| ATF(3) | Altyn Tagh | 15 ± 5 | Washburn et al. (2003) | 9 ± 2 | Chen et al. (2000) |
| ATF(4) | Altyn Tagh | 17.8 ± 3.6 | Mériaux et al. (2005) | 6 ± 2 | Chen et al. (2000) |
| BMF | Black Mango | 9.6 (+ 7.0–3.5) | Kumar et al. (2001) | 18.8 ± 3 | Jade et al. (2004) |
| CF(1) | Chaman | 30 ± 5 | Beun et al. (1979) | 16.8 ± 0.51 | Szeliga et al. (2012) |
| CF(2) | Chaman | 33.3 ± 3.0 | Ul-Hadi et al. (2013) | 8.5 ± 1.8 | Szeliga et al. (2012) |
| DKF | Darvaz-Karakul | 12.5 ± 2.5 | Trifonov (1978, 1983) | 10 ± 1 | Ischuk et al. (2013) |
| GF(1) | Ganzi | 7 ± 1 | Chevalier et al. (in press) | 6.6 ± 1.5 | Wang et al. (2013) |
| GF(2) | Ganzi | 11.3 ± 1.8 | Wen et al. (2003) | 6.6 ± 1.5 | Wang et al. (2013) |
| GF(3) | Ganzi | 7 ± 1 | Chevalier et al. (in press) | 4 ± 4 | Liang et al. (2013), and Chevalier et al. (in press) |
| GF(4) | Ganzi | 7 ± 1 | Chevalier et al. (in press) | 3 ± 2.3 | Zhao et al. (2015), and Chevalier et al. (in press) |
| GF(5) | Ganzi | 12.8 ± 1.7 | Wen et al. (2003) | 4 ± 4 | Liang et al. (2013), and Chevalier et al. (in press) |
| GF(6) | Ganzi | 13.9 ± 1.4 | Wen et al. (2003) | 4 ± 4 | Liang et al. (2013), and Chevalier et al. (in press) |
| GF(7) | Ganzi | 10 ± 0.4 | Shi et al. (2016) | 4 ± 4 | Liang et al. (2013), and Chevalier et al. (in press) |
| GF(8) | Ganzi | 12.8 ± 1.7 | Wen et al. (2003) | 3 ± 2.3 | Zhao et al. (2015), and Chevalier et al. (in press) |
| GF(9) | Ganzi | 13.9 ± 1.4 | Wen et al. (2003) | 3 ± 2.3 | Zhao et al. (2015), and Chevalier et al. (in press) |
| GF(10) | Ganzi | 10 ± 0.4 | Shi et al. (2016) | 3 ± 2.3 | Zhao et al. (2015), and Chevalier et al. (in press) |
| HRF | Herat | 2.5 ± 0.5 | Sborshchikov et al. (1981) | < 2 | Mohadjer et al. (2010) |
| HF(1) | Haiyuan | 4.5 ± 0.7 | Li et al. (2009) | 4.3 ± 1.5 | Li et al. (2009), and Zhang et al. (2004) |
| HF(2) | Haiyuan | 5 ± 2.5 | Li et al. (2009) | 4.3 ± 1.5 | Li et al. (2009), and Zhang et al. (2004) |
| KF(1) | Karakorum | 4 ± 1 | Brown et al. (2002) | 5 ± 2 | Kundu et al. (2014) |
| KF(2) | Karakorum | > 10.7 ± 0.7 | Chevalier et al. (2005) | 11 ± 4 | Banerjee and Bürgmann (2002) |
| KF(3) | Karakorum | > 10.7 ± 0.7 | Chevalier et al. (2005) | 4 ± 1 | Chen et al. (2004) |
| KF(4) | Karakorum | > 7.1 | Chevalier et al. (2012) | 4 ± 1 | Chen et al. (2004) |
| KF(5) | Karakorum | > 1.7–2.2 | Chevalier et al. (2015) | 4 ± 1 | Chen et al. (2004) |
| KF(6) | Karakorum | > 1.7–2.2 | Chevalier et al. (2015) | 11 ± 4 | Banerjee and Bürgmann (2002) |
| KF(7) | Karakorum | > 3 | Chevalier et al. (2015) | 11 ± 4 | Banerjee and Bürgmann (2002) |
| KF(8) | Karakorum | > 3 | Chevalier et al. (2015) | 3.4 ± 5 | Jade et al. (2004) |
| KF(9) | Karakorum | > 1.7–2.2 | Chevalier et al. (2015) | 3.4 ± 5 | Jade et al. (2004) |
| KF(10) | Karakorum | 5.6 (+ 1.7–1.1) | Bohon (2014) | 5 ± 2 | Kundu et al. (2014) |
| KKF(1) | Karakax | 19.9 ± 3 | Peltzer et al. (1989), and Avouac and Tapponnier (1993) | 7 ± 3 | Shen et al. (2001) |
| KKF(2) | Karakax | 6.5 | Li et al. (2012) | 7 ± 3 | Shen et al. (2001) |
| KKF(3) | Karakax | 7.8 ± 1.6 | Gong et al. (2017) | 7 ± 3 | Shen et al. (2001) |
| KLF(1) | Kunlun | 11.4 ± 1.1 | Van Der Woerd et al. (2002) | 10 ± 2 | Kirby et al. (2007) |
| KLF(2) | Kunlun | ~ 10 | Van Der Woerd et al. (2002) | 6 ± 2 | Chen et al. (2000) |
| KLF(3) | Kunlun | 5 ± 1 | Kirby et al. (2007) | < 3–5 | Kirby et al. (2007) |
| LMT(1) | Longmen Shan | 0.07 ± 0.02 | Densmore et al. (2007) | 2.4 ± 1.2 | Meng et al. (2008) |
| LMT(2) | Longmen Shan | 0.62 ± 0.31 | Densmore et al. (2007) | 2.4 ± 1.2 | Meng et al. (2008) |
| LMT(3) | Longmen Shan | 0.36 ± 0.07 | Densmore et al. (2007) | 2.4 ± 1.2 | Meng et al. (2008) |
| MFT(1) | Main Frontal | 21 ± 1.5 | Lavé and Avouac (2000) | 19.5 ± 0.5 | Jouanne et al. (2004) |
| MFT(2) | Main Frontal | 21 ± 1.5 | Lavé and Avouac (2000) | 12.2 ± 0.4 | Chen et al. (2004) |
| MFT(3) | Main Frontal | 19 ± 6 | Mugnier et al. (2004) | 19 | Jouanne et al. (1999) |
| MFT(4) | Main Frontal | > 13.8 ± 3.6 | Wesnousky et al. (1999) | 14 ± 1 | Banerjee and Bürgmann (2002) |
| MFT(5) | Main Frontal | 11 ± 5 | Powers et al. (1998) | 14 ± 1 | Banerjee and Bürgmann (2002) |
| MJF | Muji | 4.5 ± 0.2 | Chevalier et al. (2011) | 4.5 ± 0.5 | Zubovich et al. (2010) |
| MPT(1) | Main Pamir | ≥ 6 | Arrowsmith and Strecker (1999) | 12.5 ± 2.5 | Ischuk et al. (2013), and Zubovich et al. (2010) |
| MPT(2) | Main Pamir | 4.1 ± 1.6 | Arrowsmith and Strecker (1999) | 12.5 ± 2.5 | Ischuk et al. (2013), and Zubovich et al. (2010) |
| PFT(1) | Pamir Frontal | ~ 5.9 | Li et al. (2012) | 7.95 ± 1.9 | Zubovich et al. (2010), and Yang et al. (2008) |
| PFT(2) | Pamir Frontal | ≥ 6.4 | Li et al. (2012) | 7.95 ± 1.9 | Zubovich et al. (2010), and Yang et al. (2008) |
| RR(1) | Red River | < 2.7 | Weldon et al. (1994) | 1 ± 2 | Shen et al. (2005) |
| RR(2) | Red River | 2.1 ± 1.5 | Trinh et al. (2012) | < 2 | Feigl et al. (2003) |
| SF | Sagaing | 16.5 ± 9.19 | Bertrand et al. (1998) | ~ 18 | Vigny et al. (2003) |
| TF | Talas-Fergana | 10 ± 2 | Burtman et al. (1996) | 0.4 ± 2 | Mohadjer et al. (2010) |
| XXF(1) | Xianshuihe-Xiaojiang | 9.6 ± 1.7 | Xu et al. (2003) | 10 ± 2 | Zhang (2013), and Shen et al. (2005) |
| XXF(2) | Xianshuihe-Xiaojiang | ~ 18 | Allen et al. (1991) | 10 ± 2 | Shen et al. (2005) |
| XXF(3) | Xianshuihe-Xiaojiang | > 9.6 | Allen et al. (1991) | 9 ± 1.5 | Zhang (2013) |

| Fault label | Quaternary dating method | Quaternary slip rate (latitude/ longitude) | GPS slip rate (methods) | GPS slip rate (latitude/ longitude) |
|-------------|---|--|-------------------------|-------------------------------------|
| ATF(1) | ¹⁴ C | 38.19°N/ 88.51°E | Elastic dislocation | 89–91°E |
| ATF(2) | ¹⁰ Be, ²⁶ Al | 38.92°N/ 91.76°E | Vector diff erence | 92°E |
| ATF(3) | ¹⁴ C, ¹⁰ Be, ²⁶ Al | 39.4°N/ 94.4°E | Vector diff erence | 93°E |
| ATF(4) | ¹⁴ C | 38.6°N/ 90.6°E | Vector diff erence | ~ 93°E |
| BMF | ¹⁴ C | 30.48°N/ 77.20°E | Vector diff erence | 77°E |
| CF(1) | ⁴⁰ K- ⁴⁰ Ar | 32.80°N/ 67.80°E | Vector diff erence | 69–71.5°E |
| CF(2) | ¹⁰ Be | 30.75°N/ 66.48°E | Vector diff erence | 30.89°N, 66.51°E |
| DKF | RLT | 37.89°N/ 70.17°E | Vector diff erence | 68–72°E |
| GF(1) | ¹⁰ Be | 32.04°N/ 99°E | Vector diff erence | 94–98°E |
| GF(2) | LUM (TL) | 32.63°N/ 97.6°E | Vector diff erence | 94–98°E |
| GF(3) | ¹⁰ Be | 32.04°N/ 99°E | Vector diff erence | 31.95°N, 99.21°E |
| GF(4) | ¹⁰ Be | 32.04°N/ 99°E | Vector diff erence | 31.95°N, 99.21°E |
| GF(5) | LUM (TL) | 32.04°N/ 99°E | Vector diff erence | 31.95°N, 99.21°E |
| GF(6) | LUM (TL) | 31.85°N/ 99.41°E | Vector diff erence | 31.95°N, 99.21°E |
| GF(7) | ¹⁴ C | 31.85°N/ 99.40°E | Vector diff erence | 31.95°N, 99.21°E |
| GF(8) | LUM (TL) | 32.04°N/ 99°E | Vector diff erence | 31.95°N, 99.21°E |
| GF(9) | LUM (TL) | 31.85°N/ 99.41°E | Vector diff erence | 31.95°N, 99.21°E |
| GF(10) | ¹⁴ C | 31.85°N/ 99.40°E | Vector diff erence | 31.95°N, 99.21°E |
| HRF | RLT | 34.43°N/ 64.57°E | Vector diff erence | 69°E |
| HF(1) | ¹⁴ C | 36.70°N/ 105.17°E | Vector diff erence | 104–106°E |
| HF(2) | ¹⁴ C | 36.96°N/ 104.43°E | Vector diff erence | 104–106°E |
| KF(1) | ¹⁰ Be | 34°N/ 78.30°E | Vector diff erence | 78–80°E |
| KF(2) | ¹⁰ Be | 32.06°N/ 80°E | Elastic dislocation | 80°E |
| KF(3) | ¹⁰ Be | 32.06°N/ 80°E | Block model | 80°E |
| KF(4) | ¹⁰ Be | 31.29°N/ 80.70°E | Block model | 32.16°N, 79.92°E |
| KF(5) | ¹⁰ Be | 32.25°N/ 79.87°E | Block model | 32.16°N, 79.92°E |
| KF(6) | ¹⁰ Be | 32.25°N/ 79.87°E | Elastic dislocation | 32.27°N, 79.85°E |
| KF(7) | ¹⁰ Be | 32.55°N/ 79.62°E | Elastic dislocation | 32.27°N, 79.85°E |
| KF(8) | ¹⁰ Be | 32.55°N/ 79.62°E | Vector diff erence | 78–80°E |
| KF(9) | ¹⁰ Be | 32.25°N/ 79.87°E | Vector diff erence | 78–80°E |
| KF(10) | ¹⁰ Be | 34.22°N/ 79.93°E | Elastic dislocation | NW of 79°E |
| KKF(1) | RLT | 36.2°N/ 79°E | Vector diff erence | 79–80°E |
| KKF(2) | ¹⁴ C | 36.34°N/ 78.05°E | Vector diff erence | W of 80°E |
| KKF(3) | LUM (OSL) | 36.33°N/ 78.08°E | Vector diff erence | W of 80°E |
| KLF(1) | ¹⁰ Be, ²⁶ Al | 35.72°N/ 94.19°E | Elastic dislocation | 94°E |
| KLF(2) | ¹⁴ C | 35.04°N/ 99.20°E | Vector diff erence | 98°E |
| KLF(3) | ¹⁴ C | 34.20°N/ 101.38°E | Elastic dislocation | 101.5°E |
| LMT(1) | ¹⁰ Be | 31.28°N/ 103.83°E | Vector diff erence | 103–104°E |
| LMT(2) | ¹⁰ Be | 31.68°N/ 104.44°E | Vector diff erence | 103–104°E |
| LMT(3) | ¹⁰ Be | 31.13°N/ 103.67°E | Vector diff erence | 103–104°E |
| MFT(1) | ¹⁴ C | 27.16°N/ 85.49°E | Elastic dislocation | 82.5–88.5°E |
| MFT(2) | ¹⁴ C | 27.16°N/ 85.49°E | Block model | 83–88°E |
| MFT(3) | ¹⁴ C | 27.68°N/ 82.50°E | Elastic dislocation | 80.5–84°E |
| MFT(4) | ¹⁴ C | 30.20°N/ 77.83°E | Elastic dislocation | 75–80°E |
| MFT(5) | MST | 30.22°N/ 77.80°E | Elastic dislocation | 75–80°E |
| MJF(1) | ¹⁰ Be | 39.23°N/ 74.25°E | Vector diff erence | ~ 74°E |
| MPT(1) | ¹⁴ C | 39.49°N/ 72.53°E | Vector diff erence | ~ 73°E |
| MPT(2) | RLT | 39.48°N/ 72.25°E | Vector diff erence | ~ 73°E |
| PFT(1) | LUM (OSL) | 39.56°N/ 75.07°E | Vector diff erence | 73.5–76.5°E |
| PFT(2) | MST | 39.49°N/ 75.35°E | Vector diff erence | 73.5–76.5°E |
| RR(1) | ¹⁴ C | 24.06°N/ 101.58°E | Block model | 101–102°E |
| RR(2) | RLT | 22.11°N/ 104.41°E | Block model | 105°E |
| SF | ⁴⁰ K- ⁴⁰ Ar | 22.60°N/ 96.02°E | Elastic dislocation | ~ 22°N, 96°E |
| TF | ¹⁴ C | 41.56°N/ 73.26°E | Vector diff erence | 41.4°N, 73.5°E |
| XXF(1) | ¹⁴ C | 29.94°N/ 102.10°E | Block model | 101–102°E |
| XXF(2) | ¹⁴ C | 31.48°N/ 100.53°E | Block model | 99–101°E |
| XXF(3) | ¹⁴ C | 31.37°N/ 100.67°E | Block model | 99–101°E |

(30 ± 5 mm/yr for the Chaman fault) is based on a marker that is 1.9–2.3 Ma in age (Beun et al., 1979). Geologic rates averaged over timescales larger than the Quaternary are excluded from this study as they are less likely to represent slip rates associated with the current tectonic stress field.

Quaternary rates used in this study are obtained using different radiometric techniques and relative dating methods. GPS rates are based on differentiating velocity vectors for GPS sites used in slip rate calculations, or are obtained using elastic dislocation or block models. These rates are interseismic rates and do not include time intervals with large crustal earthquakes, except where explicitly noted.

2.2. Linear regression

Scatter plots with a 1:1 reference line have been used to investigate

the relationships between the GPS and the geologic slip rates (ArRajehi et al., 2010; Thatcher, 2009; Tong et al., 2014). In this study, we superimpose a 1:1 reference line on a scatter plot that compares 57 Quaternary/ GPS slip rate pairs (Fig. 3). To identify the extent to which the rates relate to each other, a least squares regression line was computed. The regression line was calculated by forcing it through the origin and to calculate an r^2 value as a measure of the statistical dependence between GPS and Quaternary slip rates. We abstain from conducting a weighted least squares using weights associated with each data point because different studies calculate and report slip rates' uncertainties differently, and not all studies describe if the value reported is a 1 or 2 sigma uncertainty.

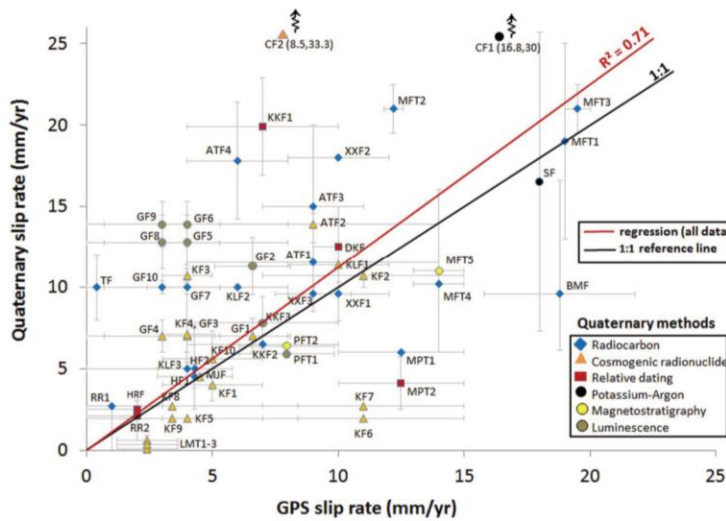


Fig. 3. Comparison of GPS slip rates with Quaternary slip rates. Symbols reflect different Quaternary dating methods used to estimate Quaternary slip rates. Error bars reflect reported uncertainties and are taken from original studies. Abbreviations of fault names are the same as those in Fig. 1. Coordinates for data points CF1 and CF2 are shown in parentheses. These points are not plotted for clarity. All plotted values are listed in Table 1.

2.3. Pearson correlation coefficients and resampling analysis

Statistical dependence of GPS and geologic rates are assessed by calculating the Pearson correlation coefficient. While other methods (e.g., Spearman's rank correlation coefficient or simple t-test) may be used to investigate the agreement of slip rates or their covariance, the PCC is more commonly used, easily calculated, and suited to the study aims. Since there is no reason to a priori question the linearity of this dependence or any other assumptions made by the PCC, and that values used in this study are carefully paired (Section 2.1) as required by the PCC, this particular measure of the degree of linear dependence is applied in this study. The sensitivity of the PCC value to slip rates associated with each fault was evaluated for 19 sample subsets (one for each fault investigated). In each subset, all data points (i.e., GPS/ Quaternary rate pairs) associated with an individual fault were excluded from calculation of the PCC. This process was repeated for each of the 19 faults investigated. Thus, each fault subset consists of the total number of data points (i.e., 57 data points) minus those associated with the individual fault excluded. Each fault subset was labeled after the name of the fault excluded from the analysis (x-axis in Fig. 4). For example, the sample subset created by the exclusion of the rate pairs for the Altyn Tagh fault (labeled as ATF in Fig. 4) consists of 53 data points. This number is obtained by excluding the 4 data points associated with this fault (ATF (1, 2, 3 and 4) in Table 1).

The literature-based uncertainties associated with each data point are taken into consideration by means of Monte Carlo style experiments. For each sample subset, Monte Carlo experiments were conducted to randomly sample from the reported confidence intervals (\pm sigma) associated with each data point. The Monte Carlo sampling is repeated one million times for each sample subset resulting in one million random sample subsets for each of the 19 sample subsets. The randomly sampled values were then used to compute the PCC without the excluded fault. This approach yields a total of 1 million PCC values for each sample subset. The PCC values were used to calculate the mean, standard deviation, minimum and maximum values for each fault subset. These values were plotted for each sample subset in Fig. 4.

The minimum PCCs required for statistical significance (above the 95% and 99% confidence levels) were calculated. The significance level is a function of both the PCC value and the degrees of freedom, which varies for each fault subset (as described in the first paragraph in this section). The significance levels are, therefore, calculated for each fault subset (shown next to each box in red in Fig. 4) and determined by a 2-tailed t-test.

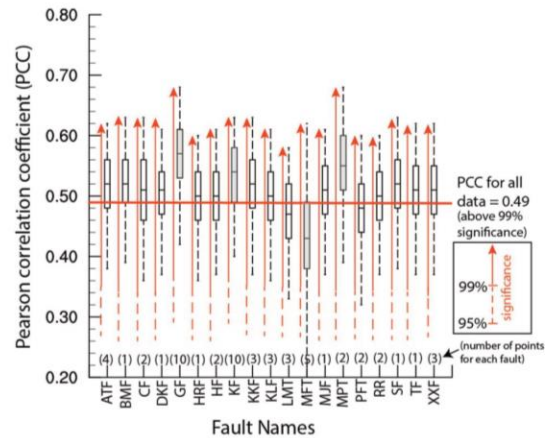


Fig. 4. Sensitivity of the PCC to GPS/ Quaternary slip rate pairs associated with individual faults. The mean PCC value for each sample subset (\pm 1 sigma), minimum and maximum (black dashed lines) as calculated from Monte Carlo experiments, are shown in the columns corresponding to each subset. The horizontal red line reflects the mean PCC value for all rate pairs (0.49). The PCC values most sensitive to slip rates associated with four fault subsets are shown in grey. The numbers shown in parentheses indicate the number of data points associated with each fault being excluded. Abbreviations of fault names are the same as those in Fig. 1. (For interpretation of the references to color in this figure legend, the reader is referred to the web version of this article.)

The procedure described above for excluding individual faults from the analysis was also applied to data points associated with individual Quaternary dating methods. This was done to evaluate if individual dating techniques have biases that strongly influence the sensitivity of the PCC (Fig. 5). Six sample subsets were created, one for each Quaternary method. In each sample subset, data points associated with a particular method were excluded from the computation of the PCC. Each sample subset, therefore, consists of the total number of data points (i.e., 57) minus those calculated using the Quaternary dating technique that was excluded. Each sample subset was named after the name of the excluded dating technique (x-axis in Fig. 5). For example, the sample subset for the radiocarbon dating method (labeled as C14 in Fig. 5) consists of 36 data points. This number is obtained by excluding the 21 data points associated with this method (Table 1). The Monte Carlo experiments and significance calculations are similarly done for

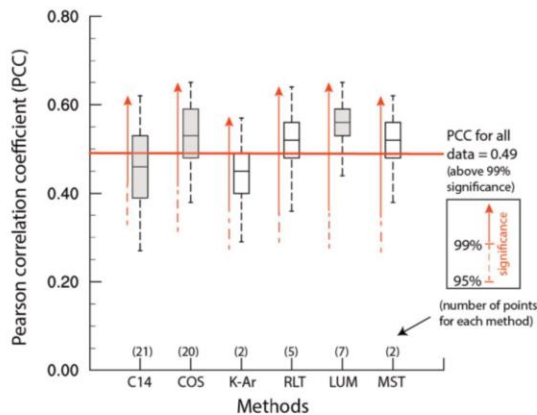


Fig. 5. Sensitivity of the PCC to the exclusion of rate pairs associated with specific Quaternary dating method. The mean PCC value for each sample subset (± 1 sigma), minimum and maximum (black dashed lines) as calculated from Monte Carlo experiments, are shown in the columns corresponding to each subset. The horizontal red line reflects the mean PCC value for all rate pairs (0.49). The PCC values most sensitive to slip rates associated with three Quaternary dating methods are shown in grey. Sample subsets are named after each dating method (C14: radiocarbon, COS: cosmogenic radionuclide, K-Ar: Potassium-Argon, RLT: relative, LUM: luminescence, MST: magnetostriatigraphy). The numbers shown in parentheses indicate the number of data points associated with each Quaternary dating method being excluded. Abbreviations of fault names are the same as those in Fig. 1. (For interpretation of the references to color in this figure legend, the reader is referred to the web version of this article.)

data points associated with each method.

3. Results

3.1. The goodness of fit

GPS and Quaternary slip rates are compared in Fig. 3 and listed in Table 1. A least squares regression through all the data points (i.e., 57 GPS/Quaternary slip rate pairs) yields an r^2 value of about 0.71 (red line in Fig. 3). The r^2 shows that a moderate percentage of the total variation in the reported Quaternary slip rates (71%) can be explained by the linear relationship between the reported GPS and the Quaternary slip rates and that a lower percentage of the total variance in the reported Quaternary slip rates (29%) remains unexplained. In this regression, not all data points are clustered tightly about the regression line. Those that plot furthest from the line belong to the Chaman fault system (i.e., CF1–2). The reported Quaternary slip rates for the Chaman fault system are more than double that of the GPS-derived rates. The Quaternary rates, however, are in agreement with each other, are measured at different locations along the fault, and are based on different Quaternary dating methods. For comparison to r^2 value of 1 (i.e., complete linear association between GPS and Quaternary slip rates), we include the 1:1 reference line (black line) in Fig. 3.

3.2. Correlation sensitivity to individual faults

Fig. 4 shows the sensitivity of the PCC to exclusion of slip rate values for individual faults. When no slip rate value is excluded, the computed PCC is ~ 0.49 (above the 99% significance level). This is shown as a red horizontal line in Fig. 4. However, the computed PCC values for all sample subsets are higher than the aforementioned 0.49 with the exception of three sample subset (i.e., LMT, MFT, and PFT on the x-axis in Fig. 4, corresponding to the Longmen Shan fault zone, Himalaya Main Frontal thrust and the Pamir Frontal thrust, respectively). The largest increase in the PCC value (from 0.49 to ~ 0.57) is achieved by excluding all slip rates reported for the Ganzi fault (i.e., GF sample subset on x-axis in Fig. 4). The mean PCC value for all sub samples are above

the 99% significance level.

3.3. Correlation sensitivity to Quaternary dating techniques

Fig. 5 shows the sensitivity of the PCC to exclusion of slip rates associated with individual Quaternary dating techniques. The largest increase in the mean PCC value is obtained for the sample subset that excludes slip rates based on luminescence techniques (LUM). This method includes both optically and thermally stimulated luminescence techniques. A slight increase in the mean PCC values of three sample subsets (i.e., COS, RLT, and MST in Fig. 5) is observed. These subsets exclude Quaternary slip rates that are based on the cosmogenic radionuclide (COS), relative (RLT), and magnetostriatigraphy (MST) dating techniques. There is a slight decrease in the PCC values for the sample subsets that exclude slip rates acquired using radiocarbon (^{14}C) and Potassium-Argon (K-Ar) dating techniques. The mean PCC values for all subsets are above the 99% significance level.

4. Discussion

4.1. Reliability of slip rates reported for individual faults

To investigate how the Quaternary slip rates used in this study compare with the GPS rates for individual faults, the sensitivity of the PCC value to exclusion of slip rate pairs for individual faults is assessed. In addition, regression through rate pairs associated with three faults (Ganzi, Karakorum and Himalayan Main Frontal thrust) is performed to obtain r^2 values. These faults have the highest number of reported GPS/Quaternary rate pairs (10, 10 and 6 rate pairs, respectively) in our dataset.

The PCC value is most sensitive to rate pairs associated with four individual faults (Ganzi, Karakorum, Himalayan Main Frontal thrust and Main Pamir thrust). The mean PCC value (above the 99% significance level) increases from 0.49 to 0.57, 0.54, and 0.55 for sample subsets that exclude rate pairs associated with the Ganzi, Karakorum and Main Pamir thrust, respectively. The mean PCC value, however, decreases from 0.49 to 0.43 when rate pairs associated with the Himalayan Main Frontal thrust are excluded. Three of the above four faults (Ganzi, Karakorum and Himalayan Main Frontal thrust) also have the highest number of reported GPS/Quaternary rate pairs. Regressions through rate pairs associated with these faults yield r^2 value of 0.82, 0.57 and 0.89, respectively (see Fig. 6). These results indicate that a higher correlation between all the GPS and Quaternary rate pairs used in this study is achieved when rate pairs associated with the Ganzi (GF), Karakorum (KF) and Main Pamir thrust (MPT) are excluded. In contrast, removal of rate pairs associated with the Himalayan Main Frontal thrust (MFT) from the analysis can yield to a lower correlation between all rate pairs used. Below we discuss if the rate pairs associated with these four faults and their observed variability in the r^2 and PCC values for individual faults is real, or if they reflect errors associated with dating techniques used.

4.1.1. The Ganzi fault

The r^2 value for rate pairs (total of 10 data points) associated with the Ganzi fault (GF) is 0.82 (Fig. 6a). However, only two out of ten reported GPS/Quaternary rate pairs (GF1 and GF3) for this fault nearly agree within their reported uncertainties. For the remaining pairs (GF2, GF4–10), the Quaternary slip rates are a factor of ≥ 2 larger than the GPS rates. The Quaternary rates in rate pairs GF2, GF5–6, and GF8–9 are from one study (Wen et al., 2003) and are based on thermoluminescence dating technique. Three of these pairs (GF2, GF5, and GF8) are obtained using the lower terrace reconstruction, and are therefore overestimated (Chevalier et al., in press). The Quaternary rate in the remaining two pairs (GF6 and GF9) is also obtained by Wen et al. (2003) using the thermoluminescence dating technique. Shi et al. (2016) measure a lower Quaternary rate at a similar location using the

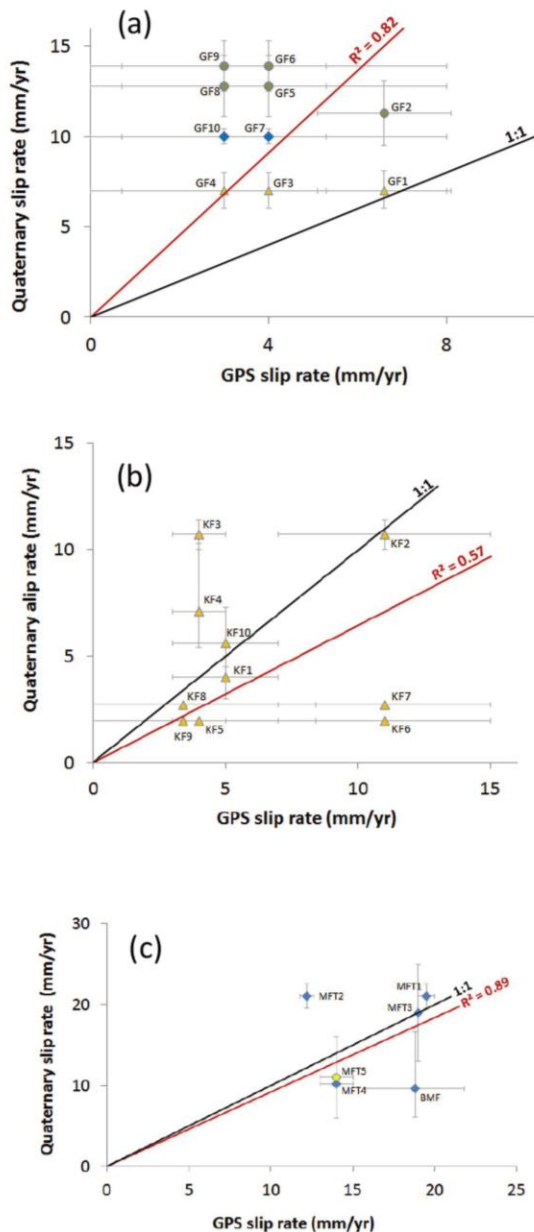


Fig. 6. Comparison of GPS/Quaternary rate pairs for (a) Ganzi fault (GF), (b) Karakorum fault (KF) and (c) Himalayan Main Frontal thrust (MFT) including Black Mango fault (BMF). Abbreviations of fault names are the same as those in Fig. 1 and Table 1. Symbols for Quaternary dating methods are the same as in Fig. 3.

radiocarbon dating technique. Their Quaternary rate of 10 ± 0.4 agrees with the upper bound of the GPS rate reported by Zhao et al. (2015). In a recent study, Chevalier et al. (in press) obtain Quaternary slip rates of 6–8 mm/yr along the Ganzi fault based on the cosmogenic radionuclide dating technique (GF1, GF3–4). These rates agree with their corresponding GPS rate within the reported uncertainties. The increase in the mean PCC value (from 0.49 to 0.57) when all rate pairs associated with the Ganzi fault are excluded, as well as the increase in the mean PCC from 0.49 to 0.56 when all rate pairs with Quaternary rates based on luminescence dating technique are excluded, indicate

that the Quaternary rates of Wen et al. (2003) strongly influence the agreement between GPS and Quaternary rates for the Ganzi fault.

4.1.2. The Karakorum fault

The r^2 value for the ten data points associated with the Karakorum fault (KF) is 0.57 (Fig. 6b). Half of the GPS/Quaternary slip rate pairs reported for this fault are in agreement within their reported uncertainties. All Quaternary rates are obtained using the cosmogenic radionuclide dating technique. The largest disagreement is observed in the KF3 and KF6–7 rate pairs. In KF3, the Quaternary slip rate of $> 10.7 \pm 0.7$ (Chevalier et al., 2005) is paired with the GPS slip rate of 4 ± 1 mm/yr (Chen et al., 2004). Brown et al. (2005) argue that Chevalier et al. (2015) have underestimated the ages of the off sets used to estimate this Quaternary rate, and suggest the possibility of a slower rate. In their later study, Chevalier et al. (2015) obtained a lower Quaternary rate (> 2 –3 mm/yr) at sites 25–55 km northwest of their 2005 measurement location, suggesting a possible late Quaternary slip rate increase toward the southeast along the fault. In KF6 and KF7, the Quaternary slip of > 2 –3 mm/yr of (Chevalier et al., 2015) is paired with the 11 ± 4 mm/yr of Banerjee and Bürgmann (2002). The GPS rate, however, is calculated from the velocity of only one station north of the fault (SHIQ) which was considered unreliable by Kundu et al. (2014). The GPS rates of Jade et al. (2004) and Chen et al. (2004) are lower (3.4 ± 5 and 4 ± 1 , respectively). Excluding these data points (KF3, KF6–7) as well as KF2 (for which the Quaternary slip rate of $> 10.7 \pm 0.7$ mm/yr is paired with the GPS rate of 11 ± 4 mm/yr) from the analysis increases the r^2 value from 0.57 to 0.84. The mean PCC value also increases slightly from 0.49 to 0.54 when all rate pairs associated with the Karakorum fault are excluded from analysis (KF in Fig. 4).

4.1.3. The Himalayan Main Frontal thrust

The r^2 value for rate pairs associated with the Himalayan Main Frontal thrust (MFT) is 0.89 (Fig. 6c). Four out of six GPS/Quaternary slip rate pairs reported for this fault agree within their uncertainties. Those not in agreement include the MFT2 and BMF (Black Mango fault). For the MFT2 data point, the Quaternary slip rate of 21 ± 1.5 mm/yr (Lavé and Avouac, 2000) is paired with the GPS slip rate of 12.2 ± 0.4 mm/yr (Chen et al., 2004). The discrepancy between these rates, as discussed in Chen et al. (2004), could be due to incorrect Quaternary and/or GPS model assumptions such as considering terrace trends as isochrons and/or ignoring the significance of strain transfer due to time-dependent earthquake cycle effects. For the Black Mango fault (BMF), the Quaternary slip rate of $9.6 (+ 7.0$ – $3.5)$ mm/yr (Kumar et al., 2001) is paired with the GPS slip rate of 18.8 ± 3 mm/yr (Jade et al., 2004). Within reported uncertainties, this Quaternary rate is almost in agreement with the GPS slip rate. The GPS rate could also be an upper bound, representing convergence between Ladakh and the Indian subcontinent as measured by the relative motions of two sites that are about 600 km apart. The variability in slip rates has also been attributed to weak geodetic constraints on the Indian plate motion and strain rates across the Himalaya (Bettinelli et al., 2006). Excluding the MFT2 and BMF data points from the analysis increases the r^2 value from 0.89 to 0.98. The high r^2 value as well as the decrease in the mean PCC value from 0.49 to 0.43 when all rate pairs associated with the Himalayan Main Frontal thrust are excluded, indicate that rate pairs for this fault strongly influence the agreement between all Quaternary and GPS rates. However, the mean PCC value is less sensitive to the exclusion of the Black Mango fault (BMF in Fig. 4) as demonstrated by a slight increase (from 0.49 to 0.52 in Fig. 4) in the mean PCC value when this rate pair is excluded from the analysis.

4.1.4. The Main Pamir thrust

The mean PCC value increases from 0.49 to 0.55 when the two rate pairs (MPT1 and MPT2) associated with the Main Pamir thrust (MPT) are excluded from the analysis. For the MPT1 rate pair, the Quaternary

rate of ≥ 6 mm/yr (Arrowsmith and Strecker, 1999) is reported as a minimum and is paired with the GPS rate of 12.5 ± 2.5 mm/yr which is reported as an upper bound on the total shortening across the entire MPT zone (Ischuk et al., 2013; Zubovich et al., 2010). This discrepancy, therefore, could be due to the real difference in what these rates actually represent (i.e., a lower and upper bound). In the MPT2 rate pair, the Quaternary slip rate of 4.1 ± 1.6 mm/yr (Arrowsmith and Strecker, 1999) is also paired with the GPS rate of 12.5 ± 2.5 mm/yr. This Quaternary slip rate, however, is not as well constrained as their ≥ 6 mm/yr as it is based on the assumption of an early Holocene age for the landforms into which beheaded drainage channels are cut. Removing the MPT1 and MPT2 data points from the regression through all the data points does not change the r^2 value significantly, but the mean PCC value remains sensitive to their exclusion.

4.2. Reliability of individual Quaternary dating techniques

The range of different dating techniques used to date fault off sets and to calculate Quaternary slip rates includes various radiometric as well as relative dating methods. The inferred Quaternary rates based on relative dating methods must be considered qualitative as none of the landforms used in estimating these rates are dated precisely. However, to avoid biasing our Quaternary slip rate selection, rates based on this method (total of 5 data points) are included in this study, and examples of discrepancies with this technique are provided in Appendix. The radiometric methods used to obtain Quaternary slip rates in this study include radiocarbon, cosmogenic radionuclide (^{10}Be and ^{26}Al), Potassium-Argon (^{40}K - ^{40}Ar), magnetostratigraphy, thermally and optically stimulated luminescence dating methods. Most of the Quaternary rates published are based on the radiocarbon and cosmogenic radionuclide dating techniques. These two dating techniques are used to determine slip rates over different timescales. The radiocarbon dating technique has an upper age limit of about 50–60 ka while the time range covered by cosmogenic radionuclide dating is suited for determining longer-term slip rates (~ 1 kys to ~ 3 Myr). This study tests how these two methods (radiocarbon and cosmogenic radionuclides) as well as the luminescence dating technique (for reasons explained below) may influence the observed relationship between the Quaternary and GPS slip rates for faults used in this study.

Overall, the regressions through rate pairs obtained using radiocarbon and cosmogenic radionuclide dating methods yield r^2 values of 0.79 and 0.55, respectively (Fig. 7a–b). The mean PCC values (above 99% significance level) for sample subsets that exclude rate pairs obtained using each individual method are 0.46 and 0.54, respectively (Fig. 5). The PCC values, however, are most sensitive to slip rates obtained using the luminescence method. Excluding rates based on luminescence dating method increases the PCC value from 0.49 to 0.56. The PCC values are less sensitive to those based on cosmogenic and radiocarbon dating techniques. A slight change in the PCC values is observed when rates associated with these methods are excluded from the analysis. Taking the number of Quaternary slip rates based on each method into account, these results indicate that unlike rate pairs based on both of the luminescence dating techniques (total of 7 pairs), slip rates based on radiocarbon (21 rate pairs) and cosmogenic radionuclide (20 rate pairs) dating techniques do not appear to significantly affect the agreement between all rate pairs.

4.2.1. Discrepancies with the radiocarbon dating technique

Despite the high r^2 value of 0.79 which was obtained for rate pairs with Quaternary slip rates based on radiocarbon dating technique (Fig. 7a), only about half of these rates agree with their corresponding GPS rates within their published uncertainties. Among the largest mismatches between GPS and Quaternary rates are the 5 rate pairs belonging to the Altyn Tagh (ATF4), Himalayan Main Frontal thrust (MFT2), Main Pamir thrust (MPT1), Talas-Fergana (TF) and Xian-shuihe-Xiaojiang (XXF2) faults. Excluding the above 5 pairs from the

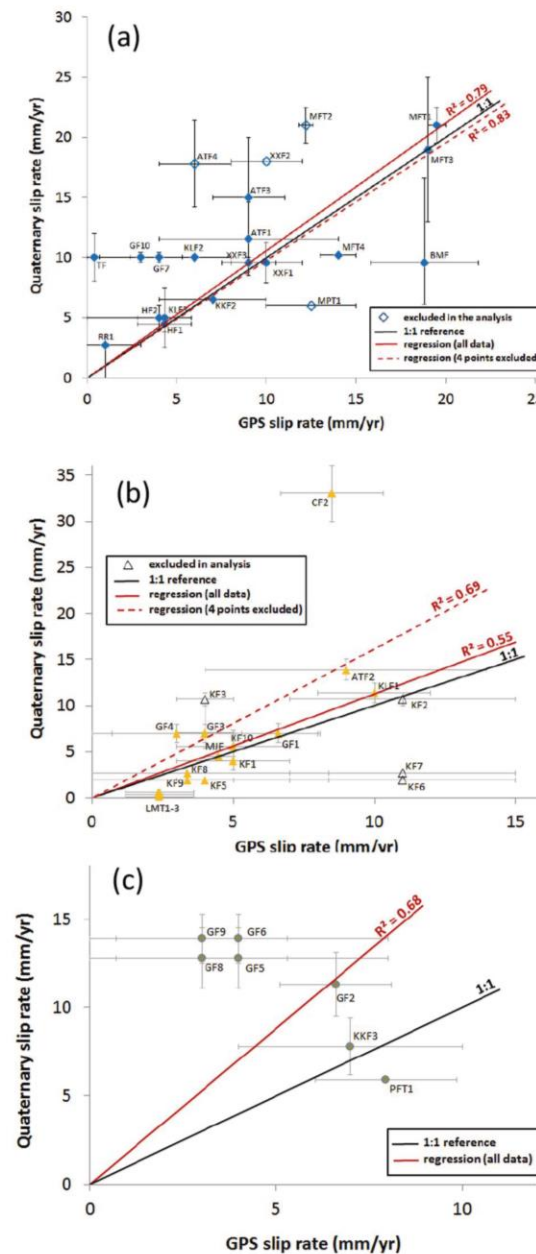


Fig. 7. Comparison of GPS/Quaternary rate pairs by Quaternary dating methods: (a) radiocarbon, (b) cosmogenic radionuclide, and (c) luminescence. (a) Excluding ATF4, MFT2, MPT1, XXF2 from the regressions analysis (for reasons explained in Section 4.2.1) increases the r^2 value from 0.79 to 0.83. (b) Excluding KF2–3 and KF6–7 from the regressions (for reasons explained in Section 4.2.2) increases the r^2 value to from 0.55 to 0.69. Abbreviations of fault names are the same as those in Fig. 1 and Table 1. Symbols for Quaternary dating methods are the same as in Fig. 3.

regression analysis increases the r^2 value from 0.79 to 0.87. Below, we summarize possible explanations for the observed disparity in rates.

For the Altyn Tagh fault, Cowgill (2007) proposes possible explanations for this discrepancy including a change in slip rate through time, systematic errors in terrace age calculation or errors resulting from extrapolation of terrace ages to off set markers that were not directly dated. According to Chen et al. (2004), the mismatches

associated with the Himalayan Main Frontal thrust (MFT2 pair) could be due to incorrect model assumptions (e.g., assumption of fault-bed fold geometry or assuming that terrace trends represent isochrons) and may require further scrutiny. The low Quaternary slip rate in the Main Pamir thrust (MPT1 pair) is reported as a minimum (Arrowsmith and Strecker, 1999) while the higher GPS rate is reported as an upper bound on the total shortening across the Main Pamir thrust zone (Ischuk et al., 2013 and Zubovich et al., 2010). The Quaternary rate reported in Allen et al. (1991) for the Xianshuihe-Xiaojiang fault (XXF2 pair) is based on only one sample from one site along the fault. Replacing this slip rate (18 mm/yr) with 15 ± 5 mm/yr (obtained from multiple measurements by Allen et al., 1991) yields a closer agreement for the XXF2 pair within uncertainty. The mismatch in the Talas-Fergana (TF in Fig. 7a) could be caused by spatial and/or temporal variations in slip according to Molnar and Dayem (2010), highlighting the need for additional GPS and Quaternary slip rate measurements on this fault.

Since the observed disparity in rates may not be real for the ATF4, MFT2, MPT1, and XXF2 pairs, we excluded them from the regression and obtained a new r^2 value of 0.83 (dashed line in Fig. 7a). In our analysis, most rate pairs that include Quaternary slip rates based on radiocarbon method are generally in agreement within their reported uncertainties, and those that disagree may reflect systematic errors in either or both geologic and GPS rate methods (e.g., ATF4, MFT2, and XXF2) or inconsistencies in how slip rates are reported (e.g., MPT1). In the case of the Talas-Fergana fault (TF pair), the variation in slip rate could be real, but more data are needed to explain the differences in rates.

The high r^2 value indicates that a large percentage of the total variation in the reported Quaternary slip rates based on the radiocarbon method can be explained by the linear relationship between the GPS and the Quaternary slip rates. The slight change in the mean PCC value (from 0.49 to 0.46 in Fig. 5) when rate pairs based on radiocarbon dating are excluded shows that these rates do not appear to affect the agreement between all rate pairs. Taken together, Quaternary rates based on radiocarbon dating techniques do not seem to bias the observed relationship between the GPS and the Quaternary slip rates.

4.2.2. Discrepancies with the cosmogenic radionuclide dating technique

In comparison with slip rates based on radiocarbon dating method, regression through rate pairs based on the cosmogenic radionuclide method (total of 20 data points) yields a lower r^2 value of 0.55 (Fig. 7b). Seven of these rate pairs that agree within their reported uncertainties belong to the Longmen Shan thrust, Karakorum, Muji, and Kunlun faults. The rate pairs that are in disagreement belong to the Chaman (i.e., CF2) and Karakorum faults (i.e., KF3, KF6, and KF7). Excluding these rate pairs from the regression increases the r^2 value to 0.90. Below, we give possible explanations for the observed disparity in these rates.

Ul-Hadi et al. (2013) determine the first ^{10}Be cosmogenic nuclide surface exposure ages on one displaced alluvial fan along a strand of the Chaman fault. Based on the ages of 8 samples from three different surfaces, they deduce a slip rate of 33.3 ± 3.0 mm/yr on a 35 ka timescale. This rate is in contrast with the geodetic rate of 8.5 mm/yr (Szeliga et al., 2012). Faster GPS rates of 16.8 ± 0.51 (Szeliga et al., 2012) and 18.1 ± 1 mm/yr (Mohadjer et al., 2010) are also reported further north along the fault where it plays into several segments. The fast Quaternary slip rate, however, agrees with the Quaternary slip rate of 25–35 mm/yr estimated by Beun et al. (1979). This rate is based on the off set of volcanic units dated at ~ 2 Ma using K-Ar dating techniques. However, these units are located > 250 km north of the alluvial surface dated by Ul-Hadi et al. (2013). Ul-Hadi et al. (2013) conclude that the contrast in slip rates is because slower GPS rates may reflect transient variations in rates of elastic strain accumulation and/or could be due to strain partitioning within the western Indian plate boundary zone. Given the absence of a dense GPS network and more studies with precisely-dated displaced landforms along the fault, the lack of detailed

mapping of regional faults, and an incomplete historical record of earthquakes, constraints for the slip rate on the Chaman fault remain weak. On the basis of available data, it is difficult to decipher between transient strain accumulation and strain partitioning to explain the contrast observed in reported slip rates.

Similarly, the Quaternary slip rate of $> 10.7 \pm 0.7$ mm/yr for the Karakorum fault (KF3 in Fig. 3) was obtained using ^{10}Be surface exposure dating of off set moraines (Chevalier et al., 2005). While this rate is in contrast with the GPS rate of 4 ± 1 mm/yr (Chen et al., 2004), it agrees with the GPS rate of 11 ± 4 mm/yr (Banerjee and Bürgmann, 2002). The latter rate, however, is based on the velocity of only one station (SHIQ) 20 km north of the fault while the former rate is constrained by the slow relative motion of two sites (SIMI and SHIQ) that lie on opposite sides of the fault. One of these sites (SHIQ) is considered to be unreliable due to high velocity uncertainties (Kundu et al., 2014). The rate of Chen et al. (2004) is also based on the assumption that there was no arc-parallel extension, and if this assumption is incorrect, this rate would be an underestimate (Chen et al., 2004). Chevalier et al. (2005) argue that the observed disparity could be real as strike-slip faults that intersect (e.g., Karakorum and the Altyn Tagh faults) might be prone to slip rate fluctuations over timescales longer than the typical seismic cycle. Brown et al. (2005), however, show that exposure ages of Chevalier et al. underestimate the age of the feature with which they are associated, and when adjusted, the slip rate is closer to ~ 5 mm/yr. More recently, Chevalier et al. (2015) determined a much lower Quaternary slip rate of > 1.7 – 2.2 mm/yr (KF6 in Fig. 3) and > 3 mm/yr (KF7 in Fig. 3) at sites located ~ 25–60 km northwest of where their higher Quaternary rate of ~ 11 mm/yr was measured. This led Chevalier et al. (2015) to suggest a possible late Quaternary slip rate increase toward the southeast, along the southernmost 500 km of the Karakorum fault. To resolve this discrepancy, more sample locations as well as measurement techniques sensitive to different timescales are needed.

We exclude the 4 rate pairs for the Karakorum fault (KF2, KF3, KF6 and KF7) from the regression, and obtain a new r^2 value of 0.69 (dashed line in Fig. 7b). The former two pairs are excluded because the Quaternary slip rate of ~ 11 mm/yr (Chevalier et al., 2005) has been suggested to be lower. The latter pairs are removed because of the high uncertainty associated with the GPS rate of Banerjee and Bürgmann (2002). We include the rate pair for the Chaman fault (CF2) in the regression since the disagreement between the Quaternary and GPS rates could be real, but more investigations at different timescales are needed to confirm this. The r^2 value of 0.69 (when the above rate pairs are excluded) means that about 70% of the total variation in the reported Quaternary slip rates based on the cosmogenic radionuclide method can be explained by the linear relationship between the Quaternary and GPS rates. The increase in the mean PCC value (from 0.49 to 0.54 in Fig. 5) when all rate pairs associated with this method are excluded is most likely due to the removal of the aforementioned rate pairs belonging to two individual faults (i.e., Karakorum and Chaman faults) where slip rates, particularly GPS-derived rates, are not well-constrained. We, therefore, conclude that the cosmogenic radionuclide dating method generally does not yield rate pairs that bias the observed relationship between the GPS and the Quaternary slip rates.

4.2.3. Discrepancies with the luminescence dating technique

Compared with the cosmogenic radionuclide dating method, regression through rate pairs based on thermally and optically stimulated luminescence dating yields a higher r^2 (0.68). However, only two of the seven rate pairs based on this method agree with their corresponding GPS rates within their reported uncertainties (Fig. 7c). These pairs belong to the Karakax fault (KKF3) and Pamir Frontal thrust (PFT1). All the rate pairs with Quaternary slip rates that are a factor of ≥ 2 larger than the GPS rates are from the thermoluminescence dating technique, measured by Wen et al. (2003) along the Ganzi fault (e.g., GF2, GF5–6, and GF8–9). Chevalier et al. (in press) consider the Quaternary rates

used in three of these rate pairs (e.g., GF2, GF5, and GF8) to be over-estimated as they are obtained using the lower terrace reconstruction which assumes that the active river on the lower tread completely refreshes the riser until the lower surface is abandoned (e.g., Cowgill, 2007). Based on cosmogenic radionuclide dating techniques, Chevalier et al. (in press) estimate lower Quaternary rates of 3–8.3 mm/yr and 7 mm/yr for sites located ~ 10 km east and ~ 20 km west of where Wen et al. (2003) measured a slip rate of 12.8 mm/yr (used in GF5 and GF8 rate pairs). Using the radiocarbon dating method, Shi et al. (2016) measure a lower Quaternary rate (~ 10 mm/yr) near where Wen et al. (2003) measure a Quaternary rate of ~ 14 mm/yr (GF6 and GF9). The lower rates for both Chevalier et al. (in press) and Shi et al. (2016) are in agreement with the reported GPS rates for the Ganzi fault (e.g., Liang et al., 2013; Wang et al., 2013; Zhao et al., 2015; and Chevalier et al., in press). We, therefore, conclude that the observed disparity in rates may not be real for the GF2, GF5–6 and GF8–9 and suggest exercising caution when using these rates. The highest increase in the PCC value (from 0.49 to 0.56 in Fig. 5) is also observed when rate pairs based on the luminescence dating method are excluded. This is because the majority of these pairs (five out of seven) are overestimated due to inaccurate geomorphic/structural reconstruction of off set landforms. In the absence of more data based on luminescence dating techniques, it is difficult to conclude if this method biases the observed relationship between the GPS and Quaternary slip rates.

4.3. Comparison with previous studies

GPS and Quaternary slip rates from this study are compared with those of Thatcher (2009) in Fig. 8. Thatcher (2009) compared GPS slip rates obtained from relative motions between adjacent blocks with Quaternary slip rates. In total, his global dataset includes 40 rate pairs (± 1 standard deviation error bars taken from original studies or estimated if unavailable) for faults from different regions including New Zealand, California, the Middle East and Tibet. In this dataset, the majority of the Quaternary rates are in agreement with the GPS rates within their reported uncertainties. Only five data points representing four faults located in the India-Asia collision zone are in this dataset (i.e., Himalayan Main Frontal thrust, Altyn Tagh, Kunlun, and Haiyuan faults). With the exception of the Himalayan Main Frontal thrust, the Quaternary slip rates for these faults are a factor of ≥ 2 larger than the reported GPS rates. This discrepancy in rates, however, is eliminated or reduced in this study following the slip rate selection criteria described in Section 2.1. Regression through the 40 data points of Thatcher (2009) yields an r^2 of 0.84.

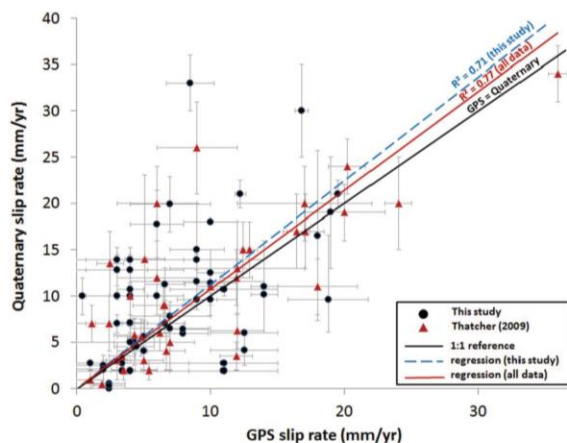


Fig. 8. Comparison of GPS and Quaternary slip rates from this study and Thatcher (2009), with error bars as assigned in original studies.

Combining our dataset with that of Thatcher (2009) allows for regression based on 97 data points. Regression based on all data points yields an r^2 value of 0.77 (solid red line in Fig. 8). This value indicates that a large percentage of the total variation in the Quaternary slip rates can be explained by the linear relationship between the GPS and the Quaternary slip rates. This agrees with the observation that most rates match each other within their reported uncertainties. Those that disagree (e.g., CF1, CF2, KF3, ATF4, XXF2, MFT2, and MPPT1, TF in Fig. 3 and Table 1) require further investigation to distinguish between incorrect rates and those that reflect true temporal/spatial variations.

4.4. Synthesis and implications

In this review, deformation rates determined from GPS and geologic techniques provide consistent slip rate information at the orogen scale. Despite the large variability in shortening rates across the Himalaya, GPS and Quaternary rates are in agreement at most individual sites along the Main Frontal thrust. Across the Kyrgyz Tien Shan, the cumulative Quaternary slip rate, accommodated by slow slip on several faults, is consistent with total north-south shortening GPS rate (Thompson et al., 2002). In the northern margin of the Chinese Pamir, slip rates measured across the Muji and Pamir Frontal thrust are comparable at Quaternary and decadal timescales across the same zone (Chevalier et al., 2011; Li et al., 2012, respectively). In addition, lower bounds on Quaternary slip rates (Arrowsmith and Strecker, 1999) are consistent with the GPS rates for the Trans-Alai thrust system (Ischuk et al., 2013; Mohadjer et al., 2010; Reigber et al., 2001 and Zubovich et al., 2010). Similarly, in the western Pamir, Quaternary rates estimated for the Darvaz-Karakul fault (Kuchai and Trifonov, 1977 and Trifonov, 1978) are close to the difference in GPS site velocities in the Pamir and the Tajik Depression (Ischuk et al., 2013). Taken together, most GPS rates appear to provide a reasonable proxy for the Quaternary rates reported for the Pamir-Tibet-Himalaya orogenic belt. Where mismatches exist, fault geometry, mechanics, and spacing are the most likely candidate influencing the equivalency between GPS and Quaternary rates at orogen scale (Li et al., 2012). This interpretation is supported by the larger variability observed in the PCC values when individual faults are excluded from the analysis (Fig. 4) when compared with when individual dating methods are removed (Fig. 5).

Though generally consistent at the orogen scale, GPS slip rates at the individual fault scale are not always representative of those based on Quaternary methods. The r^2 value of 0.71 indicates that 29% of the total variation in the Quaternary slip rates cannot be explained by the linear relationship between the GPS and Quaternary slip rates. Though > 50% of data points (total of 33 rate pairs, representing 15 faults) agree within their reported uncertainties, the remaining 24 pairs (representing 11 faults) do not. Many of the Quaternary rate pairs that do not match the GPS rates can be attributed to incorrect assumptions embedded in the geomorphic features being dated or to differences in reporting (as explained in the Discussion section). However, the discrepancy between rates may be real for a small number of faults (e.g., Talas-Fergana and Chaman faults), reflecting true temporal changes in slip rates. For this reason, disagreements between rates should be assessed on a case-by-case basis.

The individual dating methods used also influence the correlation between Quaternary and GPS slip rates. Quaternary slip rates based on the radiocarbon dating method agree better with the GPS rates than those based on cosmogenic radionuclides. This is demonstrated by regression through 21 radiocarbon data points, yielding an r^2 value of 0.79. This number can be increased to 0.87 if questionable rate pairs are removed from the regression. In comparison, regression through 20 rate pairs based on cosmogenic radionuclide method yields a lower r^2 (0.55). There is, however, a general agreement between slip rates estimated for individual faults based on different radiometric dating techniques. For instance, all slip rates based on radiocarbon and cosmogenic radionuclide methods that are reported for the Altyn Tagh

fault in this study agree within their reported uncertainties. The same observation can be made for the Quaternary slip rates reported for the Chaman fault which are based on two different radiometric dating techniques (K-Ar and cosmogenic radionuclide). In comparison, regression through 7 rate pairs based on the luminescence dating methods yields an r^2 value of 0.68. While some slip rates for individual faults that are based on the luminescence dating methods are in contrast with those based on radiometric methods (e.g., Ganzi fault), some show general agreement (e.g., Karakax fault and Pamir Frontal thrust). As discussed in Section 4.2.3, this inconsistency is a consequence of errors in the geomorphic reconstruction of off set landforms used in the estimation of Quaternary rates, and does not question the accuracy and precision of luminescence dating technique. Other Quaternary dating methods (e.g., K-Ar, relative dating and magnetostratigraphy) do not seem to bias the observed relationship between the GPS and the Quaternary slip rates as indicated by small changes in the mean PCC values when rate pairs associated with these methods are excluded from the analysis.

Short- and long-term slip rates as measured by GPS and Quaternary dating methods for faults define different kinematic conditions for the India-Asia collision zone: high rates (> 10 mm/yr) accommodated by major active faults (e.g., Himalayan Main Frontal thrust, Chaman fault system, Main Pamir thrust and Sagaing fault), and low rates (< 5 mm/yr) accommodated also by major faults (e.g., Herat, Haiyuan, Longmen Shan, and Red River faults). The fault with the fastest slip rate over both short- and long-timescales is the Himalayan Main Frontal thrust, accommodating nearly half of the total 40–50 mm/yr of convergence between India and Eurasia. The remainder of this motion is accommodated further north by slower slips on faults in and around the Tibetan Plateau (e.g., Altyn Tagh, Kunlun, and Haiyuan faults), those located in the Pamir-Hindu Kush and the Tien Shan region of Central Asia (e.g., Darvaz-Karakul fault and Main Pamir thrust) as well as active structures in the western boundary of the India-Eurasia plate (e.g., the Chaman fault system).

Quaternary rates are generally higher than the GPS rates for the large faults in the India-Asia collision zone (Fig. 3). This could be due to errors in how the Quaternary rates were determined. For example, Quaternary rates derived from geomorphic/ structural reconstruction of displaced fluvial risers, are shown to vary for the same site depending on whether the reconstruction uses the age of the upper or lower terrace for the initiation of riser off set (Cowgill, 2007). In addition, lack of reliable chronological data could result in Quaternary rates higher than GPS-derived rates. For example, the ages assumed for off set glacial features may be underestimated by a factor of 3 or more (Wright et al., 2004) resulting in fast Quaternary rates for major faults such as the Karakorum and Karakax faults in western Tibet. High Quaternary rates based on the age of one sample alone and unconfirmed by other studies should be treated with caution (e.g., ~ 18 mm/yr for Xianshuihe-Xiaojiang fault from Allen et al., 1991).

Rate mismatches where Quaternary slip rates are greater than geodetic rates, if assumed to be free from methodological error, may be attributed to nonlinear strain accumulation during the seismic cycle in combination with measurement temporal sensitivity. For example, low viscosity crust is expected to produce surface velocities greater than the long-term average early in the earthquake cycle and less than the long-term average late in the earthquake cycle. Quaternary rates span multiple earthquake cycles, and therefore, are insensitive to variability in the interseismic strain accumulation and/or post-seismic relaxation. The western boundary of the India-Eurasia plate as marked by the Chaman fault system is one region where discrepancy in rates is clearly evident and may be due to transient strain accumulation and/or strain partitioning (Ul-Hadi et al., 2013). Where GPS rates are higher than the Quaternary rates (e.g., Main Pamir thrust and Black Mango fault), the GPS rates could be the upper bounds. The results provide insights into the ongoing debates over the kinematics of deformation within the India-Asia collision zone. The disagreements over the slip rates for

major faults lie at the heart of these debates. Rapid Quaternary slip rates on major strike-slip faults (e.g., the Altyn Tagh and Karakorum faults) have been used to support the plate-like behavior of Tibet (Avouac and Tapponnier, 1993; Mériaux et al., 2005; Peltzer et al., 1989) while slow GPS rates have been used to suggest a fluid-like behavior (Bendick et al., 2000; Brown et al., 2002; Phillips et al., 2004). Our results indicate that there is a general agreement between most GPS and Quaternary rates and support the latter view by questioning the validity of rapid Quaternary rates inferred for large strike-slip faults (e.g., Altyn Tagh, Karakax, and Xianshuihe-Xiaojiang faults).

4.5. Conclusion

In this review, we compare 57 Quaternary/ GPS slip rate pairs for 19 Quaternary faults in the India-Asia collision zone. Least squares regression results suggest that a moderate percentage (71%) of the total variation in the Quaternary slip rates can be statistically explained by a linear relationship between the GPS and Quaternary rates, suggesting that a maximum of 29% of the total variance in the reported Quaternary rates may be due to other factors such as temporal variations in slip rates over the timescales individual methods are sensitive to (years to Myr), and/or methodological shortcomings. The statistical re-sampling analysis results suggest that slip rates for some individual faults significantly influence the linear relationship between GPS and Quaternary rates, and that Quaternary rates derived from the incorrect geomorphic reconstructions of landforms appear to be a controlling factor in this relationship.

Acknowledgements

We thank Marie-Luce Chevalier, Elena Grin, Anatoly Ischuk, Cassidy Jay, Lindsay Schoenbohm and Walter Szeliga for helpful discussions. The manuscript benefited from reviews by an anonymous reviewer. We thank Gillian Foulger for editorial handling. This work was supported by a European Research Council (ERC) Consolidator Grant number 615703 to Ehlers.

Appendix A. Supplementary data

Supplementary data to this article can be found online at <http://dx.doi.org/10.1016/j.earscirev.2017.09.005>.

References

- Allen, C.R., Zhuoli, L., Hong, Q., Xueze, W., Huawei, Z., Weishi, H., 1991. Field study of a highly active fault zone: the Xianshuihe fault of southwestern China. *Geol. Soc. Am. Bull.* 103 (9), 1178–1199. [http://dx.doi.org/10.1130/0016-7606\(1991\)103<1178:FSOAH>2.3.CO;2](http://dx.doi.org/10.1130/0016-7606(1991)103<1178:FSOAH>2.3.CO;2).
- ArRajehi, A., McClusky, S., Reillinger, R., Daoud, M., Alchalbi, A., Ergintav, S., Gomez, F., Sholan, J., Bou-Rabee, F., Ogubazghi, G., Hailaab, B., 2010. Geodetic constraints on present-day motion of the Arabian Plate: implications for Red Sea and Gulf of Aden rifting. *Tectonics* 29 (3). <http://dx.doi.org/10.1029/2009TC002482>.
- Arrowsmith, J.R., Strecker, M.R., 1999. Seismotectonic range-front segmentation and mountain-belt growth in the Pamir-Alai region, Kyrgyzstan (India-Eurasia collision zone). *Geol. Soc. Am. Bull.* 111 (11), 1665–1683. [http://dx.doi.org/10.1130/0016-7606\(1999\)111<1665:SRFSAM>2.3.CO;2](http://dx.doi.org/10.1130/0016-7606(1999)111<1665:SRFSAM>2.3.CO;2).
- Avouac, J.P., Tapponnier, P., 1993. Kinematic model of active deformation in central Asia. *Geophys. Res. Lett.* 20 (10), 895–898. <http://dx.doi.org/10.1029/93GL00128>.
- Banerjee, P., Bürgmann, R., 2002. Convergence across the northwest Himalaya from GPS measurements. *Geophys. Res. Lett.* 29 (13). <http://dx.doi.org/10.1029/2002GL015184>.
- Bendick, R., Bilham, R., Freymueller, J., Larson, K., Yin, G., 2000. Geodetic evidence for a low slip rate in the Altyn Tagh fault system. *Nature* 404 (6773), 69–72. <http://dx.doi.org/10.1038/35003555>.
- Bennett, R.A., Friedrich, A.M., Furlong, K.P., 2004. Codependent histories of the San Andreas and San Jacinto fault zones from inversion of fault displacement rates. *Geology* 32 (11), 961–964. <http://dx.doi.org/10.1130/G20806.1>.
- Bertrand, G., Rangin, C., Maury, R.C., Htun, H.M., Bellon, H., Guillaud, J.P., 1998. Les basaltes de Singu (Myanmar): Nouvelles contraintes sur le taux de décrochement récent de la faille de Sagaing. *Comptes Rendus de l'Académie des Sciences-Séries IIA-Earth and Planetary Science* 327 (7), 479–484. [http://dx.doi.org/10.1016/S1251-8050\(99\)80076-7](http://dx.doi.org/10.1016/S1251-8050(99)80076-7).

- Bettinelli, P., Avouac, J.P., Flouzat, M., Jouanne, F., Bollinger, L., Willis, P., Chitrakar, G.R., 2006. Plate motion of India and interseismic strain in the Nepal Himalaya from GPS and DORIS measurements. *J. Geod.* 80 (8–11), 567–589. <http://dx.doi.org/10.1007/s00190-006-0030-3>.
- Beun, N., Border, P., Carboneil, J., 1979. Premières données quantitative relatives au coulisage du décrochement de Chaman (Afghanistan du sud-est). *CR Acad. Sci. Paris* 288, 931–934.
- Bohon, W., 2014. Late Cenozoic–Recent Tectonics of the Southwestern Margin of the Tibetan Plateau, Ladakh, Northwest India. [Ph.D. thesis]. Arizona State University, Tempe, Arizona, pp. 205.
- Brown, E.T., Bendick, R., Bourles, D.L., Gaur, V., Molnar, P., Raisenbeck, G.M., You, F., 2002. Slip rates of the Karakoram fault, Ladakh, India, determined using cosmic ray exposure dating of debris flows and moraines. *J. Geophys. Res. Solid Earth* 107 (B9). <http://dx.doi.org/10.1029/2000JB000100>.
- Brown, E.T., Molnar, P., Bourles, D.L., 2005. Comment on “slip-rate measurements on the Karakoram fault may imply secular variations in fault motion”. *Science* 309 (5739), 1326. <http://dx.doi.org/10.1126/science.1112508>.
- Burtman, V.S., Skobelev, S.F., Molnar, P., 1996. Late Cenozoic slip on the Talas-Ferghana fault, the Tien Shan, central Asia. *Geol. Soc. Am. Bull.* 108 (8), 1004–1021. [http://dx.doi.org/10.1130/0016-7606\(1996\)108<1004:LCSOTT>2.3.CO;2](http://dx.doi.org/10.1130/0016-7606(1996)108<1004:LCSOTT>2.3.CO;2).
- Chen, Z.H., Burchfiel, B.C., Liu, Y., King, R.W., Royden, L.H., Tang, W., Wang, E., Zhao, J., Zhang, X., 2000. Global Positioning System measurements from eastern Tibet and their implications for India/Eurasia intercontinental deformation. *J. Geophys. Res. Solid Earth* 105 (B7), 16215–16227. <http://dx.doi.org/10.1029/2000JB000092>.
- Chen, Q., Freymueller, J.T., Yang, Z., Xu, C., Jiang, W., Wang, Q., Liu, J., 2004. Spatially variable extension in southern Tibet based on GPS measurements. *J. Geophys. Res. Solid Earth* 109 (B9). <http://dx.doi.org/10.1029/2002JB002350>.
- Chevalier, M.L., Ryerson, F.J., Tapponnier, P., Finkel, R.C., Van Der Woerd, J., Haibing, L., Qing, L., 2005. Slip-rate measurements on the Karakoram fault may imply secular variations in fault motion. *Science* 307 (5708), 411–414. <http://dx.doi.org/10.1126/science.1105466>.
- Chevalier, M.L., Li, H., Pan, J., Pei, J., Wu, F., Xu, W., Sun, Z., Liu, D., 2011. Fast slip-rate along the northern end of the Karakoram fault system, western Tibet. *Geophys. Res. Lett.* 38 (22). <http://dx.doi.org/10.1029/2011GL049921>.
- Chevalier, M.L., Tapponnier, P., Van der Woerd, J., Ryerson, F.J., Finkel, R.C., Li, H., 2012. Spatially constant slip rate along the southern segment of the Karakoram fault since 200 ka. *Tectonophysics* 530, 152–179. <http://dx.doi.org/10.1016/j.tecto.2011.12.014>.
- Chevalier, M.L., Van der Woerd, J., Tapponnier, P., Li, H., Ryerson, F.J., Finkel, R.C., 2015. Late Quaternary slip rate along the central Bangong-Chaikang segment of the Karakoram fault, western Tibet. *Geol. Soc. Am. Bull.* 128 (1–2), 284–314. <http://dx.doi.org/10.1130/B31269.1>.
- Chevalier, M.L., Leloup, P.H., Replumaz, A., Pan, J., Metois, M., Li, H. (in press). Temporally constant slip-rate along the Ganzi fault, NW Xianshuihe fault system, eastern Tibet. *Geol. Soc. Am. Bull.*, <https://doi.org/10.1130/B31691.1>.
- Cowgill, E., 2007. Impact of riser reconstructions on estimation of secular variation in rates of strike-slip faulting: revisiting the Charchen River site along the Altyn Tagh fault, NW China. *Earth Planet. Sci. Lett.* 254, 239–255. <http://dx.doi.org/10.1016/j.epsl.2006.09.015>.
- Cowgill, E., Gold, R.D., Xuanhua, C., Xiao-Feng, W., Arrowsmith, J.R., Southon, J., 2009. Low Quaternary slip rate reconciles geodetic and geologic rates along the Altyn Tagh fault, northwestern Tibet. *Geology* 37 (7), 647–650. <http://dx.doi.org/10.1130/G25623A.1>.
- Densmore, A.L., Ellis, M.A., Li, Y., Zhou, R., Hancock, G.S., Richardson, N., 2007. Active tectonics of the Beichuan and Pengguan faults at the eastern margin of the Tibetan Plateau. *Tectonics* 26 (4). <http://dx.doi.org/10.1029/2006TC001987>.
- Feigl, K.L., Cong, D.C., Becker, M., To, T.D., Neumann, K., Xuyen, N.O., 2003. April. Insignificant horizontal strain across the Red River fault near Thac Ba, Vietnam from GPS measurements 1994–2000. In: EGS-AGU-EUG Joint Assembly.
- Glotzbach, C., 2015. Deriving rock uplift histories from data-driven inversion of river profiles. *Geology* 43 (6), 467–470. <http://dx.doi.org/10.1130/G36702.1>.
- Gold, R.D., Cowgill, E., Arrowsmith, J.R., Chen, X., Sharp, W.D., Cooper, K.M., Wang, X.F., 2011. Faulted terrace risers place new constraints on the late Quaternary slip rate for the central Altyn Tagh fault, northwest Tibet. *Geol. Soc. Am. Bull.* 123 (5–6), 958–978. <http://dx.doi.org/10.1130/B30207.1>.
- Gold, R.D., Cowgill, E., Arrowsmith, J.R., Friedrich, A.M., 2017. Pulsed strain release on the Altyn Tagh fault, northwest China. *Earth Planet. Sci. Lett.* 459, 291–300. <http://dx.doi.org/10.1016/j.epsl.2016.11.024>.
- Gong, Z., Sun, J., Zhang, Z., Fu, B., Jia, Y., 2017. Optical dating of an off set river terrace sequence across the Karakax fault and its implication for the late Quaternary left-lateral slip rate. *J. Asian Earth Sci.* <http://dx.doi.org/10.1016/j.jseas.2017.07.013>.
- Hetland, E.A., Musé, P., Simons, M., Lin, Y.N., Agram, P.S., DiCaprio, C.J., 2012. Multiscale InSAR time series (MinTS) analysis of surface deformation. *J. Geophys. Res. Solid Earth* 117, B02404. <http://dx.doi.org/10.1029/2011JB008731>.
- Ischuk, A., Bendick, R., Rybin, A., Molnar, P., Khan, S.F., Kuzikov, S., Mohadjer, S., Saydullaev, U., Ilyasova, Z., Schelechkov, G., Zubovich, A.V., 2013. Kinematics of the Pamir and Hindu Kush regions from GPS geodesy. *J. Geophys. Res. Solid Earth* 118 (5), 2408–2416. <http://dx.doi.org/10.1002/jgrb.50185>.
- Jade, S., Bhatt, B.C., Yang, Z., Bendick, R., Gaur, V.K., Molnar, P., Anand, M.B., Kumar, D., 2004. GPS measurements from the Ladakh Himalaya, India: preliminary tests of plate-like or continuous deformation in Tibet. *Geol. Soc. Am. Bull.* 116 (11–12), 1385–1391.
- Jouanne, F., Mugnier, J.L., Pandey, M.R., Gamond, J.F., Le Fort, P., Serrurier, L., Vigny, C., Avouac, J.P., 1999. Oblique convergence in the Himalayas of western Nepal deduced from preliminary results of GPS measurements. *Geophys. Res. Lett.* 26 (13), 1933–1936. <http://dx.doi.org/10.1029/1999GL900416>.
- Jouanne, F., Mugnier, J.L., Gamond, J.F., Le Fort, P., Pandey, M.R., Bollinger, L., Flouzat, M., Avouac, J.P., 2004. Current shortening across the Himalayas of Nepal. *Geophys. Res. Lett.* 31, 1–4. <http://dx.doi.org/10.1111/j.1365-246X.2004.02180.x>.
- Kirby, E., Harkins, N., Wang, E., Shi, X., Fan, C., Burbank, D., 2007. Slip rate gradients along the eastern Kunlun fault. *Tectonics* 26 (2). <http://dx.doi.org/10.1029/2006TC002033>.
- Kuchai, V.K., Trifonov, V.G., 1977. Young left-lateral strike slip along the zone of the Darvaz-Karakul Fault. *Geotektonika (Moskva)* 3, 91–105.
- Kumar, S., Wesnousky, S.G., Rockwell, T.K., Ragona, D., Thakur, V.C., Seitz, G.G., 2001. Earthquake recurrence and rupture dynamics of Himalayan Frontal Thrust, India. *Science* 294 (5550), 2328–2331. <http://dx.doi.org/10.1126/science.1066195>.
- Kundu, B., Yadav, R.K., Bali, B.S., Chowdhury, S., Gahalaut, V.K., 2014. Oblique convergence and slip partitioning in the NW Himalaya: implications from GPS measurements. *Tectonics* 33 (10), 2013–2024. <http://dx.doi.org/10.1002/2014TC003633>.
- Lasserre, C., Morel, P.H., Gaudemer, Y., Tapponnier, P., Ryerson, F.J., King, G.C.P., Mévier, F., Kasser, M., Kashgarian, M., Liu, B., Lu, T., 1999. Postglacial left slip rate and past occurrence of $M \geq 8$ earthquakes on the western Haiyuan fault, Gansu, China. *J. Geophys. Res. Solid Earth* 104 (B8), 17633–17651. <http://dx.doi.org/10.1029/1998JB900082>.
- Lasserre, C., Gaudemer, Y., Tapponnier, P., Mériaux, A.S., Van der Woerd, J., Daoyang, Y., Ryerson, F.J., Finkel, R.C., Caffee, M.W., 2002. Fast late Pleistocene slip rate on the Leng Long Ling segment of the Haiyuan fault, Qinghai, China. *J. Geophys. Res. Solid Earth* 107 (B11). <http://dx.doi.org/10.1029/2000JB000060>.
- Lavé, J., Avouac, J.P., 2000. Active folding of fluvial terraces across the Swakhs Hills, Himalayas of central Nepal. *J. Geophys. Res. Solid Earth* 105 (B3), 5735–5770. <http://dx.doi.org/10.1029/1999JB900292>.
- Li, C., Zhang, P.Z., Yin, J., Min, W., 2009. Late Quaternary left-lateral slip rate of the Haiyuan fault, northeastern margin of the Tibetan Plateau. *Tectonics* 28 (5). <http://dx.doi.org/10.1029/2008TC003202>.
- Li, T., Chen, J., Thompson, J.A., Burbank, D.W., Xiao, W., 2012. Equivalency of geologic and geodetic rates in contractional orogens: new insights from the Pamir Frontal Thrust. *Geophys. Res. Lett.* 39 (15). <http://dx.doi.org/10.1029/2012GL051782>.
- Liang, S., Gan, W., Shen, C., Xiao, G., Liu, J., Chen, W., Ding, X., Zhou, D., 2013. Three-dimensional velocity field of present-day crustal motion of the Tibetan Plateau derived from GPS measurements. *J. Geophys. Res. Solid Earth* 118 (10), 5722–5732. <http://dx.doi.org/10.1002/2013JB010503>.
- Meng, G.J., Ren, J.W., Wang, M., Gan, W.J., Wang, Q., Qiao, X.J., Yang, Y.L., 2008. Crustal deformation in western Sichuan region and implications for 12 May 2008 Ms 8.0 earthquake. *Geochim. Geophys. Geosyst.* 9 (11). <http://dx.doi.org/10.1029/2008GC002144>.
- Mériaux, A.S., Tapponnier, P., Ryerson, F.J., Xu, X., King, G., Van der Woerd, J., Finkel, R.C., Li, H., Caffee, M.W., Xu, Z., Chen, W., 2005. The Aksay segment of the northern Altyn Tagh fault: tectonic geomorphology, landscape evolution, and Holocene slip rate. *J. Geophys. Res.* 110, B04404. <http://dx.doi.org/10.1029/2004JB003210>.
- Mériaux, A.S., Van Der Woerd, J., Tapponnier, P., Ryerson, F.J., Finkel, R.C., Lasserre, C., Xu, X., 2012. The Pingding segment of the Altyn Tagh Fault (91°E): Holocene slip-rate determination from cosmogenic radionuclide dating of off set fluvial terraces. *J. Geophys. Res. Solid Earth* 117 (B9). <http://dx.doi.org/10.1029/2012JB009289>.
- Mohadjer, S., Bendick, R., Ischuk, A., Kuzikov, S., Kostuk, A., Saydullaev, U., Lodi, S., Kakar, D.M., Wasy, A., Khan, M.A., Molnar, P., 2010. Partitioning of India-Eurasia convergence in the Pamir-Hindu Kush from GPS measurements. *Geophys. Res. Lett.* 37 (4). <http://dx.doi.org/10.1029/2009GL041737>.
- Molnar, P., Dayem, K.E., 2010. Major intracontinental strike-slip faults and contrasts in lithospheric strength. *Geosphere* 6 (4), 444–467. <http://dx.doi.org/10.1130/GES00519.1>.
- Mugnier, J.L., Huyghe, P., Leturmy, P., Jouanne, F., 2004. Episodicity and rates of thrust-shear motion in the Himalayas (western Nepal). *Am. Assoc. Petr. Geol. Mem.* 82, 91–114.
- Oskin, M., Perg, L., Shelef, E., Strane, M., Gurney, E., Singer, B., Zhang, X., 2008. Elevated shear zone loading rate during an earthquake cluster in eastern California. *Geology* 36 (6), 507–510. <http://dx.doi.org/10.1130/G24814A.1>.
- Peltzer, G., Tapponnier, P., Armijo, R., 1989. Magnitude of late Quaternary left-lateral displacements along the north edge of Tibet. *Science* 246 (4935), 1285–1289.
- Phillips, R.J., Parrish, R.R., Searle, M.P., 2004. Age constraints on ductile deformation and long-term slip rates along the Karakoram fault zone, Ladakh. *Earth Planet. Sci. Lett.* 226 (3), 305–319. <http://dx.doi.org/10.1016/j.epsl.2004.07.037>.
- Powers, P.M., Lillie, R.J., Yeats, R.S., 1998. Structure and shortening of the Kangra and Dehra Dun reentrants, sub-Himalaya, India. *Geol. Soc. Am. Bull.* 110 (8), 1010–1027. [http://dx.doi.org/10.1130/0016-7606\(1998\)110<1010:SASOTK>2.3.CO;2](http://dx.doi.org/10.1130/0016-7606(1998)110<1010:SASOTK>2.3.CO;2).
- Reigber, C., Michel, G.W., Galas, R., Angermann, D., Klotz, J., Chen, J.Y., Papschev, A., Arslanov, R., Tzurkov, V.E., Ishanov, M.C., 2001. New space geodetic constraints on the distribution of deformation in Central Asia. *Earth Planet. Sci. Lett.* 191 (1), 157–165.
- Sborshchikov, I.M., Savostin, L.A., Zonenshain, L.P., 1981. Present plate tectonics between Turkey and Tibet. *Tectonophysics* 79 (1–2), 45–73. [http://dx.doi.org/10.1016/0040-1951\(81\)90232-8](http://dx.doi.org/10.1016/0040-1951(81)90232-8).
- Shen, Z.K., Wang, M., Li, Y., Jackson, D.D., Yin, A., Dong, D., Fang, P., 2001. Crustal deformation along the Altyn Tagh fault system, western China, from GPS. *J. Geophys. Res. Solid Earth* 106 (B12), 30607–30621. <http://dx.doi.org/10.1029/2001JB000349>.
- Shen, Z.K., Lü, J., Wang, M., Bürgmann, R., 2005. Contemporary crustal deformation around the southeast borderland of the Tibetan Plateau. *J. Geophys. Res. Solid Earth* 110 (B11). <http://dx.doi.org/10.1029/2004JB003421>.
- Shi, F., He, H., Densmore, A.L., Li, A., Yang, X., Xu, X., 2016. Active tectonics of the Ganzi-Yushu fault in the southeastern Tibetan Plateau. *Tectonophysics* 676,

- 112–124. <http://dx.doi.org/10.1016/j.tecto.2016.03.036>.
- Stock, G.M., Frankel, K.L., Ehlers, T.A., Schaller, M., Briggs, S.M., Finkel, R.C., 2009. Spatial and temporal variations in denudation of the Wasatch Mountains, Utah, USA. *Lithosphere* GSA 1, 34–40. <http://dx.doi.org/10.1130/L15.1>.
- Styron, R., Taylor, M., Okoronkwo, K., 2010. Database of active structures from the Indo-Asian collision. *EOS Trans. Am. Geophys. Union* 91 (20), 181–182. <http://dx.doi.org/10.1029/2010EO200001>.
- Szeliga, W., Bilham, R., Kakar, D.M., Lodi, S.H., 2012. Interseismic strain accumulation along the western boundary of the Indian subcontinent. *J. Geophys. Res. Solid Earth* 117 (B8). <http://dx.doi.org/10.1029/2011JB008822>.
- Taylor, M., Yin, A., 2009. Active structures of the Himalayan-Tibetan orogen and their relationships to earthquake distribution, contemporary strain field, and Cenozoic volcanism. *Geosphere* 5 (3), 199–214. <http://dx.doi.org/10.1130/GES00217.1>.
- Thatcher, W., 2009. How the continents deform: the evidence from tectonic geodesy. *Annu. Rev. Earth Planet. Sci.* 37, 237–262. <http://dx.doi.org/10.1146/annurev.earth.031208.100035>.
- Thiede, R.C., Ehlers, T.A., 2013. Large spatial and temporal variations in Himalayan denudation. *Earth Planet. Sci. Lett.* 371–372, 278–293. <http://dx.doi.org/10.1016/j.epsl.2013.03.004>.
- Thompson, S.C., Weldon, R.J., Rubin, C.M., Abdrakhmatov, K., Molnar, P., Berger, G.W., 2002. Late Quaternary slip rates across the central Tien Shan, Kyrgyzstan, central Asia. *J. Geophys. Res. Solid Earth* 107 (B9). <http://dx.doi.org/10.1029/2001JB000596>.
- Tong, X., Smith-Konter, B., Sandwell, D.T., 2014. Is there a discrepancy between geological and geodetic slip rates along the San Andreas Fault System? *J. Geophys. Res. Solid Earth* 119 (3), 2518–2538. <http://dx.doi.org/10.1002/2013JB010765>.
- Trifonov, V.G., 1978. Late Quaternary tectonic movements of western and central Asia. *Geol. Soc. Am. Bull.* 89 (7), 1059–1072. [http://dx.doi.org/10.1130/0016-7606\(1978\)89<1059:LQTMOW>2.0.CO;2](http://dx.doi.org/10.1130/0016-7606(1978)89<1059:LQTMOW>2.0.CO;2).
- Trifonov, V.G., 1983. *Late Quaternary Tectogenesis*. Moscow, Nauka. (224 p. (in Russian)).
- Trinh, P.T., Van Liem, N., Van Huong, N., Vinh, H.Q., Van Thom, B., Thao, B.T., Tan, M.T., Hoang, N., 2012. Late Quaternary tectonics and seismotectonics along the Red River fault zone, North Vietnam. *Earth Sci. Rev.* 114 (3), 224–235. <http://dx.doi.org/10.1016/j.earsci.2012.06.008>.
- Ul-Hadi, S., Khan, S.D., Owen, L.A., Khan, A.S., Hedrick, K.A., Caffee, M.W., 2013. Slip rates along the Chaman fault: implication for transient strain accumulation and strain partitioning along the western Indian plate margin. *Tectonophysics* 608, 389–400. <http://dx.doi.org/10.1016/j.tecto.2013.09.009>.
- Van Der Woerd, J., Tapponnier, P., Ryerson, F.J., Meriaux, A.S., Meyer, B., Gaudemer, Y., Finkel, R.C., Caffee, M.W., Guoguan, Z., Zhiqin, X., 2002. Uniform postglacial slip rate along the central 600 km of the Kunlun Fault (Tibet), from 26Al, 10Be, and 14C dating of rise off sets, and climatic origin of the regional morphology. *Geophys. J. Int.* 148 (3), 356–388. <http://dx.doi.org/10.1046/j.1365-246x.2002.01556.x>.
- Vigny, C., Socquet, A., Rangin, C., Chamot-Rooke, N., Pubellier, M., Bouin, M.N., Bertrand, G., Becker, M., 2003. Present-day crustal deformation around Sagaing fault, Myanmar. *J. Geophys. Res. Solid Earth* 108 (B11). <http://dx.doi.org/10.1029/2002JB001999>.
- Wallace, K., Yin, G., Bilham, R., 2004. Inescapable slow slip on the Altyn Tagh fault. *Geophys. Res. Lett.* 31, L09613. <http://dx.doi.org/10.1029/2004GL019724>.
- Wang, Y., Wang, M., Shen, Z.K., Ge, W., Wang, K., Wang, F., Sun, J., 2013. Inter-seismic deformation field of the Ganzi-Yushu fault before the 2010 Mw 6.9 Yushu earthquake. *Tectonophysics* 584, 138–143. <http://dx.doi.org/10.1016/j.tecto.2012.03.026>.
- Washburn, Z., Arrowsmith, J.R., Dupont-Nivet, G., Feng, W.X., Qiao, Z.Y., Zhengle, C., 2003. Paleoseismology of the Xorxol segment of the central Altyn Tagh fault, Xinjiang, China. *Ann. Geophys.* 46 (5) (1015-10:34).
- Weldon, R., Sieh, K., Zhu, Q., Han, Y., Yang, J., Robinson, S., 1994. Slip Rate and Recurrence Interval of Earthquakes on the Hong He (Red River) Fault, Yunnan, PRC, paper presented at International Workshop Seismotectonics and Seismic Hazard in South East Asia. UNESCO, Hanoi.
- Wen, X., Xu, X., Zheng, R., Xie, Y., Wan, C., 2003. Average slip-rate and recent large earthquake ruptures along the Garzê-Yushu fault. *Sci. China Ser. D Earth Sci.* 46, 276–288. <http://dx.doi.org/10.1360/03dz0022>.
- Wesnously, S.G., Kumar, S., Mohindra, R., Thakur, V.C., 1999. Uplift and convergence along the Himalayan Frontal Thrust of India. *Tectonics* 18 (6), 967–976. <http://dx.doi.org/10.1029/1999TC900026>.
- Wright, T.J., Parsons, B., England, P.C., 2004. InSAR observations of low slip rates on the major faults of western Tibet. *Science* 305 (5681), 236–239. <http://dx.doi.org/10.1126/science.1096388>.
- Xu, X., Wen, X., Zheng, R., Ma, W., Song, F., Yu, G., 2003. Pattern of latest tectonic motion and its dynamics for active blocks in Sichuan-Yunnan region, China. *Sci. China Ser. D Earth Sci.* 46 (2), 210–226. <http://dx.doi.org/10.1360/03dz0017>.
- Yang, S., Li, J., Wang, Q., 2008. The deformation pattern and fault rate in the Tianshan Mountains inferred from GPS observations. *Sci. China Ser. D Earth Sci.* 51 (8), 1064–1080. <http://dx.doi.org/10.1007/s11430-008-0090-8>.
- Zhang, P.Z., 2013. A review on active tectonics and deep crustal processes of the Western Sichuan region, eastern margin of the Tibetan Plateau. *Tectonophysics* 584, 7–22. <http://dx.doi.org/10.1016/j.tecto.2012.02.021>.
- Zhang, P.Z., Shen, Z., Wang, M., Gan, W., Bürgmann, R., Molnar, P., Wang, Q., Niu, Z., Sun, J., Wu, J., Hanrong, S., 2004. Continuous deformation of the Tibetan Plateau from global positioning system data. *Geology* 32 (9), 809–812. <http://dx.doi.org/10.1130/G20554.1>.
- Zhao, B., Huang, Y., Zhang, C., Wang, W., Tan, K., Du, R., 2015. Crustal deformation on the Chinese mainland during 1998–2014 based on GPS data. *Geodesy and Geodynamics* 6 (1), 7–15. <http://dx.doi.org/10.1016/j.geog.2014.12.006>.
- Zubovich, A.V., Wang, X.Q., Scherba, Y.G., Schelochkov, G.G., Reilinger, R., Reigber, C., Mosenko, O.I., Molnar, P., Michajljow, W., Makarov, V.I., Li, J., 2010. GPS velocity field for the Tien Shan and surrounding regions. *Tectonics* 29 (6). <http://dx.doi.org/10.1029/2010TC002772>.

4.2.3 Supplements for “Review of GPS and Quaternary slip rates in the Himalaya-Tibet orogen”

Electronic supplement to:

Review of GPS and Quaternary slip rates in the Himalaya-Tibet orogen by Mohadjer et al. (2017)

Appendix A.

A1. Additional Examples of Discrepancies with relative dating techniques

To estimate a slip rate for the Karakax fault, Peltzer et al. (1989) assign an age of <8000 years to a lateral moraine located at an elevation of ~5000 meters. The authors assume that the Karakax fault must have been in the periglacial zone during much of the Würm glacial period during which the snowline was >500 m below its present position (at ~5300 m). This assumption places the area surrounding the lateral moraine site under ice, indicating that the moraine offset occurred only during the last 8000 years. Similarly, the authors infer an age of 10 ± 2 ka for the offsets of fans and terrace edges located above 4000 meters, assuming that the fans were deposited by rivers and increased runoff at the beginning of the Holocene and after the Würm glacial period. If these assumptions are incorrect, the resulting rate of 19.9 ± 3 mm/yr could be an overestimate. This Quaternary slip rate is in sharp contrast with both InSAR and GPS slip rates of 5 ± 5 and 7 ± 3 mm/yr as measured by Wright et al. (2004) and Shen et al. (2001), respectively. Based on the above arguments, we do not consider relative dates of Peltzer et al. (1989) used to calculate slip rates on the Karakax fault as accurate.

Similarly, Allen et al. (1991) use the latest Pleistocene ages that were used for slip rate determination for faults in different parts of the world to arbitrarily assign an age of 13 ka for offset moraines to calculate an average slip rate of 5.5 mm/yr for the southeastern segment of the Xianshuihe-Xiaojiang fault during Holocene time. This rate is in contrast with their two other rates that are constrained by radiocarbon dates (yielding 15 ± 5 mm/yr). Based on this observation, they concluded that the slip rate for the Xianshuihe-Xiaojiang fault decreases from 15 ± 5 mm/yr in its northernmost segment to about 5 mm/yr in its southern segment. Though their results from the northernmost segment of the fault agrees with the geodetic slip rates of 10 ± 2 mm/yr (Shen et al.,

2005 and Wang et al., 2009), the low rate inferred for the southeastern segment contradicts the GPS rate of 10 ± 2 mm/yr (Chen et al., 2000 and Shen et al., 2005). The rate comparison for the Xianshuihe-Xiaojiang fault as performed by Shen et al. (2005) suggests steady deformation rates along the fault. This combined with the Quaternary slip rate of 9.6 ± 1.7 mm/yr based on radiocarbon method that is estimated for the southeastern segment of the fault by Xu et al. (2003) may indicate that the slip rate of 5.5 mm/yr for this segment of the fault is potentially inaccurate and does not reflect true disparity.

The high slip rate of 32 ± 8 mm/yr for the Karakorum fault (Liu et al., 1991) has been challenged by others (Phillips et al., 2004; Brown et al., 2002) as potentially incorrect because postglacial ages (10 ± 2 ka) that were assigned to moraines. Based on cosmogenic dating of debris flows and moraines, Brown et al. (2002) measured a much lower rate of 4 ± 1 mm/yr. The authors report the age of the moraines (90 ± 15 ka) as direct evidence for the last major glacial advance in the region. Using this age and displacements of 300-350 meters as observed by Liu et al. (1991) a slower slip rate of 3-4 mm/yr can be estimated. This rate as well as that of Brown et al. (2002) are in agreement with both the GPS and InSAR rates of 3.4 ± 5 and 1 ± 6 mm/yr, respectively (Jade et al. 2004 and Wright et al., 2004 , respectively). The observed disparity in the KF1-2 pairs may, therefore, be due to incorrect ages of glacial landforms.

Finally, the Quaternary slip rate of 4.1 ± 1.6 mm/yr (Arrowsmith and Strecker, 1999) is a factor of 3 lower than the GPS slip rate for the Main Pamir thrust (MPT), but is also a minimum bound. This rate is based on inferred ages for a moraine and alluvial fans into which beheaded and offset ephemeral stream channels are cut. The moraine and alluvial fans deposits are assumed to be early Holocene in age (10 ka). With dextral offsets of at least 25 meters and up to 60 meters, Arrowsmith and Strecker (1999) report a Quaternary slip rate of 2.5-6 mm/yr. The upper bound on total shortening across the Main Pamir thrust is estimated to be 10-15 mm/yr using GPS data (Ischuk et al., 2013; Mohadjer et al., 2010; Zubovich et al., 2010). We, therefore, conclude that the observed disparity in rate could be related to the comparison of minimum versus maximum values for slip rates.

Despite matching the GPS rates, the 3 remaining Quaternary slip rates that are based on the relative dating method must also be considered qualitative at best. The Quaternary slip rate of 2.5 ± 0.5

mm/yr for the Herat fault (HRF) is obtained from the z-shaped bends of the Hari Rud tributaries crossing the fault (Sborshchikov et al., 1981). This rate is obtained from the inferred timing of the shaping of the river network in this region and is estimated to be ~2 Ma based on stratigraphic principles of Slavin and Demin (1972). The slip rate of 2.1 ± 1.5 mm/yr for the Red River fault (RR2) is based on assumed ages of drainage offsets along the river. Due to lack of data on rate of stream development in the region, Trinh et al. (2012) assume that the streamlets were formed after the Riss Glacial Cycle (55,000-150,000 years ago) with no reference to studies supporting the aforementioned time interval. The slip rate of 12.5 ± 2.5 for the Darvaz-Karakul fault (DKF) is based on correlation with assumed ages of offset features and deposits in the Tajik Depression (Trifonov 1978, 1983). This includes offsets of stone walls built during or since Sogdian time with inferred age of 1500 years.

References (for A1 section)

- Allen, C.R., Zhuoli, L., Hong, Q., Xueze, W., Huawei, Z. and Weishi, H., 1991. Field study of a highly active fault zone: The Xianshuihe fault of southwestern China. *Geological Society of America Bulletin*, 103(9), pp.1178-1199, doi: 10.1130/0016-7606(1991)103<1178:FSOAHA>2.3.CO;2.
- Arrowsmith, J.R. and Strecker, M.R., 1999. Seismotectonic range-front segmentation and mountain-belt growth in the Pamir-Alai region, Kyrgyzstan (India-Eurasia collision zone). *Geological Society of America Bulletin*, 111(11), pp.1665-1683, doi: 10.1130/0016-7606(1999)111<1665:SRFSAM>2.3.CO;2.
- Brown, E.T., Bendick, R., Bourles, D.L., Gaur, V., Molnar, P., Raisbeck, G.M. and Yiou, F., 2002. Slip rates of the Karakorum fault, Ladakh, India, determined using cosmic ray exposure dating of debris flows and moraines. *Journal of Geophysical Research: Solid Earth*, 107(B9), doi: 10.1029/2000JB000100.
- Chen, Z.H., Burchfiel, B.C., Liu, Y., King, R.W., Royden, L.H., Tang, W., Wang, E., Zhao, J. and Zhang, X., 2000. Global Positioning System measurements from eastern Tibet and their implications for India/Eurasia intercontinental deformation. *Journal of Geophysical Research: Solid Earth*, 105(B7), pp.16215-16227, doi: 10.1029/2000JB900092.
- Ischuk, A., Bendick, R., Rybin, A., Molnar, P., Khan, S.F., Kuzikov, S., Mohadjer, S., Saydullaev, U., Ilyasova, Z., Schelochkov, G. and Zubovich, A.V., 2013. Kinematics of the Pamir and Hindu Kush regions from GPS geodesy. *J. Geophys. Res., Solid Earth*, 118(5), pp. 2408-2416, doi: 10.1002/jgrb.50185.
- Jade, S., Bhatt, B.C., Yang, Z., Bendick, R., Gaur, V.K., Molnar, P., Anand, M.B. and Kumar, D., 2004. GPS measurements from the Ladakh Himalaya, India: Preliminary tests of plate-like or

continuous deformation in Tibet. *Geological Society of America Bulletin*, 116(11-12), pp. 1385-1391.

Liu Qing, J.P. Avouac, P. Tapponnier and Q. Zhang, Field evidence for Holocene and active faulting in western Qangtang, *Terra Abstracts*, 3, 1, E.U.G. S15- 25, p. 265, 1991.

Peltzer, G., Tapponnier, P. and Armijo, R., 1989. Magnitude of late Quaternary left-lateral displacements along the north edge of Tibet. *Science*, 246(4935), pp.1285-1289.

Mohadjer, S., Bendick, R., Ischuk, A., Kuzikov, S., Kostuk, A., Saydullaev, U., Lodi, S., Kakar, D.M., Wasy, A., Khan, M.A. and Molnar, P., 2010. Partitioning of India-Eurasia convergence in the Pamir-Hindu Kush from GPS measurements. *Geophysical Research Letters*, 37(4), doi: 10.1029/2009GL041737.

Phillips, R.J., Parrish, R.R. and Searle, M.P., 2004. Age constraints on ductile deformation and long-term slip rates along the Karakoram fault zone, Ladakh. *Earth and Planetary Science Letters*, 226(3), pp.305-319, doi: 10.1016/j.epsl.2004.07.037.

Sborshchikov, I.M., Savostin, L.A. and Zonenshain, L.P., 1981. Present plate tectonics between Turkey and Tibet. *Tectonophysics*, 79(1), pp.45-73, doi: 10.1016/0040-1951(81)90232-8.

Shen, Z.K., Lü, J., Wang, M. and Bürgmann, R., 2005. Contemporary crustal deformation around the southeast borderland of the Tibetan Plateau. *Journal of Geophysical Research: Solid Earth*, 110(B11), doi: 10.1029/2004JB003421.

Shen, Z.K., Wang, M., Li, Y., Jackson, D.D., Yin, A., Dong, D. and Fang, P., 2001. Crustal deformation along the Altyn Tagh fault system, western China, from GPS. *Journal of Geophysical Research: Solid Earth*, 106(B12), pp.30607-30621, doi: 10.1029/2001JB000349.

Slavin and Demin (1972): Slavin, V.I. and Demin, A.N., 1972. The erogenic (neotectonic) development stage of Afghanistan's territory. *Izv. Vyssh. Uchebn. Zaved., Geol. Razved., 1972(z): 60-74 (in Russian).*

Trifonov, V.G., 1978. Late Quaternary tectonic movements of western and central Asia. *Geological society of America bulletin*, 89(7), pp.1059-1072, doi: 10.1130/0016-7606(1978)89<1059:LQTMOW>2.0.CO;2

Trifonov, 1983. Late Quaternary tectogenesis (in Russian): Moscow. Nauka. pp.224.

Trinh, P.T., Van Liem, N., Van Huong, N., Vinh, H.Q., Van Thom, B., Thao, B.T., Tan, M.T. and Hoang, N., 2012. Late Quaternary tectonics and seismotectonics along the Red River fault zone, North Vietnam. *Earth-Science Reviews*, 114(3), pp.224-235, doi: 10.1016/j.earscirev.2012.06.008.

Wang, H., Wright, T.J., and Biggs, J., 2009, Interseismic slip rate of the northwestern Xianshuihe fault from InSAR data: *Geophysical Research Letters*, v. 36, L03302, doi: 10.1029/2008GL036560.

Wright, T.J., Parsons, B., England, P.C. and Fielding, E.J., 2004. InSAR observations of low slip rates on the major faults of western Tibet. *Science*, 305(5681), pp.236-239, doi: 10.1126/science.1096388.

Xu, X., Wen, X., Zheng, R., Ma, W., Song, F. and Yu, G., 2003. Pattern of latest tectonic motion and its dynamics for active blocks in Sichuan-Yunnan region, China. *Science in China Series D: Earth Sciences*, 46(2), pp.210-226, doi: 10.1360/03dz0017.

Zubovich, A.V., Wang, X.Q., Scherba, Y.G., Schelochkov, G.G., Reilinger, R., Reigber, C., Mosienko, O.I., Molnar, P., Michajljow, W., Makarov, V.I. and Li, J., 2010. GPS velocity field for the Tien Shan and surrounding regions. *Tectonics*, 29(6), doi: 10.1029/2010TC002772.

4.3 Quantifying rockfall frequency-magnitude relationship and wall retreat rates

4.3.1 Author contributions

The following section of the dissertation was submitted to *Geology* on May 7, 2019, and is currently in revision.

Mohadjer, S., Ehlers, T.A., Nettesheim, M., Ott, M.B., Glotzbach, C., and Drews, R. *Temporal variations in rockfall and rockwall retreat rates in a deglaciated valley over the last 11 ka. Geology (in revision).*

The original manuscript submitted to *Geology* is provided in section 4.3.2 and the original electronic supplement file is provided in section 4.3.3.

Six authors contributed to the work presented in the manuscript: Solmaz Mohadjer (SM), Todd A. Ehlers (TAE), Matthias Nettesheim (MN), Marco B. Ott (MBO), Christoph Glotzbach (CG), Reinhard Drews (RD). A summary of respective contributions is given in Table 4.3. The detailed contributions are as follows: TLS fieldwork and data processing was done by SM. MBO calculated talus volumes and the corresponding rockwall retreat rates with input from CG. RD contributed ideas to methods used for the calculations of the frequency-magnitude distributions and the rollover volumes. MN with input from SM and RD, wrote the MATLAB program for the frequency-magnitude calculations. SM drafted the first version of the manuscript with Figures created by SM, MN and MO. The manuscript was reviewed and edited by all authors, and is currently in revision for publication in *Geology*.

Table 4.3: Summary of contributions to joint work for the manuscript “Temporal variations in rockfall and rockwall retreat rates in a deglaciated valley over the last 11 ka”, indicating the average fraction of work of the respective author in percentage.

| Author | Position | Scientific Ideas (in %) | Data generation (in %) | Analysis and Interpretation (in %) | Paper writing (in %) |
|--------|----------|-------------------------|------------------------|------------------------------------|----------------------|
| SM | [1] | 50 | 80 | 40 | 65 |
| TAE | [2] | 30 | 5 | 10 | 10 |
| MN | [3] | 0 | 5 | 30 | 10 |
| MBO | [4] | 15 | 10 | 10 | 5 |
| CG | [5] | 5 | 0 | 5 | 5 |
| RD | [6] | 0 | 0 | 5 | 5 |

4.3.2 Manuscript (*in Revision*): Temporal variations in rockfall and rockwall retreat rates in a deglaciaded valley over the last 11 ka

Temporal variations in rockfall and rockwall retreat rates in a deglaciaded valley over the last 11 ka

Solmaz Mohadjer¹, Todd A. Ehlers¹, Matthias Nettesheim¹, Marco B. Ott¹, Christoph Glotzbach¹ and Reinhard Drews¹

¹*Department of Geosciences, University of Tübingen, Wilhelmstr. 56, 72074 Tübingen, Germany*

Abstract. The stochastic nature of rockfall in deglaciaded environments hampers the quantification of the frequency-magnitude relationship and hazard implications. In this study, we address the temporal variations in rockfall activity in the 5.2 km² calcareous cliffs of the Lauterbrunnen Valley, Switzerland. We do this using 19 campaigns of repeat terrestrial laser scans (TLS) over 5.2 years, predicted intermediate (1 ka) timescale behavior from extrapolation of the TLS derived frequency-magnitude relationship, and long-timescale (~11 ka) activity based on the volume of preserved post-glacial rockfall taluses. Results from the short-timescale observations indicate no statistically significant difference between TLS observations averaging over 1.5 vs. 5.2 years. Rockwall retreat rates in both cases are 0.03-0.08 mm/yr. In contrast, over intermediate timescales rockwall retreat rates are 0.14-0.22 mm/yr and longer term rates from talus volumes are 0.27-0.38 mm/yr. These results suggest a) short (1.5 yr) TLS inventories of rockfall in this setting provide (within uncertainties) similar frequency-magnitude relationships as longer (5.2 yr) inventories, thereby suggesting short observation periods maybe be sufficient for hazard characterization with TLS in similar settings, and b) long timescale (Holocene averaged) rockfall inventories indicate higher rates of paleorockfall activity likely due to debuttrressing and stress relaxation effects after glacial retreat.

1 Introduction

Rockfalls are efficient agents of erosion, controlling the development of rock slopes and pose a significant threat to settlements and infrastructure. Rockfalls occur frequently

in deglaciated alpine valleys where rockwalls are oversteepened, exposed, and more susceptible to failure once the glaciers retreat. Rockwall retreat rates under present-day conditions and the extent to which they change since deglaciation remain less understood. Here we investigate rockwall retreat rates over different timescales (~5 yr to ~11 ka) in the deglaciated Lauterbrunnen Valley of the Bernese Alps (Figure. 1). An improved understanding of these rates is motivated by the need to understand post-glacial erosion and the role of rockfalls in the evolution of alpine landscapes.

Rockfall supply and rockwall retreat rates are measured on various spatial and temporal scales. Rockfall datasets derived from direct measurements (e.g., TLS and photogrammetry) cover timescales from hours and days to years, and are often used in modelling rockwall retreat rates based on rockfall frequency-magnitude distributions over decadal timescales (Barlow et al., 2012; Santana et al., 2012; Rosser et al., 2005; Dussauge et al., 2003). In contrast, indirect measurements based on volumetric calculation of talus deposits have been used to estimate rockwall retreat rates over thousands of years (Siewert et al., 2012; Sass, 2007; Curry and Morris, 2004). There is a large variability in alpine rockwall retreat rates over different timescales using both measurement methods. The present-day average retreat rates for alpine environments range from 0.01 mm/yr to 0.84 mm/yr while the Holocene retreat rates range from 0.2 mm/yr to 2.5 mm/yr (Curry and Morris, 2003 and references within). The differences in rates result from different rockfall generating processes such as joint orientation, frost weathering, and paraglacial unloading after deglaciation (Arsenault and Meigs, 2005; Hinchcliffe and Ballantyne, 1999).

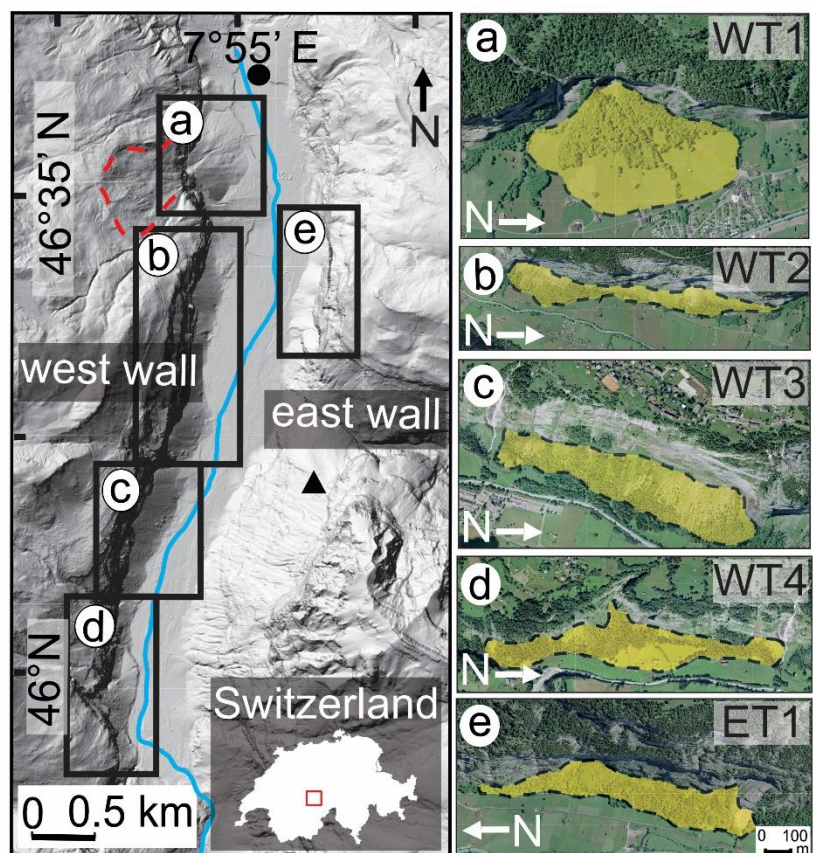
Although a number of studies measure rockwall retreat rates, few provide a complete and continuous coverage of large rock masses with uniform lithology (e.g., Guzzetti et al., 2003). Many studies compare rockwall retreat rates for localities of different environments (Siewert et al., 2012; Curry and Morris, 2004, Hinchcliffe and Ballantyne, 1999). This comparison may explain factors that cause differences in rates, but provides limited information on the long-term behavior of a given rock mass in one location. This study complements previous work by calculating rockwall retreat rates over three different

timescales (years to tens of thousands of years) for the 5.2 km² limestone rockwalls of a deglaciated valley.

1.1 Study Area

The Lauterbrunnen Valley is a deglaciated valley with near vertical walls (Figure.1 and Supplementary Figure. DR4). The steep topography of the Helvetic limestone valley walls is the result of recent deglaciation (Hergarten et al., 2012). Data on historic rockfalls show several large-scale slope failures since 1750 including the 1889 landslide that released $>10^4$ m³ of debris material into the valley (Michel, 1979). Using TLS data, Strunden et al. (2015) detected 122 rockfalls in the valley over an 18-month period. These events range in volume from 0.06 m³ to 119.34 m³, with those less than 1 m³ being most common. Using seismic signals over 6 months, Dietze et al. (2017b) detected 49 rockfalls over a 6-month period, 10% of which were influenced by freeze-thaw transitions. They inferred a systematic downward shift of a rock mass release zone, driven by a continuously lowering water table inside the rockwall.

Figure 1. Shaded relief digital elevation model of the Lauterbrunnen Valley, Switzerland (DEM courtesy of swisstopo). Black circle marks the location of the Lauterbrunnen Village, and the river Weisse Lütschine is shown in blue. Black boxes represent the location of the investigated talus cones. Talus surfaces are shown in yellow, with boundaries marked with dashed lines. The red dashed line marks the scarp of the 1889 mass wasting event. WT1-4 and ET1 are talus names.



2 Method

2.1 TLS data collection and processing

An Optech ILRIS-LR terrestrial light detection and ranging scanner was used to acquire high density 3D point clouds from 22 scan positions during each campaign. A total of 19 campaigns were carried out over a 5.2-year period between February 2012 and April 2017. Scans from the same scan position collected at subsequent times were aligned using an iterative closest point algorithm. To produce a continuous surface, triangle meshes of reference scans were computed. Surface meshes were compared with point clouds to identify rockfalls between successive campaigns. Rockfall volumes were obtained from cut and fill calculations and compared to photos to confirm if the cut values represented rockfalls. The details of TLS data collection methods, processing and error evaluation are given in Strunden et al. (2015).

2.2 Rockwall retreat rates calculations

We used three different approaches to determine rockwall retreat rates over different timescales. First, the averaged short-term retreat rates were calculated from the total volume of all measured rockfalls based on TLS observations collected over 5.2 years. Second, intermediate timescale (1 ka) rockwall retreat rates were derived from TLS measurements under the assumption of a power law distribution of rockfall event sizes. This was done by calculating nonlinear least squares regression fits in combination with maximum likelihood estimates. Third, the rockwall retreat rates over the last 11 ka were inferred from the calculation of talus volumes using TLS and 2 m resolution digital elevation model swissALTI3D, compensating for the density difference between talus bulk and intact bedrock (correcting factor of 0.77), and dividing by the rockwall surface area above each talus and talus production time (i.e., timespan elapsed since deglaciation: ~11 ka). For more details, see sections 1-2 and Figure. DR3 in the supplement.

3 RESULTS

3.1 Rockfall activity

A total of 316 rockfalls were detected from February 2012 – April 2017, 122 of which were identified by Strunden et al. (2015) in the first 18 months (Figure. 2). Rockfall volumes range from $0.030 \pm 0.004 \text{ m}^3$ to $267.27 \pm 4.39 \text{ m}^3$. Supplementary Table DR1 summarizes the events for each campaign measurement period. Small rockfalls ($< 1 \text{ m}^3$) are most common (63% of total events). 21% have volumes of 1-3 m^3 . Events larger than 50 m^3 are rare (2% of total events).

3.2 Short timescale (<5.2 yr) wall retreat rates

Spatially averaged short-term (5.2 years) wall retreat rates were calculated for the west wall by dividing the total rockfall volume (1610.87 m^3) from the west wall in the 5.2-year observation time by the area of the west wall (3.7 km^2). Similarly, the retreat rate for the east wall was obtained using 229.65 m^3 for the total rockfall volume from the east wall over an area of 1.5 km^2 . The short-term wall retreat rates for the west wall (0.08 mm/yr) and the east wall (0.03 mm/yr) are in agreement with those obtained over an 18-month period by Strunden et al. (2015).

3.3 Intermediate timescale (1 ka) wall retreat rates

The empirical log-frequency and log-magnitude distributions for the 5.2-year rockfall dataset have a rollover and power law tail (Figure. 3). A nonlinear least-squares regression and a maximum likelihood method are used to determine the frequency-magnitude relationship. The inferred rollover volumes, based on optimization of the R^2 value and the Kolmogorov-Smirnov statistic, differ for the two methods (see supplement and Figure. DR1). We observe deviations from pure power law behavior and a systematic trend in fit parameters for rollover volumes of $0.29\text{-}0.92 \text{ m}^3$. For these values, the maximum likelihood estimates of the scaling exponent b range from 0.61 to 0.72. The power law fit parameters agree with previously reported values obtained for a shorter observation duration (1.5 years) (Table DR2, C). However, the frequency of rockfalls in the 5.2-year dataset is lower compared to the 1.5-year dataset (Figure. 3). This is particularly evident for rockfalls smaller than 2 m^3 .

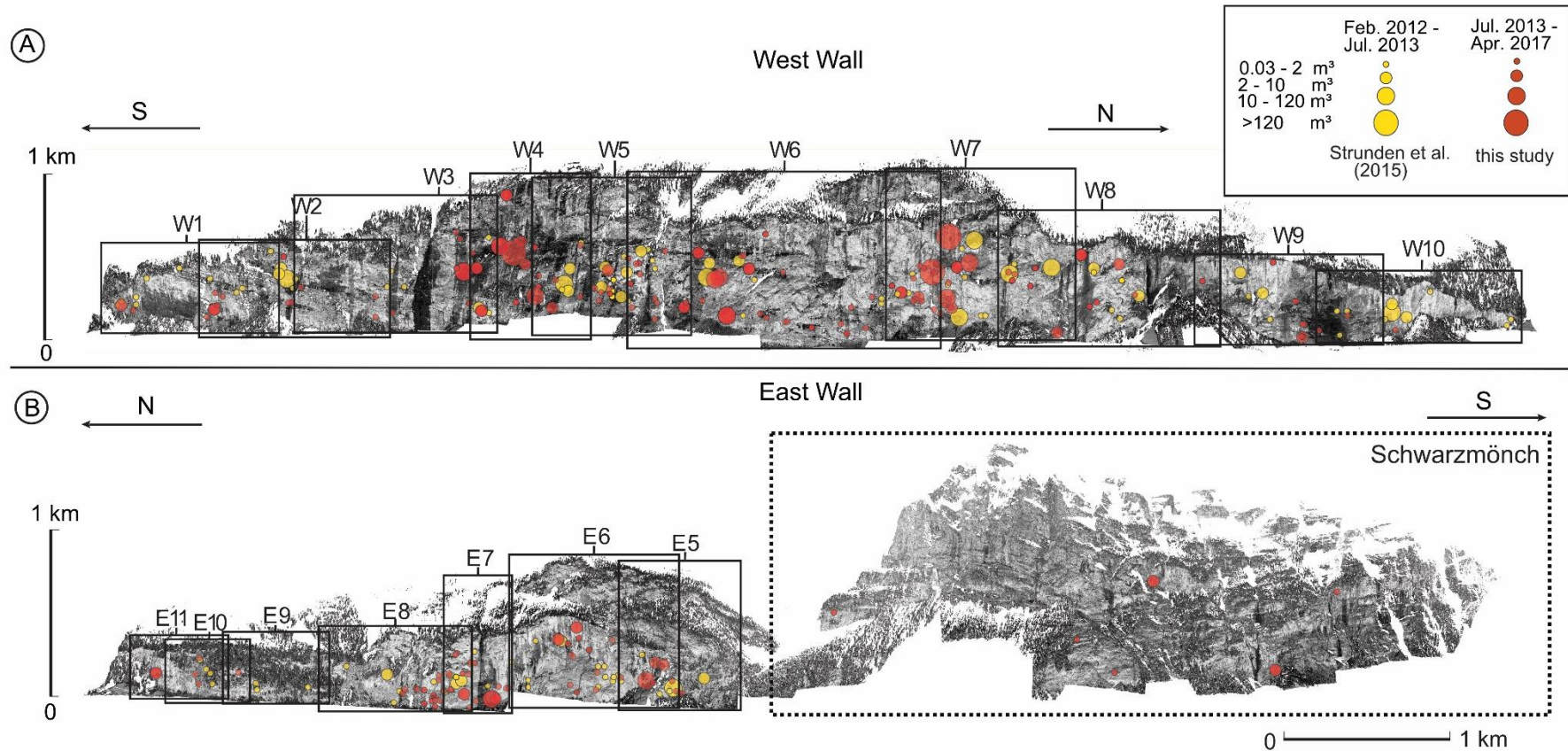


Figure 2. Composite (aligned) TLS point cloud data for both (a) west and (b) east valley walls. Yellow circles mark the location of rockfall events from Strunden et al. (2015). The location of rockfall events from this study are shown in red circles. Black boxes represent scan area of each scan location with scan name shown above each box. The rock surface of Schwarzmönch (dashed box) was not analyzed for rockfall events due to the large mean distance to the wall from the scan position and the steep inclination angle from the laser scanner.

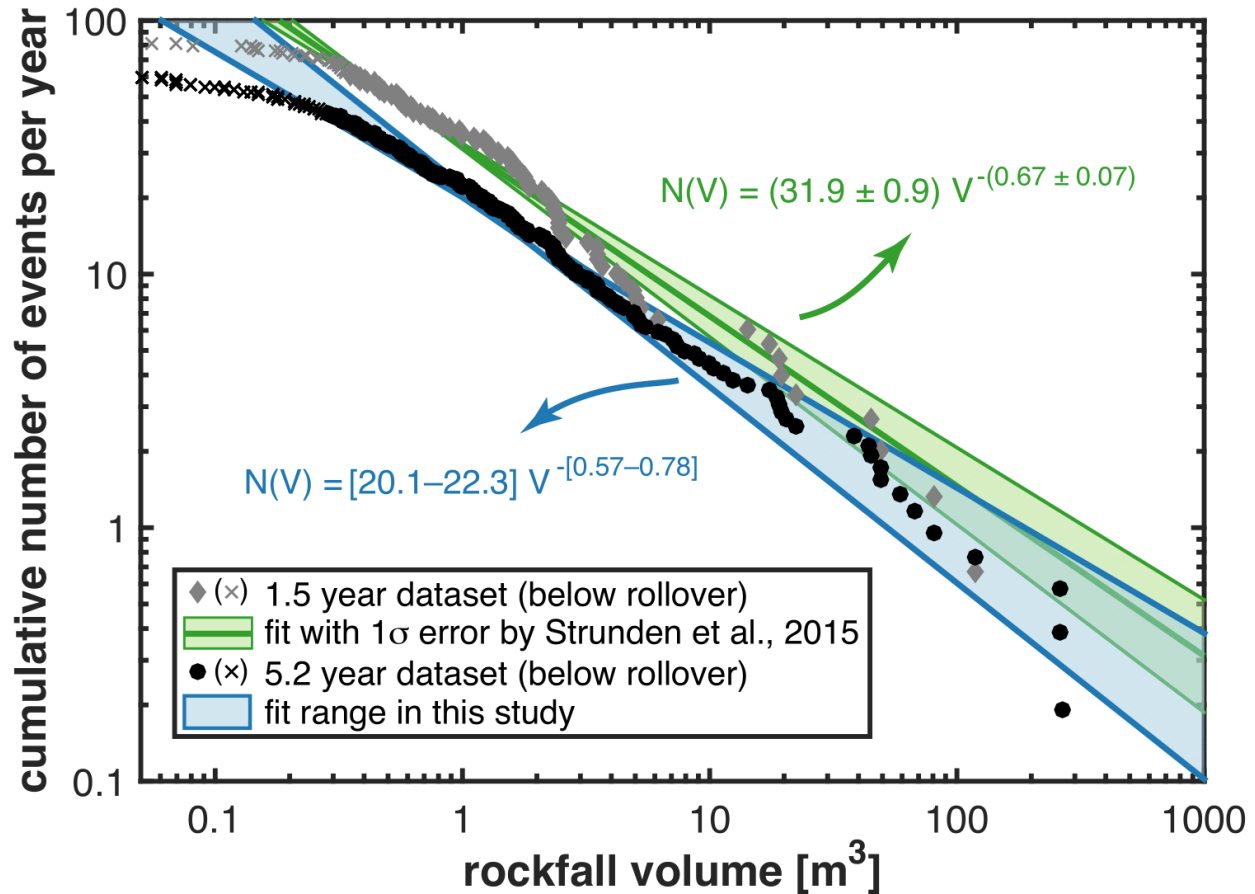


Figure 3. Cumulative probability plot for the negative power law scaling parameters obtained in this study (shaded in blue) and by Strunden et al. (2015) (shaded in green). In this study, the shaded areas represent a range of possible fits (within one-sigma standard deviation) to data using the maximum likelihood estimates approach and rollover volumes of 0.29-0.92 m³. The power law parameters from both studies are in agreement within uncertainties.

Using the above power law fit parameters, the intermediate timescale averaged total eroded volumes are calculated to be $(0.70-1.13) \times 10^3 \text{ m}^3$ and the corresponding wall retreat rates are 0.14-0.22 mm/yr. Using observations from Strunden et al. (2015), we recalculated the total eroded volume and intermediate timescale wall retreat rates (i.e., $0.62 \pm 0.13 \times 10^3 \text{ m}^3$ and $0.12 \pm 0.03 \text{ mm/yr}$, respectively). These values agree with the range of values reported in this study (see Table DR2 for all power law fit calculations).

3.4 Long timescale (11 ka) wall retreat rates

The measured talus volumes range from $2.1 \times 10^6 \text{ m}^3$ to $4.3 \times 10^6 \text{ m}^3$ (Figure. 1). These are considered minimum estimates due to possible loss of material, although no field evidence support transport of talus out of the valley. The long-term averaged wall retreat rate of 0.33 mm/yr is calculated by dividing the total talus volume estimated for each talus section by the surface area of the rockwall above it (Table DR3). Due to their complex morphology and fluvial erosion, talus sections WT1 and WT4 were excluded from retreat rate calculations. All talus sections, with the exception of WT1, are sheet talus slopes with a slope angle of $33^\circ \pm 2^\circ$.

4 Discussion

4.1 Frequency-Magnitude Analysis

Power law relationships for rockfall frequency-magnitude analysis can be used to estimate the return time of large events and long-term erosion. This study shows that these calculations are sensitive to, and depend on, the choice of rollover values. Larger rollover values yield larger values of exponent b and longer return time for a 1000 m^3 rockfall and smaller values of long-term erosion (Figure. DR2), demonstrating that a rockfall frequency-magnitude relationship does not follow a pure power law and caution must be exercised when calculating power law fit parameters. Here, these values are reported in ranges to more accurately capture the spread in data and offer a range of possible solutions (see Table DR2).

4.2 Comparison of 1.5- and 5.2-year rockfall datasets

TLS measurements collected at two different time intervals (1.5 yr and 5.2 yr) are compared to evaluate the effect of observation time on frequency-magnitude relationships. Power-law exponents from both datasets are in agreement within error (exponent b value of 0.67 ± 0.07 vs. 0.61-0.72, for 1.5 yr vs. 5.2 yr dataset, respectively) (Table DR2-C). Furthermore, short-term wall retreat rates are within the same order of magnitude for both time intervals. However, there is a systematic decrease in the relative number of smaller events for the 5.2 yr dataset (Figure. 3). Additionally, the number of

larger events ($>10 \text{ m}^3$) are higher in the 5.2 yr dataset including three rockfalls with volumes over 250 m^3 . No event of such volume exists in the 1.5 yr dataset. These differences may be explained by natural stochastic variations or by undersampling from an increased measurement interval.

4.3 Comparison of wall retreat rates

The long-term wall retreat rates in the Lauterbrunnen Valley are an order of magnitude higher than the short-term rates (0.33 vs. 0.03-0.08 mm/yr). This discrepancy can reflect sensitivity to observation timescales and/or different erosional processes at work. For example, in glaciated landscapes, glaciers not only increase erosion rates during glaciation, but there is also a post-glacial increase in rates that appears to decay over timescales of 10^3 - 10^4 years.

Short-term rates are sensitive to the timescale of observation. In the 5.2 yr period, small rockfalls ($>1 \text{ m}^3$) are the most frequent in the Lauterbrunnen Valley, and those larger than 100 m^3 (total of 4) are uncommon. However, a number of rockfall episodes (e.g., several 10^3 to 10^5 m^3 rockfalls between 1750 and 1947), have occurred in the past releasing large volumes of falling debris, forming talus slopes and depositing large boulders beyond the base of talus slopes. The short-term wall retreat rates calculated over 5.2 years exclude such large events while retreat rates calculated over longer time intervals ($\sim 11 \text{ ka}$) may include them. It is also possible that the short-term retreat rates are not significantly different from variations in the long-term rates over the past 11 ka.

Long-term rates are sensitive to changes in the stability of rockwalls, particularly soon after deglaciation during which debuttrussing and stress release associated with glacial unloading can weaken the walls and trigger rockfalls (Sass, 2007; Ballantyne, 2002; André, 1997; Wieczorek and Jäger, 1996). Since this effect diminishes through time, lower short-term rates may reflect progressive relaxation of stress release and attainment of rock mass stability (Hinchliffe and Ballantyne, 1999).

Fluctuations in climate conditions have been suggested to modify catchment-scale denudation in glaciated valleys (e.g., Yanites and Ehlers, 2012; Stock et al., 2009) and rockfall activity (Ludovic and Deline, 2010; Hales et al., 2007; André, 1997; Grove, 1972;

Starkel, 1966). Paleobotanical records point to Holocene climatic oscillations in the Central Alps (Wick and Tinner 1997), with records of cold phases between 10 ka and 2 ka BP. Similarly, based on subfossil chironomid assemblages at Hinterburgsee (~20 km northeast of our study area), Heiri et al. (2003) identified two periods of lower temperatures at 10,700-10,500 cal. BP and 8,200-7,700 cal. BP, and an abrupt shift to a cooler late-Holocene climate around 4,000-3,700 cal. BP. Most sensitive to Holocene climatic oscillations are rockfall triggering processes that are temperature/water-dependent (e.g., changes in permafrost conditions, frost-thaw cycles, and frost-cracking). Local frost shattering in combination with other factors has been shown to be responsible for rapid Holocene wall retreat rates (André, 1997). In particular, in deglaciated setting, frost action due to bedrock jointing inherited from stress release following deglaciation plays an important role in rockwall retreat rates due to rockfalls.

5 Conclusion

This study investigates the temporal variations in rockwall retreat rates in the 5.2 km² calcareous cliffs of the Lauterbrunnen Valley, Switzerland. Short-term retreat rates, power law exponents and calculations do not appear to be sensitive to observation periods of 1.5 vs. 5.2 years, apart from frequency offset. The intermediate-timescale (1 ka) retreat rate predicted by power law and long-term (11 ka) retreat rates calculated from talus accumulation are an order of magnitude higher than the short-term rates. We suggest three possibilities to explain these difference. First, lower short-term rates (<5.2 yr) reflect frequent small rockfalls, excluding rare large events that can significantly increase retreat rates over longer timescales. Second, higher long-term rates may reflect periods of increased rockfall activity enhanced by stress release due to unloading and debuttreasing of the rockwall following deglaciation, and/or the influence of frost-shattering due to climatic oscillations in the past 11 ka.

Acknowledgments

We thank Josy Burke, Sarah Falkowski, Lorenz Michel, and Michael Kloos for TLS field assistance. We are also grateful to Nick Rosser, Alex Densmore and Michael Krautblatter for valuable discussions in the early phases of this research, and to the

residents of Lauterbrunnen Valley for their support. The funding for this study was provided by the German Science Foundation (DFG) grant EH329/18-1 to TAE. The point cloud data used in this study are available upon request as is the MATLAB program used for the frequency-magnitude analysis.

References Cited

- André, M.F., 1997, Holocene rockwall retreat in Svalbard: a triple-rate evolution: *Earth Surface Processes and Landforms: The Journal of the British Geomorphological Group*, 22, no. 5, p. 423–440, doi:10.1002/(SICI)1096-9837(199705)22:5<423::AID-ESP706>3.0.CO;2-6.
- Arsenault, A.M. and Meigs, A.J., 2005, Contribution of deep-seated bedrock landslides to erosion of a glaciated basin in southern Alaska: *Earth Surface Processes and Landforms*, v. 30, no. 9, p. 1111–1125, doi:10.1002/esp.1265.
- Ballantyne, C.K., 2002, Paraglacial geomorphology: *Quaternary Science Reviews*, v. 21, p. 1935–2017, doi:10.1016/S0277-3791(02)00005-7.
- Barlow, J., Lim, M., Rosser, N., Petley, D., Brain, M., Norman, E. and Geer, M., 2012, Modeling cliff erosion using negative power law scaling of rockfalls: *Geomorphology*, v. 139, p. 416–424, doi:10.1016/j.geomorph.2011.11.006.
- Curry, A.M., Morris, C.J., 2004, Lateglacial and Holocene talus slope development and rockwall retreat on Mynydd Du, UK: *Geomorphology*, v. 58, p. 85–106, doi:10.1016/S0169-555X(03)00226-5.
- Dietze, M., Turowski, J.M., Cook, K.L., Hovius, N., 2017, Spatiotemporal patterns, triggers and anatomies of seismically detected rockfalls: *Earth Surface Dynamics*, v. 5, p. 757–779, doi:10.5194/esurf-5-757-2017.
- Dussauge, C., Grasso, J.-R., Helmstetter, A., 2003, Statistical analysis of rockfall volume distributions: Implications for rockfall dynamics: *Journal of Geophysical Research: Solid Earth*, v. 108, no. B6, p. 2286, doi:10.1029/2001JB000650.
- Dussauge-Peisser, C., Helmstetter, A., Grasso, J.R., Hantz, D., Desvarreux, P., Jeannin, M. and Giraud, A., 2002, Probabilistic approach to rock fall hazard assessment: potential of historical data analysis. *Natural Hazards and Earth System Science*, v. 2(1/2), p. 15–26.
- Grove, J.M., 1972, The incidence of landslides, avalanches, and floods in western Norway during the Little Ice Age: *Arctic and Alpine Research*, v. 4, no. 2, p. 131–138, doi:10.1080/00040851.1972.12003633.
- Hales, T.C. and Roering, J.J., 2007, Climatic controls on frost cracking and implications for the evolution of bedrock landscapes: *Journal of Geophysical Research: Earth Surface*, v. 112(F2), doi:10.1029/2006JF000616.
- Heiri, O., Lotter, A.F., Hausmann, S. and Kienast, F., 2003, A chironomid-based Holocene summer air temperature reconstruction from the Swiss Alps: *The Holocene*, v. 13, no. 4, p. 477–484, doi:10.1191/0959683603hl640ft.
- Hergarten, S., 2012, Topography-based modeling of large rockfalls and application to hazard assessment: *Geophysical Research Letters*, v. 39, no. 13, doi:10.1029/2012GL052090.

-
- Hinchliffe, S., Ballantyne, C.K., 1999, Talus accumulation and Rockwall retreat, Trotternish, isle of Skye, Scotland: *Scottish Geographical Journal*, v. 115, p. 53–70, doi:10.1080/00369229918737057.
- Michel, H., 1979, Buch der Talschaft Lauterbrunnen: Geschehnisse und Brauchtum in den Dörfern Lauterbrunnen, Wengen, Mürren, Gimmelwald, Stechelberg und Isenfluh; von den Wassern, Tieren, Pflanzen und der Bergwelt. Gemeinderat
- Ravanel, L., Allignol, F., Deline, P., Gruber, S. and Ravello, M., 2010, Rock falls in the Mont Blanc Massif in 2007 and 2008: *Landslides*, v. 7, no. 4, p. 493-501, doi:10.1007/s10346-010-0206-z.
- Rosser, N.J., Petley, D.N., Lim, M., Dunning, S.A. and Allison, R.J., 2005, Terrestrial laser scanning for monitoring the process of hard rock coastal cliff erosion: *Quarterly Journal of Engineering Geology and Hydrogeology*, v. 38, no. 4, p. 363-375, doi:10.1144/1470-9236/05-008.
- Sass, O., Krautblatter, M., 2007, Debris flow-dominated and rockfall-dominated talus slopes: Genetic models derived from GPR measurements: *Geomorphology*, v. 86, p. 176–192, doi:10.1016/j.geomorph.2006.08.012.
- Santana, D., Corominas, J., Mavrouli, O. and Garcia-Sellés, D., 2012, Magnitude–frequency relation for rockfall scars using a Terrestrial Laser Scanner: *Engineering Geology*, v. 145, p. 50-64, doi:10.1016/j.enggeo.2012.07.001.
- Siewert, M.B., Krautblatter, M., Christiansen, H.H., Eckerstorfer, M., 2012, Arctic rockwall retreat rates estimated using laboratory-calibrated ERT measurements of talus cones in Longyeardalen, Svalbard: *Earth Surface Processes and Landforms*, v. 37, p. 1542–1555. doi:10.1002/esp.3297.
- Starkel, L.: 1966, Post-glacial climate and moulding of European relief, World Climate 8000 to 0 B.C.: *Proceedings of the International Symposium: Royal Meteorological Society, London*, p. 15–32.
- Stock, G.M., Frankel, K.L., Ehlers, T.A., Schaller, M., Briggs, S.M., and Finkel, R.C., 2009, Spatial and temporal variations in denudation of the Wasatch Mountains, Utah, USA: *Lithosphere*, v. 1, p. 34–40, doi:10.1130/L15.1.
- Strunden, J., Ehlers, T.A., Brehm, D., Nettesheim, M., 2015, Spatial and temporal variations in rockfall determined from TLS measurements in a deglaciaded valley, Switzerland: *Journal of Geophysical Research: Earth Surface*, v. 120, p. 1251–1273, doi:10.1002/2014JF003274.
- Yanites, B.J., and Ehlers, T.A., 2012, Global climate and tectonic controls on the denudation of glaciaded mountains: *Earth and Planetary Science Letters*, v. 325–326, p. 63–75, doi:10.1016/j.epsl.2012.01.030.
- Wick, L. and Tinner, W., 1997, Vegetation Changes and Umbertine Fluctuations in the Central Alps as Indicators of Holocene Climatic Oscillations: *Arctic and Alpine Research*, v. 29(4), p. 445-458, doi:10.1080/00040851.1997.12003265.
- Wieczorek, G.F., Jäger, S., 1996, Triggering mechanisms and depositional rates of postglacial slope-movement processes in the Yosemite Valley, California: *Geomorphology*, v. 15, p. 17–31, doi:10.1016/0169-555X(95)00112-I.
-

4.3.3 Supplements for “Temporal variations in rockfall and rockwall retreat rates in a deglaciated valley over the last 11 ka”

Electronic supplements to:

Temporal variations in rockfall and rockwall retreat rates in a deglaciated valley over the last 11 ka by Mohadjer et al. (*in revision*)

Additional details on methods and results

This data repository contains additional details on rockwall retreat rate calculations (sections 1-2), four supplementary Figures (Figures DR1 – DR4), three data tables (Table DR1 – DR3), and additional references cited in the repository.

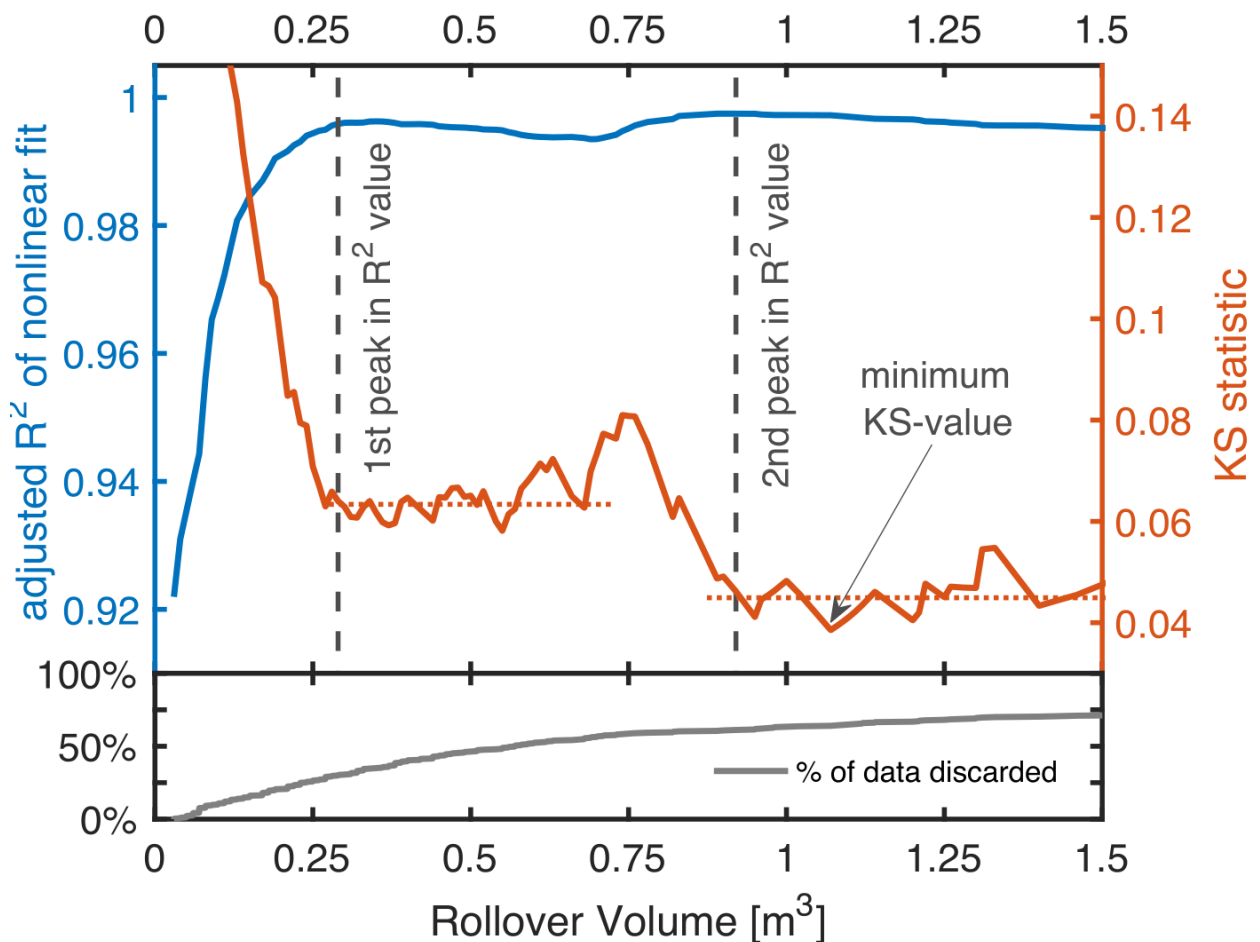
1 Intermediate Timescale (1 kyr) Rockwall Retreat Rate

To calculate the power law predicted retreat rate, power law fit parameters must be defined. Previous studies have shown that above a certain magnitude, the frequency of rockfalls and landslides appears to decay as a power-law (Strunden et al., 2015; Barlow et al., 2012; Dussauge et al., 2003; Guzzetti et al., 2003; Hunger et al., 1999). Below this magnitude, which is commonly referred to as “rollover”, there is no clear trend. The rollover might be due to undersampling of small rockfalls by data collection methods (Lim et al., 2010; Stark and Hovius, 2001) or may have a physical explanation reflecting different slope failure processes (Stark and Guzzetti, 2009; Guthrie and Evans, 2004). To fit a power law distribution of the form:

$$N(V) = a V^b$$

to the observed data, first the rollover value V_o has to be determined before the scaling exponent b can be obtained. Events smaller than the rollover value V_o are excluded in the power law fit. To estimate V_o , two approaches are used: in the first approach, we compute nonlinear fits to the data for all possible rollover volumes. From these, the best fit as determined by the highest R^2 value is selected (blue line in Figure. DR1). The second approach follows the procedure described by Clauset et al. (2007). In this approach, the choice of the rollover volume and its corresponding maximum likelihood

estimate (MLE) for the scaling exponent b are tested using the Kolmogorov-Smirnov (KS) statistic, in which the lowest value describes the best fit (orange line in Figure. DR1). Since both approaches are reasonable but result in quite different rollover volumes (0.29 vs. 1.07 m³, respectively), further investigation is necessary. Figure DR1 shows two peaks in R^2 , corresponding to two levels in the KS value. This implies deviations from pure power law behavior in the observed frequency-magnitude dataset and creates a conflict between intentions to find the best fit results and to retain data. To illustrate, at a rollover volume of 0.29 m³, 30% of recorded rockfalls are discarded in contrast to 64% at a rollover volume



of 1.07 m³.

Figure DR1. Statistical assessments of the goodness of fit: adjusted R^2 for the nonlinear regression and the Kolmogorov-Smirnov (KS) statistic for the Maximum Likelihood (ML) estimate, and how these values change depending on the imposed rollover volume. The lower panel indicates the percentage of recorded rockfalls discarded before the remaining data are fitted.

We further investigate this issue by studying the power law fit results over this range of rollover volumes. Since the position of the lowest KS value is governed mostly by data noise, we substitute the upper limit by the position of onset of the second level in KS and R^2 peak, 0.92 m^3 . Results shown in Figure DR2 reveal a systematic gradient in the scaling exponent b and derived rockfall projections with higher rollover volumes.

For the computation of the scaling exponent b , we compare nonlinear least squares regression fits with MLE, as suggested by Clauset et al. (2009) (Figure. DR2, panel a). We avoided using the linear least squares regression methods in log space as they are known to be sensitive to deviations in the tail of the distribution and to incorrectly underestimate the uncertainty associated with the data (Catani et al., 2016; Clauset et al., 2009). As Figure DR2 shows, the nonlinear regression's 95% confidence interval is substantially smaller than the ML uncertainty calculated after Clauset et al. (2007) and almost fully contained within the latter's confidence band. Furthermore, only the ML uncertainty captures the spread inherent in the data, as illustrated by the systematic gradient depending on the rollover volume. Consequently, we consider the nonlinear regression results as too constrained and report result values in the rest of this study as interval of ML estimates for the aforementioned range of rollover values.

The total long-term eroded volume was obtained by integrating the frequency density of rockfall magnitudes multiplied by the event volume following Barlow et al. (2012). The integration boundaries were chosen based on the minimum rollover volume ($V_{\min} = 0.29 \text{ m}^3$) and the estimated volume of largest historic event ~ 150 years ago ($V_{\max} = 10^4 \text{ m}^3$). Based on the total eroded volume, the corresponding intermediate timescale (power law predicted) wall retreat rate was calculated.

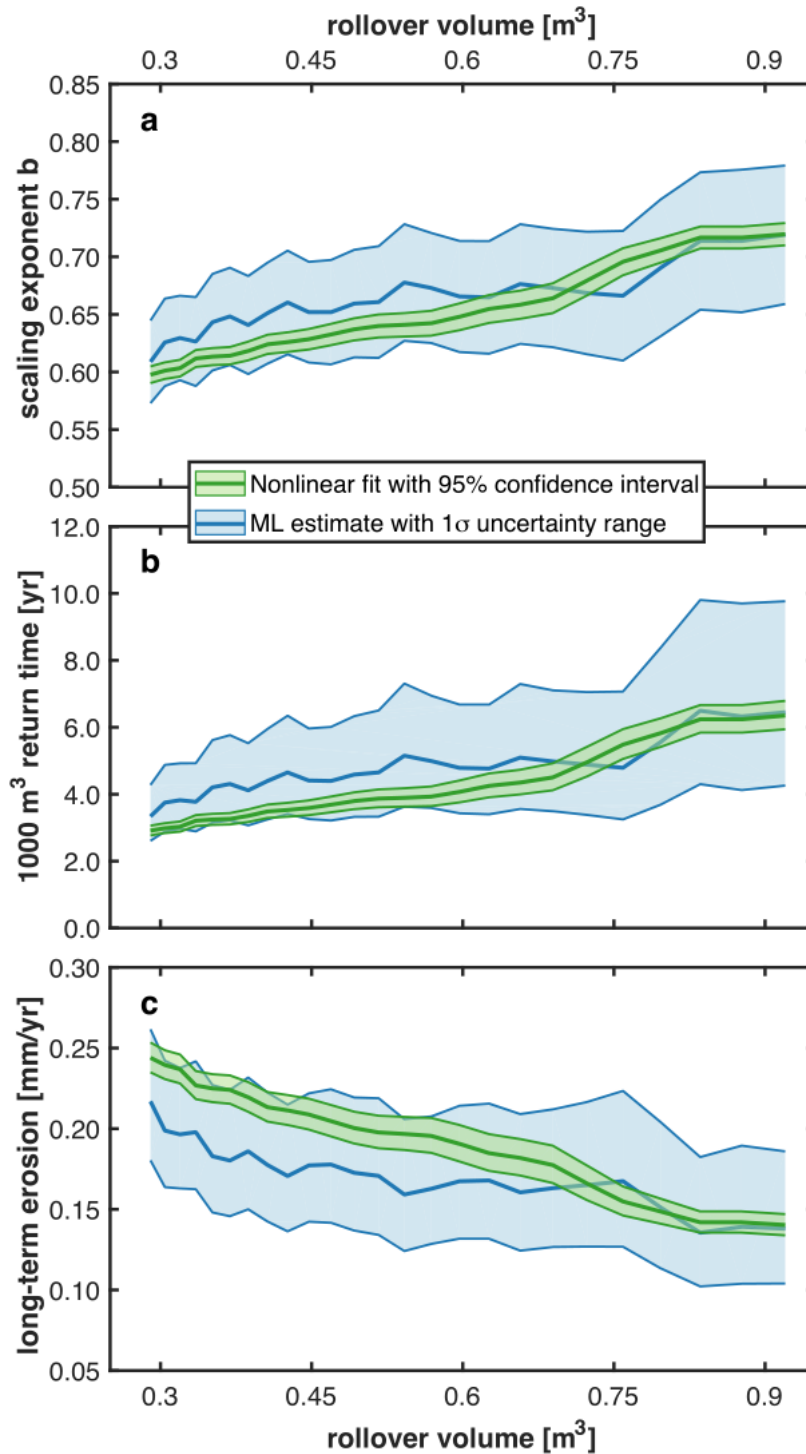


Figure DR2. Variations in (a) scaling exponent *b*, (b) return time of large rockfall events (1000 m³), and (c) the long-term wall retreat rates as function of the rollover volume range determined in Figure. DR1 for both the nonlinear regression and maximum likelihood estimation methods. Error ranges are determined by the regression's 95% confidence interval and a stochastic maximum likelihood uncertainty estimate after Clauset et al. (2007).

2 Long Timescale (11 kyr) Rockwall Retreat Rates

Talus deposits have been used to measure Holocene rockwall retreat rates (Hinchliffe and Ballantyne, 1999; Rapp, 1960; Hoffmann and Schrott, 2002; Siewert et al., 2012). The magnitude of rockwall retreat is calculated by measuring the talus volume, compensating for the density difference between talus bulk and intact bedrock, and dividing by the rockwall surface area. To calculate rockwall retreat rate, the rockwall retreat magnitude is divided by the talus production time (i.e., timespan elapsed since deglaciation). In this study, we selected five talus deposits that have well-constrained lateral extents and are not incised by waterfalls (Figure. 1). However, only three taluses (WT2, WT3, and ET1) were considered in the calculation of Holocene rockwall retreat rate. Talus WT1 and WT4 yield biased retreat rates due to complex morphology and fluvial incision, respectively.

The talus volume is estimated by reconstructing the lateral extent and surface of the talus slopes with TLS data in the JRC software and using shaded relief derived from 2-meter resolution digital elevation model swissALTI3D. Point cloud data corresponding to talus slopes were compiled and filtered to remove vegetation using the curvature filter. This procedure produced a smooth talus surface. Using the topographic meshing tool and an ordinary kriging algorithm, triangle meshes of smoothed talus surfaces were constructed and used in volume calculations. Since the Lauterbrunnen Valley contains up to 550 meters of sediments (Kellerhals and Haefeli, 1985), but only the upper 35 meters have been deposited since the Younger Dryas (Bodmer et al., 1973), the present-day height of the valley floor was set as a boundary between the present-day talus slope and the underlying valley fill when calculating talus volumes. Figure. DR3 summarizes the steps involved in TLS data processing for quantifying talus volumes.

We used a mean density correcting factor of 0.77 to compensate for the density difference between talus and intact rock. This value assumes a talus bulk debris density of 2.0 g/cm^3 and an intact rock density of 2.6 g/cm^3 based on data collected from settings with similar lithologies (e.g., Krautblatter et al., 2012 and Sass and Wollny, 2001).

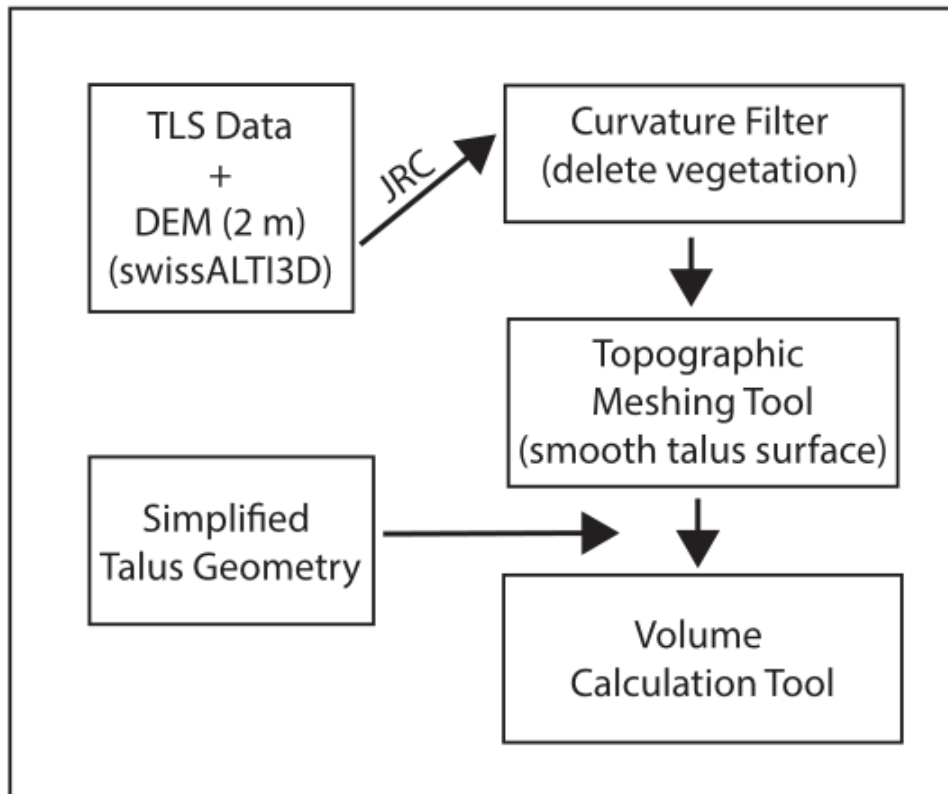


Figure DR3. Workflow for TLS data processing to quantify talus volumes.

The talus accumulation timespan or the time that has elapsed since deglaciation in the Lauterbrunnen Valley is assumed to be 11 kyr. This is based on radiocarbon ages of moraines located in the upper Lauterbrunnen Valley, ~5 km south of Stechelberg (see Figure. 1). These ages indicate that this area was ice-free at 10.39 ± 0.15 ka (Wipf, 2001). Additionally, ^{10}Be surface exposure ages of boulder and bedrock samples from a neighboring trough valley, Hasli, imply that deglaciation was completed in this area at the end of the Younger Dryas at 12.2-10.8 ka (Wirsig et al., 2016).

Rockwall retreat rates calculated from talus volumes are only rough estimates due to the aforementioned assumptions. The largest source of uncertainty is the unknown bedrock profile beneath each talus and the transition from talus deposit to valley infill. To constrain these, and to reduce possible errors, talus deposits with complex morphology

(e.g., WT1), and those that have been significantly modified (e.g., WT4) are removed from wall retreat calculations.

3 Extrapolated Return Period for Large Events

Assuming that the observed volume distribution follows a power law, the distribution can be extrapolated outside the volume range and time window (Dussauge et al., 2002). Following the approach used in Strunden et al. (2015), MLE results are extrapolated. The occurrence of a rockfall event of 10^3 m^3 is predicted to be every 3.34-6.40 years. These return periods, however, do not mean that an event larger than 1000 m^3 will reliably occur every 3-6 years, as it is only an average over long periods. Though these predictions agree with the previously estimated return periods by Strunden et al. (2015), there is a large uncertainty associated with them. This is due to the large extrapolation of rockfall volumes from our dataset (largest event $267.27 \pm 4.39 \text{ m}^3$) to an event of 10^3 m^3 . Furthermore, the rockfall distribution law may vary over time. The observation duration of 5.2 years is not much longer than the event recurrent period, and therefore, the temporal variability of rockfall distribution cannot be fully assessed. In addition, rockfall activity may depend on loading conditions such as climate, leading to temporal fluctuations of rockfall activity and power law exponents. A larger time window for rockfall activity may be achieved by utilizing historical datasets, provided they are accurate and complete.



Figure DR4. (A) The U-shaped deglaciated Lauterbrunnen Valley with steep limestone walls (looking toward the south from Wengen). (B) An example of a near-vertical rockwall.

Supplementary Table DR1. Summary of Rockfall Data Presented in Figure. 2.

| | Total # of rf* | Total # of rf* (West Wall) | Total # of rf* (East Wall) | Smallest rf* Event m ³ | Largest rf* Event m ³ | Mean rf* Volume m ³ | Median rf* Volume m ³ |
|---------------------------------|-------------------|----------------------------------|-------------------------------------|--------------------------------------|-------------------------------------|-----------------------------------|-------------------------------------|
| February/May 2012 ^a | 24 | 14 | 10 | 0.06 ± 0.01 | 6.24 ± 0.55 119.34 ± | 1.28 | 0.97 |
| June/December 2012 ^a | 32 | 25 | 7 | 0.08 ± 0.01 | 1.70 | 7.77 | 0.57 |
| January/March 2013 ^a | 37 | 26 | 11 | 0.13 ± 0.01 | 19.61 ± 0.71 | 2.13 | 0.44 |
| April/July 2013 ^a | 29 | 19 | 10 | 0.14 ± 0.04 | 80.74 ± 1.13 | 5.72 | 0.82 |
| July/September 2013 | 1 | 1 | 0 | 0.1 ± 0.01 | 0.1 ± 0.01 | 0.10 | 0.10 |
| November 2013/February 2014 | 17 | 12 | 5 | 0.06 ± 0.004 | 267.27 ± 4.39 | 19.41 | 0.28 |
| February/April 2014 | 12 | 7 | 5 | 0.03 ± 0.004 | 2.34 ± 0.09 | 0.32 | 0.12 |
| April/May 2014 | 9 | 5 | 4 | 0.06 ± 0.01 | 3.87 ± 0.13 | 1.29 | 1.07 |
| May/September 2014 | 23 | 20 | 3 | 0.05 ± 0.003 | 5.57 ± 0.28 | 0.76 | 0.21 |
| September 2014/May 2015 | 46 | 34 | 12 | 0.04 ± 0.0004 | 258.59 ± 3.68 | 14.18 | 0.45 |
| May/October 2015 | 17 | 12 | 5 | 0.07 ± 0.0004 | 43.68 ± 1.24 | 3.16 | 0.4 |
| October/December 2015 | 5 | 3 | 2 | 0.17 ± 0.01 | 5.21 ± 0.12 | 2.57 | 2.74 |
| December 2015/June 2016 | 41 | 24 | 17 | 0.03 ± 0.003 | 10.49 ± 0.16 | 2.01 | 0.68 |
| June 2016/ April 2017 | 23 | 12 | 11 | 0.17 ± 0.003 | 59.61 ± 0.89 | 6.60 | 0.62 |
| February 2012/April 2017 | 316 | 214 | 102 | 0.03 ± 0.003 | 267.27 ± 4.39 | 4.81 | 0.51 |

rf* = rockfall

^aFrom Strunden et al. (2015)

Supplementary Table DR2: Power Law Fit Parameters and Calculations

| A: Power Law Fit Parameters (CCDF^a) | | NL^b | | MLE^c | |
|--|--|-----------------------|-------------------------------------|------------------------|--|
| Power Law Calculations | mean | 95 % CI ^d | mean | 1 σ error | |
| Exponent b_{\min} @ $V_{ro}^e = 0.29$ | 0.600 | 0.007 | 0.61 | 0.04 | |
| Exponent b_{\max} @ $V_{ro}^e = 0.92$ | 0.720 | 0.010 | 0.72 | 0.06 | |
| CCDF prefactor a for b_{\min} | 21.32 | 0.13 | 20.09 | 0.09 | |
| CCDF prefactor a for b_{\max} | 22.70 | 0.13 | 22.28 | 0.10 | |
| B: Fit Results Extrapolations | | NL^b | | MLE^c | |
| Power Law Calculations | mean | 1 σ error | mean | 1 σ error | |
| 1000 m ³ return for b_{\min} (yr) | 2.91 | 0.15 | 3.34 | 0.84 | |
| 1000 m ³ return for b_{\max} (yr) | 6.4 | 0.4 | 6.4 | 2.8 | |
| Wall retreat rate for b_{\min} (mm/yr) | 0.244 | 0.009 | 0.22 | 0.04 | |
| Wall retreat rate for b_{\max} (mm/yr) | 0.140 | 0.007 | 0.14 | 0.04 | |
| C: Comparison of Results to Previous Studies | | | | | |
| Power Law Calculations | MLE^c (Strunden et al., 2015) | | MLE^c (this study) | | |
| | mean | 1 σ error | mean | 1 σ error | |
| CCDF exponent b | 0.67 | 0.07 | 0.61 - 0.72 | 0.57 - 0.78 | |
| CCDF prefactor per year | 31.90 | 0.90 | 20.1 - 22.3 | 20.0 - 22.4 | |
| 1000 m ³ return time (yr) | 3.10 | 1.50 | 3.3 - 6.4 | 2.6 - 9.8 | |
| Total eroded volume (1000 m ³) 0.001-1000 m ³ | 0.626 | 0.130 | | | |
| Wall retreat rate (mm/yr) 0.001-1000 | 0.12 | 0.03 | | | |
| Total eroded volume (1000 m ³) 0.29-1e4 m ³ | 1.31 | -0.41 + 0.62 | 0.72 - 1.13 | 0.54 - 1.36 | |
| Wall retreat rate (mm/yr) 0.29-1e4 m ³ | 0.25 | -0.08 + 0.12 | 0.14 - 0.22 | 0.10 - 0.26 | |

^aCCDF = complementary cumulative distribution function

^bNL = nonlinear method

^cMLE = maximum likelihood estimate

^dCL = confidence interval

^e V_{ro} = rollover volume

Supplementary Table DR3. Calculated Rockwall Retreat Rates Based on Talus Volumes

| Talus Section | Talus Volume (m3) | Rockwall Area (m2) | Rockwall Retreat Rate (mm/yr) |
|---------------|-------------------|--------------------|-------------------------------|
| WT1 | 6.72E+06 | 2.96E+05 | NA* |
| WT2 | 4.29E+06 | 7.93E+05 | 0.38 |
| WT3 | 3.15E+06 | 6.63E+05 | 0.33 |
| WT4 | 2.10E+06 | 4.37E+05 | NA* |
| ET1 | 2.73E+06 | 7.10E+05 | 0.27 |

* Biased retreat rates due to complex morphology associated with the 1889 mass wasting event (WT1) and fluvial erosion (WT4).

Additional References Cited

Barlow, J., Lim, M., Rosser, N., Petley, D., Brain, M., Norman, E. and Geer, M., 2012, Modeling cliff erosion using negative power law scaling of rockfalls: *Geomorphology*, v. 139, p. 416-424, <https://doi.org/10.1016/j.geomorph.2011.11.006>.

Bodmer, R., Matter, A., Scheller, E., Sturm, M., 1973, Geologische, seismische und pollenanalytische Untersuchungen im Bödeler bei Interlaken: *Mitteilungen Naturforschenden Geellschaft in Bern*, v. 30, p. 51–62, doi:10.5169/seals-319579.

Catani, F., Tofani, V. and Lagomarsino, D., 2016, Spatial patterns of landslide dimension: a tool for magnitude mapping: *Geomorphology*, v. 273, p.361-373, doi:10.1016/j.geomorph.2016.08.032.

Clauset, A., Shalizi, C.R. and Newman, M.E., 2009, Power-law distributions in empirical data: *Society for Industrial and Applied Mathematics Review*, v. 51, no. 4, p. 661-703, doi:10.1137/070710111.

Clauset, A., Young, M. and Gleditsch, K.S., 2007, On the frequency of severe terrorist events: *Journal of Conflict Resolution*, v. 51, no. 1, p.58-87, doi:10.1177/0022002706296157.

Dussauge, C., Grasso, J.-R., Helmstetter, A., 2003, Statistical analysis of rockfall volume distributions: Implications for rockfall dynamics: *Journal of Geophysical Research: Solid Earth*, v. 108 (B6), p. 2286, doi:10.1029/2001JB000650.

Guthrie, R.H. and Evans, S.G., 2004, Analysis of landslide frequencies and characteristics in a natural system, coastal British Columbia. *Earth Surface Processes and Landforms: The Journal of the British Geomorphological Research Group*, v. 29, no. 11, p.1321-1339, doi:10.1002/esp.1095.

Guzzetti, F., Reichenbach, P. and Wieczorek, G.F., 2003, Rockfall hazard and risk assessment in the Yosemite Valley, California, USA: *Natural Hazards and Earth System Science*, v. 3, no. 6, p.491-503.

Hinchliffe, S., Ballantyne, C.K., 1999, Talus accumulation and Rockwall retreat, Trotternish, isle of Skye, Scotland: *Scottish Geographical Journal*, v. 115, p. 53–70, doi:10.1080/00369229918737057.

-
- Hoffmann, T., Schrott, L., 2002, Modelling sediment thickness and rockwall retreat in an Alpine valley using 2D-seismic refraction (Reintal, Bavarian Alps): *Zeitschrift für Geomorphologie, NF Supplementband 127*, p. 153–173.
- Hungr, O., Evans, S.G. and Hazzard, J., 1999, Magnitude and frequency of rock falls and rock slides along the main transportation corridors of southwestern British Columbia: *Canadian Geotechnical Journal*, v. 36, no. 2, p.224-238, doi:10.1139/t98-106.
- Kellerhals, P., Haefeli, C., 1985, *Hydrogeologie Bördeli-Interlaken: Wasser und Energiewirtschaftsamt des Kanton Bern (WEA)*, Bern, Switzerland.
- Krautblatter, M., Moser, M., Schrott, L., Wolf, J. and Morche, D., 2012, Significance of rockfall magnitude and carbonate dissolution for rock slope erosion and geomorphic work on Alpine limestone cliffs (Reintal, German Alps): *Geomorphology*, v. 167, p.21-34, doi:10.1016/j.geomorph.2012.04.007.
- Lim, M., Rosser, N.J., Allison, R.J. and Petley, D.N., 2010, Erosional processes in the hard rock coastal cliffs at Staithes, North Yorkshire: *Geomorphology*, v. 114, no. 1-2, p.12-21, doi:10.1016/j.geomorph.2009.02.011.
- Rapp, A., 1960, Recent development of mountain slopes in Kärkevagge and surroundings, Northern Scandinavia: *Geografiska Annaler*, v. 42, no. 2-3, p. 65–200, doi:10.1080/20014422.1960.11880942.
- Sass, O., Wollny, K., 2001, Investigations regarding Alpine talus slopes using ground-penetrating radar (GPR) in the Bavarian Alps, Germany: *Earth Surf. Process. Landforms*, v. 26, p. 1071–1086. doi:10.1002/esp.254
- Siewert, M.B., Krautblatter, M., Christiansen, H.H., Eckerstorfer, M., 2012, Arctic rockwall retreat rates estimated using laboratory-calibrated ERT measurements of talus cones in Longyeardalen, Svalbard: *Earth Surface Processes and Landforms*, v. 37, p. 1542–1555, doi:10.1002/esp.3297.
- Stark, C.P. and Guzzetti, F., 2009, Landslide rupture and the probability distribution of mobilized debris volumes: *Journal of Geophysical Research: Earth Surface*, v. 114(F2), doi:10.1029/2008JF001008.
- Stark, C.P. and Hovius, N., 2001, The characterization of landslide size distribution: *Geophysical Research Letters*, v. 28, no. 6, p.1091-1094.
- Strunden, J., Ehlers, T.A., Brehm, D., Nettesheim, M., 2015, Spatial and temporal variations in rockfall determined from TLS measurements in a deglaciated valley, Switzerland: *Journal of Geophysical Research: Earth Surface*, v. 120, p. 1251–1273, doi:10.1002/2014JF003274.
- Wipf, A., 2001. Gletschergeschichtliche Untersuchungen im spät-und postglazialen Bereich des Hinteren Lauterbrunnentals (Berner Oberland, Schweiz): *Geographica Helvetica*, v. 56, no. 2, p. 133–144, doi:10.5194/gh- 56-133-2001.
- Wirsig, C., Zasadni, J., Ivy-Ochs, S., Christl, M., Kober, F., Schlüchter, C., 2016, A deglaciation model of the Oberhasli, Switzerland: *Journal of Quaternary Science*, v. 31, p. 46–59, doi:10.1002/jqs.2831.
-

4.4 Determining temporal, spatial and geometric details of rockfalls using terrestrial laser scanning and environmental seismology

4.4.1 Author contributions

The following section of the dissertation has been published and is available online: <https://doi.org/10.5194/esurf-5-653-2017>. The full citation is:

Dietze, M., Mohadjer, S., Turowski, J.M., Ehlers, T.A. and Hovius, N., 2017. Seismic monitoring of small alpine rockfalls—validity, precision and limitations. Earth Surface Dynamics, 5(4), pp.653-668.

The original manuscript is provided in section 4.4.2 and the original electronic supplement file is provided in section 4.4.3.

Five authors contributed to the work presented in this paper: Michael Dietze (MD), Solmaz Mohadjer (SM), Jens M. Turowski (JMT), Todd A. Ehlers (TAE), and Niels Hovius (NH). A summary of the respective contributions is provided in Table 4.4. The detailed contributions are as follow: MD developed the overall idea, and contributed to seismic survey fieldwork and data processing. SM contributed to TLS fieldwork and data processing. JMT, TAE and NH contributed to equipment provision, project planning and data analysis. Manuscript writing and Figure preparation was mostly done by MD with inputs from all co-authors. SM prepared Figure 4 in the manuscript.

Table 4.4: Summary of contributions to joint work for the paper “Seismic monitoring of small rockfalls- validity, precision and limitations”, indicating the average fraction of work of the respective author in percentage.

| Author | Position | Scientific Ideas (in %) | Data generation (in %) | Analysis and Interpretation (in %) | Paper writing (in %) |
|--------|----------|-------------------------|------------------------|------------------------------------|----------------------|
| MD | [1] | 50 | 80 | 50 | 80 |
| SM | [2] | 20 | 20 | 20 | 5 |
| JMT | [3] | 10 | 0 | 10 | 5 |
| TAE | [4] | 10 | 0 | 10 | 5 |
| NH | [5] | 10 | 0 | 10 | 5 |

4.4.2 Paper (co-authorship): “Seismic monitoring of small alpine rockfalls – validity, precision and limitations”

Earth Surf. Dynam., 5, 653–668, 2017
<https://doi.org/10.5194/esurf-5-653-2017>
 © Author(s) 2017. This work is distributed under
 the Creative Commons Attribution 3.0 License.



Earth Surface
Dynamics

Open Access
EGU

Seismic monitoring of small alpine rockfalls – validity, precision and limitations

Michael Dietze¹, Solmaz Mohadjer², Jens M. Turowski¹, Todd A. Ehlers², and Niels Hovius¹

¹GFZ German Research Centre for Geosciences, Section 5.1 Geomorphology, Potsdam, Germany

²University of Tübingen, Department of Geosciences, Tübingen, Germany

Correspondence to: Michael Dietze (mdietze@gfz-potsdam.de)

Received: 28 February 2017 – Discussion started: 16 March 2017

Revised: 7 September 2017 – Accepted: 12 September 2017 – Published: 16 October 2017

Abstract. Rockfall in deglaciated mountain valleys is perhaps the most important post-glacial geomorphic process for determining the rates and patterns of valley wall erosion. Furthermore, rockfall poses a significant hazard to inhabitants and motivates monitoring efforts in populated areas. Traditional rockfall detection methods, such as aerial photography and terrestrial laser scanning (TLS) data evaluation, provide constraints on the location and released volume of rock but have limitations due to significant time lags or integration times between surveys, and deliver limited information on rockfall triggering mechanisms and the dynamics of individual events. Environmental seismology, the study of seismic signals emitted by processes at the Earth’s surface, provides a complementary solution to these shortcomings. However, this approach is predominantly limited by the strength of the signals emitted by a source and their transformation and attenuation towards receivers. To test the ability of seismic methods to identify and locate small rockfalls, and to characterise their dynamics, we surveyed a 2.16 km² large, near-vertical cliff section of the Lauterbrunnen Valley in the Swiss Alps with a TLS device and six broadband seismometers. During 37 days in autumn 2014, 10 TLS-detected rockfalls with volumes ranging from 0.053 ± 0.004 to 2.338 ± 0.085 m³ were independently detected and located by the seismic approach, with a deviation of 81^C₂₉ m (about 7 % of the average inter-station distance of the seismometer network). Further potential rockfalls were detected outside the TLS-surveyed cliff area. The onset of individual events can be determined within a few milliseconds, and their dynamics can be resolved into distinct phases, such as detachment, free fall, intermittent impact, fragmentation, arrival at the talus slope and subsequent slope activity. The small rockfall volumes in this area require significant supervision during data processing: 2175 initially picked potential events reduced to 511 potential events after applying automatic rejection criteria. The 511 events needed to be inspected manually to reveal 19 short earthquakes and 37 potential rockfalls, including the 10 TLS-detected events. Rockfall volume does not show a relationship with released seismic energy or peak amplitude at this spatial scale due to the dominance of other, process-inherent factors, such as fall height, degree of fragmentation, and subsequent talus slope activity. The combination of TLS and environmental seismology provides, despite the significant amount of manual data processing, a detailed validation of seismic detection of small volume rockfalls, and revealed unprecedented temporal, spatial and geometric details about rockfalls in steep mountainous terrain.

1 Introduction

Rockfall is a dominant geomorphic process shaping the steepest slopes and landforms that constitute significant portions of mountainous terrain. Despite their small volumes (10^1 – 10^3 m³) in comparison with other mass wasting processes, such as rock avalanches (10^2 – 10^5 m³) and rockslides ($> 10^6$ m³) (Krautblatter et al., 2012), rockfalls can pose a significant hazard, due to their rapid evolution, high velocity and impact energy, and proximity to infrastructure. Thus, precise information on released volume, timing, location, dynamics and triggers is essential for understanding the underlying mechanisms, improving process-based models, and building robust mitigation and early warning systems. The unpredictable occurrence of rockfalls hinders detailed investigation of their dynamics and drivers under natural conditions. Direct observation of events is rare and restricted to, for example, the Yosemite Valley, with thousands of camera-equipped tourists per day (Stock et al., 2013). Typical approaches to deliver information about rockfalls are deterministic and probabilistic susceptibility analysis, predictive modelling, a posteriori mapping of detachment zones, released volumes and pathways by aerial and satellite imagery or repeated terrestrial laser scan (TLS) surveying (Volkwein et al., 2011). The last of these techniques (Ring, 1963) provides high-resolution spatial data of topographic change attributable to rock detachment (e.g. Rabatel et al., 2008; Zimmer et al., 2012; Strunden et al., 2014) but is time consuming during recording and evaluation and primarily suited for monthly to annual lapse times. Over the integration time between two consecutive scans it is possible to identify spatial activity patterns, released volume ranges and magnitude–frequency relationships (Strunden et al., 2014). However, multiple rockfall releases from the same location cannot be resolved. Likewise, the relation between processes and external triggers remains obscured by the relatively coarse time resolution associated with many repeat TLS studies. Hence, insight into the individual stages of a single event (i.e. detachment, fall, impact and disintegration, duration, multiple failures) is also not possible.

Seismic methods provide a solution for this shortcoming. Broadband seismometer networks have been used to detect and locate a wide variety of Earth surface processes, such as landslides (e.g. Dammeier et al., 2011; Burtin et al., 2013; Ekström and Stark, 2013), rockslides and rock avalanches (e.g. Hibert et al., 2011; Lacroix and Helmstetter, 2011), debris flows (Burtin et al., 2014) and bed load transport in rivers (e.g. Burtin et al., 2008; Gimbert et al., 2014). This emerging research field and the use of seismic noise cross-correlation methods to investigate the states and changes of subsurface conditions are referred to as environmental seismology (Larose et al., 2015). Recent studies (e.g. Helmstetter and Garambois, 2010; Hibert et al., 2011; Burtin et al., 2014; Farin et al., 2015) have focused on monitoring activity at catchment or sub-catchment scale, usually either with

limited validation against independent data, focusing on detachment volumes above 10^3 m³, or working under very controlled, laboratory-like experimental conditions.

Combining TLS and seismic data may provide essential and complementary information on rockfall dynamics and characteristics. This could allow assessing the performance of the seismic approach in terms of correctly identified events, missed events, additional events and spurious events. Further, the combined approach could contribute information beyond the TLS data, such as the existence of rockfalls from the same location but subsequent activity periods or insight into individual stages of a rockfall sequence. In this study, we investigate the validity of environmental seismology to detect and locate rockfall events that are independently identified by TLS surveys in a steep valley of the European Alps. This validation includes exploring the limits of seismic detection in terms of rockfall size and the accuracy of individual event location.

2 Study area

The Lauterbrunnen Valley in the central Swiss Alps is a deglaciated U-shaped valley. It is flanked by up to 1000 m high, Mesozoic limestone cliffs with sometimes almost vertical walls (88.5°) and several hanging valleys that host more than 70 waterfalls. Talus slopes at the base of the cliff, reaching around 150 m above the valley floor, argue for substantial and sustained rockfall. The steepest wall section separates the town of Mürren above the cliff from the town of Lauterbrunnen in the valley (Fig. 1). Our study focused on this wall, which has minimal snow and vegetation cover throughout the year. The surrounding area contains further rockfall-prone locations that can deliver rockfall signals, such as the steep slopes of the Chânelegg and the ridge south of the Ägertenbach (Fig. 1a). The steep topography of the Lauterbrunnen Valley with a few small ledges (Fig. 4b) implies a significant free-fall phase of detached rocks, followed by rock mass impacts on the cliff face or the talus slopes below, eventually grading into moderate translocation processes on the less than 250 m long depositional areas. Rockfall activity in the Lauterbrunnen Valley has been monitored by repeated TLS since 2012 (Strunden et al., 2014), yielding 122 detected rockfalls (523.72 m³ in total) over an 18-month investigation period. These events appear to be evenly distributed throughout valley walls (15.13 events per year and km²) with most frequent events being smaller than 1 m³.

3 The seismic view on rockfall

The seismic approach to studying Earth surface processes (Fig. 2, i.e. event 7 from Table 1) utilises the ground motion recorded by a network of sensors. These signals can be studied in the time domain (i.e. time series of ground velocity) and frequency domain (i.e. the frequency spectrum

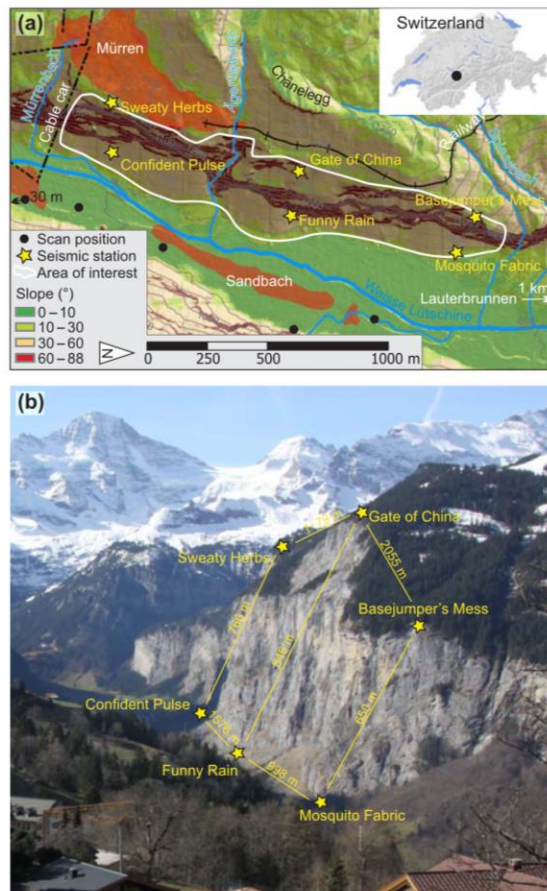


Figure 1. The study area Lauterbrunnen Valley. (a) Schematic map with location of seismic stations, TLS positions and anthropogenic noise sources (settlements, technical infrastructure). (b) Photograph of the instrumented east-facing cliff face of the Lauterbrunnen Valley with the Breithorn and Tschingelhorn in the background. Seismic stations (yellow stars) are separated by 1200 m on average.

of the entire signal), or in combination (i.e. spectrograms, stacked spectra of time slices of the signal). A rockfall event manifests as a series of short and long pulses of ground velocity above the ambient background noise level (Fig. 2a), with characteristic frequency contents over the entire frequency band above 5 Hz (Fig. 2b), usually dominated by the 10–30 Hz band (e.g. Hibert et al., 2014). This characteristic pattern makes rockfalls distinct from other seismic sources, such as earthquakes and anthropogenic noise. The individual pulses and their spectral properties can be interpreted genetically, e.g. as successive rock mass impacts, fragmentation and subsequent slope activity (e.g. Burtin et al., 2014; Hibert et al., 2014). Each signal pulse, emitted at a source location, travels predominantly as a surface wave (e.g. Dammeier

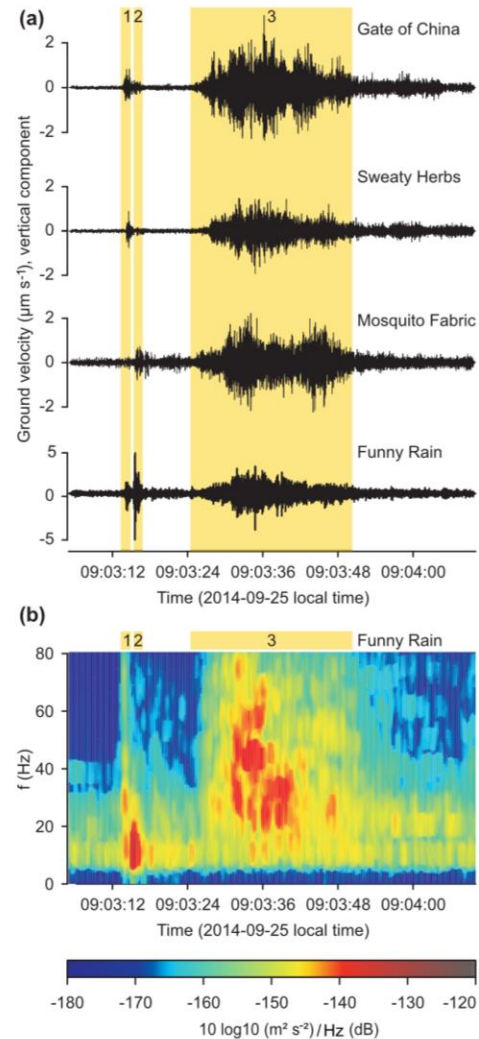


Figure 2. Anatomy of a $0.891 \times 0.038 \text{ m}^3$ large rockfall event (event 7 from Table 2). (a) Seismic waveforms of four stations filtered between 1 and 90 Hz of four stations (see Fig. 1 for locations). (b) Power spectral density estimate of station "Funny Rain". Two distinct, short seismic activity phases (yellow polygons 1 and 2) are followed by an emergent and prolonged period of activity (yellow polygon 3) after 7.5 s of calm.

et al., 2011; Levy et al., 2015; Burtin et al., 2016) with a finite velocity. Thus, in a homogeneous medium, the seismic signal arrives at different seismic stations at different times and with systematic, frequency- and distance-dependent changes of the signal properties. These property changes can be significantly altered due to heterogeneous rock and structure characteristics in natural environments. Nevertheless, the time offsets with which signals are recorded at the stations al-

lows finding a location in space that best explains the overall spread of signal arrival times at all stations. Thus, seismic signals have the potential to deliver unique, important information about rockfall dynamics and location, if comparison with independent data can confirm the validity of the approach.

4 Methods

4.1 Equipment and deployment

High-resolution point clouds with a limit of detection (i.e. the smallest resolvable length fraction at the cliff surface) of about 11 cm were generated by TLS, using an Optech ILRIS-LR terrestrial light detection and ranging scanner with a scan frequency of 10 kHz and a reflectivity of 80 % at 3 km distance. Scans were recorded during two field campaigns on 22 September 2014 and 28 October 2014. The TLS data collection and processing approach used in this study is identical to that of previous work conducted in the same study area (for details see Strunden et al., 2014). To ensure sufficient overlap and to avoid topographic shading effects, the study area was scanned from five different positions (see Fig. 1a).

Seismic activity was measured by six Nanometrics Trillium Compact 120s three-component broadband seismometers. The ground velocity signals were recorded with Omnirecs Cube ext³ data loggers, sampling at 200 Hz, with gain set to 1 and a GPS flush time of 30 min. Deployment sites were chosen to optimise the potential for rockfall location along the east-facing rock wall below the town of Mürren. Stations were separated from each other laterally by 1000–2050 m and vertically by 650–850 m. Three stations were deployed along the upper limits of the talus slopes at the cliff base and three stations on top of the cliff (Fig. 1). Each seismic sensor was installed in a small hand-dug pit at 30–40 cm depth. Seismic activity was recorded for 89 days, between 1 August and 28 October 2014. In this study only the period bracketed by the two TLS surveys is analysed (22 September–28 October). For event location a digital elevation model (DEM) of the wider study area with 5 m grid size (swissALTI3D) was used, transformed to the UTM coordinate system and resampled to 10 m grid size.

4.2 TLS data processing

Point clouds were processed with the “Joint Research Center 3-D Reconstructor 2” software (Gexcel, 2017), adjusted manually and merged using visually unaffected control points along the cliff and a best-fit algorithm to minimise differences in the overlapping data. Rockfall detachment locations and volumes were calculated from the two data sets using the inspection tool and the cut and fill algorithm. Photographs recorded during scanning were used to confirm that the detected volume changes were not caused by processes other than rockfall (e.g. vegetation growth). Measurement

uncertainty was estimated based on scan differences from stable control regions (for details see Strunden et al., 2014). Detachment area coordinates were obtained by georeferencing the rasterised point cloud data on referenced topographic maps and orthoimages. Given the typical rockfall volumes < 1 m³ (Strunden et al., 2014), location uncertainty should mainly result from the georeferencing process and is quantified by the root mean square error (RMSE). All location coordinates were rounded to the full metre and transformed to the UTM coordinate system.

4.3 Seismic data processing: event detection

A single seismic station records 200 samples per second and geometric signal component, resulting in more than 311 million measured values per day. Hence, potential rockfall events must be identified (picked) automatically from the stream of data before they can be located and described (Fig. 3). However, for rockfall events with volumes usually below 1 m³ (Strunden et al., 2014) it is challenging to find reasonable parameter settings for any picking algorithm. Therefore, the seismic time series of all operating stations were manually screened during a control period, 22 September–1 October, to find reference events for parameter definitions.

We used an STA-LTA-ratio algorithm (Allen, 1982), calculating the continuous ratio between a long-term moving average (LTA) and a short-term moving average (STA) of the signal envelope. When the onset of an event is recorded, it will not affect the LTA value but have a significant effect on the STA value, thus increasing the ratio. When the seismic signal returns to background, the STA values approach the LTA value again, which lowers the ratio towards one. The STA-LTA-ratio picker thus has four relevant parameters: the sizes of the STA window and LTA window, a threshold value to define the start of an event and another threshold value to define the end of an event (Fig. 3).

In the case of the Lauterbrunnen Valley, the STA window was set to 0.5 s and the LTA window to 180 s, based on the experiences of Burtin et al. (2014) from another steep mountainous catchment. The window sizes obviously affect the number and timing of the initially picked events. Thus, to be sensitive to short-lasting and low-magnitude rockfall events, we used this short STA versus long LTA value. The threshold values for defining the start and end of an event were adjusted based on manually identified events from the control period (Sect. 5.2). The LTA value was set to constant after an event onset to avoid spurious changes of the ratio for long-lasting events (Burtin et al., 2014).

The STA-LTA-ratio algorithm was applied to the envelope of the bandpass-filtered (third-order Butterworth filter) vertical component signal of the central cliff top station “Gate of China” (Figs. 1, 3). The filter cutoff frequencies were set to 10 and 30 Hz to isolate the typical frequencies of rockfalls and rock avalanches (Helmstetter and Garambois, 2010; Hib-

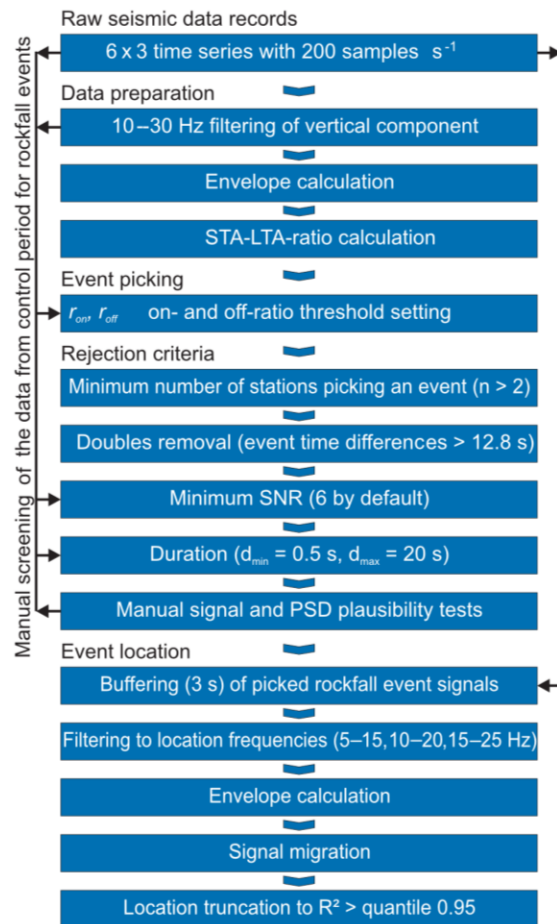


Figure 3. Schematic flow chart of the work flow for seismic data analysis. Arrows along left side of the boxes indicate utilisation of control period data.

ert et al., 2014; Burtin et al., 2014; Zimmer and Sitar, 2015). Since a significant rockfall should be detected by more than one station, we require that all events interpreted are identifiable at this central station. Furthermore, this station was chosen because of its remote location, away from potential sources of anthropogenic and fluvial noise, in order to reduce the initial number of spurious detections. Events that were not co-detected by at least two other stations within a time window of 1.75 s were removed from the data set (Fig. 3). The value of 1.75 s corresponds to the maximum travel time of a seismic S wave within the entire seismic network when using a low S-wave velocity in limestone of 2000 ms^{-1} (Bourbie et al., 1987). This value is also similar to the apparent velocities of local earthquakes and rockfalls as discussed by Burtin et al. (2009) and Helmstetter and Garambois (2010). In general, a rockfall event can consist

of multiple block releases and impacts, and subsequent hill-slope activity, all at different locations. Not accounting for such effects by setting the 1.75 s criteria would introduce artifacts that bias the subsequent location approach. Similarly, if two consecutive picked events showed a time offset smaller than 12.8 s, then only the first one was kept. The selected value of 12.8 s corresponds to the maximum possible free-fall time of a rock mass from the top of the highest cliff part. This ensured that rockfalls with multiple impacts were not identified as separate events. However, this also implies that in the case of two unrelated rockfalls, occurring within this time window, the latter one would be ignored.

Further options to reduce false detections can be setting thresholds for minimum and maximum event duration, signal amplitude variance throughout the network, comparison with existing catalogues (e.g. the Swiss earthquake catalogue), and signal-to-noise ratio (SNR) (Burtin et al., 2014, 2016), the latter being the ratio of the maximum and average value of the signal envelope of an event. However, all these thresholds must be adjusted to an existing data set of potential rockfall events and their effects should be inspected. For the subsequent analysis, minimum and maximum duration as well as SNR were used as rejection criteria, with parameters adjusted based on the control period (Fig. 3, Sect. 5.2).

The waveforms of all remaining events were inspected manually for plausibility, validity and the possibility to locate their source. This included the following criteria (see Fig. 2 for an example of how the criteria are matched): (i) they should not exhibit the typical features of earthquakes, such as distinct P- and S-wave arrivals, a long coda (i.e. the exponentially decaying tail of the signal), frequencies below 2 Hz, and similar amplitudes at all seismic stations for low frequencies; (ii) they must show significant differences in signal amplitudes due to the source receiver distance-related attenuation within the network; and (iii) they should either exhibit the presence of one or more erratic peaks in the seismogram as the result of impulsive impacts (Zimmer and Sitar, 2015) or show an avalanche-like emergent signal, i.e. several seconds rise time of the signal from background, followed by a long decay into background noise after reaching a maximum amplitude (e.g. Suriñach et al., 2005; Vilajosana et al., 2008; Zimmer et al., 2012). The temporal evolution of potential event signals was further inspected using power spectral density (PSD) estimates. These were calculated according to the method of Welch (1967) with moving time windows of 1.4 and 1.1 s to generate the spectra, each with an overlap of 90 %, and the individual spectra were corrected using the multitaper method. Rockfall events typically exhibit a burst of seismic energy over a wide frequency range during the first impulsive impact, possibly followed by subsequent activity in the 10–30 Hz frequency band (Vilajosana et al., 2008; Dammeier et al., 2011; Hibert et al., 2011). The detected potential events should agree with these observations. All successfully evaluated events were used for subsequent analyses.

4.4 Seismic data processing: event location

Locating the source of the seismic signals emitted by rockfalls can be challenging due to the emergent onset of events, superposition of many impact signals, significant high-frequency content, missing constraints on specific seismic wave types and differences between waveform properties at different stations. The latter is due to the preferential signal attenuation of higher-frequency waves, fragmentation of rocks during impact and changing amplitudes with time due to the moving source approaching or passing by a station (Burtin et al., 2013, 2016). Approaches that use the full waveform (Lacroix and Helmstetter, 2011) or its envelope (Burtin et al., 2013) are more appropriate to locate the source of seismic signals resulting from such processes. They are based on calculating average cross-correlations of signal pairs, each shifted by the time delay experienced due to the distance of a grid cell to a seismic station. The grid pixel with the highest overall correlation value is deemed to be the most likely source location. When encountering moving sources, signal migration needs to be performed for each impact signal separately to avoid “blurring” of the location estimate. The probabilistic signal migration approach further requires constraints on the average seismic wave velocity within the area of interest, a suitable frequency window for processing the signals and a topographic correction of the ray paths (Burtin et al., 2013).

Velocity tests were performed with two approaches. For all 37 picked potential rockfall events, the seismic wave velocity within rock was changed between 700 and 4000 m s⁻¹ to inspect its influence on the average cross correlation strength of the signal envelopes at different stations. In a further independent approach we used the TLS-based rockfall detachment locations to evaluate the effect of the different wave velocities considered, based on the average difference between the seismic and TLS locations. This second approach is only possible when independent information of rockfall locations is present and can also be seen as a validation of the first approach.

Similar to the velocity, the frequency band used in the location routine can have an influence on the location estimate. Both parameters are interconnected and may be optimised with respect to the overall highest cross-correlation value of the location estimate. However, in this study the average seismic wave velocity is regarded a global, spatially and temporally constant parameter and was not adjusted for different frequency bands. For rock avalanches along the steeply inclined slopes of the Illgraben catchment and a widely distributed network of nine seismometers, Burtin et al. (2013) chose the frequency window with the highest SNR. In the case of the Lauterbrunnen Valley, the seismic signals were much more heterogeneous among the stations. There was no common frequency with high SNR at all stations. Hence, we used fixed windows of 5–15, 10–20 and 15–25 Hz, depending on the dominant frequency range of the first impact sig-

nals. Usually, an event could be located at comparable positions with all three frequency windows. In that case, the window with the highest cross-correlation value was chosen. In cases where none of the three windows resulted in a stable location along the cliff face or other potential rock release zones inside the study area, the frequency windows were adjusted manually based on the dominant frequency range in the PSD. In a second step, the frequency windows of all events were subsequently adjusted manually to minimise the difference between the seismic and TLS-based location estimates of rockfall events. Obviously, this optimisation is only possible when independent location constraints are present and will have different frequency values for each event. Thus, it is used here to evaluate the appropriateness of the fixed frequency window approach and to explore the maximum possible location precision available with the data, methodology and landscape setting of this specific experiment.

Topography correction is necessary because rockfalls and other gravitational mass wasting processes generate surface waves that propagate following the topography (Dammeier et al., 2011; Hibert et al., 2014; Lin et al., 2015; Burtin et al., 2016). The results of this correction were stored in distance maps. These are station-specific grids of the same resolution as the input DEM (10 m) where the cumulative direct distance of each pixel to a seismic station has been modified by that part where the direct distance was above the actual surface elevation (Burtin et al., 2014). Specifically, the distance between each pixel and station is approximated as a straight line of pixel-sized segments in three-dimensional space (xyz vectors) and whenever the z value (elevation) of a segment is above the DEM-based z value, it is replaced by the latter. The final distance is calculated as the sum of vector magnitudes. To ensure that topographic modification of the wave path is resolved, it is important that the wavelength (i.e. the ratio of wave velocity and frequency) is several times smaller than the average distance between seismic source and the recording station. For typical wave velocities in limestone between 2000 and 3300 m s⁻¹ (Bourbie et al., 1987; Helmstetter and Garambois, 2010) and useful frequencies of 10–30 Hz, the wavelengths are a few hundred metres, which is adequate for the average distance between seismic stations (Fig. 1b).

All picked events were clipped with a buffer of 3 s before and after the event and then migrated. Locations with a cross-correlation value R^2 below the 0.95 quantile were removed and the remaining values were normalised between 0 and 1. Events located along the margin pixels of the distance map of the study area were rejected. Only events inside the area of interest (Fig. 1) were used for validation. The threshold quantile value of 0.95 to clip location areas is arbitrary though in the range of values from the literature (Burtin et al., 2014). The effect of this value on the number of rockfall locations inside the resulting uncertainty polygon was tested by changing the value from 0.9 to 1.0 and recording the number of TLS-based detachment locations and corresponding downs-

lope trajectories, which remained inside the uncertainty polygons.

Location differences $1 P_{\max}$ were calculated as the minimum planform Euclidean distance between the highest value of the seismic location estimate (P_{\max}) and the downslope trajectory line of the corresponding TLS-based detachment pixel. The direction of the trajectory line was defined by the average cliff face azimuth ($99 \square 44^\circ$). This approach was chosen because seismic signals can only be emitted at the detachment zone or rockfall impact sites below it, and since the cliff face is nearly 90° steep there is a high likelihood that the rock mass will follow the line of steepest descent without much deviation. Uncertainties arising from deviations of the rock mass from this line could not be accounted for.

All seismic analyses were performed in the R environment for statistical computing (version 3.3.1) (R Development Core Team, 2015) using the packages *eseis* (Dietze, 2016), *sp* (Pebesma and Bivand, 2005; Bivand et al., 2013; Pebesma and Bivand, 2016) and *raster* (Hijmans, 2016).

5 Results

5.1 Lidar-detected rockfalls

Between 22 September and 28 October, 10 rockfall events were detected by TLS. The events were spread over the entire monitored part of the cliff, but the southern section, near stations “Sweaty Herbs” and “Confident Pulse”, hosted 50 % of all events. The smallest detected rockfall (event 5 in Table 1) had a volume of $0.053 \square 0.004 \text{ m}^3$, while the largest rockfall (event 10 in Table 1) had a volume of $2.338 \square 0.085 \text{ m}^3$. The average volume of rockfalls in this period was 0.482 m^3 . A summary of all rockfall events including location coordinates based on TLS and seismic data is shown in Table 1. With only one exception (event 6), all rockfalls detached from the lower part of the cliff, some almost at the base (Fig. 4b, Table 1). The georeferenced RMSE in the event locations was between 4.8 and 17.5 m. The range in RMSE values calculated depends on the number of identified ground control points (between 8 and 17 per scene) as well as the size and perspective of the referenced image.

5.2 Continuous seismic data processing

Over the entire monitoring period there were always at least four seismic stations operating simultaneously. Due to topographic shielding, the basal stations needed several days after deployment and maintenance to receive a GPS signal, necessary for time synchronisation. Two seismic stations failed during the monitoring period (“Basejumper’s Mess” on 29 August and “Confident Pulse” on 27 September), due to progressive sensor tilting caused by slope movement or sediment settling. However, the remaining stations provided sufficient data for detection and location of events – i.e. all

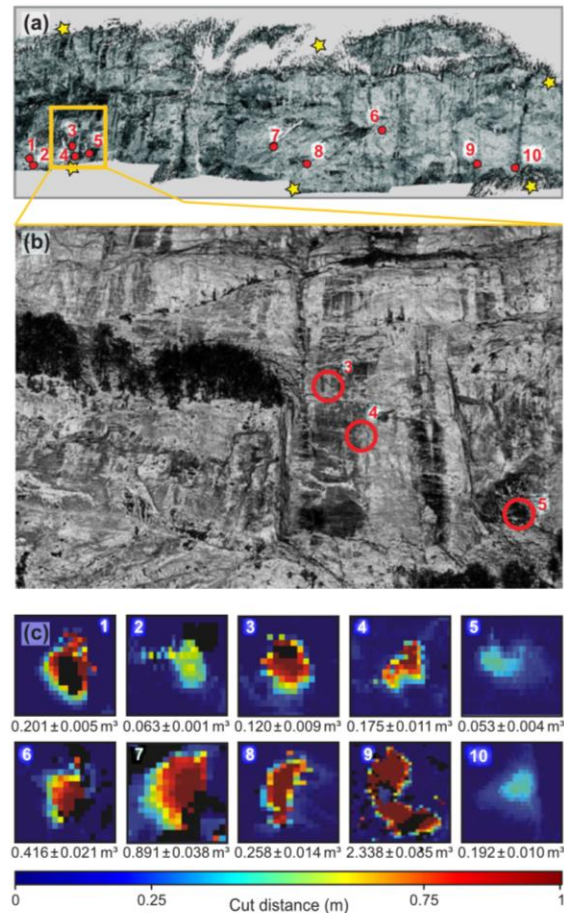


Figure 4. Rockfall detachment zones determined from TLS mapping. (a) Overview (aligned point cloud data) of the about 2.7 km long, instrumented east-facing stretch of the Lauterbrunnen Valley with rockfall detachment zones (red dots) and seismic stations (yellow stars, station names and distances see Fig. 1). (b) Close-up of the southern rock wall section with the detachment zones of events 3–5 at elevations less than 100 m above the talus slope. (c) Boxes show rockfall detachment patterns on the rock wall. Released rock volumes and uncertainties are given below each box. Event numbers are the same as in (a) and Tables 1 and 2.

event descriptions are based on data from four seismic stations.

Manual screening of seismic records during the control period (22 September and 1 October) yielded evidence of two rockfalls, events 7 and 10 of the final data set (Table 2). One of these rockfalls (event 7, Fig. 5b) generated two short, distinct bursts of seismic energy, less than 2 s apart, followed by a rise of the seismic signal about 7.5 s later (see Fig. 2 for details). The first burst contains frequencies between 30 and 60 Hz, while the second peak mainly has frequencies

Table 1. Rockfall location summary. Subscript TLS denotes UTM coordinates from aligned TLS point cloud data. Subscript seis denotes coordinates based on seismic signal processing, i.e. site/point of the highest location probability (P_{\max}). Ranges of z coordinates are determined as min–max range of a 3 by 3 pixel matrix around the detected location. P diameter is the greatest lateral diameter of the location uncertainty polygon (Fig. 9). $1 P_{\max}$ is the deviation of the most likely seismic location estimate from the rockfall trajectory as determined from TLS surveys. The values outside parentheses give deviations with default settings, while values in parentheses give smallest possible deviations with optimised location frequency windows (only possible when independent location data are available).

| ID | x_{TLS} (m) | y_{TLS} (m) | z_{TLS} (m) | V_{TLS} (m ³) | x_{seis} (m) | y_{seis} (m) | z_{seis} (m) | P diameter (m) | $1 P_{\max}$ (m) |
|----|----------------------|----------------------|----------------------|------------------------------------|-----------------------|-----------------------|-----------------------|----------------|------------------|
| 1 | 415 511 | 5 156 535 | 964–1036 | 0.201 \square 0.005 | 415 485 | 5 156 551 | 1063–1119 | 860 | 760 (31) |
| 2 | 415 523 | 5 156 542 | 952–1022 | 0.063 \square 0.006 | 415 505 | 5 156 541 | 1005–1063 | 792 | 50 (18) |
| 3 | 415 541 | 5 156 844 | 1084–1138 | 0.201 \square 0.005 | 415 515 | 5 156 841 | 1141–1192 | 943 | 27 (27) |
| 4 | 415 566 | 5 156 845 | 1018–1100 | 0.175 \square 0.011 | 415 505 | 5 156 871 | 1184–1218 | 968 | 92 (66) |
| 5 | 415 591 | 5 156 934 | 1009–1062 | 0.053 \square 0.004 | 415 635 | 5 156 991 | 999–1054 | 587 | 147 (63) |
| 6 | 415 950 | 5 158 213 | 1170–1314 | 0.416 \square 0.021 | 415 965 | 5 158 241 | 1182–1224 | 687 | 21 (21) |
| 7 | 415 952 | 5 157 829 | 1048–1123 | 0.891 \square 0.038 | 416 015 | 5 157 781 | 907–927 | 858 | 117 (37) |
| 8 | 416 005 | 5 157 897 | 916–1026 | 0.258 \square 0.014 | 416 015 | 5 157 891 | 889–954 | 614 | 251 (4) |
| 9 | 416 116 | 5 158 797 | 919–1002 | 0.192 \square 0.010 | 416 065 | 5 158 811 | 1117–1217 | 498 | 70 (53) |
| 10 | 416 037 | 5 158 649 | 979–1114 | 2.338 \square 0.085 | 416 095 | 5 158 691 | 922–939 | 361 | 60 (52) |

below 20 Hz. The subsequent strengthening signal is again dominated by frequencies between 30 and 80 Hz. The entire sequence was recorded by all operating stations, though with different amplitudes, from about $\square 0.38 \mu\text{s}^{-1}$ at station “Sweaty Herbs” to $\square 4.9 \mu\text{s}^{-1}$ at station “Funny Rain”. The maximum time offset between event onsets at the stations was 0.51 s. The STA-LTA-ratio values reached up to 7 for the first two peaks and decreased below 2 before grading to the next rise.

Based on the above characteristics of event 7 and similar properties for event 10 from the control period, the parameters for event picking of the entire data set were defined, i.e. the STA-LTA-ratio threshold to define the start of an event was set to 5, the threshold for defining the end of an event to 3. Note that this approach does not yield a correct start and end time. However, the location approach is not based on exact onset times but is used with the addition of a 3 s wide buffer before and after an event. The minimum SNR of an event at the picking station “Gate of China” was set to 6.

The instrumented study area comprises many further environmental sources that generate seismic signals with frequencies above 1 Hz. Figure 5a shows a 24 h PSD as an example. From 04:00 to 21:00 (UTC, i.e. 2 h to local time) there are pulses of seismic activity in the 5–80 Hz range, occurring every 20 min. Until 02:00 there is continuous activity with frequencies above 30 Hz and over the day there is a progressively decreasing signal between 5 and 15 Hz, which in general depicts the runoff of the Weisse Lütschine (FOEN, 2017), the main river draining the Lauterbrunnen Valley, and is in agreement with the seismic signature of turbulent water flow (Gimbert et al., 2014). Around 02:45, 05:10 and 17:50 and 18:05 there are seismic events with very low frequency content (maximum energy below 2 Hz). Figure 5c shows that the seismic properties of all these other sources can be very similar to the waveforms of rockfalls. Between 04:00 and

21:00 (UTC) a train runs every 20 min between Mürren and the cable car station of Lauterbrunnen. The passage of this train is recorded in a repeating succession of spikes of seismic energy in the PSD from Fig. 5a. Although this signature is easily discernible because it repeats at expected times during the day (i.e. Swiss trains always run on time), it also shows two distinct peaks that cross the STA-LTA-ratio start and end thresholds for rockfall detection, and it shows similar amplitudes and amplitude differences between the recording stations. Also, the SNR values are comparable with those of rockfalls. The second panel of Fig. 5c shows the impact of rain drops on the ground above the seismic sensor. Attribution of this signal to rain drops is based on the notion that these irregular short pulses only occurred during rainy conditions (Fig. 6a and b) and, furthermore, were predominantly registered by stations under forest cover in contrast to sensors deployed at grass-covered sites (Fig. 6c versus d). We attribute this phenomenon to trees collecting small rain drops and releasing them after some time as larger drops. Trees continue to release such drops even after the atmospheric rain input has stopped. In contrast, grass covered areas receive the precipitation directly and are subject to systematically smaller drops, especially during gentle rain events. The irregular occurrence of the seismic pulses makes an origin due to passing animals or humans unlikely, as one would expect a growing and decreasing amplitude during approaching, passing and leaving the station (a signature inherent to many base jumpers hiking past the stations on top of the cliff during sunny days). The signal of a raindrop is also similar to the rockfall signal although it contains seismic energy over nearly the entire frequency range and lasts less than half a second. Such signals can trigger the STA-LTA-ratio algorithm if they were recorded by chance at more than two stations within the defined maximum time window of 1.75 s. The last panel of Fig. 5c shows an earthquake. The signal

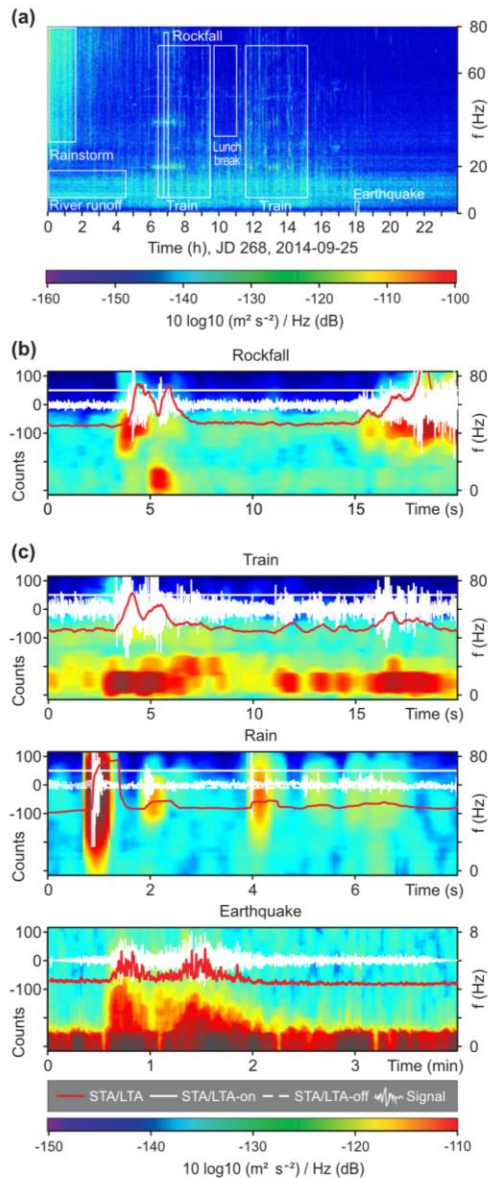


Figure 5. Example day (25 September 2014) showing seismic characteristics of environmental sources in the Lauterbrunnen Valley. (a) 24 h PSD with interpreted sources indicated. Data recorded at station “Mosquito Fabric” and filtered between 1 and 90 Hz. (b) Seismic record of rockfall event 7 (Table 2). (c) Seismic records of other sources registered by the station “Gate of China”. Note change in axes scales for the earthquake event. Panels (b) and (c) contain the PSD (background image; colour bar applies to b and c) and waveform data (semitransparent line graph) as well as the picker algorithm characteristics (STA-LTA-ratio, “on” and “off” thresholds).

of this tele-seismic event is dominated by frequencies below 4 Hz and lasts more than 1 min. There are also local earthquakes in the seismic records that show a more sudden onset, contain higher frequencies and last much less than a minute. But all earthquake signals are clearly different from rockfalls. Their waveforms usually show the distinct arrivals of P and S waves and a coda, their PSDs exhibit a significant portion of energy below 10 Hz, and their waveforms and spectral properties are relatively uniform among records of the different seismic stations.

Thus, to eliminate false events picked by the STA-LTA-ratio approach the minimum duration of an event was set to 0.5 s to remove rain-related picks and the maximum duration was set to 20 s to remove earthquakes. The minimum average SNR value among all stations was set to 6. The STA-LTA-ratio approach yielded a total of 2175 potential events. After application of the automated rejection criteria the number decreased to 511. These 511 events had to be manually screened and included 455 spurious or unknown events, 19 short earthquakes and 37 potential rockfall signals. The most common spurious event type was associated with train traffic. This type of signal could not be eliminated by any automatic routine and had to be removed manually. The remaining earthquakes had an average STA-LTA-based duration of $11:9^{4.6}_{4.0}$ s (median and quartiles) and were also removed manually. The 37 detected potential rockfall events had STA-LTA-based durations of $4:7^{2.8}_{2.0}$ s. Several of the potential rockfall events had very weak seismic signals, with average SNRs below 8 (eight cases), but the majority generated average SNRs of $11:2^{2.8}_{2.6}$.

5.3 Seismic wave velocity estimate

A necessary step for successful location of the potential rockfall events was to find a plausible estimate of the average seismic wave velocity (Fig. 7). Both approaches, optimising the average location estimate value (i.e. R^2 at P_{\max}) and minimising the difference between seismic location and TLS-based coordinates, point at a common value around 2700 m s^{-1} . While for the latter approach the velocity range with minimum offsets is narrow, with not much argument for an uncertainty range, there is no such clear result for the former approach. The solid black lines in Fig. 7 show two velocity ranges with high P_{\max} values, between 1000 and 1800 m s^{-1} and between 2200 and 3000 m s^{-1} . Due to the recent deglaciation and persistent rockfall activity, the limestone cliffs of Lauterbrunnen appear rather compact and only marginally weathered. Thus, there is no reason to assume much lower values than those of 2000 – 3300 m s^{-1} for S waves in limestone from empiric tests (Bourbie et al., 1987). Accordingly, the first local maximum at lower velocities did not yield any consistent rockfall locations along the cliff, even when the other criteria clearly pointed at a rockfall. The average R^2 values for the higher velocity range from a broad plateau of equally likely velocities includ-

Table 2. Rockfall events detected by seismic monitoring. IDs correspond to those in Table 1. Duration as estimated from signal wave form interpretation (not including subsequent talus slope activity). SNR denotes range of signal-to-noise ratios among all recording stations. f_{default} describes the default frequency range for location, and f_{opt} denotes the frequency range after optimisation. A is the amplitude range among the stations.

| ID | Time (UTC) | Duration (s) | SNR | f_{default} (Hz) | f_{opt} (Hz) | A (nm s ⁻¹) |
|----|---------------------|--------------|------------|---------------------------|-----------------------|-------------------------|
| 1 | 2014-10-12 22:45:50 | 1 | 8.7–25.9 | 10–20 | 10.0–23.0 | 1356–11 945 |
| 2 | 2014-10-15 01:58:32 | 4 | 5.2–49.4 | 10–20 | 11.0–21.0 | 1062–4128 |
| 3 | 2014-10-20 19:11:09 | 5 | 10.7–35.8 | 10–20 | 10.0–20.0 | 619–2405 |
| 4 | 2014-10-20 15:05:34 | 7 | 14.0–55.86 | 15–25 | 16.0–26.0 | 722–3229 |
| 5 | 2014-10-22 11:47:28 | 2 | 5.7–11.9 | 10–20 | 11.0–19.9 | 1442–3831 |
| 6 | 2014-10-02 17:59:50 | 4 | 6.48–11.76 | 5–15 | 5.0–16.0 | 1055–2077 |
| 7 | 2014-09-25 07:03:13 | 6 | 7.5–19.9 | 10–20 | 2.8–5.6 | 962–5980 |
| 8 | 2014-10-26 20:08:45 | 2 | 6.0–14.2 | 10–20 | 7.0–13.0 | 1277–306 905 |
| 9 | 2014-10-17 00:09:25 | 8 | 5.5–11.1 | 5–15 | 4.7–15.2 | 828–1806 |
| 10 | 2014-10-01 09:23:05 | 10 | 17.0–59.1 | 5–35 | 1.0–35.0 | 3123–4491 |

ing 2700 m s⁻¹. Thus, based on information from both approaches, the average seismic wave velocity for running the location routine was set to 2700 m s⁻¹. Without the existence of independent locations of rockfall detachment zones, seismic velocity can only be constrained with low uncertainty by active seismics.

5.4 Location of rockfalls

The application of the location routine to the 37 potential rockfall events placed nine of them in the area of interest covered by our TLS surveys and the seismic network (Fig. 1). Eight further events were located along the west-facing valley side. Most of these had poor location constraints due to low SNR or inappropriate fits of the overall time delays of the signal envelopes. The other events could either only be located along the margins of the distance maps as the closest approximation for more distant sources or were located west of the Lauterbrunnen Valley, higher in the catchment. One event, which showed all characteristics of a very proximal rockfall and subsequent rock avalanche but exhibited an extraordinarily wide frequency range (event 10 in Fig. 9), could successfully be located within the area of interest by manually setting the location frequency window to 5–35 Hz.

Thus, after extensive processing and manual verification, all 10 TLS-detected rockfalls could be independently located by the seismic approach. SNRs of all 10 events were above 5 and up to 59, depending on the magnitude of the event and the distance of the source to a seismic station. With the exception of the manually adjusted settings for event 10, the default settings resulted in an average difference between TLS (i.e. line of steepest descent from detachment zone) and seismic location of 81^C₂₉⁵⁹ m. The maximum difference was 761 m (event 1, Table 1) because a significant part of the location estimate polygon for this event, including the location of P_{max} , was placed on the other valley side, separated from the cliff face by the entire valley floor. However, all TLS-based

events were located within the default uncertainty areas defined by the 0.95 quantile, most of which were elongated by several 100 m in the north–south direction in plan view (Table 1). Some areas of uncertainty extend into the valley floor (events 6–8), but most were entirely within the cliff face. In five of the 10 cases, P_{max} is located higher on the cliff than the TLS-based detachment zones (i.e. events 1, 2, 3, 4, 9). We see the main causes for deviations in inhomogeneities of the solid media, resulting in spatially non-uniform seismic velocities. Specifically, there should be a velocity difference between the solid limestone that forms the cliff and the debris fabric that constitutes the talus slopes. Thus, especially impact locations close to or at these talus slopes may be affected by larger deviations because the average seismic velocity successively fails to explain the arrival times of signals at the seismic stations.

Adjusting the frequency windows for the location routine to minimise the differences to the TLS data usually required shifts by less than 4 Hz. Events 7 and 8 required greater adjustments, as low-frequency windows yielded much better results (Table 2). Optimising the location settings resulted in average location differences of 33^C₆²⁰ m with a maximum deviation of 66 m and a minimum deviation of 4 m.

Increasing the quantile thresholds to define the uncertainty polygons for each location estimate reduces their area, which eventually leads to a drop of the number of matches with TLS-based event location (Fig. 8). Up to a threshold value of 0:973, all 10 rockfalls are included in the uncertainty areas.

6 Discussion

6.1 Rockfall detection from continuous seismic data

The challenge of detecting rockfalls with the seismic approach is to identify a few short target signals in month-long records of hundreds of samples per second. This is especially relevant for the small rockfall events of this study. Thus, the

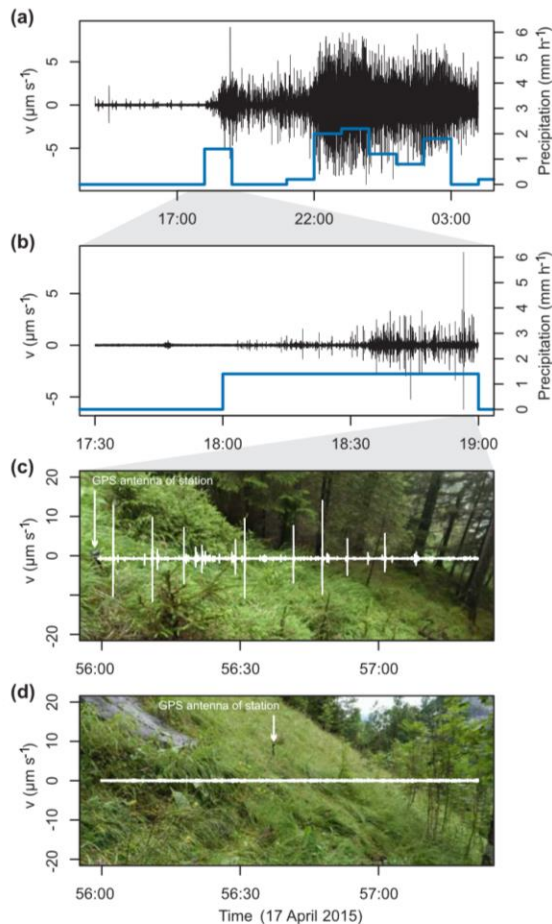


Figure 6. Seismic signal characteristics during a gentle rain event without windy conditions (hourly meteorological data from Meteo-media station in Mürren). Panels (a) to (c) show the vertical component signal (filtered between 1 and 90 Hz) of station “Basejumper’s Mess”. Panel (d) shows the same time interval as (c) but for station “Funny Rain”. Background images of (c) and (d) show the deployment situation of the two stations under a dense coniferous forest cover and on grass land, respectively. Note overall increase in seismic signal amplitudes during the rain event and short irregular signal pulses only under forest cover, interpreted as impacts of large drops collected and amalgamated by the trees. Trees continue to release drops even after the precipitation record shows no further atmospheric rain input (a).

described routine for data processing is neither intended to be nor capable of coming close to automatic detection and location of rockfalls of this size. The workflow of signal processing and analysis significantly reduced the number of initially picked events by a factor of 4. This provided a reasonable base for the subsequent manual identification of likely rockfall events. The STA-LTA-ratio threshold values (i.e. 5 and 3)

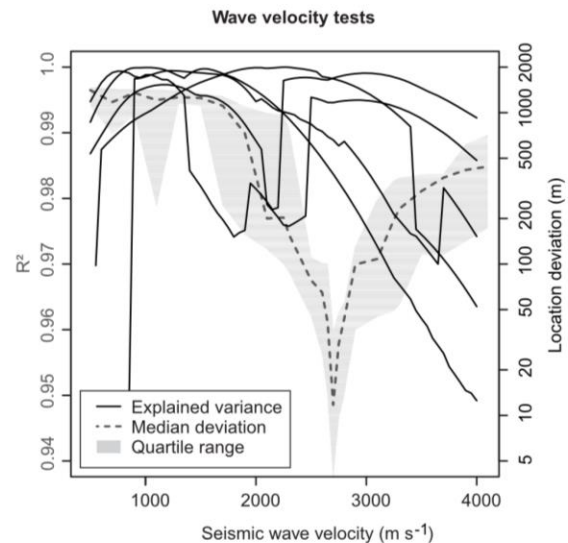


Figure 7. Tests of the most likely average value for the seismic wave velocity. Black solid lines show location approach correlation coefficient (average of all R^2) for velocity values ranging between 700 and 4000 m s^{-1} for all events that reached an $R^2 > 0.94$. The dashed grey line (median) and shaded area (interquartile range) depict deviation of seismically detected from TLS-based event locations. Both measures point at 2700 m s^{-1} as the most likely average seismic wave velocity in the study area. The secondary R^2 maximum at lower velocities did not yield locations inside the area of interest despite high R^2 values.

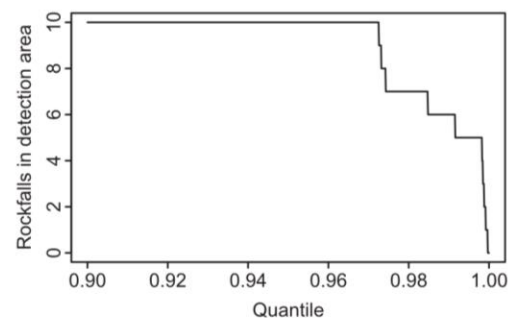


Figure 8. Number of rockfall trajectories inside location estimate polygons as function of minimum location estimate quantile.

as well as the SNR threshold value (i.e. 6), determined from the two manually identified events in the control period, allowed detection of all 10 rockfalls shown by the TLS data, even though all other events involved smaller volumes than the two manually identified ones. The initial filter frequency window for the STA-LTA-ratio approach of 10–30 Hz might have benefited from a lower cutoff frequency since some of

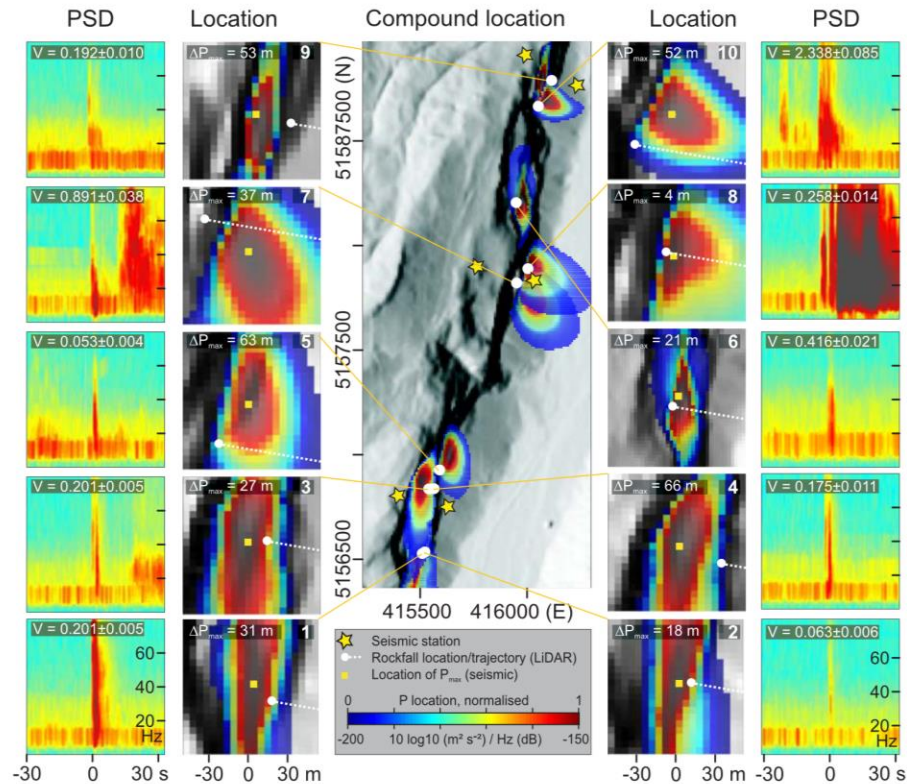


Figure 9. Seismic location of the 10 TLS-based rockfall events. Compound location map shows an overlay of all 10 detected events with coloured polygons corresponding to locations with cross-correlation values above the 0.973 quantile. Location close-up boxes are centred at P_{\max} , i.e. the location with the highest cross-correlation value. PSD boxes show the spectral evolution of each event as recorded by station “Funny Rain”. Event start is indicated by time zero. For event duration see Table 2. $1 P_{\max}$ is the deviation of seismic location estimate from rockfall trajectory along steepest path. Locations of all rockfalls shown based on optimised location frequency windows for illustrative reasons (see Table 1 for default deviations).

the rockfalls showed optimal location frequencies well below this value (Table 1).

The monitored section of the Lauterbrunnen Valley is a comparably noisy environment. The example PSD (Fig. 5a) shows ample signals from sources other than rockfall activity. A major source of falsely picked events was passing trains (87 %). For rockfalls as small as those detected in this study, raising the initial SNR threshold to exclude signals associated with train activity would result in rejecting most of the rockfall events. However, for rockfall volumes one or more orders of magnitude larger, this simple parameter adjustment should yield a significantly better detection result. The 19 detected earthquakes could have been removed based on differences in the relationships between magnitude, duration and frequency content (e.g. Manconi et al., 2016) or multivariate classification approaches (e.g. Provost et al., 2017). However, the duration distributions of rockfalls versus earthquakes already allowed a sufficient discrimination. Thus, al-

though the data processing workflow is far from automatic and leaves 1 order of magnitude more events than the actual number determined from manual evaluation, it provides a systematic and reproducible way to detect rockfalls close to the lower limit of detection.

6.2 Rockfall location

All 10 TLS-based rockfall events were confirmed with an average location error along the rockfall trajectory of 33 m when the frequency window of the location algorithm was adjusted manually. Without this optimisation, which is only possible when reference data are available, the location deviation was 81 m on average. This is comparable with errors of about 80 m from a rock avalanche study on Montserrat, Lesser Antilles, with a network of 11 stations (Levy et al., 2015). However, that study had a larger network aperture and focused on event volumes of 10^3 – 10^6 m³. Instead, rock mass volumes in the Lauterbrunnen Valley were generally well be-

low 1 m^3 and our study had only four operating seismic stations, organised in a topology and station spacing that are comparable to those from other studies (Hibert et al., 2014; Burtin et al., 2016).

The TLS-based detachment locations and their rockfall trajectories are within the areas defined by the 0.95 quantile threshold (Fig. 9). Only when independent constraints on the location of the seismically recorded events are available is it possible to investigate the validity and effectiveness of this arbitrary threshold. In this study area, the threshold can be increased up to 0.973 to still provide a valid uncertainty estimate for possible rockfall locations/trajectories. Effectively, this means that the area of each uncertainty polygon can be decreased by 45 %.

An important issue is that for some rockfalls the best location estimate (P_{\max}) is above the actual rockfall detachment zone. This may be related to the extreme topography of the Lauterbrunnen Valley. The studied rock wall is up to 800 m high, yet it is represented by as little as four plan view pixels in the 10 m DEM and distance maps (cf. ranges of Z_{seis} in Table 1). Arguably, the lateral offset of rockfall location P_{\max} from the line of steepest descent is more important from a hazards point of view.

Assigning the locations of the 10 seismically detected rockfalls to those detected by TLS is unambiguous in most cases. However, rockfalls with comparable volumes from similar detachment heights can be hard to distinguish. For example, events 3 and 4 are located 44 m apart, at 1108 and 1064 m a.s.l., and released 0.201 and 0.175 m^3 of rock, respectively. Accordingly, their seismic waveforms and PSDs (Fig. 9) look very similar and there remains ambiguity about the seismic identification as stated in Table 1. This has consequences for the temporal information associated with the seismic data. But in this case, both events occurred on 20 October, one at 15:00, the other at 19:00. Ambiguity also arises for events 1 and 2. However, there the rockfall volumes allow for a better matching with the seismic results. Event 1 entrained 0.201 m^3 , whereas event 2 mobilised only 0.063 m^3 from a near-identical position and fall height. Accordingly, the emitted seismic energy of event 1 should be significantly higher than event 2, which is reflected in the corresponding PSD, where event 1 shows a much longer and more powerful signal. Hence, if the geometric properties of the released rock masses are sufficiently distinct, it is possible to disentangle nearby events from the detailed seismic information.

For large ($> 10^4\text{ m}^3$) gravitational mass wasting processes there appear to be robust relationships between released volumes and a series of seismic attributes (Dammeier et al., 2011; Ekström and Stark, 2013). However, such large events affect significant areas, even entire slopes. In contrast, the small volumes mobilised in the Lauterbrunnen Valley do not show such clear volume-based relationships (apart from the one example described above). The largest event (2.338 m^3) did not yield the highest signal intensities or longest duration, and vice versa for the smaller events. The combination

of released volume; detachment height above cliff base; the number, distance and strength of intermediate impacts; the degree of fragmentation during the fall phase; and the fate to the rock mass on the talus slope (direct deposition, subsequent downhill translocation, entrainment of impacted talus) resulted in a polymorphic seismic signal, which complicates direct links of seismic parameters with geometric or kinetic properties of the detected rockfalls at this spatial scale. To explore such questions about relations among volume, detachment height, fragmentation and debris entrainment upon impact – all obviously more useful for larger rock volumes than found in this study – the combination of TLS and seismic monitoring provides all necessary sources of information. The high temporal resolution and ability to detect small volumes makes especially the seismic technique particularly interesting for studies of relations between rockfalls and environmental conditions that are suspected to cause them (Dietze et al., 2017).

The apparent seismic detection limit for rockfall volumes in the Lauterbrunnen Valley is well below 1 m^3 . This is remarkable given that the stations are mostly more than one km apart and that most of the rockfalls used for validation originated at the lower cliff parts, resulting in limited kinetic energy upon impact. Location feasibility is, however, not only determined by the rockfall volume and drop height. The distance between impact location and location of the seismic stations, the inelastic attenuation properties of the rock and the energy dissipation due to rock fragmentation (e.g. Hibert et al., 2011) also determine the potential to successfully locate the rockfall. The possibility to analyse rockfalls as small as 0.053 m^3 , impacting at distances of 170–1950 m from the seismic stations, makes seismic monitoring a method that is able to reveal events well below the resolution of most other post-event survey techniques, such as aerial and satellite imagery analysis.

Unlike other rockfall survey techniques, seismic methods allow for monitoring of rockfalls with high temporal resolution, down to fractions of a second. During the first half of the monitored month only two rock masses were released, while the other half of the month saw the majority of events. Beyond this, the high temporal resolution allows connecting the events to ambient conditions and trigger mechanisms and studying process interactions (e.g. Helmstetter and Garambois, 2010; Burtin et al., 2014; Zimmer and Sitar, 2015).

6.3 Rockfall anatomies

Seismic monitoring allows detailed insight into the dynamics of rockfalls. The exemplary event (Fig. 2) consisted of three distinct phases and lasts in total for almost a minute. Phase 1 (less than 1 s duration) is the first notable seismic activity after minutes of calm at all stations. It reflects the seismic signal associated with initiation of the rockfall event. The high-frequency content may correspond to either the rebound of the cliff after detachment of the mass (e.g. Hibert et al.,

2011) or the opening and propagation of fractures rather than impacts of a moving rock mass. The latter interpretation is supported by seismic records from the Illgraben, Rhone Valley, Switzerland, that show an exponentially increasing density of signals, which indicate cracking or fracture propagation (Zeckra et al., 2015) starting days before a 10^4 m^3 large rock avalanche took place (Burtin et al., 2016). The spectral properties of these signals (short, less than 1 s pulses at 20–50 Hz), recorded by a seismic station about 150 m away from the initiation zone of the rockslide are very similar to the first phase of the rockfall from the Lauterbrunnen Valley (Fig. 2).

Phase 2 (1 s duration) begins 1.7 s after this fracture propagation phase and may reflect the impact of the released rock mass on the cliff face. The predominantly low-frequency content implies that the mass is still intact upon the first collision. Low frequencies can only be generated by large rock masses that convey a high momentum rather than a series of smaller particles hitting a surface simultaneously (Burtin et al., 2016). The strong impact likely caused fragmentation of the rock, because there is no low-frequency content in any of the later signals from this event. The rock fragments experienced a free-fall phase (calm period in all signal waveforms) of approximately 7.5 s, corresponding to a drop height of 271 m. With a detachment elevation between 1048 and 1123 m a.s.l. this places the impact somewhere in the central part of the talus slope that reaches from 910 m a.s.l. at the cliff base to 820 m a.s.l. on the valley floor.

Phase 3 (about 40 s duration) represents the continuous impact of the fragmented rock mass on the talus slope for tens of seconds. This activity very likely graded into a phase of downslope translocation of debris and entrainment of further talus. The PSD of phase 3 shows the typical properties characteristic of rock avalanches (e.g. Suriñach et al., 2005).

Similar insights into the anatomy of events are possible for the remaining nine rockfalls, though often with less rich detail or variability. Readers are invited to explore the data contained in the Supplement. This one anatomy of an example event highlights the universality of seismic sensors to investigate the dynamics of a rapid mass wasting process at a level of detail that would otherwise require an expensive and time-consuming multi-sensor approach, consisting of, for example, video imagery, prior and a posteriori TLS scans, perhaps further acoustic sensors, and post-event field mapping. Furthermore, the area of interest can only be small to be covered by these alternative techniques. Thus, the installation must be placed at “the right spot”, instead of relying on the flexibility to monitor a wider area with a seismic network.

7 Conclusions

The detachment locations of 10 rockfall events, as small as $0.053 \square 0.004 \text{ m}^3$ and totaling a volume of $4.789 \square 0.100 \text{ m}^3$, were detected by TLS over 37 days. Using broadband seismometers, these events were independently detected and lo-

cated with an average deviation of 81^{C59}_{29} m . Further seismic rockfall signals were detected and located outside this instrumented cliff area. The seismic signatures allow (i) insight into the dynamics of single events, (ii) quantification of the exact event onset time and duration, and (iii) calculating minimum fall heights. It is thus possible to monitor rockfalls *sensu stricto* with a significant free-fall phase and a pronounced short impact phase. This extends the previous field of applications of environmental seismology to more extreme settings. Our results suggest that seismic monitoring with a network geometry comparable to other natural-scale experiments (e.g. Lacroix and Helmstetter, 2011; Burtin et al., 2014) is a valid approach to catchment-wide detection, location and characterisation of Earth surface activity in an exceptionally steep terrain. Our data complement work that has focused on the coupling of rockfall to other processes in the sediment cascade of mountainous landscapes (e.g. Krautblatter et al., 2012).

Further advantages of seismic rockfall monitoring are (i) its ability to detect events independent of visibility conditions, a major limitation of remote sensing techniques, including time lapse camera surveys, and (ii) the large size of the area that can be monitored with a limited number of stations.

The main limitations of this approach include that estimates of rock volume based on the emitted seismic energy or peak ground acceleration were not possible for the small rockfall events identified in this study. This was mainly due to the influence of intrinsic factors, such as the proportion of energy consumed for fragmentation during the event or contribution of mobilised debris to the seismic signals upon impact on the talus slope. A further challenge is the high effort due to manual removal of false events under such conditions. This drawback represents a serious issue when attempting fully automated approaches of rockfall detection.

While the combined description of event location and precise timing information of rockfall activity would provide access to trigger mechanism analysis in principle (Dietze et al., 2017), the number of detected events from this study is too small for this goal. At larger scales (regarding released volumes and monitored area) there are first-order effects that allow relating seismic metrics to process parameters (e.g. Hibert et al., 2011; Dammeier et al., 2011; Ekström and Stark, 2013). Thus, when increasing the monitored area and focusing on larger released volumes ($> 10^4 \text{ m}^3$), environmental seismology could become a real alternative to classic rockfall observatory instruments, with the capability to go beyond these by simultaneously recording proxies of environmental triggers and resolving process coupling and interaction.

There is a potential to optimise the parameters for event location but there is no straightforward way to do this without independent auxiliary information. Hence, a realistic location error range along the trajectory of released rocks is 52–140 m (interquartile range). The height and location of the detachment zone can only be provided by seismic meth-

ods if the detachment process can be recorded and the subsequent impacts of the released rock mass can be located with sufficient confidence to allow back-calculation of the falling time. Rockfall release zones that are separated below the level of seismic location confidence can be deciphered from each other if the released volumes are different from each other and generate sufficiently distinct seismic characteristics. Hence, combining seismic and TLS methods can provide a very detailed complementary picture of rockfall activity.

Code and data availability. The seismic data used in this study are available in the Supplement, along with a detailed documentation about how to use them to reproduce the results of this study. The digital elevation model data set cannot be made freely available, but may be replaced by equivalent data to reproduce the results. TLS point cloud data are available upon request.

The Supplement related to this article is available online at <https://doi.org/10.5194/esurf-5-653-2017-supplement>.

Author contributions. MD contributed to seismic fieldwork and data analysis. SM contributed to TLS fieldwork and data processing. JMT, TAE and NH contributed to equipment provision, project planning and data analysis. All authors contributed to manuscript preparation.

Competing interests. The authors declare that they have no conflict of interest.

Special issue statement. This article is part of the special issue “4-D reconstruction of earth surface processes: multi-temporal and multi-spatial high resolution topography”. It is not associated with a conference.

Acknowledgements. The field work campaigns generously benefited from the support of Maggi Fuchs, Michael Krautblatter, Torsten Queißer and Fritz Haubold. The authors are thankful for these creative involvements. We further thank Josy Burke and Lorenz Michel for TLS field assistance. We are also thankful to the GIPP seismic device pool for providing six TC120s sensors and Cube³ data loggers. We also thank Valerie Zimmer, Clément Hibert, Agnès Helmstetter, an anonymous referee and the associate editor for their input to improve previous versions of the article.

The article processing charges for this open-access publication were covered by a Research Centre of the Helmholtz Association.

Edited by: Carlos Castillo

Reviewed by: Valerie Zimmer, Agnès Helmstetter, Clément Hibert, and one anonymous referee

References

- Allen, R.: Automatic phase pickers: Their present use and future prospects, *B. Seismol. Soc. Am.*, 72, S225–S242, 1982.
- Bivand, R. S., Pebesma, E. J., and Gomez-Rubio, V.: *Applied spatial data analysis with R*, Springer, 2013.
- Bourbie, T., Coussy, O., and Zinszner, B.: *Acoustics of porous media*, Gulf Publishing Company, 1987.
- Burtin, A., Bollinger, L., Vergne, J., Cattin, R., and Nabelek, J. L.: Spectral analysis of seismic noise induced by rivers: A new tool to monitor spatiotemporal changes in stream hydrodynamics, *J. Geophys. Res.*, 113, B05301, <https://doi.org/10.1029/2007JB005034>, 2008.
- Burtin, A., Bollinger, L., Cattin, R., Vergne, J., and Nabelek, J. L.: Spatiotemporal sequence of Himalayan debris flow from analysis of high-frequency seismic noise, *J. Geophys. Res.-Earth*, 114, f04009, <https://doi.org/10.1029/2008JF001198>, 2009.
- Burtin, A., Hovius, N., Milodowski, D. T., Chen, Y.-G., Wu, Y.-M., Lin, C.-W., Chen, H., Emberson, R., and Leu, P.-L.: Continuous catchment-scale monitoring of geomorphic processes with a 2-D seismological array, *J. Geophys. Res.*, 118, 1956–1974, <https://doi.org/10.1002/jgrf.20137>, 2013.
- Burtin, A., Hovius, N., McArdell, B. W., Turowski, J. M., and Vergne, J.: Seismic constraints on dynamic links between geomorphic processes and routing of sediment in a steep mountain catchment, *Earth Surf. Dynam.*, 2, 21–33, <https://doi.org/10.5194/esurf-2-21-2014>, 2014.
- Burtin, A., Hovius, N., and Turowski, J. M.: Seismic monitoring of torrential and fluvial processes, *Earth Surf. Dynam.*, 4, 285–307, <https://doi.org/10.5194/esurf-4-285-2016>, 2016.
- Dammeier, F., Moore, J. R., Haslinger, F., and Loew, S.: Characterization of alpine rockslides using statistical analysis of seismic signals, *J. Geophys. Res.*, 116, F04024, <https://doi.org/10.1029/2011JF002037>, 2011.
- Dietze, M.: *esais: Environmental seismology toolbox, r package version 0.3.1*, 2016.
- Dietze, M., Turowski, J. M., Cook, K. L., and Hovius, N.: Spatiotemporal patterns and triggers of seismically detected rockfalls, *Earth Surf. Dynam. Discuss.*, <https://doi.org/10.5194/esurf-2017-20>, in review, 2017.
- Ekström, G. and Stark, C. P.: Simple Scaling of Catastrophic Landslide Dynamics, *Science*, 339, 1416–1419, <https://doi.org/10.1126/science.1232887>, 2013.
- Farin, M., Mangeney, A., Toussaint, R., Rosny, J. d., Shapiro, N., Dewez, T., Hibert, C., Mathon, C., Sedan, O., and Berger, F.: Characterization of rockfalls from seismic signal: Insights from laboratory experiments, *J. Geophys. Res.-Sol. Ea.*, 120, 7102–7137, <https://doi.org/10.1002/2015JB012331>, 2015.
- FOEN: Hydrological data and forecasts, available at: <http://www.hydrodaten.admin.ch/en/2200.html>, last access: 11 April 2017.
- Gexcel: available at: <http://www.gexcel.it/en/>, last access: 31 August 2017.
- Gimbert, F., Tsai, V. C., and Lamb, M. P.: A physical model for seismic noise generation by turbulent flow in rivers, *J. Geophys. Res.*, 119, 2209–2238, <https://doi.org/10.1002/2014JF003201>, 2014.

- Helmstetter, A. and Garambois, S.: Seismic monitoring of Sechillienne rockslide (French Alps): Analysis of seismic signals and their correlation with rainfalls, *J. Geophys. Res.*, 115, F03016, <https://doi.org/10.1029/2009JF001532>, 2010.
- Hibert, C., Mangeney, A., Grandjean, G., and Shapiro, N. M.: Slope instabilities in Dolomieu crater, Réunion Island: From seismic signals to rockfall characteristics, *J. Geophys. Res.*, 116, F04032, <https://doi.org/10.1029/2011JF002038>, 2011.
- Hibert, C., Mangeney, A., Grandjean, G., Baillard, C., Rivet, D., Shapiro, N. M., Satriano, C., Maggi, A., Boissier, P., Ferrazzini, V., and Crawford, W.: Automated identification, location, and volume estimation of rockfalls at Piton de la Fournaise volcano, *J. Geophys. Res.*, 119, 1082–1105, <https://doi.org/10.1002/2013JF002970>, 2014.
- Hijmans, R. J.: raster: Geographic Data Analysis and Modeling, available at: <https://CRAN.R-project.org/package=raster> (last access: 10 October 2017), r package version 2.5-8, 2016.
- Krautblatter, M., Moser, M., Schrott, L., Wolf, J., and Morche, D.: Significance of rockfall magnitude and carbonate dissolution for rock slope erosion and geomorphic work on Alpine limestone cliffs (Reintal, German Alps), *Geomorphology*, 167–168, 21–34, <https://doi.org/10.1016/j.geomorph.2012.04.007>, 2012.
- Lacroix, P. and Helmstetter, A.: Location of Seismic Signals Associated with Microearthquakes and Rockfalls on the Séchillienne Landslide, French Alps, *B. Seismol. Soc. Am.*, 101, 341–353, <https://doi.org/10.1785/0120100110>, 2011.
- Larose, E., Carrière, S., Voisin, C., Bottelin, P., Baillet, L., Guéguen, P., Walter, F., Jongmans, D., Guillier, B., Garambois, S., Gimbert, F., and Massey, C.: Environmental seismology: What can we learn on earth surface processes with ambient noise?, *J. Appl. Geophys.*, 116, 62–74, <https://doi.org/10.1016/j.jappgeo.2015.02.001>, 2015.
- Levy, C., Mangeney, A., Bonilla, F., Hibert, C., Calder, E. S., and Smith, P. J.: Friction weakening in granular flows deduced from seismic records at the Soufrière Hills Volcano, Montserrat, *J. Geophys. Res.-Sol. Ea.*, 120, 7536–7557, <https://doi.org/10.1002/2015JB012151>, 2015.
- Lin, C. H., Jan, J. C., Pu, H. C., Chen, C. C., and Wu, Y. M.: Landslide seismic magnitude, *Earth Planet. Sc. Lett.*, 429, 122–127, <https://doi.org/10.1016/j.epsl.2015.07.068>, 2015.
- Manconi, A., Picozzi, M., Coviello, V., De Santis, F., and Elia, L.: Real-time detection, location, and characterization of rockslides using broadband regional seismic networks, *Geophys. Res. Lett.*, 43, 6960–6967, <https://doi.org/10.1002/2016GL069572>, 2016.
- Pebesma, E. J. and Bivand, R. S.: Classes and methods for spatial data in R, *R News*, 5, 2005.
- Pebesma, E. J. and Bivand, R. S.: sp: Classes and Methods for Spatial Data, available at: <https://CRAN.R-project.org/package=sp> (last access: 10 October 2017), r package version 1.2-3, 2016.
- Provost, F., Hibert, C., and Malet, J.-P.: Automatic classification of endogenous landslide seismicity using the Random Forest supervised classifier, *Geophys. Res. Lett.*, 44, 113–120, <https://doi.org/10.1002/2016GL070709>, 2017.
- Rabatel, A., Deline, P., Jaillet, S., and Ravael, L.: Rock falls in high-alpine rock walls quantified by terrestrial lidar measurements: A case study in the Mont Blanc area, *Geophys. Res. Lett.*, 35, L10502, <https://doi.org/10.1029/2008GL033424>, 2008.
- R Development Core Team: R: A Language and Environment for Statistical Computing, Vienna, Austria, available at: <http://CRAN.R-project.org> (last access: 10 October 2017), 2015.
- Ring, J.: The laser in astronomy, *New Scientist*, 344, 672–673, 1963.
- Stock, G., Collins, B., Santaniello, D., Zimmer, V., Wieczorek, G., and Snyder, J.: Historical rock falls in Yosemite National Park, U.S. Geological Survey Data Series 746, p. 17, 2013.
- Strunden, J., Ehlers, T. A., Brehm, D., and Nettesheim, M.: Spatial and temporal variations in rockfall determined from TLS measurements in a deglaciated valley, Switzerland, *J. Geophys. Res.*, 120, 1–23, <https://doi.org/10.1002/2014JF003274>, 2014.
- Suriñach, E., Vilajosana, I., Khazaradze, G., Biescas, B., Furdada, G., and Vilaplana, J. M.: Seismic detection and characterization of landslides and other mass movements, *Nat. Hazards Earth Syst. Sci.*, 5, 791–798, <https://doi.org/10.5194/nhess-5-791-2005>, 2005.
- Vilajosana, I., Suriñach, E., Abellán, A., Khazaradze, G., García, D., and Llosa, J.: Rockfall induced seismic signals: case study in Montserrat, Catalonia, *Nat. Hazards Earth Syst. Sci.*, 8, 805–812, <https://doi.org/10.5194/nhess-8-805-2008>, 2008.
- Volkwein, A., Schellenberg, K., Labiouse, V., Agliardi, F., Berger, F., Bourrier, F., Dorren, L. K. A., Gerber, W., and Jaboyedoff, M.: Rockfall characterisation and structural protection – a review, *Nat. Hazards Earth Syst. Sci.*, 11, 2617–2651, <https://doi.org/10.5194/nhess-11-2617-2011>, 2011.
- Welch, P.: The use of fast Fourier transform for the estimation of power spectra: A method based on time averaging over short, modified periodograms, *IEEE T. Acoust. Speech*, 15, 70–73, 1967.
- Zeckra, M., Hovius, N., Burtin, A., and Hammer, C.: Automated Detection and Classification of Rockfall Induced Seismic Signals with Hidden-Markov-Models, 2015 AGU Fall Meeting 2015 – NH34A-04, 2015.
- Zimmer, V. L. and Sitar, N.: Detection and location of rock falls using seismic and infrasound sensors, *Eng. Geol.*, 193, 49–60, 2015.
- Zimmer, V. L., Collins, B. D., Stock, G. M., and Sitar, N.: Rock fall dynamics and deposition: an integrated analysis of the 2009 Ah-wiyah Point rock fall, Yosemite National Park, USA, *Earth Surf. Proc. Landg.*, 37, 680–691, <https://doi.org/10.1002/esp.3206>, 2012.

4.4.3 Supplements for “Seismic monitoring of small alpine rockfalls–validity, precision and limitations”

Supplementary material

Michael Dietze

April 11, 2017

The article “Validity, precision and limitations of seismic-based rockfall monitoring” by Michael Dietze, Solmaz Mohadjer, Jens M. Turowski, Todd Ehlers and Niels Hovius, submitted to Earth Surface Dynamics, uses records of terrestrial laser scanning and broadband seismometers to investigate rockfall activity in a part of the Lauterbrunnen Valley, Bernese Oberland, Switzerland. This supplementary material provides the seismic signals of ten rockfall events, co-detected by both methods.

The documentation explains the general work that is needed to reproduce the main results discussed in the manuscript. However, there may be some changes in the parameter settings that cannot be fully implemented, here. One example is the setup of the STA/LTA picking routine, which needed adjustments simply due to the short lengths of the clipped seismic signals.

Content of the supplementary material

- Readme.pdf - the information document you are reading by now
- ASCII files labelled event_n.txt - seismic data of ten rockfall events
- seismic_stations.txt - summary of the seismic stations
- lidar.txt - lidar-detected rockfall information

Software requirements

As far as possible, all data preparation, analysis and visualisation steps were made using free and open software. To work with the seismic signals the following software needs to be or is recommended to be installed:

- R
- RStudio

Furthermore, the following R-packages need to be installed. Please consider that this documentation cannot guide you through the sometimes rocky paths to successful installations of R-packages. The internet is indeed a very good resource to solve issues during installation.

- raster (`install.packages(pkgs = "raster")`)
- sp (`install.packages(pkgs = "sp")`)
- devtools (`install.packages(pkgs = "devtools")`)
- eseis (`devtools::install_github(repo = "coffeemugger/eseis")`)

The package eseis is the central tool for working with seismic data in R. It is hosted on GitHub. All other packages are hosted on CRAN.

Loading the rockfall data sets

The content of the zip-archive rockfalls.zip needs to be extracted. The following code will import the data set of the first event to R. Note that “~/Downloads/” is the path to the extracted files and may need adjustments.

```
## load event 1
event_1 <- read.table(file = "~/Downloads/event_1.txt",
                      header = TRUE,
                      sep = ",",
                      stringsAsFactors = FALSE)
```

```
## show structure of the imported data set
str(event_1)
```

```
## 'data.frame':   12199 obs. of  5 variables:
## $ Time : chr  "2014-10-12 22:45:20.005" "2014-10-12 22:45:20.009" "2014-10-12 22:45:20.015" "2014-10-12 22:45:20.021" ...
## $ LAU02: int  61436 61467 61449 61432 61445 61451 61458 61444 61448 61451 ...
## $ LAU03: int  59069 59070 59062 59060 59059 59060 59066 59061 59062 59080 ...
## $ LAU04: int  63202 63174 63162 63163 63145 63157 63168 63154 63161 63143 ...
## $ LAU05: int  63488 63489 63492 63512 63510 63527 63541 63508 63455 63445 ...
```

The data set is a data frame with 12199 samples. The first element (column) is the time stamp as POSIXct-string. The subsequent four elements contain the raw seismic signals of the vertical component from four stations: LAU02 to LAU05.

To set these data into context, the seismic station summary file is needed, as well. It can be loaded in a similar way:

```
## load station summary file
stations <- read.table(file = "~/Downloads/seismic_stations.txt",
                      header = TRUE,
                      stringsAsFactors = FALSE)
```

```
## show content of the imported data set
print(stations)
```

```
##      ID      name      x      y      z sensor_type logger_type
## 1 LAU02 Gate of China 415766.2 5157910 1524      TC120s      Cube3ext
## 2 LAU03 Blatters Herbs 415398.0 5156814 1595      TC120s      Cube3ext
## 3 LAU04 Mbsquito Fabric 416236.0 5158777 832      TC120s      Cube3ext
## 4 LAU05      Funny Rain 416035.2 5157843 888      TC120s      Cube3ext
```

Each seismic station has an ID (corresponding to the names of the seismic signals of each event), a station name, location information in UTM coordinates, the elevation of deployment and information about the sensor and logger type.

Finally, to load the lidar-based rockfall events, the following code is needed. The volumes are given in m^3 , the coordinates in the UTM system. IDs correspond to those of the event files.

```
## load event 1
lidar <- read.table(file = "~/Downloads/lidar.txt",
                   header = TRUE,
                   sep = ",",
                   stringsAsFactors = FALSE)
```

```
## show content of the imported data set
print(lidar)
```

```
##      ID volume..m3. volume_error..m3.  x..UTM  y..UTM
## 1      1      0.201      0.0046020 415511.2 5156535
## 2      2      0.063      0.0066810 415522.5 5156542
## 3      3      0.201      0.0046020 415541.4 5156844
```

```
## 4 4      0.175      0.0113370 415565.5 5156845
## 5 5      0.053      0.0043365 415591.4 5156934
## 6 6      0.416      0.0208125 415950.0 5158213
## 7 7      0.891      0.0384285 415952.1 5157829
## 8 8      0.258      0.0138285 416005.0 5157897
## 9 9      0.192      0.0100230 416116.3 5158797
## 10 10    2.338      0.0854475 416037.4 5158649
```

Further requirements

Due to copyright reasons it was not possible to also deliver the digital elevation model (DEM) used to run the localisation routines. You may need to provide such a DEM by your own. The DEM used by the authors was provided by swissALTI3D. If you wish or need to use your own DEM make sure it is in metric units (e.g., the UTM reference system). You can basically import all common file formats to R using the package 'raster', such as GeoTiff, Erdas Imagine img, ESRI grids and many more that are or can be converted into matrix-like objects. Usually, search engines like 'Startpage' are very generous in providing useful help for importing geodata to R.

General workflows

Again, this documentation cannot give detailed into the R-package `eseis`. Please see the documentation of this package, e.g. by typing `?eseis` in the R console. Most of the following text uses event 7 as example, because it corresponds to figure 7 of the accompanying manuscript. There are a few preparation steps needed:

```
## load package
library("eseis")

## load event 7
data <- read.table(file = "~/Downloads/event_7.txt",
                  header = TRUE,
                  sep = ",",
                  stringsAsFactors = FALSE)

## assign time and signal data
t <- as.POSIXct(x = data$Time, tz = "UTC")
s <- as.list(data[, 2:5])
```

Picking event onsets and durations

The following code snippet filters the raw signals of all stations to the frequency window of interest for rockfall detection. The result is tapered to remove edge effects. Then, the signal envelope is calculated and the STA/LTA picking routine is applied to the first trace (i.e., LAU02, "Gate of China"). Note that due to the short length of the signal trace the STA/LTA setup differs from the values proposed in the manuscript.

```
## filter signal
s_f <- signal_filter(data = s,
                    dt = 1/200,
                    f = c(10, 30))

## taper signal to remove edge effects
s_f <- signal_taper(data = s_f, n = 1000)
```

```

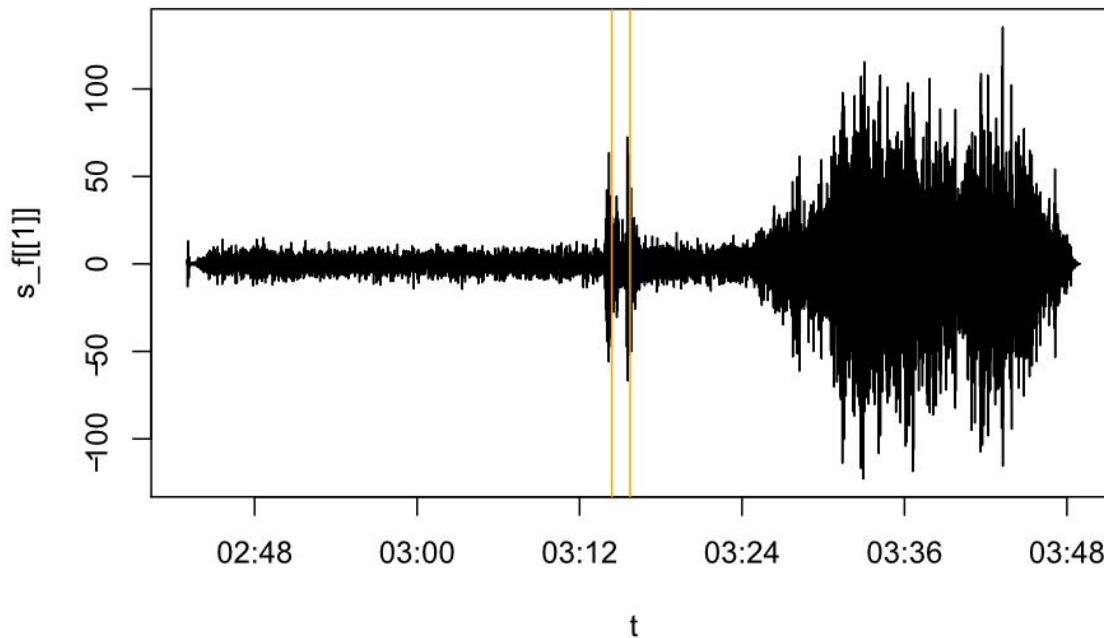
## calculate envelopes
s_e <- signal_envelope(data = s_f)

## pick events
events <- signal_alta(data = s_e[[1]],
                      time = t,
                      dt = 1/200,
                      sta = 100,
                      lta = 5000,
                      freeze = TRUE,
                      on = 5,
                      off = 3)

print(events)

## ID          start duration
## 1  1 2014-09-25 07:03:14 0.6710000
## 2  2 2014-09-25 07:03:15 0.5310001
## plot signal and event onsets
plot(x = t, y = s_f[[1]], type = "l")
abline(v = events$start, col = "orange")

```



Deconvolution of signals

Deconvolution is needed to remove the instrument response of the data and to plot it in meaningful units ($10 \log_{10} m^{2/s^2}$, dB).

```

## check that used sensors and loggers are in library
list_sensor()[[1]]

```

```

## $ID

```

```

## [1] "TC120s"
##
## $name
## [1] "Trillium Compact 120s"
##
## $manufacturer
## [1] "Nanonetics"
##
## $type
## [1] "broadband sei smoneter"
##
## $n_components
## [1] 3
##
## $comment
## [1] "Data taken from data base of Arnaud Burtin"
##
## $poles
## [1] 3.691e-02+3.702e-02i 3.691e-02-3.702e-02i -3.430e+02+0.000e+00i
## [4] -3.700e+02+4.670e+02i -3.700e+02-4.670e+02i -8.360e+02+1.522e+03i
## [7] -8.360e+02-1.522e+03i -4.900e+03+4.700e+03i -4.900e+03-4.700e+03i
## [10] -6.900e+03+0.000e+00i -1.500e+04+0.000e+00i
##
## $zeros
## [1] 0+ 0i 0+ 0i -392+ 0i -1960+ 0i -1490+1740i -1490-1740i
##
## $s
## [1] 749.1
##
## $k
## [1] 4.34493e+17

```

```
list_logger()[[1]]
```

```

## $ID
## [1] "Cube3ext"
##
## $name
## [1] "Cube 3ext"
##
## $manufacturer
## [1] "Omirecs"
##
## $type
## [1] "The greatest data logger in the world"
##
## $n_components
## [1] 3
##
## $comment
## [1] ""
##
## $AD
## [1] 2.4414e-07

```

```
## deconvolve signal
s_d <- signal_deconvolve(data = s,
                          dt = 1/200,
                          sensor = "TC120s",
                          logger = "Cube3ext")
```

Plotting the waveforms of seismic data

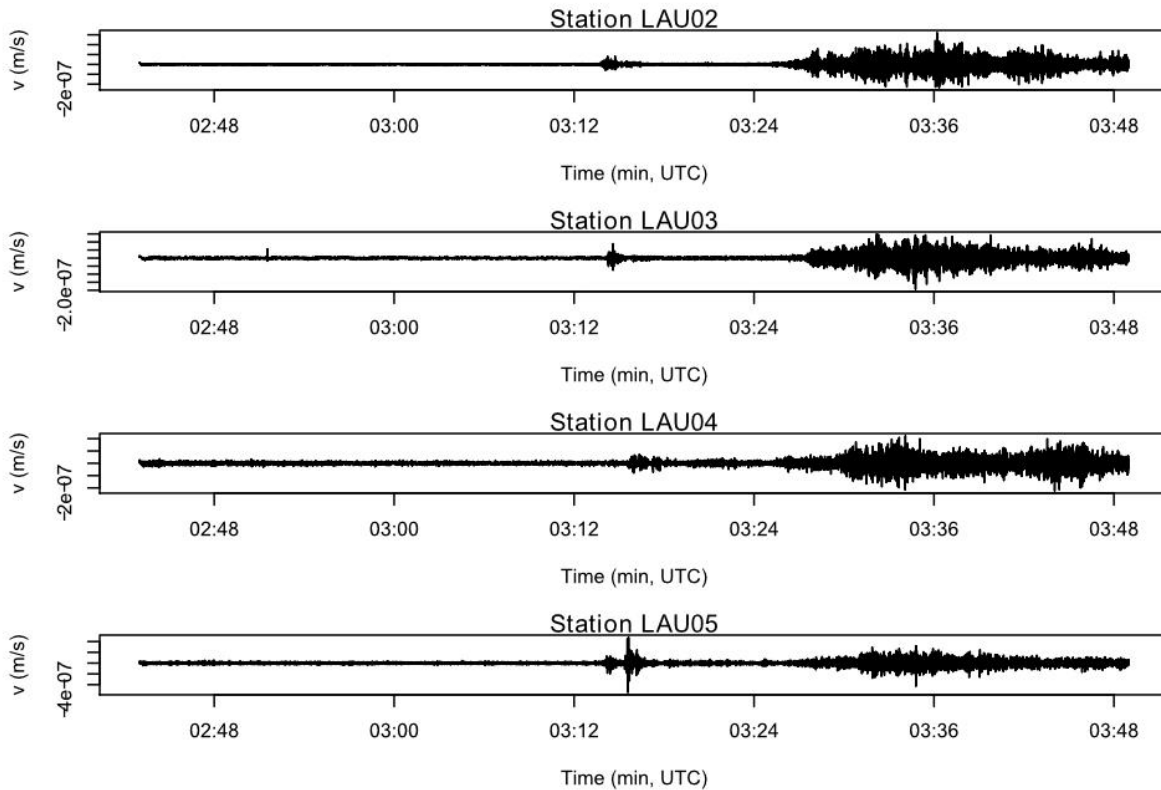
```
## filter (and taper) deconvolved signals
s_f_plot <- signal_filter(data = s_d,
                          dt = 1/200,
                          f = c(1, 90),
                          p = 0.01)

## prepare plot area
par(mfcol = c(4, 1), mar = c(5, 4, 1, 0))

## plot signals
for(i in 1:length(s_f_plot)) {

  plot(x = t,
        y = s_f_plot[[i]],
        type = "l",
        main = paste("Station", stations$D[i]),
        xlab = "Time (min, UTC)",
        ylab = "v (m/s)")

}
```

Calculating and plotting power spectral density estimates (PSD)

```
## truncate the signal and time vectors to the actual event
t_lim <- as.POSIXct(c("2014-09-25 07: 03: 12 UTC",
                    "2014-09-25 07: 03: 49 UTC"),
                  tz = "UTC")

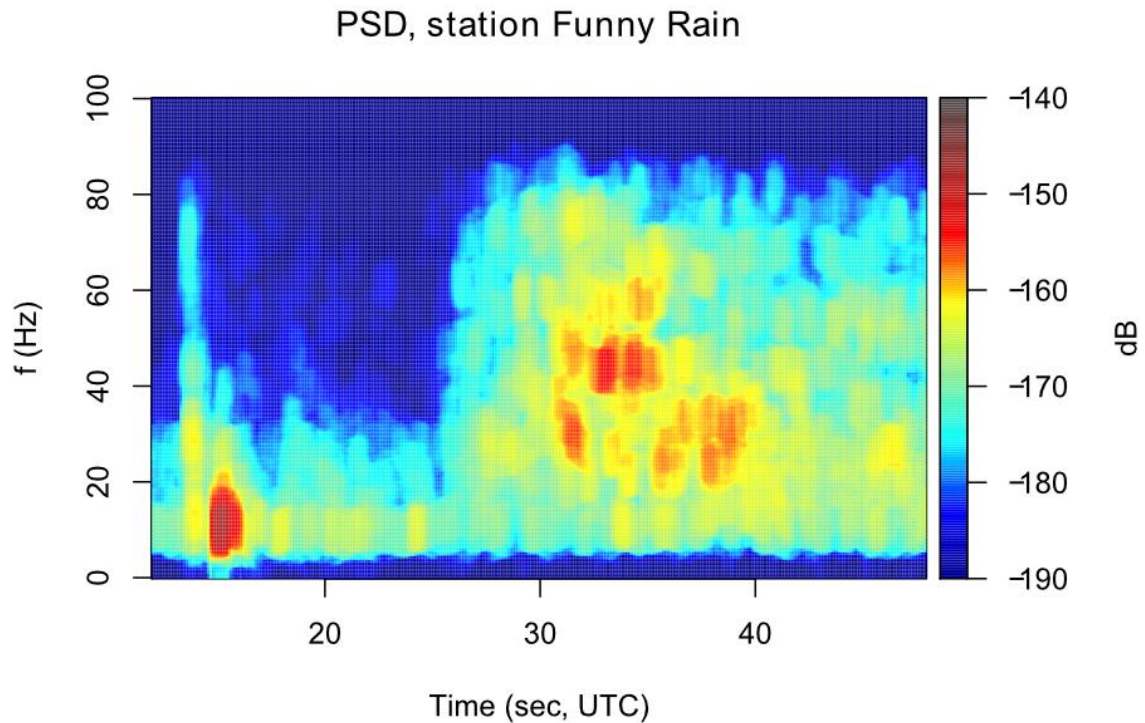
t_cut <- t[t >= t_lim[1] & t <= t_lim[2]]
s_cut <- lapply(X = s_f_plot, FUN = function(x) {

  x[t >= t_lim[1] & t <= t_lim[2]]
})

## calculate PSD
PSD <- signal_spectrogram(data = s_cut,
                          time = t_cut,
                          dt = 1/200,
                          Welch = TRUE,
                          window = 1.0,
                          overlap = 0.9,
                          window_sub = 0.8,
                          overlap_sub = 0.9,
                          multitaper = TRUE)

## plot PSD of station LAU05
```

```
plot_spectrogram(data = PSD[4],
  legend = "dB",
  xlim = c(-190, -140),
  xlab = "Time (sec, UTC)",
  ylab = "f (Hz)",
  main = "PSD, station Funny Rain")
```



Locating events

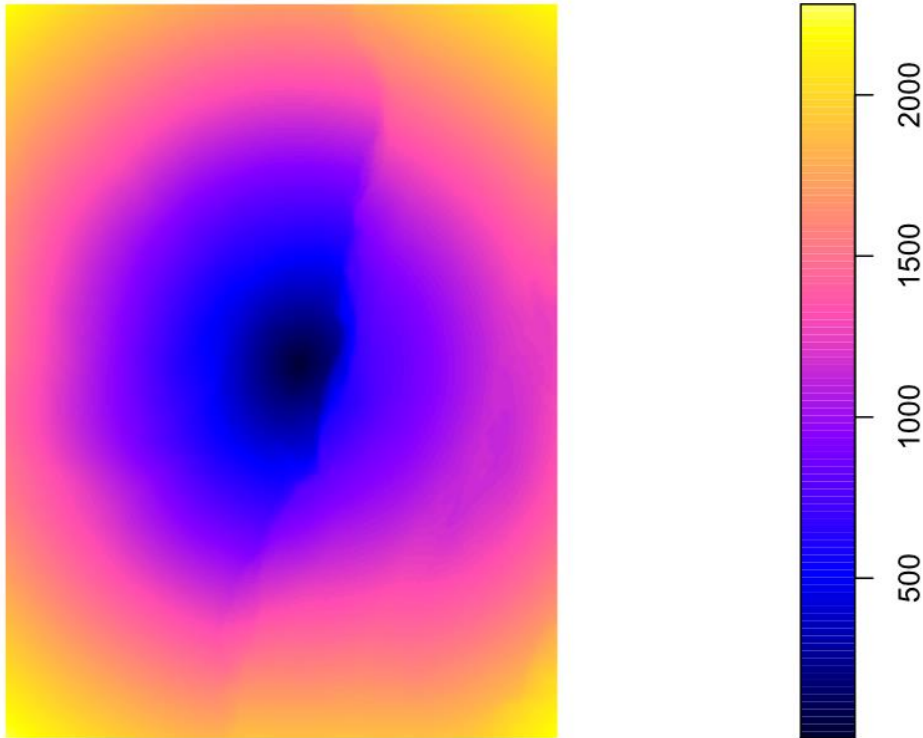
Locating events requires a DEM (see above). This DEM is used for the topography correction process. The workflow requires first to generate distance maps and inter-station distances, which are both required in the next step: signal migration.

Generate distance maps and inter-station distance matrix

```
## Loading required package: sp
## [1] "Processing station distances"
## generate distance data sets
D_data <- spatial_distance(stations = stations[, 3:4],
  dem = dem)

## plot distance map for station LAU02
plot(D_data$maps[[1]])

## show interstation distances
print(D_data$stations)
```



```
##           1           2           3           4
## 1    0.0000 1479.734 1625.5933  846.7072
## 2 1479.7343    0.000 3454.8019 3212.6337
## 3 1625.5933 3454.802    0.0000  998.1759
## 4  846.7072 3212.634  998.1759    0.0000
```

Migrate the signals

```
## filter signals to localisation window
s_migrate <- signal_filter(data = s,
                           dt = 1/200,
                           f = c(10, 20))

## calculate envelopes
s_migrate <- signal_envelope(data = s_migrate)

## convert signal list to matrix
s_migrate <- do.call(rbind, s_migrate)

## truncate time and signals to event +/- 2 seconds
t_lim <- as.POSIXct(c("2014-09-25 07:03:11 UTC",
                     "2014-09-25 07:03:21 UTC"),
                  tz = "UTC")

t_migrate <- t[t >= t_lim[1] & t <= t_lim[2]]
s_migrate <- s_migrate[,t >= t_lim[1] & t <= t_lim[2]]

## migrate the signal of rockfall 7
```

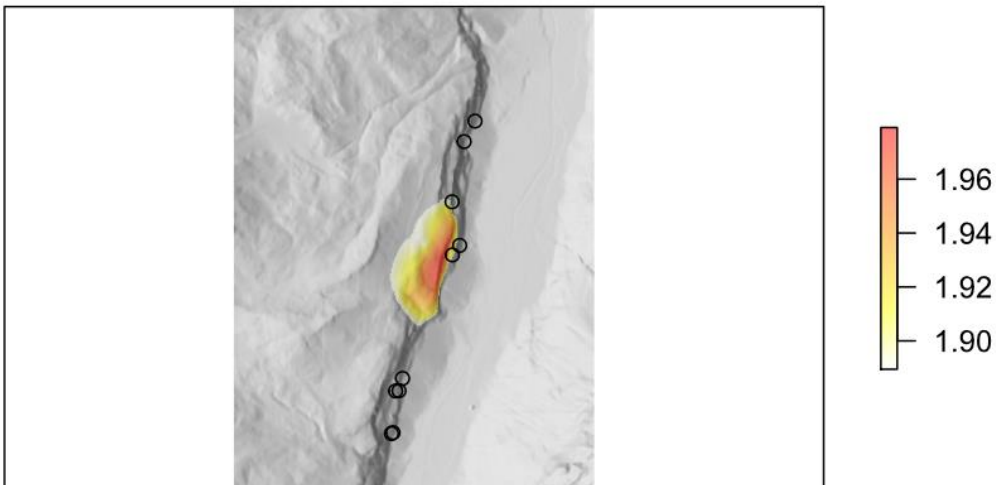
```

P <- spatial_migrate(data = s_migrate,
  d_stations = D_data$stations,
  d_map = D_data$maps,
  v = 2700,
  dt = 1/200,
  normalise = TRUE)

## [1] "No snr given. Will be calculated from signals"
## remove values below likelihood threshold
P_min <- 0.97
P_data@values[P_data@values < quantile(P_data@values,
  P_min,
  na.rm = TRUE)] <- NA

## plot output as hillshade overlay and add lidar points
plot(hs,
  col = grey.colors(250),
  legend = FALSE,
  ann = FALSE,
  axes = FALSE)
plot(P,
  add = TRUE,
  col = adjustcolor(col = rev(heat.colors(250)),
    alpha.f = 0.5))
points(x = lidar$x, y = lidar$y)

```



5 Conclusions

Geohazards are common phenomena in mountain environments. Studies related to geohazards in the India-Asia collision orogen and the European Alps have generated a large amount of data that have provided insights into regional- and continental-scales tectonics as well as geohazards in the region. By analyzing new and published datasets using a relational database and statistical methods (e.g., correlation analysis, frequency-magnitude calculations), results from this dissertation contribute to a better understanding of mountain landscape evolution and geohazards.

Four hypotheses have been investigated:

- 1) Quaternary fault locations, fault attributes and seismicity provide similar information on the spatial distribution of earthquake hazard as do conventional hazard maps. (Paper A in section 4.1.2, published)
- 2) Fault slip rates from GPS and geologic techniques provide consistent spatial and temporal slip rate information at the orogen scale, suggesting that over the Quaternary, there is minimal transience in slip rates (Paper B in section 4.2.2, published)
- 3) Rockfall frequency-magnitude calculations from laser scanning measurements are not sensitive to observation duration of 1.5 vs. >5 years. (Paper C in section 4.3.2, in revision)
- 4) Over different timescales (10^0 - 10^4 years), rockwall retreat rates can vary by an order of magnitude in a deglaciated alpine landscape. (Paper C in section 4.3.2, in revision)

In the following section, the results from section 4 are summarized and hypotheses outlined in section 2 are evaluated. Finally, the last section provides an outlook into future work related to geohazards in the India-Asia collision orogen and deglaciated valleys in the European Alps.

5.1 A summary – The hypotheses revisited

The India-Asia collision zone is a highly deformed orogen where a significant portion of the population live in structures that are vulnerable to earthquakes. Large earthquakes have devastated the region multiple times in the past, and with population growth and rapid urbanization in earthquake-prone areas, the potential impact of future earthquakes

has increased significantly. As demonstrated in section 4.1.2, the spatial distribution of earthquake hazards can be constrained by using a relational database where important earthquake-related datasets can be combined to reveal patterns in faulting and seismicity at regional- and orogen-scales. Regions that exhibit both Quaternary faulting and high seismicity, as revealed by our database, are similar to those that have been identified to be hazardous by conventional hazard maps. Likewise, regions showing little evidence for Quaternary faulting and instrumental/historical seismicity (e.g., the central Tarim Basin, inner Mongolia, and some parts of central Afghanistan) are comparable to those identified by conventional hazard maps as low hazard areas. Our database shows that nearly all regions of high seismicity overlap with where Quaternary faults have been mapped. These regions include but not limited to the Himalayan range, Tien Shan, Pamir and Hindu Kush mountain ranges. However, not all faulted areas within these regions show high levels of seismicity. For example, the database reveals both intense faulting and little seismicity throughout the Kyrgyz central Tien Shan. Hazard maps that are solely based on recorded seismicity have misleadingly identified these regions as low hazard (e.g., the Longmenshan fault system that produced the 2008 M7.9 Wenchuan earthquake). By including available paleoseismic, geodetic and geologic data related to Quaternary faulting, and without assumptions embedded in seismic hazard modelling, the relational database highlights and addresses the limitations of earthquake-related datasets, and hence, reveals a more accurate spatial pattern of hazards. **These observations address hypothesis 1:** a relational database can provide similar (if not more realistic) information on the spatial distribution of seismic hazards at regional- and continental-scales, as do conventional hazard maps.

By centralizing and displaying multiple datasets, the database can be used to document spatial and temporal variability in data. This variability can be further investigated through statistical analysis. For example, for many of the Quaternary faults documented in the fault database, there appears to be a large variability in slip rates obtained from different methods over different timescales. Whether this variability is real or is caused by limitations in the measurement techniques has been the subject of an ongoing debate. The statistical analysis of 57 GPS/Quaternary slip rate pairs for 19 Quaternary faults in the India-Asia collision zone, shows that a moderate percentage (71%) of the total variation in the Quaternary slip rates can be statistically explained by a linear relationship between the GPS and Quaternary rates. The remaining 29% may be caused by other factors including temporal variations in slip rates over the timescales individual methods are sensitive to (years to Myr), and/or methodological shortcomings. The analysis also reveals individual faults and Quaternary dating methods that appear to influence the relationship between GPS and Quaternary slip rates. Taken together, the results indicate that there is a general agreement between most GPS and Quaternary slip rates, and **partially support hypothesis 2**. Furthermore, the results suggest a fluid-like

behavior of Tibet by favoring slower slip rates for major strike-slip faults bounding the Tibetan Plateau (e.g., the Altyn Tagh and Karakorum faults).

Frequency-magnitude analysis is a statistical method that can be used to investigate the relationship between two variables (i.e., event frequency and size) in order to estimate and forecast patterns in data. Most hazards display a relationship between the occurrence rate and magnitude of an event. For rockfalls, the general pattern detected from their frequency-magnitude distribution is approximated by a negative power law. Our analysis of the TLS-derived rockfall inventory of 316 events detected over 5.2 years (February 2012 – April 2017) show a power law distribution with exponent b value of 0.61-0.72. When extrapolated, this relationship predicts the occurrence of a rockfall event of 1000 m³ to be every 3.34-6.40 years. This prediction was confirmed by the occurrence of a large rockfall (>3000 m³) in November 2018. Our results are in agreement within error with those obtained by Strunden et al. (2015) which were based on the analysis of a TLS-derived inventory of 122 rockfalls over 1.5 years. **These results support hypothesis 3** by showing that short-timescale observations indicate no statistically significant difference between TLS observations averaging over 1.5 versus 5.2 years. Therefore, short observation periods may be sufficient for establishing frequency-magnitude relationships and hazard characterization with TLS in similar settings.

Based on the above TLS rockfall inventory, the spatially averaged short-term (5.2 years) wall retreat rates are 0.03-0.08 mm/yr. These rates are significantly lower than the averaged long-term rates (0.33 mm/yr over ~11 ka) obtained from talus volume measurements. Three possibilities for these differences are: (1) short-term rates exclude large rockfall events and mainly reflect frequent small events, (2) long-term rates reflect periods of enhanced rockfall activity. This is typical of deglaciated settings where stress release due to unloading and debuttreassing of the rockwall following deglaciation has been shown to increase rockfall activity. (3) Enhanced rockfall activity can also be the effect of frost-shattering caused by climatic oscillations in the past 11 ka. **These observations support hypothesis 4**, and shed lights on post-glacial erosion and the role of rockfalls in the evolution of alpine landscapes.

5.2 Outlook and future work

In the past few decades, technological developments have contributed new tools for geohazards investigations in both space and time. These tools have generated a large amount of data that can be used to investigate mountain building processes and associated hazards over different spatial and temporal scales. All four studies in this dissertation use published and new datasets relevant to geohazards in order to document

the spatial and temporal patterns in geohazard datasets and to identify potential factors influencing these patterns.

While the relational Quaternary fault database provides constraints on the spatial location of earthquake hazards within the India-Asia collision zone, it reveals several issues that future studies should aim to address. These issues are rooted in fault data collection methods, reporting, representation and limitations. There currently exists no standard guideline for documenting and reporting fault position data, fault attributes (e.g., slip rates) and their associated uncertainties. For many of the faults in the India-Asia collision zone, fault geometries are poorly constrained, making only two-dimensional representations of fault traces possible. This leaves out potentially active nonplanar faults and those that are concealed beneath the Earth's surface (i.e., blind faults). Additionally, the instrumental, historical, and paleoseismic records of earthquakes for this region are shown to be short, incomplete, and sometimes inaccurate. Therefore, caution is required when assuming that these records can accurately sample a fault's seismic cycle and its fluctuations. To address these issues, we suggest that future studies related to earthquake hazards in the region focus on consistent documentation and reporting of fault related data, evaluation and improvement of historical archives, expansion of paleoseismic studies, and densification of geodetic network where fault geometry and deformation rates remain poorly constrained. Earthquake hazard maps face similar limitations, and only after recent devastating earthquakes (e.g., 2008 Wenchuan earthquake), their poor performance were revealed and explained. Objective analysis and testing of hazard maps as well as clear communication of uncertainties embedded in hazard map predictions with target users are essential steps in making them more useful to those who benefit from them.

Similarly, the analysis of GPS and Quaternary fault slip rates from the India-Asia collision zone shows how inconsistencies in calculating and reporting slip rate values and associated uncertainties contribute to the observed disparity between these rates. Therefore, development of reporting guidelines for calculating and reporting slip rates is not only of value to future seismic hazard studies but also allows for a more accurate comparison between results from different studies. This analysis calls for future studies to further investigate the deformation rates associated with specific Quaternary faults (e.g., Chaman, Karakorum and Talas Fergana faults) and specific Quaternary dating methods in order to distinguish between correct rates and those that reflect true temporal/spatial variations. Hence, we highlight slip rates values that should be treated with caution, and factors that should be taken into account when comparing rates from different methods.

The latter part of this study (section 4.3 and 4.4) provides new insights into post-glacial erosion and the evolution of the deglaciated Lauterbrunnen Valley in the Bernese Alps. Although this dissertation extends the observation duration of the TLS-derived

rockfall inventory by more than 4 years, several questions remain unresolved. While present-day rockfall activity appears to be widely distributed around the valley and correlate with freeze-thaw cycles (Strunden et al., 2015) and vegetation cover (Brehm, 2013; Ott, 2017), the spatial and temporal distributions of long-term rockfall activity and potential triggering factors remain unclear. Though debuttressing of rockwall following deglaciation and/or frost-shattering due to climatic oscillations in the past 11 ka have been suggested to enhance rockfall activity following deglaciation, it remains unclear if these factors affected (or continue to affect) the long-term rockfall activity in the Lauterbrunnen Valley. Future studies combining TLS data with cosmogenic surface exposure dating of rockfall scars as well as those at the bottom of the walls (following an approach developed by Domènech et al., 2018) may shed light on rockfall activity and possible triggering mechanisms in the past 11 ka.

The TLS-derived rockfall inventory covers an observation duration of ~5 years. This observation time can be extended further back in time using historical archives. Evidence of past rockfall events (e.g., large individual boulders) are common throughout the valley. However, data related to these events are sparse and often descriptive. This is one research area where future studies can significantly contribute to. Historical archives can be improved by detailed documentation of location and timing of large individual boulders that are deposited beyond the base of the talus slopes. Quaternary dating methods such as cosmogenic surface exposure dating (^{36}Cl) and dendrogeomorphological techniques can be applied to constrain the timing of these events. On the basis of in situ observation, historical reports, and/or techniques such as photogrammetry, boulder volumes can be constrained. Combining historical rockfall events with recent events increases the completeness of rockfall inventory which is essential for constructing a robust frequency-magnitude relationship.

Similar to historical events, reconstruction of talus deposits, volumes and long-term rockwall retreat calculations can benefit from a more quantitative assessment. Ott (2017) inferred the long-term rockwall retreat rate based on simplified geometries of talus deposits with little information about the underlying topography. Since no absolute date is available for the timing of last deglaciation in the Lauterbrunnen Valley, those obtained for neighboring valleys were assumed. Similarly, mean values for bedrock and talus density from previous studies conducted in similar settings were used. To more accurately document the long-term rockwall retreat rates in the Lauterbrunnen Valley, we suggest that future studies focus on more quantitative measurements of talus morphology, volumes, timing of talus accumulation, and talus material density.

As shown in this dissertation, accurate and substantially complete datasets are key to our understanding of the spatio-temporal dynamics and evolution of mountain landscape as well as mapping and monitoring mountain hazards. However, for geohazards datasets to be useful scientifically and societally, they should be usable and

used by diverse users. In the past three years, our fault database has provided up-to-date information on Quaternary faulting and seismicity within the India-Asia collision zone. The database is currently used by the global science community for a wide range of research studies. For example, our fault trace datasets have been used to constrain fault geometry and rupture behavior of recent earthquakes in the Pamir (Bie et al., 2018; Sangha et al., 2017), and to reconstruct and characterize historical and paleo-earthquakes in the Fann and Tien Shan mountains (Deev et al., 2018; Owczarek et al., 2017; Patyniak et al., 2017). Other studies that have utilized our fault trace dataset relate to geothermal energy (Magsi, 2018), denudation rates (Grin et al., 2018), geodesy (Perry et al., 2019), and tectonic evolution (Glorie et al., 2019; Komatsu, 2016) of the India-Asia collision zone. Additionally, our fault slip rate data have been used to constrain regional kinematic and dynamic models (Flesch et al., 2018; Jay et al., 2017 and 2018).

While academics are using the database for research investigations, it is not clear if (and how) the database engages the nonacademic users. Despite encouraging all users to submit new content and/or feedback via the website email or by completing the online feedback form on the website, very few use these services and those that do are academic users. Other feedback collection approaches such as short surveys and usability tests are necessary. The feedback data can then be analyzed for identifying trends in database usage and for making the database more useful to nonacademic users.

References for Sections 1-3 and 5

Abdrakhmatov, K. Y., Aldazhanov, S. A., Hager, B. H., Hamburger, M. W., Herring, T. A., Kalabaev, K. B., Makarov, V. I., Molnar, P., Panasyuk, S. V., Prilepin, M. T., Reilinger, R. E., Sadybakasov, I. S., Souter, B. J., Trapeznikov, Y. A., Tsurkov, V. Y., and Zubovich, A. V., 1996. Relatively recent construction of the Tien Shan inferred from GPS, *Nature*, 384, pp.450–453.

Abdrakhmatov, K., H.-B. Havenith, D. Delvaux, D. Jongmans, and P. Trefois, 2003. Probabilistic PGA and Arias intensity maps of Kyrgyzstan (Central Asia), *J. Seismol.*, 7, pp.203–220.

Abellán, A., Oppikofer, T., Jaboyedoff, M., Rosser, N.J., Lim, M., and Lato, M.J., 2014. Terrestrial laser scanning of rock slope instabilities. *Earth Surf. Process. Landf.* 39, pp.80–97, doi:10.1002/esp.3493.

Abellán, A., Vilaplana, J.M., Calvet, J., García-Sellés, D. and Asensio, E., 2011. Rockfall monitoring by Terrestrial Laser Scanning—case study of the basaltic rock face at Castellfollit de la Roca (Catalonia, Spain). *Natural Hazards and Earth System Sciences*, 11(3), pp.829-841.

Advance National Seismic System Comprehensive Catalog (ANSS ComCat): available at <http://earthquake.usgs.gov/earthquakes/search/>, last access: December 2014.

Advanced Industrial Science and Technology (AIST), Active Fault Database of Japan, April 4, 2016 version, Research Information Database DB095, National Institute of Advanced Industrial Science and Technology, Japan, available at: https://gbank.gsj.jp/activefault/index_e_gmap.html (last access: June 2017), 2016.

Barlow, J., Lim, M., Rosser, N., Petley, D., Brain, M., Norman, E. and Geer, M., 2012. Modeling cliff erosion using negative power law scaling of rockfalls. *Geomorphology*, 139, pp.416-424.

Bendick, R., Bilham, R., Khan, M. A., and Khan, S. F., 2007. Slip on active wedge thrust from geodetic observations of the 8 October 2005 Kashmir earthquake, *Geology*, 35, pp.267–270.

Bendick, R., Khan, S. F., Burgmann, R., Jouanne, F., Banerjee, P., Khan, M. A., and Bilham, R., 2015. Postseismic relaxation in Kashmir shows lateral variations in crustal architecture and materials, *Geophys. Res. Lett.*, 42, pp.4375–4383.

Bennett, G.L., Molnar, P., Eisenbeiss, H. and McArdell, B.W., 2012. Erosional power in the Swiss Alps: characterization of slope failure in the Illgraben. *Earth Surface Processes and Landforms*, 37(15), pp.1627-1640.

-
- Biagi, V.D., Napoli, M.L., Barbero, M. and Peila, D., 2017. Estimation of the return period of rockfall blocks according to their size. *Natural Hazards and Earth System Sciences*, 17(1), pp.103-113.
- Bie, L., Hicks, S., Garth, T., Gonzalez, P. and Rietbrock, A., 2018. 'Two go together': Near-simultaneous moment release of two asperities during the 2016 Mw 6.6 Muji, China earthquake. *Earth and Planetary Science Letters*, 491, pp.34-42.
- Bilham, R., 2009. The seismic future of cities. *Bulletin of Earthquake Engineering*, 7(4), pp.839-887, doi:10.1007/s10518-009-9147-0.
- Bilham, R., 2019. Himalayan earthquakes: a review of historical seismicity and early 21st century slip potential. *Geological Society, London, Special Publications*, 483, pp.483. doi:10.1144/SP483.16.
- Bilham, R., K. Larson, and J. Freymueller, 1997. GPS measurements of present-day convergence across the Nepal Himalaya, *Nature*, 386, pp.61–64.
- Bindi, D., K. Abdrakhmatov, S. Parolai, M. Mucciarelli, G. Grünthal, and A. Ischuk, 2012. Seismic hazard assessment in Central Asia: Outcomes from a site approach, *Soil Dynam. Earthq. Eng.* 37, pp.84–91.
- Brehm, D., 2013. LiDAR measurements of rockfall and ice cover in a deglaciated valley, Lauterbrunnen, Switzerland. master's thesis, University of Tübingen, Tübingen.
- Calais, E., Freed, A., Mattioli, G., Amelung, F., Jónsson, S., Jansma, P., Hong, S.H., Dixon, T., Prépetit, C. and Momplaisir, R., 2010. Transpressional rupture of an unmapped fault during the 2010 Haiti earthquake. *Nature Geoscience*, 3(11), pp.794.
- Cardona, O. D., 2005. Indicators for Disaster Risk and Risk Management. Program for Latin America and the Caribbean: Summary Report, Manizales, Columbia: Instituto de Estudios Ambientales, Universidad Nacional de Columbia.
- Carrea, D., Abellan, A., Derron, M.H. and Jaboyedoff, M., 2015. Automatic rockfalls volume estimation based on terrestrial laser scanning data. In *Engineering Geology for Society and Territory-Volume 2* (pp. 425-428). Springer, Cham.
- Chevalier, M.L., Ryerson, F.J., Tapponnier, P., Finkel, R.C., Van Der Woerd, J., Haibing, L., Qing, L., 2005. Slip-rate measurements on the Karakorum fault may imply secular variations in fault motion. *Science* 307 (5708), 411–414. doi:10.1126/science.1105466.
- Chevalier, M.L., Tapponnier, P., Van der Woerd, J., Ryerson, F.J., Finkel, R.C., and Li, H., 2012. Spatially constant slip rate along the southern segment of the Karakorum fault since 200 ka, *Tectonophysics*, 530–531, 152–179. doi:10.1016/j.tecto.2011.12.014.
-

-
- Christophersen, A., Litchfield, N., Berryman, K., Thomas, R., Basili, R., Wallace, L., Ries, W., Hayes, G.P., Haller, K.M., Yoshioka, T. and Koehler, R.D., 2015. Development of the Global Earthquake Model's neotectonic fault database. *Natural Hazards*, 79(1), pp.111-135.
- Clauset, A., Young, M. and Gleditsch, K.S., 2007. On the frequency of severe terrorist events: *Journal of Conflict Resolution*, 51(1), pp.58-87, doi:10.1177/0022002706296157.
- Deev, E., Korzhenkov, A., Turova, I., Pavlis, T.L., Luzhanskii, D., Mažeika, J., Abdieva, S. and Yudakhin, A., 2018. Large ancient earthquakes in the western Issyk-Kul basin (Kyrgyzstan, northern Tien Shan). *Journal of Asian Earth Sciences*, 166, pp.48-65.
- Dietze, M., Mohadjer, S., Turowski, J.M., Ehlers, T.A. and Hovius, N., 2017a. Seismic monitoring of small alpine rockfalls—validity, precision and limitations. *Earth Surface Dynamics*, 5(4), pp.653-668.
- Dietze, M., Turowski, J.M., Cook, K.L. and Hovius, N., 2017b. Spatiotemporal patterns, triggers and anatomies of seismically detected rockfalls. *Earth Surface Dynamics*, 5(4).
- Domènech, G., Corominas, J., Mavrouli, O., Merchel, S., Abellán, A., Pavetich, S. and Rugel, G., 2018. Calculation of the rockwall recession rate of a limestone cliff, affected by rockfalls, using cosmogenic chlorine-36. Case study of the Montsec Range (Eastern Pyrenees, Spain). *Geomorphology*, 306, pp.325-335.
- Dussauge, C., Grasso, J.R. and Helmstetter, A., 2003. Statistical analysis of rockfall volume distributions: Implications for rockfall dynamics. *Journal of Geophysical Research: Solid Earth*, 108(B6).
- Dussauge, C., Helmstetter, A., Grasso, J.R., Hantz, D., Desvarreux, P., Jeannin, M. and Giraud, A., 2002. Probabilistic approach to rock fall hazard assessment: potential of historical data analysis. *Natural Hazards and Earth System Science*, 2 (1/2), pp.15-26.
- Dusterhus, A., Rovere, A., Carlson, A., Horton, B., Klemann, V., Tarasov, L., Barlow, N., Bradwell, T., Clark, J., Dutton, A. and Gehrels, W.R., 2016. Palaeo-sea-level and palaeo-ice-sheet databases: problems, strategies, and perspectives. *Climate of the Past*, 12(4), pp.911-921.
- Flesch, L., Bendick, R. and Bischoff, S., 2018. Limitations on inferring 3D architecture and dynamics from surface velocities in the India-Eurasia collision zone. *Geophysical Research Letters*, 45(3), pp.1379-1386.
- Gallen, S.F., Clark, M.K., Godt, J.W., Roback, K. and Niemi, N.A., 2017. Application and evaluation of a rapid response earthquake-triggered landslide model to the 25 April 2015 Mw 7.8 Gorkha earthquake, Nepal. *Tectonophysics*, 714, pp.173-187.
-

-
- García Mayordomo, J., Insua Arévalo, J.M., Martínez Díaz, J.J., Jiménez Díaz, A., Martín Banda, R., Martín Alfageme, S.R., Álvarez Gómez, J.A., Rodríguez Peces, M.J., Pérez López, R., Rodríguez Pascua, M.Á. and Masana Closa, E., 2012. The Quaternary active faults database of Iberia (QAFI v. 2.0), *Journal of Iberian Geology*, 38(1), pp. 285-302.
- Gautam, D. and Rodrigues, H., 2015, October. Architectural and structural characteristics of indigenous Newari Chhen: Study of seismic risk and resilience in the historic urban nucleus of Bhaktapur city, Nepal. In *14th International Symposium on New Technologies for Urban Safety of Mega Cities in Asia (USMCA-2015)*, October (pp. 29-31).
- Gautam, D., Prajapati, J., Paterno, K.V., Bhetwal, K.K. and Neupane, P., 2016. Disaster resilient vernacular housing technology in Nepal. *Geoenvironmental Disasters*, 3(1), p.1.
- Glorie, S., Otasevic, A., Gillespie, J., Jepson, G., Danišik, M., Zhimulev, F.I., Gurevich, D., Zhang, Z., Song, D. and Xiao, W., 2019. Thermo-tectonic history of the Junggar Alatau within the Central Asian Orogenic Belt (SE Kazakhstan, NW China): Insights from integrated apatite U/Pb, fission track and (U–Th)/He thermochronology. *Geoscience Frontiers*, doi:10.1016/j.gsf.2019.05.005.
- Goldstein, M.L., Morris, S.A. and Yen, G.G., 2004. Problems with fitting to the power-law distribution. *The European Physical Journal B-Condensed Matter and Complex Systems*, 41(2), pp.255-258.
- Grämiger, L.M., Moore, J.R., Gischig, V.S. and Loew, S., 2018. Thermomechanical stresses drive damage of Alpine valley rock walls during repeat glacial cycles. *Journal of Geophysical Research: Earth Surface*, 123(10), pp.2620-2646.
- Grin, E., Schaller, M. and Ehlers, T.A., 2018. Spatial distribution of cosmogenic ¹⁰Be derived denudation rates between the Western Tian Shan and Northern Pamir, Tajikistan. *Geomorphology*, 321, pp.1-15.
- Guerin, A., D'Amato, J., Hantz, D., Rossetti, J.P. and Jaboyedoff, M., 2014. Investigating rockfall frequency using terrestrial laser scanner (Grenoble area, France). In *2014 Vertical Geology Conference. Lausanne*.
- Guzzetti, F., Malamud, B.D., Turcotte, D.L. and Reichenbach, P., 2002. Power-law correlations of landslide areas in central Italy. *Earth and Planetary Science Letters*, 195(3-4), pp.169-183.
- Guzzetti, F., Reichenbach, P. and Wieczorek, G.F., 2003. Rockfall hazard and risk assessment in the Yosemite Valley, California, USA. *Natural Hazards and Earth System Science*, 3(6), pp.491-503.
- Haller, K.M., Machette, M.N., Dart, R.L. and Rhea, B.S., 2004. US Quaternary fault and fold database released. *Eos, Transactions American Geophysical Union*, 85(22), pp.218-218.
-

-
- Halvorson, S.J. and Hamilton, J.P., 2007. Vulnerability and the erosion of seismic culture in mountainous Central Asia. *Mountain Research and Development*, 27(4), pp.322-331.
- He, W., Xiong, Z., Yuan, D. Y., Ge, W. P., and Liu, X. W., 2007. Paleoearthquake study on the Maqu fault of East Kunlun Active Fault, *Earthquake Res. China*, 22, pp.126–133.
- Hergarten, S., 2012. Topography-based modeling of large rockfalls and application to hazard assessment. *Geophysical research letters*, 39(13).
- Herman, F., Seward, D., Valla, P.G., Carter, A., Kohn, B., Willett, S.D. and Ehlers, T.A., 2013. Worldwide acceleration of mountain erosion under a cooling climate. *Nature*, 504(7480), p.423.
- Hewitt, K. and Mehta, M., 2012. Rethinking risk and disasters in mountain areas. *Journal of Alpine Research| Revue de Géographie Alpine*, 100-1.
- Horsburgh, J.S., Tarboton, D.G., Piasecki, M., Maidment, D.R., Zaslavsky, I., Valentine, D. and Whitenack, T., 2009. An integrated system for publishing environmental observations data. *Environmental Modelling & Software*, 24(8), pp.879-888.
- Ischuk, A., Bendick, R., Rybin, R., Molnar, P., Khan, S. F., Kuzikov, S., Mohadjer, S., Saydullaev, U., Ilyasova, Z., Schelochkov, G., and Zubovich, A. V., 2013. Kinematics of the Pamir and Hindu Kush regions from GPS geodesy, *J. Geophys. Res.-Sol. Ea.*, 118, pp.1–9.
- Ischuk, A., Bjerrum, L.W., Kamchybekov, M., Abdrakhmatov, K. and Lindholm, C., 2018. Probabilistic Seismic Hazard Assessment for the Area of Kyrgyzstan, Tajikistan, and Eastern Uzbekistan, Central Asia Probabilistic Seismic Hazard Assessment for the Area of Kyrgyzstan, Tajikistan, and Eastern Uzbekistan. *Bulletin of the Seismological Society of America*, 108(1), pp.130-144.
- Janeras, M., Jara, J.A., López, F., Marturià, J., Royán, M.J., Vilaplana, J.M., Aguasca, A., Fàbregas, X., Cabranes, F. and Gili, J.A., 2015. Using several monitoring techniques to measure the rock mass deformation in the Montserrat Massif. In *IOP Conference Series: Earth and Environmental Science* (Vol. 26, No. 1, p. 012030). IOP Publishing.
- Jay, C.N., Flesch, L.M. and Bendick, R.O., 2017. Kinematics and dynamics of the Pamir, Central Asia: Quantifying surface deformation and force balance in an intracontinental subduction zone. *Journal of Geophysical Research: Solid Earth*, 122(6), pp.4741-4762.
- Jay, C.N., Flesch, L.M. and Bendick, R.O., 2018. Kinematics and dynamics of the Pamir, Central Asia: Quantifying the roles of continental subduction in force balance. *Journal of Geophysical Research: Solid Earth*, 123(9), pp.8161-8179.
- Jomard, H., Cushing, E.M., Palumbo, L., Baize, S., David, C. and Chartier, T., 2017. Transposing an active fault database into a seismic hazard fault model for nuclear

facilities—Part 1: Building a database of potentially active faults (BDFa) for metropolitan France. *Natural Hazards and Earth System Sciences*, 17(9), pp.1573-1584.

Jouanne, F., Mugnier, J.L., Gamond, J.F., Le Fort, P., Pandey, M.R., Bollinger, L., Flouzat, M. and Avouac, J.P., 2004. Current shortening across the Himalayas of Nepal. *Geophysical Journal International*, 157(1), pp.1-14.

Klinger, Y., Xu, X., Tapponnier, P., Van der Woerd, J., Lasserre, C. and King, G., 2005. High-resolution satellite imagery mapping of the surface rupture and slip distribution of the $M_w \sim 7.8$, 14 November 2001 Kokoxili earthquake, Kunlun fault, northern Tibet, China. *Bulletin of the Seismological Society of America*, 95(5), pp.1970-1987.

Komatsu, T., 2016, Cenozoic Tectonic Evolution of the Pamir: A Review. *Journal of Geography (Chigaku Zasshi)*, 125(5), pp. 661-698. doi:10.5026/jgeography.125.661.

Korjenkov, A. M., Rust, D., Tibaldi, A., and Abdieva, S. V., 2012. Parameters of the Strong Paleoearthquakes Along the Talas-Fergana Fault, the Kyrgyz Tien Shan, *Earthquake Research and Analysis – Seismology, Seismotectonic and Earthquake Geology*, edited by: D'Amico, S., InTech, Croatia.

Krautblatter, M., Funk, D. and Günzel, F.K., 2013. Why permafrost rocks become unstable: a rock–ice-mechanical model in time and space. *Earth Surface Processes and Landforms*, 38(8), pp.876-887.

Kumar, A., and Pushplata, 2013. Vernacular practices: as a basis for formulating building regulations for hilly areas. *International Journal of Sustainable Built Environment*, 2(2), pp.183-192.

Kumar, S., Wesnousky, S. G., Rockwell, T. K., Briggs, R. W., Thakur, V. C., and Jayangondaperumal, R., 2006. Paleoseismic evidence of great surface rupture earthquakes along the Indian Himalaya, *J. Geophys. Res.-Sol. Ea.*, 111, B03304.

Lacroix, P., 2016. Landslides triggered by the Gorkha earthquake in the Langtang valley, volumes and initiation processes. *Earth, Planets and Space*, 68(1), p.46.

Langridge, R.M., Ries, W.F., Litchfield, N.J., Villamor, P., Van Dissen, R.J., Barrell, D.J.A., Rattenbury, M.S., Heron, D.W., Haubrock, S., Townsend, D.B. and Lee, J.M., 2016. The New Zealand active faults database. *New Zealand Journal of Geology and Geophysics*, 59(1), pp.86-96.

Lari, S., Frattini, P. and Crosta, G.B., 2014. A probabilistic approach for landslide hazard analysis. *Engineering geology*, 182, pp.3-14.

Lunina, O.V., Caputo, R., Gladkov, A.A. and Gladkov, A.S., 2014. Southern East Siberia Pliocene–Quaternary faults: database, analysis and inference. *Geoscience Frontiers*, 5(4), pp.605-619.

-
- Magsi, H.Z., 2018. Geothermal and Kinetic Energy Influence on the Melting of Permafrost at High Altitudes, Hindu Kush Karakoram, Western Himalayas. *Bahria University Research Journal of Earth Sciences*, 3.
- Malamud, B.D., Turcotte, D.L., Guzzetti, F. and Reichenbach, P., 2004. Landslide inventories and their statistical properties. *Earth Surface Processes and Landforms*, 29(6), pp.687-711.
- Michel, H., 1979, Buch der Talschaft Lauterbrunnen: Geschehnisse und Brauchtum in den Dörfern Lauterbrunnen, Wengen, Mürren, Gimmelwald, Stechelberg und Isenfluh; von den Wassern, Tieren, Pflanzen und der Bergwelt. Gemeinderat.
- Michetti, A. M., Serva, L., and Vittori, E., 2000. ITHACA Italy Hazard from Capable Faults: a database of active faults of the Italian onshore territory, CD-Rom and explicative notes, ANPA, Rome.
- Migliaccio, F., Locati, M., Carrion, D., Manenti, L. and Martocchia, M., 2019. A prototype HGIS for managing earthquake data from historical documents. *Geomatics, Natural Hazards and Risk*, 10(1), pp.118-135.
- Mohadjer, S., Bendick, R., Ischuk, A., Kuzikov, S., Kostuk, A., Saydullaev, U., Lodi, S., Kakar, D. M., Wasy, A., Khan, M. A., Molnar, P., Bilham, R., and Zubovich, A. V., 2010. Partitioning of India-Eurasia convergence in the Pamir-Hindu Kush from GPS measurements, *Geophys. Res. Lett.*, 37, L04305, doi:10.1029/2009GL041737.
- Mohadjer, S., Ehlers, T.A., Bendick, R., Stübner, K. and Strube, T., 2016. A Quaternary fault database for central Asia. *Natural Hazards and Earth System Sciences*, 16(2), pp.529-542. doi:10.5194/nhess-16-529-2016.
- Mulargia, F., Stark, P.B. and Geller, R.J., 2017. Why is probabilistic seismic hazard analysis (PSHA) still used? *Physics of the Earth and Planetary Interiors*, 264, pp.63-75.
- Ortega, J., Vasconcelos, G., Rodrigues, H., Correia, M. and Lourenço, P.B., 2017. Traditional earthquake resistant techniques for vernacular architecture and local seismic cultures: A literature review. *Journal of Cultural Heritage*, 27, pp.181-196.
- Orzetto, 2010, An illustration of the coefficient of determination for a linear regression, File licensed under Creative Commons Attribution-Share Alike 3.0 Unported (CC BY-SA 3.0), File retrieved from: <https://tinyurl.com/y42xypeb>
- Ott, M.B., 2017, Quantification of present and Holocene rockfall activity in the Lauterbrunnen Valley (Switzerland), Master thesis, University of Tübingen, Tübingen.
- Overpeck, J.T., Meehl, G.A., Bony, S. and Easterling, D.R., 2011. Climate data challenges in the 21st century. *Science*, 331(6018), pp.700-702.

-
- Owczarek, P., Opała-Owczarek, M., Rahmonov, O. and Mendecki, M., 2017. 100 Years of earthquakes in the Pamir region as recorded in juniper wood: a case study of Tajikistan. *Journal of Asian Earth Sciences*, 138, pp.173-185.
- Pagani, M., Garcia-Pelaez, J., Gee, R., Johnson, K., Poggi, V., Styron, R., Weatherill, G., Simionato, M., Viganò, D., Danciu, L., and Monelli, D., 2018. Global Earthquake Model (GEM) Seismic Hazard Map (version 2018.1 - December 2018), doi:10.13117/GEM-GLOBAL-SEISMIC-HAZARD-MAP-2018.1.
- Patyniak, M., Landgraf, A., Dzhumabaeva, A., Abdrakhmatov, K.E., Rosenwinkel, S., Korup, O., Preusser, F., Fohlmeister, J., Arrowsmith, J.R. and Strecker, M.R., 2017. Paleoseismic Record of Three Holocene Earthquakes Rupturing the Issyk-Ata Fault near Bishkek, North Kyrgyzstan Paleoseismic Record of Three Holocene Earthquakes Rupturing the Issyk-Ata Fault near Bishkek. *Bulletin of the Seismological Society of America*, 107(6), pp.2721-2737.
- Perry, M., Kakar, N., Ischuk, A., Metzger, S., Bendick, R., Molnar, P. and Mohadjer, S., 2019. Little Geodetic Evidence for Localized Indian Subduction in the Pamir-Hindu Kush of Central Asia. *Geophysical Research Letters*, 46(1), pp.109-118.
- Picarelli, L., Oboni, F., Evans, S.G., Mostyn, G., and Fell, R., 2005. Hazard characterization and quantification. In: Hungr, O., Fell, R., Couture, R., Eberhardt, E. (Eds.), *Landslide Risk Management*. Taylor and Francis, London, pp. 27–61.
- Puetz, S.J., 2018. A relational database of global U-Pb ages. *Geoscience Frontiers*, 9, pp. 877-891, doi:10.1016/j.gsf.2017.12.004.
- Ran, Y., Chen, L., Chen, J., Wang, H., Chen, G., Yin, J., Shi, X., Li, C., and Xu, X., 2010. Paleoseismic evidence and repeat time of large earthquakes at three sites along the Longmenshan fault zone, *Tectonophysics*, 491, pp.141–153.
- Reigber, C., Michel, G. W., Galas, R., Angermann, D., Klotz, J., Chen, J. Y., Papschev, A., Arslanov, R., Tzurkov, V. E., and Ishanov, M. C., 2001. New space geodetic constraints on the distribution of deformation in Central Asia, *Earth Planet. Sci. Lett.*, 191, pp.157-165.
- Robinson, A. C., 2009. Geologic offsets across the northern Karakorum fault: Implications for its role and terrane correlations in the western Himalayan-Tibetan orogen, *Earth Planet. Sci. Lett.*, 279, pp.123–130.
- Rosser, N., Lim, M., Petley, D., Dunning, S. and Allison, R., 2007. Patterns of precursory rockfall prior to slope failure. *Journal of geophysical research: earth surface*, 112(F4).
- Ruleman, C. A., Crone, A. J., Machette, M. N., Haller, K. M., and Rukstales, K. S., 2007. Map and Database of Probable and Possible Quaternary Faults in Afghanistan, United

-
- States Geological Survey Open-File Report, 2007-1103, available at: <http://pubs.usgs.gov/of/2007/1103/> (last access: July 2015).
- Sangha, S., Peltzer, G., Zhang, A., Meng, L., Liang, C., Lundgren, P. and Fielding, E., 2017. Fault geometry of 2015, Mw7. 2 Murghab, Tajikistan earthquake controls rupture propagation: Insights from InSAR and seismological data. *Earth and Planetary Science Letters*, 462, pp.132-141.
- Santana, D., Corominas, J., Mavrouli, O. and Garcia-Sellés, D., 2012. Magnitude–frequency relation for rockfall scars using a Terrestrial Laser Scanner. *Engineering geology*, 145, pp.50-64.
- Sawyer, D.S., Henning, A.T., Shipp, S. and Dunbar, R.W., 2005. A data rich exercise for discovering plate boundary processes. *Journal of Geoscience Education*, 53(1), 65-74.
- Schiffman, C., Bali, B. S., Szeliga, W., and Bilham, R., 2013. Seismic slip deficit in the Kashmir Himalaya from GPS observations, *Geophys. Res. Lett.*, 40, pp.5642–5645.
- Schild, A., 2008. ICIMOD's position on climate change and mountain systems. *Mountain Research and Development*, 28(3), pp.328-332.
- Schneider, A., Hommel, G. and Blettner, M., 2010. Linear regression analysis: part 14 of a series on evaluation of scientific publications. *Deutsches Ärzteblatt International*, 107(44), p.776.
- Schwarz, A., 2019. Assessing the performance of structure-from-motion and terrestrial LiDAR for rockfall detection, Master thesis, University of Tübingen, Tübingen.
- Strecker, M. R., Hilley, G. E., Arrowsmith, J. R., and Coutand, I., 2003. Differential structural and geomorphic mountain-front evolution in an active continental collision zone: the northwest Pamir, southern Kyrgyzstan, *Geol. Soc. Am. Bull.*, 115, pp.166–181.
- Stein, S., Geller, R.J. and Liu, M., 2012. Why earthquake hazard maps often fail and what to do about it. *Tectonophysics*, 562, pp.1-25.
- Strunden, J., Ehlers, TA, Brehm, D. and Nettesheim, M., 2015. Spatial and temporal variations in rockfall determined from TLS measurements in a deglaciated valley, Switzerland. *Journal of Geophysical Research: Earth Surface*, 120 (7), pp.1251-1273.
- Taylor, M. and Yin, A., 2009. Active structures of the Himalayan-Tibetan orogen and their relationships to earthquake distribution, contemporary strain field, and Cenozoic volcanism, *Geosphere*, 5, pp.199–214.
- Tobler, D. and Keusen, H.R., 2013. Hazard Zoning in Areas with Major Deep-Seated Landslides: Case Study from Switzerland. In *Landslide Science and Practice* (pp. 337-343). Springer, Berlin, Heidelberg.

-
- Tonini, M. and Abellan, A., 2014. Rockfall detection from terrestrial LiDAR point clouds: A clustering approach using R. *Journal of Spatial Information Science*, 2014(8), pp.95-110.
- Ul-Hadi, S., Khan, S.D., Owen, L.A., Khan, A.S., Hedrick, K.A., Caffee, M.W., 2013. Slip rates along the Chaman fault: implication for transient strain accumulation and strain partitioning along the western Indian plate margin. *Tectonophysics*, 608, pp.389–400.
- Ullah, S., Bindi, D., Pilz, M., Danciu, L., Weatherill, G., Zuccolo, E., Ischuk, A., Mikhailova, N., Abdrakhmatov, K., and Parolai, S., 2015. Probabilistic seismic hazard assessment for Central Asia, *Ann. Geophys.* 58, no. 1, S0103, 21 pp., doi: 10.4401/ag-6687.
- United States Geological Survey (USGS), 2014. Largest and Deadliest Earthquakes by Year: 1990–2014, available at: <http://earthquake.usgs.gov/earthquakes/eqarchives/year/byyear.php> (last access: 24 July 2015).
- van Veen, M., Hutchinson, D.J., Kromer, R., Lato, M. and Edwards, T., 2017. Effects of sampling interval on the frequency-magnitude relationship of rockfalls detected from terrestrial laser scanning using semi-automated methods. *Landslides*, 14(5), pp.1579-1592.
- Veikkolainen, T.H., Biggin, A.J., Pesonen, L.J., Evans, D.A. and Jarboe, N.A., 2017. Advancing Precambrian palaeomagnetism with the PALEOMAGIA and PINT (QPI) databases. *Scientific data*, 4, p.170068.
- Wang, H., Liu, M., Cao, J., Shen, X. and Zhang, G., 2011. Slip rates and seismic moment deficits on major active faults in mainland China. *Journal of Geophysical Research: Solid Earth*, 116(B2)
- Washburn, Z., Arrowsmith, J. R., Dupont-Nivet, G., Feng, W. X., Qiao, Z. Y., and Zhengle, C., 2003. Paleoseismology of the Xorxol Segment of the Central Altyn Tagh Fault, Xinjiang, China, *Ann. Geophys.-Italy*, 46, pp.1015–1034.
- Zhang, P., Yang, Z.X., Gupta, H.K., Bhatia, S.C. and Shedlock, K.M., 1999. Global seismic hazard assessment program (GSHAP) in continental Asia, *Annali di Geofisica*, 42(6), pp.1167-1190.
- Zubovich, A. V., Wang, X., Scherba, Y. G., Schelochkov, G. G., Reilinger, R., Reigber, C., Mosienko, O. I., Molnar, P., Michajljow, W., Makarov, V. I., Li, J., Kuzikov, S. I., Herring, T. A., Hamburger, M. W., Hager, B. H., Dang, Y., Bragin, V. D., and Beisenbaev, R. T., 2010. GPS velocity field for the Tien Shan and surrounding regions, *Tectonics*, 29, TC6014, doi:10.1029/2010TC002772.

Appendix A: Location of data files

This appendix indicates the location of data files created during the PhD project and stored on the server of the Earth Surface Dynamics group at the University of Tübingen.

A.1 Manuscripts

All papers and manuscripts presented in section 4 of this dissertation are located at:

</esd/esd01/docs/solmazm/papers>

where the subfolders for the different manuscripts exist (/paper_1, /paper_2, /paper_3, /paper_4). In each subfolder, files containing the text, figures, tables, and the correspondence during the review process are stored. These files are stored in folders titled: /text, /figures, /tables, /review.

A.2 Datasets & Source Codes

Several datasets and source codes have been generated during this PhD project:

All datasets and documentations related to **section 4.1** of this dissertation (Quaternary fault database) are located in the following folders:

- ArcGIS files: /esd/esd01/share/arc/central_asia/solmaz with the following relevant subfolders:
 - Final ArcMap: /database_arcmap/
 - Earthquake data: /points/earthquakes
- ASTER DEM and other background files:
/esd/esd01/share/arc/central_asia/Roland/CentralAsia with the following subfolders:
 - ASTER DEM: /final/
 - Country boundaries: /Country Boundaries/data0
- Database source code files:
/esd/esd01/docs/solmazm/dissertation/source_code/fault_database
 - Also available on ESD GIT Server: <https://esdynamics.geo.uni-tuebingen.de/git/willi/openfaults>

All datasets and documentations related to **section 4.2** of this dissertation (Review of GPS and Quaternary fault slip rates) are located in the following folders:

- ArcGIS files: /esd/esd01/share/arc/central_asia/solmaz
 - Final ArcMap: /database_arcmap/

- Slip rate analysis source code:
/esd/esd01/docs/solmazm/dissertation/source_code/slip_rate_analysis
 - The latest version is also available on ESD GIT Server:
<https://esdynamics.geo.uni-tuebingen.de/git/willi/>

All datasets and documentations related to **section 4.3** of this dissertation (Quantifying rockfall frequency-magnitude relationships and wall retreat rates) are located in the following folders:

- TLS campaign data: /esd/esd02/data/lidar_data_vol1/Switzerland/Lauterbrunnen/
 - Raw TLS data and photos: [/raw data](/raw_data)
- JRC Reconstructor project files:
/esd/esd02/data/lidar_data_vol1/Switzerland/Lauterbrunnen/archive_smohadjer_JRC_proj
- Rockfall frequency-magnitude analysis source code:
/esd/esd01/docs/solmazm/dissertation/source_code/rockfall_frequency_magnitude
 - The latest version is also available on ESD GIT Server:
<https://esdynamics.geo.uni-tuebingen.de/git/willi/FrequencyMagnitudeAnalysis>
- TLS fieldwork files (e.g., scan positions and equipment checklist):
/esd/esd02/data/lidar_data_vol1/Switzerland/Lauterbrunnen/Documentation

A.3 Dissertation Files

Files used to create this dissertation are located at:

</esd/esd01/docs/solmazm/dissertation>

where the subfolders for text and figures used for creating this dissertation exist (/text, /figures).

References for section 1-3 and 5 of this dissertation are accessible via Ehlers ESD Group Library on Zotero:

- /regions/ and the following subfolders: Central Asia, Alps Europe, Lauterbrunnen
- /geologic hazards/ and the following subfolders: active_faults and mass_wasting (/power_law)
- and others such as /database/, /remote sensing/, /teaching/, and /not geology/